

Turbulent large-scale structures over heterogeneous surfaces

Zur Erlangung des akademischen Grades eines
Doktors der Ingenieurwissenschaften (Dr.-Ing.)

von der KIT-Fakultät für Maschinenbau des
Karlsruher Instituts für Technologie (KIT)

angenommene

Dissertation

von

M.Sc. Kay Schäfer

Tag der mündlichen Prüfung:

16. Februar 2023

Hauptreferentin:

Prof. Dr.-Ing. Bettina Frohnappel

Korreferenten:

Prof. Dr. Markus Uhlmann

Prof. Dr. Juan Pedro Mellado



This document is licensed under a Creative Commons Attribution-ShareAlike 4.0 International License (CC BY-SA 4.0):
<https://creativecommons.org/licenses/by-sa/4.0/deed.en>

Abstract

Surfaces with heterogeneous properties occur in many engineering and geophysical flows, as atmospheric flows over urban and rural areas illustrates. However, due to the multitude of surface patterns, variation in textures and a variety of different scales, the current knowledge on the influence of heterogeneous surfaces on the exchange processes of momentum, heat and mass transport of turbulent flows is limited. The aim of the thesis is to contribute to a better understanding of these processes by focusing on a specific subtype of heterogeneous surface, that is spanwise heterogeneous surfaces, where the surface heterogeneity occurs perpendicular to the main flow direction. These surfaces are known to generate turbulent secondary motions, which appear as large-scale counter-rotating vortices aligned with the flow. These can significantly alter the exchange processes of turbulent flows. One objective of the thesis is to investigate the influence of lateral variations in surface drag in combination with relative wall elevation on the formation of secondary motions. In addition, the influence of spanwise heterogeneous surfaces on turbulent large-scale structures, which can also be found above homogeneous wall conditions, is examined. All investigations of the thesis are based on direct numerical simulations (DNS), which resolve all relevant turbulent scales. For secondary motions over alternating smooth- and rough-wall strips, it is found that the strength of secondary motions correlates with the relative height difference between these strips, independent of which strip is protruding. However, the rotational direction of the secondary motions depends whether the roughness strip is protruding or recessed, which is related to the distribution of wall-normal deflections of spanwise velocity at the protruding strip edges. The interaction and coexistence of secondary motions with large-scale and very-large-scale motions (LSM/VLSM) is investigated in turbulent open-channel flows with streamwise-aligned ridges. The results shows that coexistence between secondary motions and VLSMs is possible for large ridge spacings $S \geq 4\delta$, where δ is the half-channel height, such that VLSMs emerge in the valleys between the ridges that are unaffected by secondary motions. Reducing the strength of secondary motions by decreasing the ridge height, eventually leads to the reappearance of VLSMs at the ridges. By means of proper orthogonal decomposition (POD), instantaneous large-scale structures are detected for dense ridge spacings ($S \leq \delta$), that resemble LSMs and extending over adjacent ridges, which is not evident from the mean secondary motions. In addition, the influence of spanwise heterogeneous surfaces on turbulent convective large-scale structures, which form under the concurrent action of buoyancy and shear, are examined in turbulent channel flows with streamwise-aligned ridges. Among these structures are streamwise rolls, which are long coherent structures aligned with the flow direction. Their range of occurrence is significantly reduced by spanwise heterogeneous surfaces compared to homogeneous smooth-wall conditions, which is related to the increased drag exerted by the ridges. Furthermore, the ridges can introduce slow dynamics of the streamwise rolls in case the spanwise ridge spacing is in the order of the roll's width.

Kurzfassung

Oberflächen mit heterogenen Eigenschaften kommen in vielen technischen und geophysikalischen Strömungen vor, wie beispielsweise atmosphärische Strömungen über urbanen und ländlichen Flächen verdeutlichen. Aufgrund der zahlreichen Oberflächenformen, unterschiedlicher Texturen und der Vielzahl involvierter Skalen ist das derzeitige Wissen über den Einfluss heterogener Oberflächen auf die Austauschprozesse von Impuls-, Wärme- und Stofftransport in turbulenten Strömungen jedoch begrenzt. Das Ziel dieser Arbeit ist es, zu einem besseren Verständnis dieser Prozesse beizutragen, indem der Fokus auf eine spezielle Unterart heterogener Oberflächen gelegt wird, nämlich auf spannweitig heterogene Oberflächen, bei denen die Oberflächenheterogenität senkrecht zur Hauptströmungsrichtung auftritt. Diese Oberflächen sind bekannt dafür turbulente Sekundärströmungen auszubilden, welche die Austauschprozesse turbulenter Strömung erheblich verändern. Diese Sekundärströmungen treten dabei in Form von großskaligen und gegenläufigen Wirbeln senkrecht zur Hauptströmungsrichtungen auf. Die Thesis untersucht einerseits den Einfluss von seitlichen Variationen des Oberflächenwiderstands in Kombination mit unterschiedlichen relativen Wandhöhen auf die Entstehung von Sekundärströmungen. Andererseits, wird der Einfluss von spannenweitig heterogenen Oberflächen auf turbulente großskalige Strukturen untersucht, welche auch über homogenen Wandbedingungen anzutreffen sind. Die Untersuchungen in dieser Arbeit basieren auf direkten numerischen Simulationen (DNS), die alle relevanten turbulenten Skalen auflösen. Für Sekundärströmungen über abwechselnd glatten und rauen Wandstreifen wird gezeigt, dass deren Stärke mit dem relativen Höhenunterschied zwischen den Streifen korreliert, unabhängig davon welcher Streifen hervorsteht. Die Drehrichtung der Sekundärströmung hängt jedoch davon ab, ob der Rauheitsstreifen hervorsteht oder vertieft ist, was mit der Verteilung der wandnormalen Ablenkungen der spannweitigen Geschwindigkeit an den hervorstehenden Streifenkanten zusammenhängt. Die Interaktion und Koexistenz zwischen Sekundärströmungen mit *large-* und *very-large-scale motions* (LSM/VLSM) wird in turbulenten Strömungen offener Kanäle mit in Strömungsrichtung orientierten Stegen untersucht. Die Ergebnisse zeigen, dass Koexistenz zwischen Sekundärströmungen und VLSMs bei großen Stegabständen $S \geq 4\delta$ möglich ist, wobei δ die halbe Kanalhöhe ist. Somit können VLSMs in den von Sekundärströmungen unbeeinflussten Bereichen der Täler zwischen den Stegen entstehen. Desweiteren kann gezeigt werden, dass die verringerte Stärke der Sekundärströmung durch Abnahme der Steghöhe schließlich zum Wiederauftreten von VLSMs in Stegnähe führt. Mit Hilfe der *proper orthogonal decomposition* (POD) werden für enge Stegabstände ($S \leq \delta$) instantane großskalige turbulente Strukturen aufgedeckt. Diese Strukturen ähneln LSMs und erstrecken sich über benachbarte Stege, was aus den mittleren Sekundärströmungen nicht ersichtlich ist. Zusätzlich wird in turbulenten Kanalströmungen mit Stegen untersucht, wie sich spannweitig heterogene Oberflächen auf großskalige turbulente konvektive Strukturen auswirken, die sich unter der gleichzeitigen Wirkung von Auftrieb und Scherung

bilden. Zu diesen konvektiven Strukturen gehören *streamwise rolls*, die lange, kohärente und in Strömungsrichtung ausgerichtete Rollen darstellen. Diese treten bei spannweitig heterogenen Oberflächen im Vergleich zu homogenen, glatten Wandbedingungen in einem reduzierten Bereich auf, was mit einem durch die Stege erhöhten induzierten Widerstand assoziiert wird. Darüber hinaus können die Stege eine langsame Dynamik der *streamwise rolls* verursachen, sofern der spannweite Stegabstand in der Größenordnung der Breite der *streamwise rolls* liegt.

Acknowledgements

This work and my turbulent journey to achieve the results of this thesis would not have been possible without the many people who have accompanied and supported me over the past years, and to whom I would like to express my sincere gratitude. First of all, I would like to thank Prof. Dr.-Ing. Bettina Frohnäpfel for the opportunity to conduct this exciting research topic, her critical eye for the big picture, and for her support and openness to new ideas. Furthermore, I would like to thank Prof. Dr. Markus Uhlmann for the review of this thesis and for the exciting lectures on turbulence during my studies, which definitely paved my interest for it. Likewise, I warmly thank Prof. Dr. Juan Pedro Mellado for reviewing this thesis, as well as for the many exciting and instructive discussions during my PhD, which have greatly influenced my personal and scientific development. I would like to thank Prof. Dr.-Ing. Carsten Proppe kindly for chairing my doctoral committee.

This work would not have been possible without the support and many collaboration within the ISTM. First of all, I would like to thank Dr.-Ing. Alexander Stroh for introducing me to the fascinating world of secondary motions and sharing his never-ending enthusiasm for it. Besides, I am grateful for the many discussions with Dr.-Ing. Davide Gatti on the many facets of turbulent flows and details of computational fluid dynamics, as well as his personal support and open nature for any of my questions. Also, many thanks to Dr.-Ing. Jochen Kriegseis for his welcoming nature and good humor, as well as for the enthusiasm for modal decomposition and the many exciting discussions we had about it.

In addition, I would like to express a special thanks to all my present and former colleagues Andrea Andreolli, Andrea Codrignani, Anna Daub, Annika Frede, Arjun Kaithakkal, Christian Sachs, Daniel Klauber, David Lah, David Müller, Erik Hansen, Francesco Secchi, Franco Magagnato, Frieder Kaiser, Georg Fahland, Heiko Bandler, Jacopo Serpieri, Jiasheng Yang, Jonathan Neuhauser, Karin Fritsch-Kirchner, Lars von Deyn, Marc Hehner, Maximilian Dreisbach, Nima Samkhaniani, Pourya Forooghi, Robin Leister, Saskia Pasch, Sebastian Blessing, Sibela Hasecic, Siegfried Häcker, Steffen Straub, Tobias Karl and Vishnu Venugopal for the wonderful time and nice atmosphere at ISTM.

Many of the results and findings in this thesis would not have been possible without the great help of my students Agnes Krimmel, Emanuel Taschner, Gabriel Thäter, Jonathan Kosteletzky and Riko Haase.

I had very nice research stays in Poitiers and London, and would like to thank Eric Lamballais, Sylvain Laizet, Cédric Flageul and Rodrigo Vicente Cruz for their support with Xcompact3d and the exciting scientific discussions.

I would like to thank Prof. Dr.-Ing. Leonid Goubergrits for the opportunity to work at the ICM during my stays in Berlin and also to all colleagues at the ICM for the nice coffee breaks and social activities.

Finally, I would like to thank my friends and family for their support during the PhD and for the non-scientific and relaxing balance during my free time. In particular, I am grateful for the tireless and loving support of my partner Katharina, who has always encouraged me in my plans and ideas.

Related publications

The content of the thesis is based on the following references published during the PhD study. In particular, the results from Stroh et al. (2020b), Schäfer et al. (2022b) and Schäfer et al. (2022a) are presented and direct quotations from these publications are highlighted. The contribution of the co-authors of the publications is highly acknowledged.

Peer-reviewed journal articles

J. Neuhauser, K. Schäfer, D. Gatti, and B. Frohnäpfel. Simulation of turbulent flow over roughness strips. *Journal of Fluid Mechanics*, 945:A14, 2022. doi: 10.1017/jfm.2022.536.

K. Schäfer, B. Frohnäpfel, and J. P. Mellado. The effect of spanwise heterogeneous surfaces on mixed convection in turbulent channels. *Journal of Fluid Mechanics*, 950:A22, 2022a. doi: 10.1017/jfm.2022.773.

K. Schäfer, A. Stroh, P. Forooghi, and B. Frohnäpfel. Modelling spanwise heterogeneous roughness through a parametric forcing approach. *Journal of Fluid Mechanics*, 930:A7, 2022b. doi: 10.1017/jfm.2021.850.

A. Stroh, K. Schäfer, P. Forooghi, and B. Frohnäpfel. Secondary flow and heat transfer in turbulent flow over streamwise ridges. *International Journal of Heat and Fluid Flow*, 81, 2020a.

A. Stroh, K. Schäfer, B. Frohnäpfel, and P. Forooghi. Rearrangement of secondary flow over spanwise heterogeneous roughness. *Journal of Fluid Mechanics*, 885, 2020b. doi: 10.1017/jfm.2019.1030.

Conference contributions with own presentation

K. Schäfer, A. Stroh, B. Frohnäpfel, and D. Gatti. Investigation of turbulent budgets in channels with secondary motions induced by streamwise-aligned ridges. *Proceedings of the 11st International Symposium on Turbulence and Shear Flow Phenomena*, 2019.

K. Schäfer, B. Frohnäpfel, and D. Gatti. Dynamics of secondary motions in turbulent channel with streamwise ridges. *Proceedings of the 12th International Symposium on Turbulence and Shear Flow Phenomena*, 2022.

Contents

Abstract	i
Kurzfassung	iii
Acknowledgements	v
Related publications	vii
1 Introduction	1
1.1 Motivation	1
1.2 Research objectives and procedure	3
2 Fundamentals	5
2.1 Governing equations of hydrodynamics	5
2.2 Turbulent wall-bounded flows	7
2.2.1 Law of the wall	10
2.2.2 Monin-Obukhov similarity theory	11
2.2.3 Statistical description for spanwise heterogeneous surfaces	11
2.3 Turbulent large-scale structures	13
2.3.1 Large-scale and very-large-scale motions	13
2.3.2 Secondary motions	14
2.3.3 Convective flow structures	17
2.4 Numerical methods	18
2.4.1 Compact finite differences	18
2.4.2 Immersed boundary method	20
2.5 Proper orthogonal decomposition	22
3 Ridge- and strip-type induced secondary motions	25
3.1 Flow configuration	26
3.1.1 Parametric forcing approach	28
3.2 Results	29
3.2.1 Global flow properties	29
3.2.2 Secondary motions	35
3.2.3 Turbulence flow properties	39
3.3 Discussion	43
3.3.1 Rotational direction of secondary motions	43
3.3.2 Modelling spanwise heterogeneous surfaces	44
3.4 Summary	46

4	Interaction between secondary motions and turbulent large-scale structures	49
4.1	Flow configuration	50
4.2	Results	51
4.2.1	Mean flow properties	51
4.2.2	Instantaneous flow fields	55
4.2.3	Spectral analysis	57
4.2.4	Ridge height influence on secondary motions	61
4.2.5	Proper orthogonal decomposition	63
4.3	Discussion and summary	71
5	The effects of heterogeneous surfaces on mixed convection	75
5.1	Flow configuration	75
5.1.1	Cases	77
5.2	Results	79
5.2.1	Global flow properties	79
5.2.2	Instantaneous flow fields	83
5.2.3	Mean flow properties	87
5.2.4	Turbulent properties	91
5.2.5	Dynamics of streamwise rolls	97
5.2.6	Reynolds and domain size effects	100
5.3	Discussion and summary	102
6	Conclusion and Outlook	105
	Bibliography	109
	List of Figures	115
	List of Tables	121
	Nomenclature	123
A	Appendix	129
A.1	Additional cross-plane figures for ridge- and strip-type induced secondary motions	129
A.2	Validation of code implementation for mixed convection flows in Xcompact3d	132
A.3	Grid convergence study with Gaussian ridges for mixed convection flows	134

1 Introduction

1.1 Motivation

Turbulent flows in nature and engineering applications are often bounded by surfaces or walls. Strong shear is driving the turbulence in the vicinity of the walls and the surface properties have a crucial influence on the exchange of momentum, heat and scalar concentration. While prediction of mean flow over homogeneous smooth walls is well understood, environmental and engineering flows often involve walls with heterogeneous properties. A prominent example is the atmospheric boundary layer, where topographical heterogeneities occur, for instance, at the transitions between urban and rural areas. Due to the multitude of possible surface combinations and patterns triggering different flow processes and interactions, many scientific questions remain open. Better knowledge about the influence of heterogeneous surfaces on the exchange processes of turbulent flows is of great importance to improve the prediction of current weather and climate models (Bou-Zeid et al. 2020).

Even though many surfaces have complex heterogeneities, as the examples of urban topographies show, there exist less complex heterogeneous surfaces exhibiting variations only in one spatial direction. An illustrative example are the sand dunes in the Namib Desert, which are shown by satellite images in figure 1.1 (a). The sand dunes are longitudinal and quasi-aligned with the main wind direction and typical heights are in the order of 20-50m. The topographical variations of the sand dunes occur in the lateral direction, and neighbouring sand dune ridges are separated by about 2-3 km and their length can range up to several hundred of kilometers (Hanna 1969, Shao 2008). The formation mechanism of the longitudinal sand dunes is attributed to large-scale counter-rotating vortices or rolls, which are illustrated in the sketch in figure 1.2. The counter-rotating rolls are assumed to concentrate the mobile sand particles in the convergence region of the rolls and thereby forming the sand dune ridges. These counter-rotating rolls often occur in the atmosphere even over homogeneous surfaces, for instance, when cold air flows over warmer ocean, cloud streets can emerge as shown in figure 1.1 (b) (Etling and Brown 1993). Cloud streets form in the upper part of the upward motion of these large-scale rolls, where water vapor condenses due to the colder high-altitude air. In hydraulic flows such as rivers, similar to the example of sand dunes but without buoyancy effects, it was found that roll-like structures are responsible for the formation of sand ridges aligned with the flow direction (Colombini 1993, Scherer et al. 2022). These examples illustrate that large-scale flow structures have a great influence on atmospheric and subaqueous processes and can affect and form surface structures.

In technical flows, the opposite effect is often observed: large-scale flow structures are formed above rigid surface heterogeneities, resulting from protrusion or erosion during operation. In

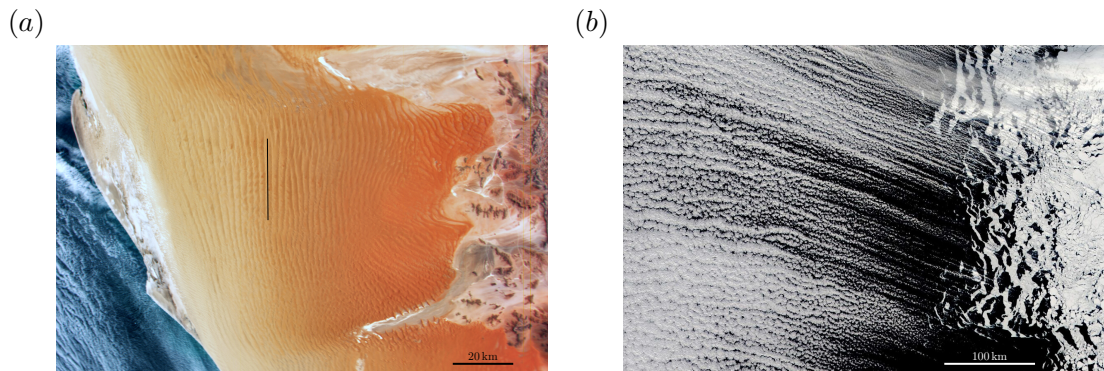


Figure 1.1: Longitudinal sand dunes in Namib Desert in (a) (taken and adopted from (NASA Earth Observatory 2020)) and cloud streets near Antarctica in (b) (taken and adopted from (NASA Earth Observatory 2018)). The black solid line in (a) indicates the alignment of one sand dune ridge with the main flow direction of the prevailing wind out of the south.

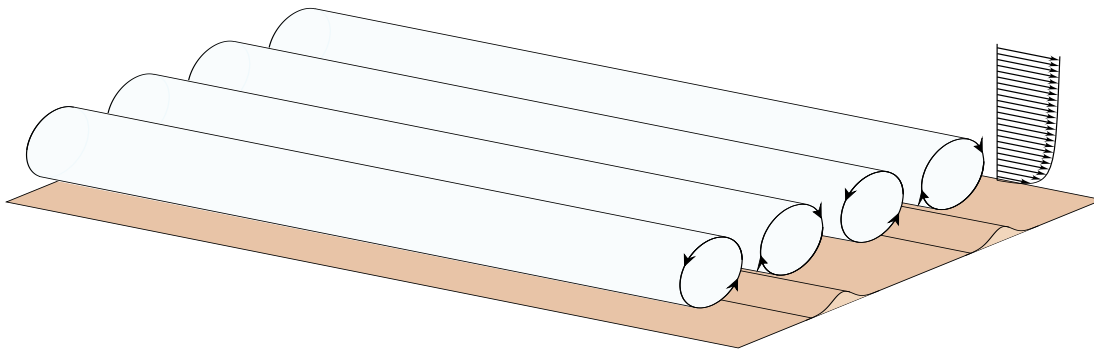


Figure 1.2: Simplified sketch of counter-rotating rolls aligned with longitudinal sand dunes as shown in figure 1.1 (a). The longitudinal sand dunes are located in the updraft region of the counter-rotating rolls. The rolls are aligned with the main flow direction, which is indicated by the mean velocity profile in the right part of the figure. Sketch was adapted and extended from Hanna (1969).

case the surface heterogeneity occurs transverse to the main turbulent flow direction, these flow structures are known as secondary motions. In contrast to the above mentioned flow structures observed in the atmosphere, secondary motions cannot be easily detected in instantaneous velocity fields, since they are immersed in the regular turbulence, but instead are seen as counter-rotating vortices in the mean velocity field. Secondary motions occur over surfaces that are generally divided into two classes, ridge- and strip-type surfaces (Wang and Cheng 2006). Ridge-type surfaces are characterised by significant differences in surface elevation. Strip-type surfaces, on the other hand, exhibit lateral differences in their surface textures, such as in experiments with alternating smooth-wall and rough sandpaper strips (Hinze 1967). Although secondary motions were observed early on and it was speculated that they significantly contribute to the heat transfer increase in engineering flows over ridge-type surfaces (Taslim et al. 1996), it is only in recent years that they have begun to be studied systematically. This thesis focuses primarily on ridge-type surfaces as a simplified model for heterogeneous surfaces, which can trigger secondary motions, to investigate their influence and the effects of heterogeneous surfaces on the turbulent exchange processes.

1.2 Research objectives and procedure

The objective of the thesis is to improve the physical understanding of spanwise heterogeneous surfaces on the formation of turbulent large-scale structures, such as secondary motions, and their influence on exchange processes of turbulent flows. An additional objective is to clarify the extent to which secondary motions have similarities and differences to other known large-scale structures and how they can interact with them. These objectives are investigated using simplified flow configurations, to break down the complex physical processes and interactions that occur in real-world problems in order to target individual effects or specific interactions. For this purpose, high-fidelity data of turbulent channel flow with spanwise heterogeneous surfaces are generated by means of direct numerical simulations (DNS) to allow addressing these questions in detail.

A fundamental question is whether secondary motions induced by either strip- or ridge-type surfaces share a common formation mechanism. This question is addressed by investigating turbulent channel flow with alternating rough- and smooth-wall strips, which are aligned with the flow direction. For this configuration the combined effects of lateral variations of surface drag and relative height differences can be systematically varied in order to shed light on the transition between strip- and ridge-type behaviour of secondary motions. This allows to check to which degree the proposed formation mechanisms of secondary motions over strip-type surfaces based on considerations of the imbalance of production and dissipation of turbulent kinetic energy (Hinze 1967, 1973, Anderson et al. 2015) are valid in presence of relative height differences. Furthermore, it can be analysed at which point the additional turbulent transport of turbulent kinetic energy found for ridge-type surfaces (Hwang and Lee 2018) starts to become important.

Many studies have focused on the influence of secondary motions on mean turbulent properties. However, the dynamics of secondary motions and the instantaneous structures contributing to their formation have gained less attention to date. Recent experimental studies have shown that instantaneous structures associated with mean secondary motions have certain similarities to turbulent large-scale motions (Zampiron et al. 2020, Wangsawijaya et al. 2020). These turbulent large-scale motions occur naturally over smooth surface conditions, where they appear in instantaneous flow fields as very long and persistent low- and high-momentum regions aligned with the main flow direction. These structures can meander arbitrarily in space and time, such that their instantaneous footprints disappear in long time averages and are no longer detectable. Therefore, the goal of the second investigation is to better quantify the instantaneous characteristics of secondary motions and their interaction with turbulent large-scale motions. This investigation is based on temporally and spatially highly resolved simulation data to unravel the similarities and differences between secondary motions and turbulent large-scale structures.

As the examples of sand dunes and cloud streets illustrate, buoyancy effects play an important role in atmospheric processes and are relevant for the formation of large-scale flow structures. In contrast, buoyancy effects are usually absent in engineering flows or are negligible since the effects of strong pressure gradients determine the exchange processes of the flow. Although secondary motions have been intensively investigated in the hydraulic and engineering communities, the influence

of buoyancy on the formation of secondary motions has not been systematically studied to date. Therefore, the final investigation of this thesis addresses two questions: first, how do buoyancy effects influence turbulent secondary motions; and second, how can buoyancy-driven large-scale structures interact with secondary motions and how are these structures affected by presence of heterogeneous surfaces.

2 Fundamentals

This chapter presents the fundamental equations of fluid motion and the theoretical frame of turbulent wall-bounded flows. A brief literature review about turbulent large-scale structures is presented in section 2.3. The numerical methods used in this thesis are presented in section 2.4 and the proper orthogonal decomposition is explained in section 2.5.

2.1 Governing equations of hydrodynamics

The following derivation of the governing equations of hydrodynamics are based on the textbooks of Tritton (1977), Pope (2000) and Kundu et al. (2016). The derivation of the equations for fluid motion is based on the fundamental assumption of the continuum hypothesis. This states that the fluid volume under consideration consists of infinitesimally small fluid elements for which the macroscopic quantities such as density, pressure, temperature and velocity can be defined. Thus, these quantities can be represented in the fluid volume as continuous functions in space and time. This presupposes that a sufficiently large number of molecules is present in the fluid elements such that the macroscopic quantities are obtained by averaging over the molecules' properties.

From the principle of conservation of mass follows the continuity equation of a fluid element in differential form

$$\frac{\partial \rho}{\partial t} + \frac{\partial}{\partial x_i}(\rho u_i) = 0, \quad (2.1)$$

which can be alternatively written as

$$\frac{1}{\rho} \left(\frac{\partial \rho}{\partial t} + u_i \frac{\partial \rho}{\partial x_i} \right) + \frac{\partial u_i}{\partial x_i} = \frac{1}{\rho} \frac{D\rho}{Dt} + \frac{\partial u_i}{\partial x_i} = 0, \quad (2.2)$$

with $D(\cdot)/Dt$ representing the material derivative. In this thesis only incompressible flows are considered, which implies that density variations of fluid particles are not present or negligible small compared to the divergence of velocity $\partial u_i/\partial x_i$, such that the continuity equation in 2.2 simplifies for incompressible flows to

$$\frac{\partial u_i}{\partial x_i} = 0. \quad (2.3)$$

Thus, the continuity equation of incompressible flows represents a kinematic condition that the velocity field is divergence-free (Pope 2000).

Based on Newton's second law, the momentum equation describes the acceleration of a fluid element as a result of surface and body forces, which for incompressible flows can be written as

$$\frac{\partial u_i}{\partial t} + u_j \frac{\partial u_i}{\partial x_j} = \frac{1}{\rho} \frac{\partial \tau_{ij}}{\partial x_j} + f_i, \quad (2.4)$$

with the fluid density ρ , the stress tensor τ_{ij} and the body force term f_i . The stress tensor describes all surface forces acting on the fluid element, while volume forces, such as gravity or the Coriolis force, are considered in the body force term f_i . In this thesis only Newtonian fluids with constant properties are considered, such that the stress tensor depends linearly on the velocity gradients in the form of

$$\tau_{ij} = -p\delta_{ij} + \mu \left(\frac{\partial u_i}{\partial x_j} + \frac{\partial u_j}{\partial x_i} \right), \quad (2.5)$$

with pressure p , the Kronecker delta δ_{ij} and the dynamic viscosity μ .

Combining equations 2.3, 2.4 and 2.5 yields the well-known Navier-Stokes equations

$$\frac{\partial u_i}{\partial t} + u_j \frac{\partial u_i}{\partial x_j} = -\frac{1}{\rho} \frac{\partial p}{\partial x_i} + \nu \frac{\partial^2 u_i}{\partial x_j \partial x_j} + f_i, \quad (2.6)$$

where ν is the kinematic viscosity.

In flows in which additional convection occurs, i.e. the fluid transfers heat, a third transport equation is required to describe these physical processes. Based on the conservation of the total energy, which is composed of internal and kinetic energy, and the assumptions of an incompressible fluid and ideal gas, the following transport equation for the temperature T is obtained

$$\frac{\partial T}{\partial t} + u_j \frac{\partial T}{\partial x_j} = \alpha \frac{\partial^2 T}{\partial x_j \partial x_j} + Q_s, \quad (2.7)$$

with the temperature diffusivity α and heat source term Q_s . The temperature equation relates the change of temperature of a fluid element to thermal conduction (first term on right-hand side) and heat sources, such as radiation, in the fluid (Tritton 1977).

Boussinesq approximation

In a number of flows, such as atmospheric or geophysical flows, buoyancy effects characterised by density differences within the fluid play an important role. The Boussinesq approximation is an extension of the incompressible Navier-Stokes equations to account for buoyancy effects only in the gravitational term, which is for instance a valid approximation for flows with small temperature variations within the fluid (Kundu et al. 2016).

In this framework the density depends only on temperature $\rho(T)$ in the gravitational term, such that the body force term in the Navier-Stokes equation is given by $f_i = -\rho(T)/\rho_0 g \delta_{i2}$. Here, ρ_0 represents a reference density, which replaces ρ in the Navier-Stokes equation 2.6, and the gravity

is assumed to be aligned with the wall-normal direction x_2 throughout this thesis. For the density variation, a linear approach of the density with temperature is introduced

$$\rho(T) = \rho_0(1 - \beta(T - T_0)), \quad (2.8)$$

with thermal expansion coefficient β and reference temperature T_0 . Introducing this Ansatz to the Navier-Stokes equation yields

$$\frac{\partial u_i}{\partial t} + u_j \frac{\partial u_i}{\partial x_j} = -\frac{1}{\rho_0} \frac{\partial p}{\partial x_i} + \nu \frac{\partial^2 u_i}{\partial x_j \partial x_j} - g(1 - \beta(T - T_0)) \delta_{i2}. \quad (2.9)$$

The equation can be further simplified by introducing a new pressure $p^* = p + \rho_0 g x_2$, which includes the hydrostatic pressure, and a new temperature $T^* = T - T_0$. This results in the familiar representation of the Navier-Stokes equation under the Boussinesq approximation

$$\frac{\partial u_i}{\partial t} + u_j \frac{\partial u_i}{\partial x_j} = -\frac{1}{\rho_0} \frac{\partial p^*}{\partial x_i} + \nu \frac{\partial^2 u_i}{\partial x_j \partial x_j} + \beta g T^* \delta_{i2}. \quad (2.10)$$

The asterisks of pressure and temperature as well as the index of the reference density ρ_0 are omitted in the following representations of the Boussinesq approximation.

2.2 Turbulent wall-bounded flows

Many technical and environmental flows are turbulent and are influenced by the presence of walls, such as in channel or pipe flows, and in atmospheric boundary layer flows by the earth's surface. The turbulence of these wall-bounded flows is usually driven and sustained by strong shear near the wall, and in case of atmospheric flows also buoyancy effects contribute to the turbulence production. Turbulent flows are characterised by unsteady and chaotic fluid motion, which complicates the description and prediction of instantaneous velocity fields, which is why a statistical description of turbulent flows is used. The common procedure to describe turbulent flows is the Reynolds decomposition, which decomposes the instantaneous velocity u_i into a mean $\langle \bar{u}_i \rangle$ and fluctuating part u'_i , such that the Reynolds decomposition is given by

$$u_i(x, y, z, t) \equiv \langle \bar{u}_i \rangle(y) + u'_i(x, y, z, t), \quad (2.11)$$

where the overbar indicates $\overline{(\cdot)}$ time- and streamwise averaging and angular brackets $\langle \cdot \rangle$ averaging in the spanwise direction. Throughout the thesis, as an alternative to the index notation, the spatial coordinates are also represented by $(x, y, z) = (x_1, x_2, x_3)$ representing the streamwise, wall-normal and spanwise directions, respectively, and the corresponding velocity components are $(u, v, w) = (u_1, u_2, u_3)$. In addition, only turbulent channel flows are considered here, such that in all presented cases the main flow and pressure gradient are aligned with the streamwise direction.

By introducing the Reynolds decomposition in equation 2.3, 2.7 and 2.10 and subsequent averaging in time and horizontal directions, the mean continuity equation, Reynolds-averaged Navier-Stokes

equations (RANS) under the Boussinesq approximation, and the mean temperature equation are given by

$$\frac{\partial \langle \bar{u}_i \rangle}{\partial x_i} = 0, \quad (2.12)$$

$$\frac{\partial \langle \bar{u}_i \rangle}{\partial t} + \langle \bar{u}_j \rangle \frac{\partial \langle \bar{u}_i \rangle}{\partial x_j} = -\frac{1}{\rho} \frac{\partial \langle \bar{p} \rangle}{\partial x_i} + \nu \frac{\partial^2 \langle \bar{u}_i \rangle}{\partial x_j \partial x_j} + \beta g \langle \bar{T} \rangle \delta_{i2} - \frac{\partial}{\partial x_j} \langle \bar{u}'_i \bar{u}'_j \rangle, \quad (2.13)$$

$$\frac{\partial \langle \bar{T} \rangle}{\partial t} + \langle \bar{u}_j \rangle \frac{\partial \langle \bar{T} \rangle}{\partial x_j} = \alpha \frac{\partial^2 \langle \bar{T} \rangle}{\partial x_j \partial x_j} + \langle \bar{Q}_s \rangle - \frac{\partial}{\partial x_j} \langle \bar{T}' \bar{u}'_j \rangle, \quad (2.14)$$

where $\langle \bar{u}'_i \bar{u}'_j \rangle$ represent the Reynolds stresses and $\langle \bar{T}' \bar{u}'_j \rangle$ the turbulent heat fluxes.

The turbulent kinetic energy k is defined by

$$k \equiv \frac{1}{2} \langle \bar{u}'_i \bar{u}'_i \rangle. \quad (2.15)$$

The transport equation of turbulent kinetic energy is

$$\frac{\partial k}{\partial t} + \langle \bar{u}_j \rangle \frac{\partial k}{\partial x_j} = \frac{\partial \mathcal{T}'_i}{\partial x_i} - \langle \bar{u}'_i \bar{u}'_j \rangle \frac{\partial \langle \bar{u}_i \rangle}{\partial x_j} - \varepsilon + \beta g \langle \bar{u}'_i \bar{T}' \rangle \delta_{i2}, \quad (2.16)$$

where \mathcal{T}'_i is the turbulent transport of k , ε the dissipation and the second and last term on the right-hand side represent the shear production and buoyant production of turbulent kinetic energy. The dissipation is defined by

$$\varepsilon \equiv 2\nu \langle \bar{s}_{ij} \bar{s}_{ij} \rangle, \quad (2.17)$$

where s_{ij} is the fluctuating rates of strain

$$s_{ij} = \frac{1}{2} \left(\frac{\partial \bar{u}'_i}{\partial x_j} + \frac{\partial \bar{u}'_j}{\partial x_i} \right). \quad (2.18)$$

The turbulent transport \mathcal{T}'_i due to turbulent fluctuations, pressure fluctuations and viscous stresses is defined by

$$\mathcal{T}'_i \equiv \frac{1}{2} \langle \bar{u}'_i \bar{u}'_j \bar{u}'_j \rangle + \frac{1}{\rho} \langle \bar{u}'_i \bar{p}' \rangle - 2\nu \langle \bar{u}'_j \bar{s}_{ij} \rangle. \quad (2.19)$$

For a fully-developed and statistically stationary turbulent channel, which is also statistically homogeneous in the spanwise direction, the mean streamwise momentum equation 2.20 reduces to

$$\frac{d \langle \bar{p} \rangle}{dx} = \frac{d}{dy} \left(\mu \frac{d \langle \bar{u} \rangle}{dy} - \rho \langle \bar{u}' \bar{v}' \rangle \right) = \frac{d\tau}{dy}, \quad (2.20)$$

$$-\langle \bar{Q}_s \rangle = \frac{d}{dy} \left(\alpha \frac{d \langle \bar{T} \rangle}{dy} - \langle \bar{v}' \bar{T}' \rangle \right) = \frac{dq}{dy}, \quad (2.21)$$

where τ is the total shear stress, q the total heat flux and the notation $d(\cdot)/dx_i$ represents derivation of variables, which depend only on one single parameter. Note, that the heat source term is a

constant here, since it is considered as statistically homogeneous in all spatial directions and in time.

The momentum and heat flux at the wall are represented by the wall-shear stress τ_w and wall heat flux q_w which are defined as

$$\tau_w \equiv \mu \left(\frac{d\langle \bar{u} \rangle}{dy} \right)_{y=0} \quad \text{and} \quad q_w \equiv -\alpha \left(\frac{d\langle \bar{T} \rangle}{dy} \right)_{y=0}. \quad (2.22 \text{ a,b})$$

Integration of the momentum equation 2.20 and introducing the wall-shear stress τ_w and half-channel height δ results in the following solution of the total shear stress

$$\tau(y) = \tau_w \left(1 - \frac{y}{\delta} \right). \quad (2.23)$$

Two scenarios are considered in this thesis for the solution of the total heat flux q , which depend on the type of heat source term. In the first case when the channel experiences a constant cooling or heating by $\langle \bar{Q}_s \rangle$, a linear relationship for q results, analogous to the solution of τ in equation 2.23

$$q(y) = q_w \left(1 - \frac{y}{\delta} \right). \quad (2.24)$$

In the second case, when no heat source term $\langle \bar{Q}_s \rangle$ is present, the gradient of the total heat flux is zero in equation 2.21, hence q is constant across the entire channel height.

The important physical parameters of the flow near the wall are the viscosity, the wall-shear stress and wall heat flux. With these quantities the viscous scales can be constituted, which are the friction velocity u_τ , the viscous length scale δ_ν and the friction temperature T_τ defined as

$$u_\tau \equiv \sqrt{\frac{\tau_w}{\rho}}, \quad \delta_\nu \equiv \nu \sqrt{\frac{\rho}{\tau_w}} = \frac{\nu}{u_\tau} \quad \text{and} \quad T_\tau \equiv \frac{q_w}{u_\tau}. \quad (2.25 \text{ a,b,c})$$

Based on the viscous velocity scale the friction Reynolds number is defined

$$Re_\tau \equiv \frac{u_\tau \delta}{\nu} = \frac{\delta}{\delta_\nu}, \quad (2.26)$$

which can be interpreted as the scale separation between outer and inner length scales. Normalization of the wall-normal coordinate y by the viscous length scale is denoted by

$$y^+ \equiv \frac{y}{\delta_\nu}, \quad (2.27)$$

which is also referred to as a measure wall-normal distance in wall units.

2.2.1 Law of the wall

Dimensional analysis allows theoretical estimates of the functional form of the mean velocity profile for turbulent channel flows. The following derivation follows the procedure outlined in Pope (2000) and buoyancy effects are not considered, which will be part of section 2.2.2. The mean velocity $\langle \bar{u} \rangle$, or the mean velocity gradient in wall-normal direction $d\langle \bar{u} \rangle/dy$, depends on the physical parameters, ν , δ , u_τ and y , such that by applying the Buckingham Π theorem, a functional relationship of the dimensionless velocity gradient exists

$$\frac{y}{u_\tau} \frac{d\langle \bar{u} \rangle}{dy} = \Phi \left(\frac{y}{\delta_\nu}, \frac{y}{\delta} \right), \quad (2.28)$$

with the two dimensionless parameters y/δ_ν and y/δ . Note that the non-dimensionalisation of the velocity gradient was achieved with the length scale y , instead of δ and δ_ν , since these length scales will be neglected as relevant reference parameters of the physical problem in the following.

Close to the wall, such that the limit $y/\delta \ll 1$ holds, the functional relation Φ asymptotically tends to a functional relation $\Phi_I(y/\delta_\nu)$, which is independent of y/δ . By applying Taylor series expansion of $\Phi_I(y/\delta_\nu)$ and the no-slip condition at the wall a linear relationship is obtained

$$u^+ = y^+, \quad (2.29)$$

also known as the law of the wall. This relation is confirmed by experimental and numerical measurements and is found to be universal among channel, pipe and boundary layer flows, where it is a valid approximation of the mean velocity within the viscous sublayer $y^+ < 5$.

In the outer layer, the mean velocity profile is independent of viscosity, such that the functional relationship Φ is independent of y/δ_ν and tends asymptotically to the function $\Phi_0(y/\delta)$. Between the outer and inner layer, there is an overlap region $y^+ \gg 1$ and $y/\delta \ll 1$, where both functional relations are equivalent, which can be only valid if both relations tend to a constant

$$\frac{y}{u_\tau} \frac{d\langle \bar{u} \rangle}{dy} = \Phi_I \left(\frac{y}{\delta_\nu} \right) = \Phi_0 \left(\frac{y}{\delta} \right) = \frac{1}{\kappa}, \quad (2.30)$$

with the von Kármán constant κ . Integration of equation 2.30 yields the well-known logarithmic law of the wall

$$\langle \bar{u} \rangle^+ = \frac{1}{\kappa} \log(y^+) + A_w, \quad (2.31)$$

where the constant A_w and κ have empirically determined values in the range of $A_w = 5.2$ and $\kappa = 0.4$ (Pope 2000, Wyngaard 2010).

Analogously, a log-law can also be derived for the temperature profile if the additional condition applies that the wall-normal region lies above the region in which thermal diffusion effects are important. From this assumption follows

$$\langle \bar{T} \rangle^+ = \frac{\langle \bar{T} \rangle}{T_\tau} = \frac{1}{\kappa_T} \log(y^+) + A_T(Pr), \quad (2.32)$$

with the constant $\kappa_T \approx 0.47$ and the value A_T depends on the considered Prandtl number $Pr = \nu/\alpha$ (Chung et al. 2021).

2.2.2 Monin-Obukhov similarity theory

In case of buoyancy effects the Monin-Obukhov similarity theory generalizes the logarithmic law of the wall for non-neutral stratification, which is widely used to describe turbulent momentum and heat fluxes in the atmospheric boundary layer (Obukhov 1946, Monin and Obukhov 1954, Wyngaard 2010). In addition to the previous considerations, the mean velocity and temperature depend on the wall heat flux q_w , thermal expansion coefficient β and gravitational acceleration g , such that a new length scale can be formed by dimensional reasons, which is the Obukhov length L , defined as

$$L \equiv \frac{-u_\tau^3}{\kappa q_w \beta g}. \quad (2.33)$$

A physical interpretation of the Obukhov length $|L|$ is that it represents the wall-normal height y_e at which shear production of turbulent kinetic energy equals that due to bouyant production (see equation 2.16). This can be shown by approximating the momentum and heat flux by u_τ and q_w , respectively, as well as using the relation of the logarithmic law of the wall, it follows

$$\langle u'v' \rangle \frac{d\langle \bar{u} \rangle}{dy} = \beta g \langle v'T' \rangle \quad (2.34)$$

$$u_\tau^2 \frac{u_\tau}{\kappa y_e} = \beta g q_w, \quad (2.35)$$

$$y_e = \frac{u_\tau^3}{\kappa \beta g q_w} = |L|. \quad (2.36)$$

Introducing the Obukhov length L as a new length scale, the Buckingham Π theorem states functional relationships of the dimensionless velocity and temperature gradients in the overlap region by

$$\frac{y}{u_\tau} \frac{\partial \langle \bar{u} \rangle}{\partial y} = \frac{1}{\kappa} \phi_m \left(\frac{y}{L} \right) \quad \text{and} \quad \frac{y}{T_\tau} \frac{\partial \langle \bar{T} \rangle}{\partial y} = \frac{1}{\kappa} \phi_h \left(\frac{y}{L} \right), \quad (2.37 \text{ a,b})$$

where ϕ_m and ϕ_h are the universal functions of momentum and heat flux. These universal functions depend on the kind of stratification of the flow and existing relationships are determined by experimental measurements in the atmospheric surface layer (Wyngaard 2010).

2.2.3 Statistical description for spanwise heterogeneous surfaces

In case of spanwise heterogeneous surfaces, such as the example of the streamwise-aligned sand dunes in chapter 1, the spanwise direction is no longer statistically homogeneous. To account for the local differences of the flow in the spanwise direction, a triple decomposition is introduced (Raupach

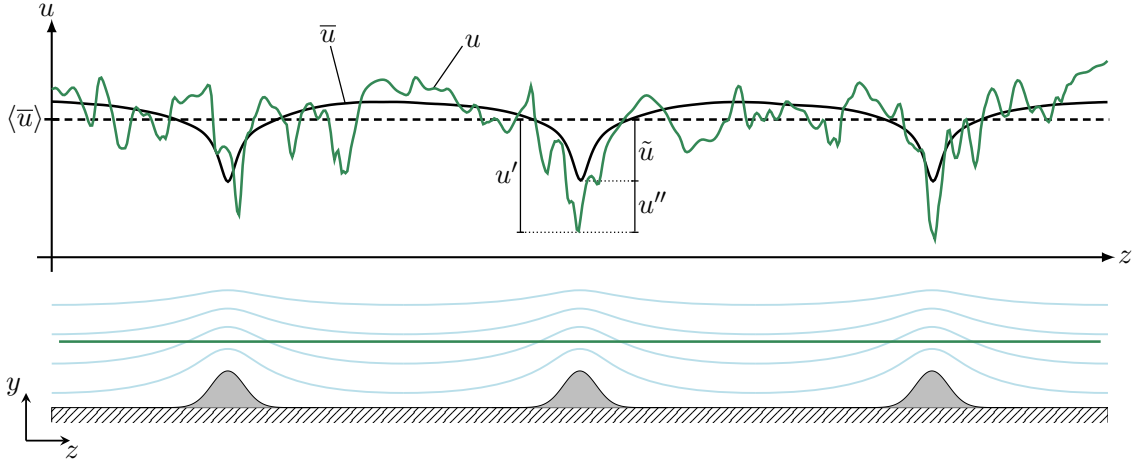


Figure 2.1: Illustration of the triple decomposition for the streamwise velocity u over a spanwise heterogeneous surface consisting of streamwise-aligned ridges. In the bottom panel the light blue lines represent isolines of constant \bar{u} and the green line indicates the wall-normal location at which the velocity profiles are shown in the upper panel. In the upper panel the instantaneous velocity u is represented by the green line, while the black line indicates the local mean \bar{u} and the dashed black line the global mean $\langle \bar{u} \rangle$.

and Shaw 1982), which decomposes the turbulent fluctuation u'_i of the Reynolds decomposition in equation 2.11 into a coherent contribution \tilde{u}_i (or dispersive contribution) and random fluctuation u'' , such that the instantaneous velocity can be decomposed into

$$u_i(x, y, z, t) = \langle \bar{u}_i \rangle(y) + \tilde{u}_i(y, z) + u''_i(x, y, z, t). \quad (2.38)$$

The sum of the first two terms on the right-hand side results in the local mean \bar{u}_i , which is the time- and streamwise-averaged mean

$$\bar{u}_i(y, z) \equiv \langle \bar{u}_i \rangle(y) + \tilde{u}_i(y, z). \quad (2.39)$$

With this definition equation 2.38 can be alternatively written as

$$u_i(x, y, z, t) = \bar{u}_i(y, z) + u''_i(x, y, z, t), \quad (2.40)$$

from which it is evident, that the random fluctuation u'' is the fluctuation from the local mean \bar{u}_i . From these definitions it follows that $\langle \tilde{u} \rangle = 0$ and $\overline{u''} = 0$ hold. The relations of the triple decomposition are illustrated in figure 2.1 for the streamwise velocity u in a cross-section over spanwise heterogeneous surface consisting of streamwise-aligned ridges. The velocity profiles shown in the upper panel are extracted along the green line in the bottom panel, which is located at a constant wall-normal location above the ridges. In the vicinity of the ridges the time- and streamwise averaged velocity \bar{u} is lower compared to the regions in the valley, which results in negative and positive variations of \tilde{u} in these regions, respectively.

As a consequence of the triple decomposition covariances of flow variables, such as the Reynolds shear stresses $\langle u'_i u'_j \rangle$, contain two contributions

$$\langle u'_i u'_j \rangle = \langle \tilde{u}_i \tilde{u}_j \rangle + \langle u''_i u''_j \rangle, \quad (2.41)$$

where $\langle \tilde{u}_i \tilde{u}_j \rangle$ represents coherent covariances, resulting from spanwise spatial correlations of local mean quantities, and $\langle u_i'' u_j'' \rangle$ are random covariances.

In case of spanwise heterogeneous surfaces with a periodically repeating pattern in the spanwise direction, the procedure of phase-averaging can be introduced to average the local mean quantities for the repeating pattern or phases. The phase-averaged local mean $\langle \bar{u}_i \rangle_\phi$ is defined by

$$\langle \bar{u}_i \rangle_\phi(y, \bar{z}) \equiv \frac{1}{N_\phi} \sum_{j=1}^{N_\phi} \bar{u}_i(y, [z_{\phi,j} - W_\phi/2, z_{\phi,j} + W_\phi/2]), \quad (2.42)$$

where \bar{z} represents the phase-averaged spanwise coordinate, N_ϕ is the number of repeating phases, $z_{\phi,j}$ is the spanwise position of the centre of the j -th phase in the total spanwise direction and W_ϕ is the spanwise width of the phase window. The range of values of \bar{z} can be chosen as $[0, W_\phi]$ or alternatively as $[-W_\phi/2, W_\phi/2]$.

2.3 Turbulent large-scale structures

In wall-bounded turbulent flows a variety of different large-scale structures exist. In this section a brief review of three types of turbulent large-scale structures is presented, which are the subject of the current thesis. Turbulent large-scale structure emerging over smooth-wall conditions are discussed in section 2.3.1, while those initiated by surface heterogeneities are presented in section 2.3.2. For flows in which buoyancy effects play a relevant role, convective large-scale structures can arise, which are outlined in section 2.3.3.

2.3.1 Large-scale and very-large-scale motions

While the coherent structures near the wall of turbulent shear flows, which consist of low-momentum streaks and quasi-streamwise vortices, have been observed as early as the 1960s and since then have been well studied and understood (Kline et al. 1967, Kim et al. 1987), significant insights into coherent structures in the logarithmic and outer region have been achieved in recent decades. These include the observation that coherent structures with very large length scales occur in the outer region and contribute significantly to the production and transport of turbulent kinetic energy and Reynolds shear stresses, which are referred to large-scale motion (LSM) and very-large-scale motion (VLSM) (Kim and Adrian 1999, Adrian et al. 2000, Ganapathisubramani et al. 2003, Monty et al. 2009).

The LSMs and VLSMs can be distinguished on the one hand by their streamwise length scale, which for instance in internal flows (pipe and channel flows) is significantly smaller for LSMs than for VLSMs. On the other hand, VLSMs exhibit mainly streamwise turbulent kinetic energy, while LSMs are characterised by intense wall-normal and spanwise turbulent kinetic energy (Hwang 2015, de Giovanetti et al. 2017). The streamwise wavelength of LSMs is in the order of $\lambda_x \approx 1 - 5\delta$ (Monty et al. 2009, de Giovanetti et al. 2017), where δ is here representing either the boundary

layer depth, half-channel height or pipe radius. VLSMs have been first observed and termed by Kim and Adrian (1999) in turbulent pipe flows, where they appear as alternating regions of low and high momentum with streamwise length scales of $\lambda_x \approx 12 - 14\delta$. Turbulent channel flows also show similar streamwise length scales of VLSMs ($14\delta < \lambda_x < 20$) as those observed in pipe flows (Monty et al. 2009), and recently VLSM have been identified in rough-bed open-channel flows with $\lambda_x \approx 10 - 40\delta$ (Cameron et al. 2017). In turbulent boundary layers very long meandering streamwise velocity fluctuations have been found by Hutchins and Marusic (2007), who termed them as superstructures, which have smaller streamwise length scales $\lambda_x \approx 6\delta$ as the VLSMs found in pipe or channel flows. Despite the structural similarities between VLSM and superstructures, they should not be confused with each other as noted by Monty et al. (2009), as there are significant differences in their energy distribution. The VLSM in internal flows extend beyond the logarithmic layer into the outer region, and the streamwise length scales grows with the distance to the wall, whereas superstructures in boundary layer flows are only evident in the logarithmic layer (Monty et al. 2009). Thus, the energy spectrum in the outer region for internal flows shows two energetic peaks associated with LSM and VLSM, respectively, whereas the spectrum of boundary layer flows shows a single peak with a length scale matching that of LSM from internal flows.

2.3.2 Secondary motions

Secondary motions represent a distinct mean fluid motion that occurs in wall-bounded flows in the cross-sectional plane perpendicular to the main flow direction. The first observations of secondary motions were made by Nikuradse (1926) and Prandtl (1926) in flows with non-circular pipes, where the secondary motions form as counter-rotating vortices transporting fluid from the bulk towards the corners. Later, Prandtl divided secondary motions into two categories, which are known today as secondary motions of Prandtl's first kind, occurring in bent pipe flows or meandering rivers, and secondary motions of Prandtl's second kind, forming only in turbulent flows due to spatial heterogeneity of Reynolds stresses (Bradshaw 1987). In the following text the term secondary motions will only refer to secondary motions of Prandtl's second kind.

Secondary motions were later also found over plane wall-bounded turbulent flows with spanwise heterogeneous surface properties, as shown by Hinze's experiments in wide channels with attached streamwise-aligned roughness strips on the smooth channel wall (Hinze 1967, 1973). In these experiments, the secondary motions manifest at the roughness transition as downwelling fluid motion over the roughness strips, while upwelling motion occurs over the smooth-wall strips. Hinze suggested that the formation of the secondary motions is a result of an imbalance between the production and dissipation of turbulent kinetic energy, such that the secondary motion transports turbulence rich fluid to regions of turbulence poor fluid. These secondary motions, occurring over spanwise heterogeneous rough surfaces, were shown to be generated by spanwise heterogeneous distributions of Reynolds stresses and are thus secondary motions of Prandtl's second kind (Anderson et al. 2015).

Spanwise heterogeneous surfaces initiating secondary motions are generally divided into two surface types, namely strip- and ridge-type surfaces (Colombini and Parker 1995, Wang and

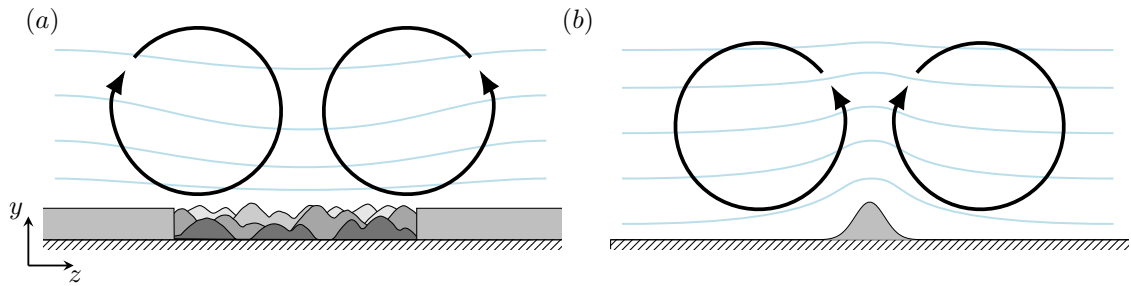


Figure 2.2: Schematic of secondary motions over spanwise heterogeneous surfaces of strip (a) and ridge-type (b). Ridge-type surfaces are characterised by spanwise differences in the wall elevation, while these are absent or negligible for strip-type surface and the heterogeneity consists of spanwise variations of wall-shear stress. The secondary motions are represented by large-scale counter-rotating vortices, where for strip-type surfaces the upward motion appears above the lower wall-shear stress strip and for ridge-type surfaces above the streamwise-aligned ridges. The light blue lines depict isolines of constant mean streamwise velocity and their up- and downward bulging is associated with low- and high-momentum pathways, respectively.

Cheng 2006), which are illustrated in figure 2.2. Strip-type surfaces, are characterised by spanwise differences in wall properties, while no significant differences in wall elevation occur, such as those represented by the alternating streamwise-aligned smooth- and rough-wall strips as shown in figure 2.2 (a). Numerically, strip-type surfaces can be modeled by alternating strips with different wall boundary conditions, such as different wall-shear stress conditions (Willingham et al. 2014, Chung et al. 2018), variations in slip lengths (Neuhauser et al. 2022) or strips with non- and hydrophobic surfaces (Türk et al. 2014, Stroh et al. 2016). Ridge-type surfaces are characterised by significant differences in spanwise wall elevation, such as those represented by streamwise-aligned ridges in figure 2.2 (b). The investigated geometries of ridge-induced secondary motion include triangles (Goldstein and Tuan 1998, Wang and Cheng 2006, Stroh et al. 2020a, Medjnoun et al. 2020, Zampiron et al. 2020), rectangles (Wang and Cheng 2006, Hwang and Lee 2018, Medjnoun et al. 2018, 2020), lego bricks (Vanderwel and Ganapathisubramani 2015, Vanderwel et al. 2019), Gaussian ridges (Schäfer et al. 2022a), semicircles (Medjnoun et al. 2020) and streamwise-aligned densely packed pyramids (Yang and Anderson 2017). Many of the aforementioned studies have examined surfaces whose heterogeneity consists of either clear differences in wall elevation or in surface roughness, whereas only a few studies have examined combinations of both surface heterogeneities. Among these are, for example, smooth walls with protruding roughness strips (Stroh et al. 2020b, Schäfer et al. 2022b) and protruding smooth ridges over rough valleys (Zampiron et al. 2020, Schäfer et al. 2022b).

Besides the counter-rotating vortices, the secondary motions over ridge- and strip-type surface show a spanwise heterogeneity in their mean streamwise velocity, which consists of alternating low-momentum pathways (LMP) and high-momentum pathways (HMP) (Barros and Christensen 2014, Willingham et al. 2014). In general, the LMPs occur in the upwelling region of the secondary motions, while the HMPs occur in the downwelling region, which in turbulent boundary layers is associated with a thickening and thinning of the boundary layer thickness (Barros and Christensen 2014, Vanderwel and Ganapathisubramani 2015, Medjnoun et al. 2020). For ridge-type surface, the upward motion of the secondary motions and LMPs occur above the elevated ridges, or for wide ridges at the transition from valley to ridge, which is indicated by the upward bulging of isolines of the mean streamwise velocity in figure 2.2 (b), and at the same time, the downward motion

and HMPs occur in the valleys between the ridges (Hwang and Lee 2018). The upward motion of secondary motions and LMPs are found for strip-type surfaces above the lower wall stress strips and downward motion and HMPs above the high wall stress strips (see figure 2.2 (a))(Chung et al. 2018, Wangsawijaya et al. 2020).

The size and strength of secondary motions depends for ridge-type surfaces on the spanwise ridge spacing S , while for strip-type surfaces on the spanwise wavelength of the alternating roughness strips (Vanderwel and Ganapathisubramani 2015, Chung et al. 2018). Depending on S three different regimes can be distinguished. The intermediate regime where S is in the order of the boundary layer thickness δ is characterised by secondary motions with the largest strength and by δ -scale spacing counter-rotating vortices filling the entire cross-sectional domain (Vanderwel and Ganapathisubramani 2015, Chung et al. 2018). For the limiting regime $S \gg \delta$, the secondary motion remains anchored to the ridges or for strip-type roughness at the roughness transition and maintains its δ -scaling (Vanderwel and Ganapathisubramani 2015, Hwang and Lee 2018, Chung et al. 2018, Wangsawijaya et al. 2020). For the other extreme case $S \ll \delta$, the spatial extent of the secondary motion decreases and the mean flow is unaffected by the secondary motion in the region $y \gtrsim S$ (Vanderwel and Ganapathisubramani 2015, Chung et al. 2018).

Most of the aforementioned studies on secondary motion have focused on mean properties, while the time-dependent behaviour of secondary motion has been investigated by a few studies recently. These studies have found that instantaneous structures associated with secondary motions meander laterally in time (Vanderwel et al. 2019, Zampiron et al. 2020, Wangsawijaya et al. 2020, Wangsawijaya and Hutchins 2022). For ridge-type induced secondary motions this meandering is speculated to be associated with an inflection point instability of the mean streamwise velocity in the spanwise direction (Zampiron et al. 2020). However, for strip-type induced secondary motions this meandering is speculated to be associated with spanwise-locked turbulent large-scale structures (LSM/VLSM) at the roughness transition (Wangsawijaya et al. 2020). Similar observations were also made for converging/diverging riblets, which generate secondary motion not due to roughness heterogeneity, but due to the different anisotropy of the roughness strips (Kevin et al. 2017, 2019). There, the time-averaged secondary motion were identified as artefacts of low-momentum large-scale streaks which are accompanied by unsteady and spanwise asymmetric large-scale roll modes. Coexistence between secondary motions and VLSMs was found for strip-type roughness independent of the strip width (Wangsawijaya et al. 2020), while secondary motions over ridge-type surfaces suppress the occurrence of VLSM for $S \leq 2\delta$ (Zampiron et al. 2020). Recently, the interaction of LSMs with mobile sediment beds were studied in hydraulic open-channel flows (Scherer et al. 2022). It was found that the sand particles accumulate to streamwise-elongated sand ridges below the low-speed streak of LSMs, which is attributed to a top-down mechanism such that the sediment bed adapts to changes of the outer LSMs. At the sediment ridges secondary motions are observed for finite time intervals ($\mathcal{O}(10)$ bulk time units), suggesting that for hydraulic flows secondary motions are the statistical footprint of the lateral organisation of large-scale structures.

2.3.3 Convective flow structures

In case buoyancy effects play an important role in the flow in addition to shear effects, new forms of turbulent large-scale structures can emerge, which can be observed for instance in atmospheric boundary layer flows. A distinction between stable and unstable stratification is necessary, i.e. whether denser fluid is located below or above lighter fluid, respectively, which leads to different formations of buoyancy-induced large-scale flow structures. In this thesis, only the flow organisation of unstable stratification is considered, while for stably stratified flows the reader is referred to existing review literature on this topic (Mahrt 1999). Since for unstable stratified flows both shear and buoyancy contribute to the heat transfer, the term mixed convection flows is used for these kind of flows. This illustrates that the convection of the flow is composed of the two extreme forms of forced and natural convection. In the former case, when buoyancy plays a minor role and the heat transfer is mainly due to shear, the velocity field is not affected by the temperature, which applies for the large-scale flow structures discussed in the previous sections. For natural convection the flow is driven solely by buoyancy effects and density differences, for which an example is the canonical Rayleigh-Bénard flow configuration. For mixed convection both shear and buoyancy effects influence the flow to a similar extent such that both physical effects contribute to the generation of turbulence (as discussed in section 2.2.2 and shown by equation 2.16). (Tritton 1977, Wyngaard 2010)

"In mixed convection flows [...] different turbulent large-scale flow structures have been identified and the organisation depends on the relative strength between shear and buoyancy effects, such as in turbulent channel flows (Pirozzoli et al. 2017), turbulent Couette flows (Blass et al. 2020) and in the atmospheric boundary layer (ABL) (Deardorff 1972, LeMone 1973, Moeng and Sullivan 1994, Khanna and Brasseur 1998). The transition between different flow organisations is accompanied by an alteration of the effective heat and momentum transfer in the flow. In the case of strong buoyancy effects and weak shear, open cells form in the flow, which resemble Rayleigh-Bénard convection, while in the case of weak to moderate buoyancy effects and strong shear, the flow organises into horizontal rolls aligned with the main flow direction (Khanna and Brasseur 1998, Pirozzoli et al. 2017, Salesky et al. 2017). These streamwise rolls [depict counter-rotating motion in the cross-section of the flow], with the up- and downdraft region of the roll occurring where localised buoyancy forces accumulate. At very strong shear, with negligible buoyancy effects, the flow organisation in turbulent channels resembles that of classical Poiseuille flows (Pirozzoli et al. 2017) and in the case of neutral ABL that of flat-plate boundary layers (Khanna and Brasseur 1998)." (Schäfer et al. 2022a)

"The transition between the different flow topologies of mixed convection can be characterised by various stability parameters. In the atmospheric science community, the stability parameter $-z_i/L$ is used to classify the transitions between rolls and cellular structures, which expresses the ratio of the boundary layer depth z_i and the Obukhov length L . [...] In the case of convective boundary layers, large ratios of $-z_i/L$ are indicative of the formation of convective cells, while small values are typical for roll formation (Khanna and Brasseur 1998, Salesky et al. 2017). An alternative stability parameter to characterise the relative importance of buoyancy effects and shear is the

Richardson number Ri . For mixed convection in turbulent channel flows, low Ri corresponds to pure forced convection, intermediate values of Ri to roll formation and large Ri values to natural convection with cell-like structures (Pirozzoli et al. 2017). Independent of the chosen stability parameter the exact range at which the transition between the different flow regimes occurs is still under debate with recent studies focusing on the transition between rolls and cells (Salesky et al. 2017) and the transition between neutral to moderately convective conditions (Jayaraman and Brasseur 2021). (Schäfer et al. 2022a)

2.4 Numerical methods

In this thesis the continuity equation as well as the transport equations of momentum and temperature presented in section 2.1, are numerically solved by direct numerical simulations, which resolve all relevant time and spatial scales of turbulent flows. The results in chapter 3 are based on the spectral solver SIMSON (Chevalier et al. 2007), employing Fourier and Chebyshev decomposition for the spatial discretization. The open-source code Xcompact3d is used for the results in the subsequent chapters 4 and 5, which is based on compact finite differences for the spatial discretization, combining numerical efficiency and accuracy for simulations of turbulent flows (Laizet and Lamballais 2009, Bartholomew et al. 2020). The numerical representation of complex geometries in the flow is achieved by means of an immersed boundary method (IBM) in Xcompact3d. The code has been extended by the author to simulate the Navier-Stokes equation under the Boussinesq approximation (see section 2.1) and the IBM was adopted for heat transfer problems. This section presents briefly the concept of compact finite differences and the employed IBM of Xcompact3d.

2.4.1 Compact finite differences

Compact finite-differences represent an improved evaluation of derivatives with a spectral-like accuracy (Lele 1992) than compared to classical finite difference methods. The following part follows the derivation presented in Lele (1992). The compact finite difference approximation of the first and second derivative is illustrated in the following for a one-dimensional and arbitrary flow quantity $f(x)$, where x represents the spatial coordinate. A uniform grid distribution for the discretization of the domain $[0, L_x]$ is applied, where L_x is the domain length. The discrete coordinate position x_i and the functional values $f_i = f(x_i)$ of the N_x grid points are given at $x_i = (i - 1)\Delta x$ for $1 \leq i \leq N_x$, where Δx is the distance between the grid points. The first derivative $f'_i = df(x_i)/dx$ at the position x_i can be numerically represented in the form of

$$\alpha_1 f'_{i-1} + f'_i + \alpha_1 f'_{i+1} = a_1 \frac{f_{i+1} - f_{i-1}}{2\Delta x} + b_1 \frac{f_{i+2} - f_{i-2}}{4\Delta x}. \quad (2.43)$$

A sixth-order compact finite difference representation of the first derivative is achieved by using the parameter set

$$\alpha_1 = \frac{1}{3}, \quad a_1 = \frac{14}{9}, \quad b_1 = \frac{1}{9}. \quad (2.44)$$

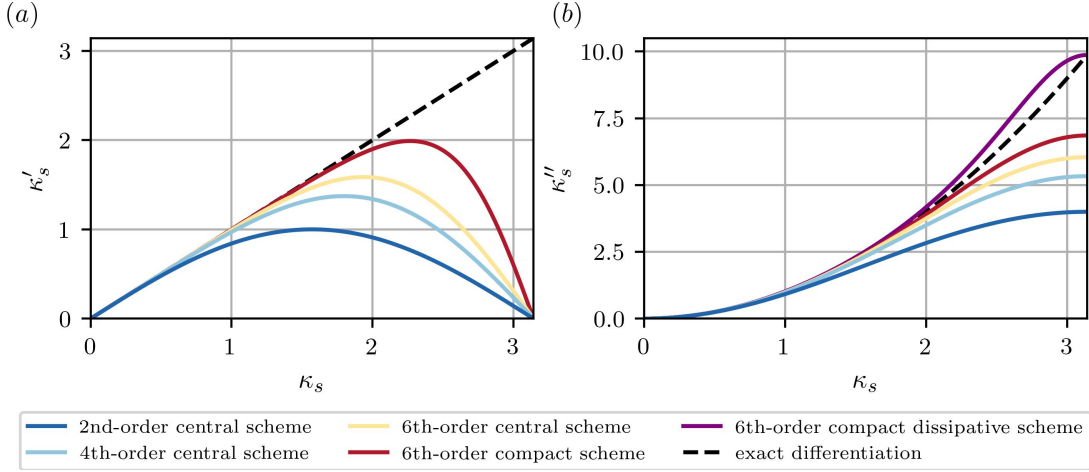


Figure 2.3: Modified wavenumbers of first derivative in (a) and of second derivative in (b) for different differentiation schemes. The purple line in (b) represents a sixth-order compact finite difference scheme which is slightly over-dissipative compared to the exact differentiation scheme.

Thus, the evaluation of the derivative f'_i depends on the function values and the unknown derivative values at neighbouring grid points, which result in the solution of a linear system with cyclic tridiagonal form. The well-known second order central finite difference approximation is recovered by $\alpha_1 = 0$, $a_1 = 1$ and $b_1 = 0$, without the requirement to solve a linear equation system.

Similar to the approximation of the first derivative, the compact finite difference approximation of the second derivative f''_i is given by

$$\alpha_2 f''_{i-1} + f''_i + \alpha_2 f''_{i+1} = a_2 \frac{f_{i+1} - 2f_i + f_{i-1}}{(\Delta x)^2} + b_2 \frac{f_{i+2} - 2f_i + f_{i-2}}{4(\Delta x)^2} \quad (2.45)$$

$$+ c_2 \frac{f_{i+3} - 2f_i + f_{i-3}}{9(\Delta x)^2}. \quad (2.46)$$

A compact finite-difference approximation of sixth order for the second derivative is obtained by the parameter set

$$\alpha_2 = \frac{2}{11}, \quad a_2 = \frac{12}{11}, \quad b_2 = \frac{3}{11}, \quad c_2 = 0. \quad (2.47)$$

The approximation error introduced by the compact-finite difference scheme for the first and second derivatives can be quantified by the concept of modified wavenumbers. For this purpose, the function f is assumed to be periodic over the domain $[0, L_x]$, such that the discretized function f_i can be represented by a Fourier series with Fourier coefficients \hat{f}_i . Instead of the wavenumber κ_x , a scaled wavenumber $\kappa_s = \kappa_x \Delta x$ is introduced and its range is in $[0, \pi]$ due to the conjugate symmetry of the Fourier coefficients $\hat{f}_i = \hat{f}_i^*$ (where $*$ denotes the complex conjugate) for real-valued f_i . By introducing the Fourier series into equation 2.43, the relation $\hat{f}'_i = i\kappa'_s \hat{f}_i$ is obtained, where \hat{f}'_i are the Fourier coefficients of the first derivative, i is the complex number and κ'_s represents the modified wavenumber given by

$$\kappa'_s(\kappa_s) = \frac{a_1 \sin(\kappa_s) + (b_1/2) \sin(2\kappa_s)}{1 + 2\alpha_1 \cos(\kappa_s)}. \quad (2.48)$$

Similar, a relation for the modified wavenumber of the second derivative κ_s'' is obtained in the form of

$$\kappa_s''(\kappa_s) = \frac{2a_2(1 - \cos(\kappa_s)) + (b_2/2)(1 - \cos(2\kappa_s)) + (2c_2/9)(1 - \cos(3\kappa_s))}{1 + 2\alpha_2 \cos(\kappa_s)}. \quad (2.49)$$

The modified wavenumbers depend on the used discretization scheme and figure 2.3 presents the distributions for different schemes of central finite differences and a sixth-order compact finite difference scheme. The exact derivation by the Fourier series corresponds to a straight line for the first derivation and a parabola for the second derivation, which are indicated by the black dashed lines. As can be seen, the compact finite difference scheme is closer to the exact differentiation for a larger range of wavenumbers than compared to the different central finite difference schemes, which holds for both the first and second derivatives. At the same time, it is evident that an increase of the order of the central finite difference scheme improves the discretization error.

Figure 2.3 (b) shows that the second derivative of the sixth-order compact finite difference scheme has a sub-dissipative behaviour, since it remains below the exact differentiation. Including the parameter c_2 in equation 2.46 for the approximation of the second derivative the numerical dissipation behaviour of the second derivative approximation can be controlled, while preserving a sixth-order compact scheme with marginal numerical extra costs (Lamballais et al. 2011). A relationship between the set of parameters to preserve the sixth order of the scheme while prescribing the value of the modified wavenumber $\kappa_{s,c}'' = \kappa_s''(\kappa_{s,c})$ at the cutoff wavenumber $\kappa_{s,c} = \pi$, is derived in Lamballais et al. (2011). For $\kappa_{s,c}'' = \pi^2$ this results in a parameter set for the second derivative with

$$a_2 \approx 0.3645, \quad a_2 \approx 0.6799, \quad b_2 \approx 1.1913, \quad c_2 \approx -0.1005, \quad (2.50)$$

which is shown in figure 2.3 (b). As can be observed, this scheme depicts a slight over-dissipative behaviour for large wavenumbers, which at the same time remains closer to the exact differentiation than the classical sixth-order compact finite difference scheme. Due to the negligible numerical extra costs this set of parameters is used for the simulations in this thesis presented in chapter 4 and 5.

2.4.2 Immersed boundary method

The immersed boundary method is a procedure to represent solid bodies in flow simulations which are based on a Cartesian grid. This is achieved by either introducing a forcing term in the Navier-Stokes equation, or by modifying the values of the grid points in the vicinity of the solid body, where the former approach has been termed "continuous forcing approach" and the latter "discrete forcing approach" (Mittal and Iaccarino 2005). The method of (Goldstein et al. 1993) belongs to the category of continuous forcing approach for rigid bodies, which assumes a forcing term of the form of a proportional-integral controller. This method can be easily integrated into spectral methods, as for example in the solver SIMSON, which is used for the simulation in chapter 3. The IBM used in Xcompact3d (Gautier et al. 2014) falls into the category of discrete forcing approaches, where the desired boundary condition at the solid interface can be directly achieved

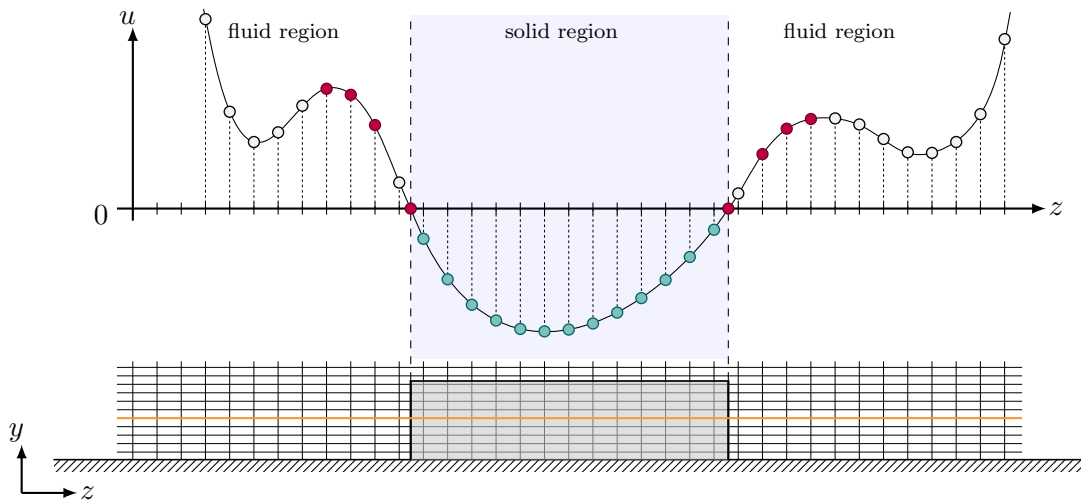


Figure 2.4: Illustration of polynomial reconstruction of the alternating direction immersed boundary method in Xcompact3d for a rectangular ridge in the y - z cross-section. The orange line in the bottom panel indicates the grid line along which the reconstruction in the z -direction is illustrated in the upper panel. The Lagrange polynomial is based on the red points in the fluid domain and the interface points, such that the interpolation of the velocity values inside the solid region results in the green points.

by adjusting the grid point values close to the solid or in the solid. Thus, the interface of the solid body can be located between grid points of the Cartesian mesh, allowing the representation of more complex geometries (Gautier et al. 2014).

The approach of Gautier et al. (2014) employs an polynomial reconstruction method, based on Lagrange polynomials, such that the fluid values inside the body are interpolated by means of fluid grid points close to the wall and the desired boundary conditions at the solid interface. This approach achieves a sharp interface between solid and fluid with a continuous functional representation across the fluid-solid interface. The reconstruction of the velocities is applied in the direction of the corresponding spatial derivative, resulting in an alternating direction forcing strategy, such that the reconstruction of one spatial direction is independent of the other directions. Figure 2.4 illustrates this procedure for a rectangular ridge along the z -direction. The orange line in the bottom panel indicates the grid line of the numerical mesh at which the reconstruction of the velocity is illustrated in the upper panel. The velocity values and spatial position of the red points are used for the Lagrange polynomial and the green points are the reconstructed values inside the solid region from the Lagrange interpolation. This reconstructed velocity field is subsequently used to evaluate the derivative in the z -direction. As noted by Gautier et al. (2014) the first fluid point next to the solid-fluid interface is neglected due to stability reasons of the the polynomial reconstruction in case this point is close to the fluid-solid interface. In the numerical solver, this reconstruction method of the IBM is used during the evaluation of the spatial derivatives, such that no explicit forcing term appears in the Navier-Stokes equations.

2.5 Proper orthogonal decomposition

Turbulent flows depict complex spatio-temporal behaviour which makes their mathematical modelling considerably difficult. The observation of coherent structures in turbulent flows, which represent characteristic reoccurring patterns of the flow and which are energetically dominant in many flows, suggesting that a low-dimensional model of the flow can be obtained by considering only dominant coherent structures (Holmes et al. 2012). The proper orthogonal decomposition (POD) is a reduced-order model technique which was introduced for turbulent flows by Lumley (1967) to extract dominant coherent structures from experimental and numerical data. This approach is used in chapter 4 to extract characteristic instantaneous large-scale structures in turbulent channel flows with secondary motions. The subsequent introduction of the POD are based on the description of Holmes et al. (2012) and Taira et al. (2017).

The POD first splits the instantaneous velocity vector field $\mathbf{u}(\mathbf{x}, t) = (u(\mathbf{x}), v(\mathbf{x}), w(\mathbf{x}))^T$, with spatial vector $\mathbf{x} = (x, y, z)$, into the velocity fluctuation $\mathbf{u}' = \mathbf{u} - \overline{\mathbf{u}}$ (here $\overline{(\cdot)}$ indicating a temporal mean). Subsequently, \mathbf{u}' is decomposed by means of a separation of variables in the form of

$$\mathbf{u}'(\mathbf{x}, t) = \sum_{k=1}^N a_k(t) \Phi_k(\mathbf{x}), \quad (2.51)$$

where $\Phi_k(\mathbf{x})$ are the spatial POD modes, which form an orthonormal basis, $a_k(t)$ are the corresponding temporal coefficients of the POD modes and N is the total number of modes. The modal decomposition of the POD is optimal in the sense that the first n modes of the POD capture more energy of the velocity field on average than any other basis with the same number of modes.

For the computation of the POD velocity fields $\mathbf{u}'(\mathbf{x}, t)$ at M different and uncorrelated time instances, with N_s discrete spatial points \mathbf{x}_i with $i = 1, \dots, N_s$, are collected. The velocity field at time instance t_j is stored in a velocity snapshot $\mathbf{u}^j = (\mathbf{u}'(\mathbf{x}_1, t_j), \mathbf{u}'(\mathbf{x}_2, t_j), \dots, \mathbf{u}'(\mathbf{x}_{N_s}, t_j))^T$ of the form of a column vector. For three velocity components the velocity snapshot has size $\mathbf{u}^j \in \mathbb{R}^{N \times 1}$ with $N = 3 \cdot N_s$. The M velocity snapshots are stored in the data matrix \mathbf{U} in the form of

$$\mathbf{U} = \begin{pmatrix} | & | & & | \\ \mathbf{u}^1 & \mathbf{u}^2 & \dots & \mathbf{u}^M \\ | & | & & | \end{pmatrix} \in \mathbb{R}^{N \times M}. \quad (2.52)$$

The spatial POD modes Φ_k , here considered as column vectors, result as the eigenvectors from the solution of the eigenvalue problem

$$\mathbf{C} \Phi_k = \lambda_k \Phi_k, \quad (2.53)$$

with the correlation matrix $\mathbf{C} = (\mathbf{U}\mathbf{U}^T)/M \in \mathbb{R}^{N \times N}$ and the corresponding eigenvalues λ_k of the mode Φ_k . The eigenvalues are sorted by their values in descending order such that $\lambda_1 > \lambda_2 > \dots > \lambda_N$. The temporal coefficient $a_k(t)$ of Φ_k is obtained by projecting the velocity data onto the spatial mode by

$$\mathbf{a}_k = \mathbf{U}^T \Phi_k, \quad (2.54)$$

with $\mathbf{a}_k = (a_k(t_1), a_k(t_2), \dots, a_k(t_M))^T$. The relation between the temporal coefficients and eigenvalues is obtained by using the orthogonality of the spatial modes and relation 2.53, which yields

$$\lambda_k = \mathbf{a}_k \cdot \mathbf{a}_k = \sum_{i=1}^M a_k(t_i) a_k(t_i), \quad (2.55)$$

where (\cdot) represents the vector scalar product. The turbulent kinetic energy of the velocity field is obtained by summation over all N eigenvalues of the POD modes

$$k = \frac{1}{2} \sum_{k=1}^N \lambda_k. \quad (2.56)$$

The procedure described above is known as direct method of POD, which can efficiently solve the eigenvalue problem for the case that the number of spatial degrees N is significantly larger than the number of snapshots M . In the opposite case for $M > N$, the so-called POD method of snapshot can be used, which was suggested by Sirovich (1987), and which determines the same dominant spatial POD modes by solving the eigenvalue problem of the temporal correlation matrix $\mathbf{C}_t = (\mathbf{U}^T \mathbf{U})/M \in \mathbb{R}^{M \times M}$ instead

$$\mathbf{C}_t \boldsymbol{\Psi}_k = \lambda_k \boldsymbol{\Psi}_k, \quad (2.57)$$

with eigenvectors $\boldsymbol{\Psi}_k$ and eigenvalues λ_k . The relation between the direct and snapshot POD can be shown by means of the singular value decomposition (SVD) of the data matrix

$$\mathbf{U} = \mathbf{L} \boldsymbol{\Sigma} \mathbf{R}^T, \quad (2.58)$$

where $\mathbf{L} \in \mathbb{R}^{N \times N}$ and $\mathbf{R} \in \mathbb{R}^{M \times M}$ are orthogonal matrices and $\boldsymbol{\Sigma} \in \mathbb{R}^{N \times M}$ contains the singular values σ_i along its diagonal. By substituting the SVD of \mathbf{U} into the definition of the correlation matrices \mathbf{C} and \mathbf{C}_t , it follows that the eigenvectors $\boldsymbol{\Phi}_k$ and $\boldsymbol{\Psi}_k$ corresponds to the column vectors of \mathbf{L} and \mathbf{R} , respectively. In addition, the singular values are related to the eigenvalues by $\sigma_i^2 = M \lambda_i$.

The method of snapshot will be used for the computation of the POD in chapter 4, due to the large number of spatial grid points of the investigated cross-sectional velocity planes.

3 Ridge- and strip-type induced secondary motions

Spanwise heterogeneous surfaces inducing secondary motions are generally divided into ridge- and strip-type surfaces. For the former case differences in the lateral surface height are essential for the formation of secondary motion, while for the latter case variations in the lateral surface drag are relevant. In previous studies, either ridge- or strip-type induced secondary motions were investigated separately. Therefore, the aim of this chapter is to investigate the influence of the combined effects of both surface types, i.e. lateral drag and wall height variations, on the formation of secondary motions. For this purpose, alternating streamwise-aligned rough- and smooth-wall strips in a turbulent channel flow are investigated, where the relative wall height difference between the strips are systematically varied. This allows to study the relative effects of strip- and ridge-type surfaces on the formation on secondary motions.

The numerical framework of the present flow configuration is structured as follows. In a first step, for some characteristic heterogeneous cases, i.e. protruding, intermediate and recessed roughness, the rough surfaces are numerically represented by an IBM method, which numerically fully resolves the individual roughness elements. In a second step, the rough surfaces are represented by the PFA roughness model, which represents the effects of roughness as a statistically homogeneous model and which has been successfully applied for turbulent flows over homogeneous rough surfaces. By the comparison between the two approaches, it can be tested to what extent heterogeneous rough surfaces can be represented by the simplified PFA model. If this is applicable, parameter studies of geometrical surfaces properties of heterogeneous surfaces, such as the relative height difference, can be performed by the PFA with less numerical effort.

This chapter is based on the publications *Rearrangement of secondary flow over spanwise heterogeneous roughness* (Stroh et al. 2020b) and *Modelling spanwise heterogeneous roughness through a parametric forcing approach* (Schäfer et al. 2022b). Compared to the publications, the notation for random stresses, as well as some symbols of physical quantities have been adapted to be consistent with the notation introduced in this thesis. In addition, results of a simulation with larger relative height difference between the alternating rough- and smooth-wall strips are included in this chapter, which were not presented in the previous publications.

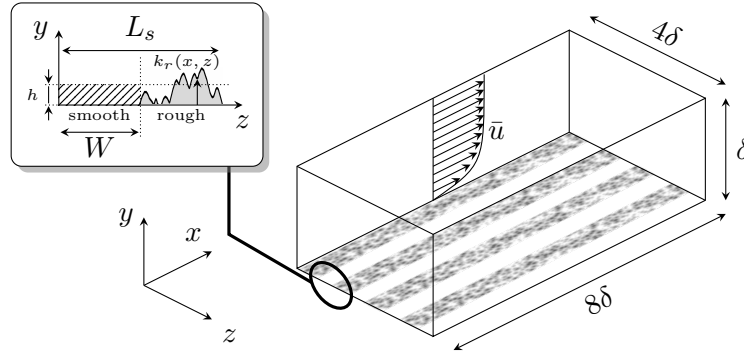


Figure 3.1: Schematic of the open channel domain with alternating rough- and smooth-wall strips at the bottom wall.

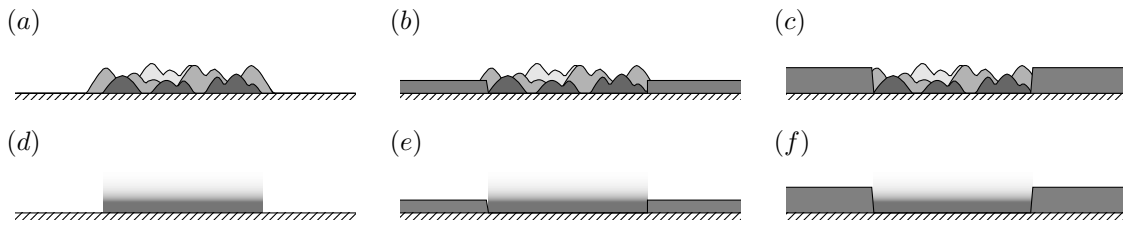


Figure 3.2: Variation of the smooth-wall elevation for fully-resolved roughness cases in (a, b, c) and modelled roughness cases (d, e, f). Case (a) and (d) corresponds to protruding roughness, (b) and (e) to an intermediate roughness and (c) and (f) to a recessed roughness configuration.

3.1 Flow configuration

The flow configuration in this chapter is a fully developed turbulent open channel flow with spanwise alternating rough- and smooth-wall strips as depicted by the sketch in figure 3.1. The flow is driven by a constant pressure gradient which is prescribed to maintain a constant friction Reynolds number of $Re_\tau = 500$ for the different DNS. The friction Reynolds number $Re_\tau = u_\tau \delta_{eff} / \nu$ is based on the effective half-channel height δ_{eff} , which considers the reduction of cross-sectional area due to the introduction of structured surface and its determination will be described below. The continuity and Navier-Stokes equation

$$\frac{\partial u_i}{\partial x_i} = 0, \quad (3.1)$$

$$\frac{\partial u_i}{\partial t} + \frac{\partial u_i u_j}{\partial x_j} = -\frac{1}{\rho} \frac{\partial p}{\partial x_i} + \nu \frac{\partial^2 u_i}{\partial x_j \partial x_j} + \Pi \delta_{i1} + F_{IBM,i} + F_{r,i} \quad (3.2)$$

are solved numerically by the spectral solver SIMSON (Chevalier et al. 2007), where the horizontal direction are discretized by Fourier decomposition and the wall-normal direction employs Chebyshev discretization. The term Π represents the forcing term to maintain a constant pressure gradient, while $F_{IBM,i}$ and $F_{r,i}$ represent the volume forcing terms for the IBM and PFA, respectively. The IBM is based on the method of Goldstein et al. (1993). In the horizontal directions of the open channel periodic boundary conditions are applied, while for the wall-normal direction no-slip boundary conditions are imposed at the bottom wall and symmetry boundary conditions

($v = 0, \partial u/\partial y = \partial w/\partial y = 0$) at the upper boundary. The domain size of the open channel is $L_x \times L_y \times L_z = 8\delta \times \delta \times 4\delta$.

The height of the smooth-wall strip h is systematically varied to realise different relative wall positions between the alternating smooth and rough strips. Thus, three different roughness types can be represented, a protruding roughness, an intermediate roughness and a recessed roughness, which are depicted in figure 3.2 (a-c). While the elevated smooth-wall strips are numerically represented by the IBM, the rough stripes are either resolved by the IBM or modeled by the PFA. In contrast to the IBM, the PFA does not fully resolve the individual roughness elements numerically, but models their effects on the flow as a horizontally homogeneous distribution, such that there are no differences between the different roughness strips. The PFA model will be described in more detail in the next section. In this investigation three heterogeneous roughness cases are performed with the IBM to represent the three different roughness types, while a larger parameter sweep of different h -cases is conducted with the PFA model. "The modelled roughness cases employ two sets of grid resolutions, one being the same as for the resolved roughness cases with a grid resolution $(N_x, N_y, N_z) = (768, 301, 384)$ and a second set with lower resolution in the streamwise and wall-normal directions with $(N_x, N_y, N_z) = (384, 201, 384)$. This allows us to confirm that the grid resolution for the case of the PFA roughness model can be reduced to standard DNS resolution without significant impact on the results."(Schäfer et al. 2022b)

"The spanwise wavelength, L , of one pair of smooth- and rough-wall patches is fixed to $L/\delta = 1$ and the ratio of the smooth-wall width W to the wavelength is set to $W/L_s = 0.5$. The striped surface texture is generated by distributing randomly several discrete roughness elements and deleting those elements whose roughness centre position is placed in a smooth-wall strip, while fulfilling the prescribed roughness statistics. Thus, the individual roughness strips are not identical in their detailed topography. Moreover, foothills of roughness elements placed closely to the rough-smooth border can protrude slightly into the smooth-wall strip. For the homogeneous rough surface the mean elevation of the rough surface is $\bar{k}_r = 0.043\delta$, the maximum roughness height $k_{r,max} = 0.1\delta$ and the root mean square of the roughness height distribution is $k_{r,rms} = 0.024\delta$."(Schäfer et al. 2022b) The skewness and kurtosis of the homogeneous roughness are prescribed as $Sk = 0.079$ and $Ku = 2.24$, respectively.

"The introduction of the rough surface strips and the elevation of the smooth-wall strips on top of the bottom wall ($y = 0$) leads to a local surface elevation and in consequence to a reduction of the effective cross-section seen by the fluid, while the numerical domain size is kept constant. The effective half-channel height δ_{eff} is obtained by subtracting the global melt-down height h_{eff} from the constant half-channel height δ , such that $\delta_{eff} = \delta - h_{eff}$. Here, h_{eff} is obtained by averaging the surface elevation over the full channel length and width, including roughness and elevated smooth-wall regions. In order to maintain the same friction Reynolds number among all configurations, the effective half-channel height is taken into account for the adjustment of the pressure gradient Π ."(Schäfer et al. 2022b)

"In order to obtain statistically converged results, statistics were time integrated over a period of at least 50 flow-through time units. [...] For the present data sets the spatial averages in wall-parallel

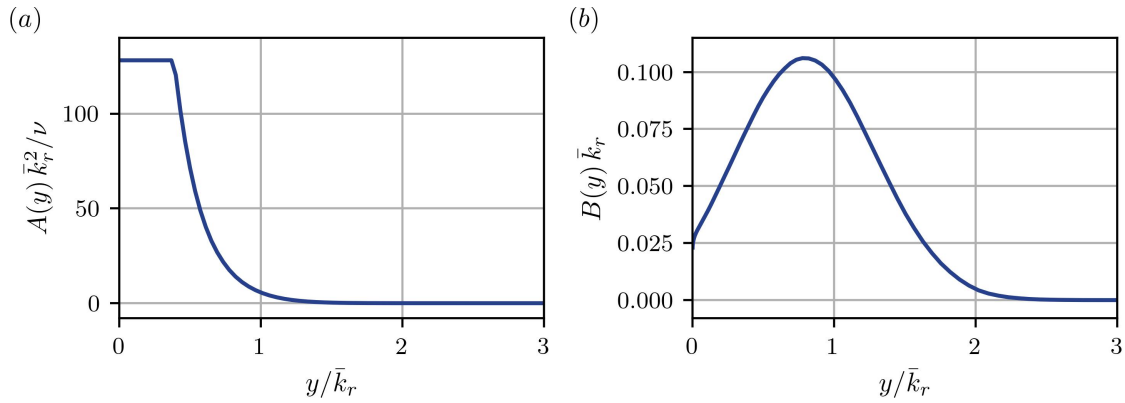


Figure 3.3: The PFA model functions A and B over the wall-normal distance y normalised using the kinematic viscosity ν and the mean roughness height \bar{k}_r . Adopted from Schäfer et al. (2022b).

planes are obtained through extrinsic averaging, which includes the solid region with zero velocity values."(Schäfer et al. 2022b)

3.1.1 Parametric forcing approach

"The PFA forcing term $F_{r,i}$ consists of the sum of a linear and a quadratic contribution of the form

$$F_{r,i} = -A(y)u_i - B(y)u_i|u_i|. \quad (3.3)$$

The general idea behind the derivation of the two model functions - $A(y)$ and $B(y)$ - is briefly presented in the following while full details can be found in Forooghi et al. (2018). The first and second terms on the right-hand side of 3.3 aim to reproduce the viscous drag and form drag per unit volume caused by roughness elements at a certain wall distance y , respectively. An analogy between roughness and porous media is employed to derive an expression for the first function, based on the Kozney-Carman porous medium permeability model

$$A(y) = k_K \frac{\nu s(y)^2}{\epsilon(y)^3}. \quad (3.4)$$

In 3.4 ϵ (porosity) is the fluid volume per unit total volume, s is the total surface area of the roughness per unit total volume and k_K is an empirical constant. In order to find the values of s and ϵ as functions of y , the roughness perimeter (area) resulting from intersection of y -planes with the roughness surface (volume) is used. The function $B(y)$ is derived such that the corresponding term represents the form drag due to all roughness elements. That is

$$B(y) = c_D \frac{s_f(y)}{2} \quad (3.5)$$

where s_f denotes the total ‘windward-projected’ surface area of roughness per total volume and c_D is the effective drag coefficient of the roughness. One should keep in mind that the three functions $s_f(y)$, $s(y)$ and $\epsilon(y)$ are uniquely determined based on the specific roughness geometry. They can also be considered as statistical representations of a roughness topography. The two constants k_K

and c_D serve as model constants, which enable tuning of the model. The values of these constants have been tuned by Forooghi et al. (2018) based on a number of DNS cases with homogeneous roughness with systematically varied topographies. In the present work, we slightly readjust the constants in order to reproduce the mean velocity profile for the specific roughness topography under consideration as closely as possible the homogeneous rough case. Note that the PFA forcing is not applied in the wall-normal direction, i.e. $F_{r,2} = 0$ following the suggestion by Busse and Sandham (2012). "(Schäfer et al. 2022b)

"Obviously, $A(y)$ and $B(y)$ are zero for $y > k_{r,max} = 0.1\delta$ and their specific distributions, as shown in figure 3.3, are restricted to $y \leq k_{r,max} = 0.1\delta = 2.3\bar{k}$ as there is no roughness above this height. Close to the wall, porosity approaches zero, leading for $A(y)$ to assume very large values. Therefore, as visible in figure 3.3 (a), $A(y)$ is bounded near the wall to ensure numerical stability. This has a negligible effect on the flow since the mean velocity is very small for $y < \bar{k}/2$."(Schäfer et al. 2022b)

3.2 Results

3.2.1 Global flow properties

The global flow properties of the homogeneous smooth and rough configurations and the heterogeneous roughness surfaces with different smooth-wall heights h are listed in table 3.1. For the homogeneous rough case and three heterogeneous rough surfaces with different smooth-wall heights $h = 0, 0.97\bar{k}_r, 1.70\bar{k}_r$, the rough surfaces are modeled once by the IBM and also by the PFA. These PFA cases are performed with two different numerical resolutions, to test the resolution requirements for the representation of heterogeneous rough surfaces. In addition, further configurations using the PFA model were considered with smooth-wall elevations in the range $0.5\bar{k}_r \leq h \leq 3.00\bar{k}_r$. "Note that the definition of \bar{k}_r is based on the homogeneous rough reference."(Schäfer et al. 2022b)

"The PFA model was originally developed to represent the effect of homogeneous rough surfaces on a turbulent flow field and is applied to spanwise heterogeneous roughness in the present investigation. In order to match the skin friction coefficient of a particular homogeneous rough surface with high accuracy, the coefficients in the model functions A and B of equation 3.3 require a fine tuning which yields the particular distribution of A and B shown in figure 3.3 for the present homogeneous rough reference surface."

"The reduced cross-sectional area of the channel - through the introduction of IBM-based roughness elements or the PFA model - is taken into account through the effective half-channel height δ_{eff} introduced in section 3.1. Therefore, the bulk velocity u_b is evaluated as

$$u_b = \frac{1}{\delta_{eff}} \int_0^{\delta} \langle \bar{u} \rangle (y) dy. \quad (3.6)$$

case	roughness	representation	resolution	$\delta_{\text{eff}}/\delta$	Re_τ	Re_b	u_b^+	$C_f/C_{f,s}$
smooth	-	-	high	1.000	499.98	9046.6	18.09	1.00
smooth	-	-	low	1.000	500.00	9042.6	18.09	1.00
rough	hom.	IBM - resolved	high	0.957	500.44	5240.8	10.47	2.99
rough	hom.	PFA - model	high	0.957	499.90	5224.2	10.45	3.00
rough	hom.	PFA - model	low	0.957	500.25	5229.0	10.45	3.00
$h = 0$	het.	IBM - resolved	high	0.978	499.58	5755.5	11.52	2.47
$h = 0$	het.	PFA - model	high	0.978	500.05	5937.5	11.87	2.32
$h = 0$	het.	PFA - model	low	0.978	500.01	5909.1	11.82	2.34
$h = 0.50\bar{k}_r$	het.	PFA - model	low	0.968	500.09	5978.3	11.95	2.29
$h = 0.97\bar{k}_r$	het.	IBM - resolved	high	0.958	500.04	5981.5	11.96	2.29
$h = 0.97\bar{k}_r$	het.	PFA - model	high	0.958	500.43	5991.3	11.97	2.28
$h = 0.97\bar{k}_r$	het.	PFA - model	low	0.958	499.82	6005.0	12.01	2.27
$h = 1.25\bar{k}_r$	het.	PFA - model	low	0.952	500.20	6010.1	12.01	2.27
$h = 1.50\bar{k}_r$	het.	PFA - model	low	0.947	499.97	5997.4	11.99	2.27
$h = 1.70\bar{k}_r$	het.	IBM - resolved	high	0.943	500.01	6050.1	12.10	2.24
$h = 1.70\bar{k}_r$	het.	PFA - model	high	0.943	499.87	5927.1	11.86	2.33
$h = 1.70\bar{k}_r$	het.	PFA - model	low	0.943	499.77	5960.7	11.93	2.30
$h = 2.00\bar{k}_r$	het.	PFA - model	low	0.936	500.14	5915.6	11.83	2.34
$h = 2.50\bar{k}_r$	het.	PFA - model	low	0.925	499.99	5811.9	11.62	2.42
$h = 3.00\bar{k}_r$	het.	PFA - model	low	0.914	499.94	5665.0	11.33	2.55

Table 3.1: Global flow properties from DNS of the homogeneous smooth- and rough-wall cases and the heterogeneous smooth-rough cases with varying smooth-wall distance h . Adopted from Schäfer et al. (2022b).

Since the simulations are run at constant Re_τ the introduction of roughness leads to a reduced bulk Reynolds number $Re_b = u_b \delta_{\text{eff}}/\nu$ and a decrease of the normalised bulk velocity u_b^+ (where the superscript + represents viscous units obtained through a normalisation with the friction velocity u_τ). Note that u_τ is defined through the effective wall-shear stress which is obtained through an extrapolation of the linear total shear stress distribution to the location $y_0 = \delta - \delta_{\text{eff}}$ (Chan-Braun et al. 2011). The reduced flow rate in the rough channel at constant Re_τ translates into an increased friction coefficient $C_f = 2u_\tau^2/u_b^2$ compared with the smooth-wall reference. As reported in Forooghi et al. (2018) the tuned PFA model captures the drag increase in terms of $C_f/C_{f,s}$ (where $C_{f,s}$ represents the skin friction drag coefficient of a smooth wall at the same Re_τ) very well for the homogeneous rough surface. In addition, it can be seen that the reduction of the spatial resolution to standard DNS dimensions for the PFA model does not influence the global flow parameters."(Schäfer et al. 2022b)

As can be seen, the heterogeneous roughness cases exhibit a strong increase of C_f than compared to the smooth-wall case. This translates into a reduction of u_b by 33-37% for the different heterogeneous rough cases, and a reduction of 42% for the homogeneous rough case. In order to determine the contribution of secondary motion on the skin friction, the assumption is made

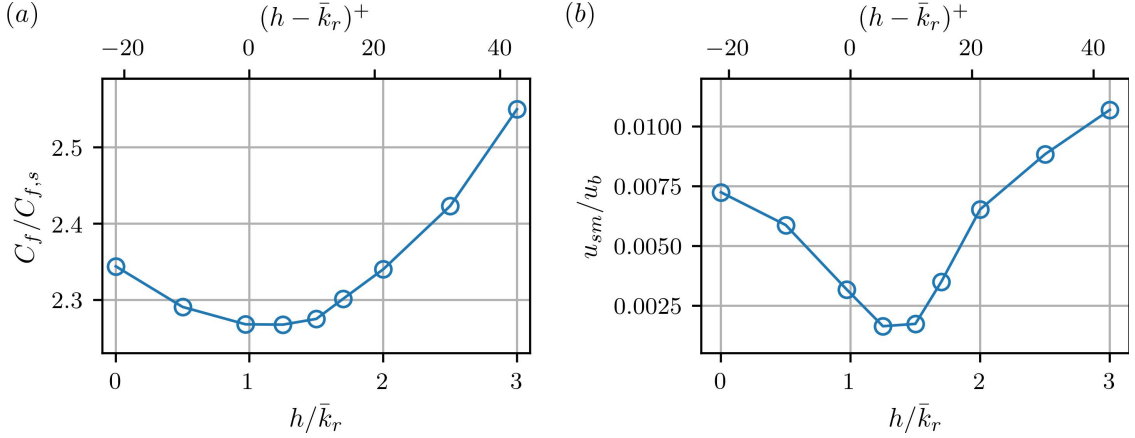


Figure 3.4: Influence of smooth-wall height h on skin friction coefficient C_f in (a) and intensity of secondary motions u_{sm} in (b) for the PFA modelled cases.

that C_f of alternating smooth- and rough-wall strips without secondary motions $C_{f,ns}$ can be determined from an area-average of flow properties of the homogeneous rough and smooth-wall cases. For a channel with constant pressure gradient it follows that the global $u_b = 0.5(u_{b,s} + u_{b,r})$ is the area-average of the flow rates over the rough and smooth strips. Eventually, since u_τ is kept constant for both surfaces, a power mean for the global C_f is obtained (Neuhauser et al. 2022), and eventually follows

$$\frac{C_{f,ns}}{C_{f,s}} = \left(\frac{1}{2} \left(1 + \sqrt{\frac{C_{f,s}}{C_{f,r}}} \right) \right)^{-2} = 1.608. \quad (3.7)$$

The comparison of the heterogeneous rough cases to $C_{f,ns}/C_f$ clearly shows a significantly higher relative drag increase for all h values. Among the IBM-resolved cases $h = 0$ has the largest relative drag increase of 53.7% compared to $C_{f,ns}/C_f$.

"The general drag increasing impact of the inhomogeneous roughness on c_f above the area-averaged value is well captured by the PFA model. However, we find an underprediction of $c_f/c_{f,s}$ for $h = 0$ and an overprediction for $h = 1.70\bar{k}_r$, while there is a very good match for $h \approx \bar{k}_r$. A reduction of the resolution for the modelled roughness to the one of a standard smooth-wall DNS has a negligible to small effect on the obtained results, which is largest for $h = 1.70\bar{k}_r$ with a difference of less than 2% for $c_f/c_{f,s}$. Therefore, the additional variations of h investigated with the PFA model only are simulated with low resolution. All results presented in the following refer to the low resolution configuration." (Schäfer et al. 2022b)

The effect of the smooth-wall strip height h on C_f is shown for the different PFA cases in figure 3.4 (a). As can be seen, C_f has a global minimum in the range of $h = 1.25\bar{k}_r$, where the mean height of the roughness strip and the smooth-wall strip height are similar. Considering the relative height difference $h - \bar{k}_r$, the profile of C_f is almost symmetrical around the zero value of $h - \bar{k}_r$, such that for positive and negative relative height differences which are equal in absolute terms, also equal C_f values are obtained. Moreover, when the relative height difference exceeds about 10 plus units, the relative increase in C_f with $h - \bar{k}_r$ is stronger, as can be seen for cases $h > 1.5$.

In case of heterogeneous rough surfaces secondary motions are present which will be shown in section 3.3.1. The strength or intensity of secondary motions is here quantified by the square root of the cross-sectional averaged kinetic energy of the cross-sectional velocity components (Scherer et al. 2022), which is defined by

$$u_{sm} = \left(\frac{1}{L_z \delta_{eff}} \int_0^{L_z} \int_0^\delta (\tilde{v}^2 + \tilde{w}^2) dy dz \right)^{1/2}. \quad (3.8)$$

The intensity of the secondary motions for the different heterogeneous rough surfaces with respect to h is shown in figure 3.4 (b). The weakest secondary motion is found for $h = 1.25\bar{k}_r$ and $h = 1.50\bar{k}_r$, while the strongest intensity is found for $h = 3.00\bar{k}_r$. The latter one is in a similar range of values as found for secondary motion intensities of mobile sediment ridges in open-channel flows (Scherer et al. 2022). Similar to C_f , the intensity of the secondary motions increases with larger relative height differences $h - \bar{k}_r$, taking into account the slight offset towards positive values for $h - \bar{k}_r$.

"Figure 3.5 shows the streamwise mean velocity profiles (averaged in time and the two wall-parallel spatial directions) in logarithmic scaling. The zero wall location is placed at a distance of δ from the channel centre for all cases. Figure 3.5 (a) contains the velocity profiles for the resolved and modelled homogeneous rough surface for reference. Slight deviations in the region in the range $\bar{k}_r < y < k_{r,max}$ are visible that can be traced back to a similar but not identical wall-normal force distribution in case of IBM and PFA. Overall, very good agreement between these two approaches is obtained. This is in agreement with the very similar integral u_b^+ values reported in table 1. The roughness function ΔU^+ is 8.002 and 8.046 for the resolved and modelled roughness, respectively."(Schäfer et al. 2022b)

"As will be shown later, the streamwise mean velocity exhibits spanwise variations up to the channel centre in some of the heterogeneous rough cases. Nevertheless, these spanwise-averaged velocity profiles can provide some insight into the differences for modelled and resolved roughness reported in table 3.1. In the case of $h = 0$ it can be seen that, in contrast to the homogeneous rough case, differences between IBM and PFA already emerge below $y = \bar{k}_r$. The PFA model leads to higher average velocities in this region. In this case the roughness strips are exposed to the surrounding flow (compare figure 3.2). As outlined in section 3.1, individual roughness elements whose centre is in the rough region can extend with their foothills into the otherwise smooth region (see figure 3.2) for the present set-up. These roughness elements, which slightly stick out of the rough region, are not modelled in the PFA approach, which is restricted to a force distribution in the rough region (see figure 3.2 (d)). Therefore, the additional drag exerted by the spanwise protruding roughness elements leads to larger global drag for the IBM case (see table 3.1) and a reduced average streamwise velocity (see figure 3.5). With increasing h this effect is reduced and eventually flipped since spanwise protruding roughness elements are merged with the surrounding elevated smooth-wall area. In consequence, IBM and PFA results agree much better for $h > 0$ (see figure 3.5 (b, c)). In the case of $h = 1.70\bar{k}_r$, u_b^+ for the resolved roughness exceeds the one of the corresponding modelled case by 3 – 4% (depending on the resolution). Translated into a drag coefficient, the PFA model thus produces larger drag than the IBM approach for this

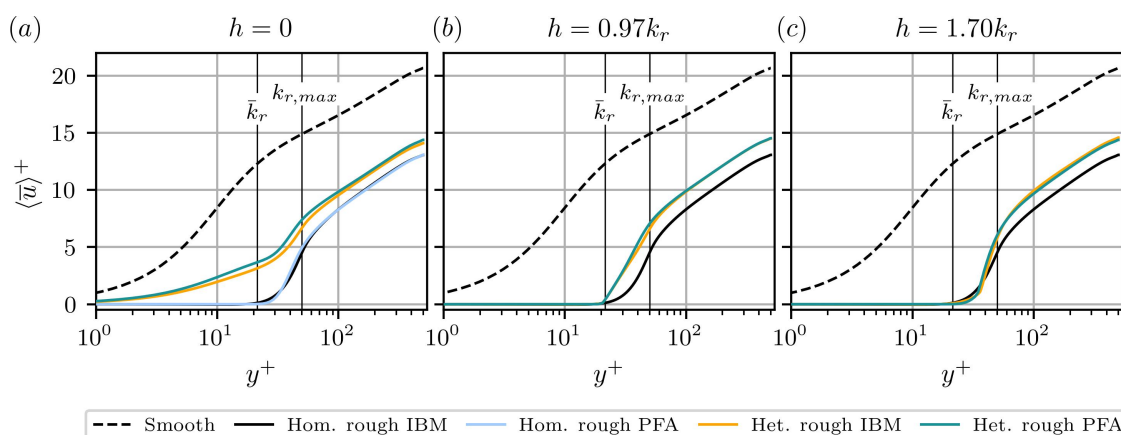


Figure 3.5: Comparison of the streamwise mean velocity profiles between IBM and PFA model cases for three smooth-wall elevations $h = 0$ (a), $h = 0.97\bar{k}_r$ (b) and $h = 1.70\bar{k}_r$ (c). In (a) the homogeneous rough PFA case is presented by the light blue line. Adopted from Schäfer et al. (2022b).

case. This difference can be related to an effectively narrower rough-wall region in case of IBM (since roughness elements at the edges are partially merged with the elevated smooth wall) which allows us to generate higher flow rates for the same pressure drop, opposite to the effectively wider rough-wall region for $h = 0$. However, the comparison between IBM and PFA for this case is more complex, as can be seen from the streamwise velocity profiles at different spanwise locations discussed in the following."(Schäfer et al. 2022b)

"The data displayed in figure 3.6 are obtained based on averaging in time, streamwise direction and exploiting the spanwise periodicity. The resulting spanwise coordinate $\bar{z} = z/\delta$ is in the range $0 \leq \bar{z} \leq 1$ with its origin $\bar{z} = 0$ placed at the centre of the smooth-wall patch. The centre of the roughness patch is located at $\bar{z} = 0.50$ and the transition between rough to smooth occurs at $\bar{z} \approx 0.25$. Therefore, the blue shaded colours correspond to spanwise locations over the smooth surface patch while red shaded colours represent locations over the rough surface part. The velocity profiles at different spanwise locations collapse in the outer flow region for some of the investigated cases only (see figure 3.6 (b, f)). The other cases reveal spanwise variations far into the bulk flow, indicating the presence of strong secondary motions, which are addressed in detail in the following section. From figure 3.6 it is apparent that the influence of the secondary flow on the streamwise mean flow among IBM and PFA differs, especially in the case of $h = 1.70\bar{k}_r$. A strong spanwise inhomogeneity is present for IBM in the range $0.18 \leq y/\delta \leq 0.85$ (figure 3.6 (c)) in contrast to a more homogeneous streamwise flow field for PFA figure 3.6 (f)). The increased velocities for IBM discussed above can be seen to originate from the flow above the rough surface part. In this case the PFA forcing is located below the surrounding smooth-wall strips (see figure 3.2 (f)) while individual IBM roughness peaks reach beyond $y = h$ (see figure 3.2 (c)). At the same time, streamwise velocity can establish in between the IBM roughness elements. We will turn again to the discussion of larger drag for PFA in the case of $h = 1.70\bar{k}_r$ after the discussion of secondary motions (section 3.2.2) and turbulent flow properties (section 3.2.3)."(Schäfer et al. 2022b)

"To a weaker extent differences between IBM and PFA are also present for $h = 0$ and $h \approx \bar{k}_r$. The high momentum pathways are located above the smooth surface parts for these cases (blue shaded colours) which corresponds to the flow distribution one would expect from a laminar flow

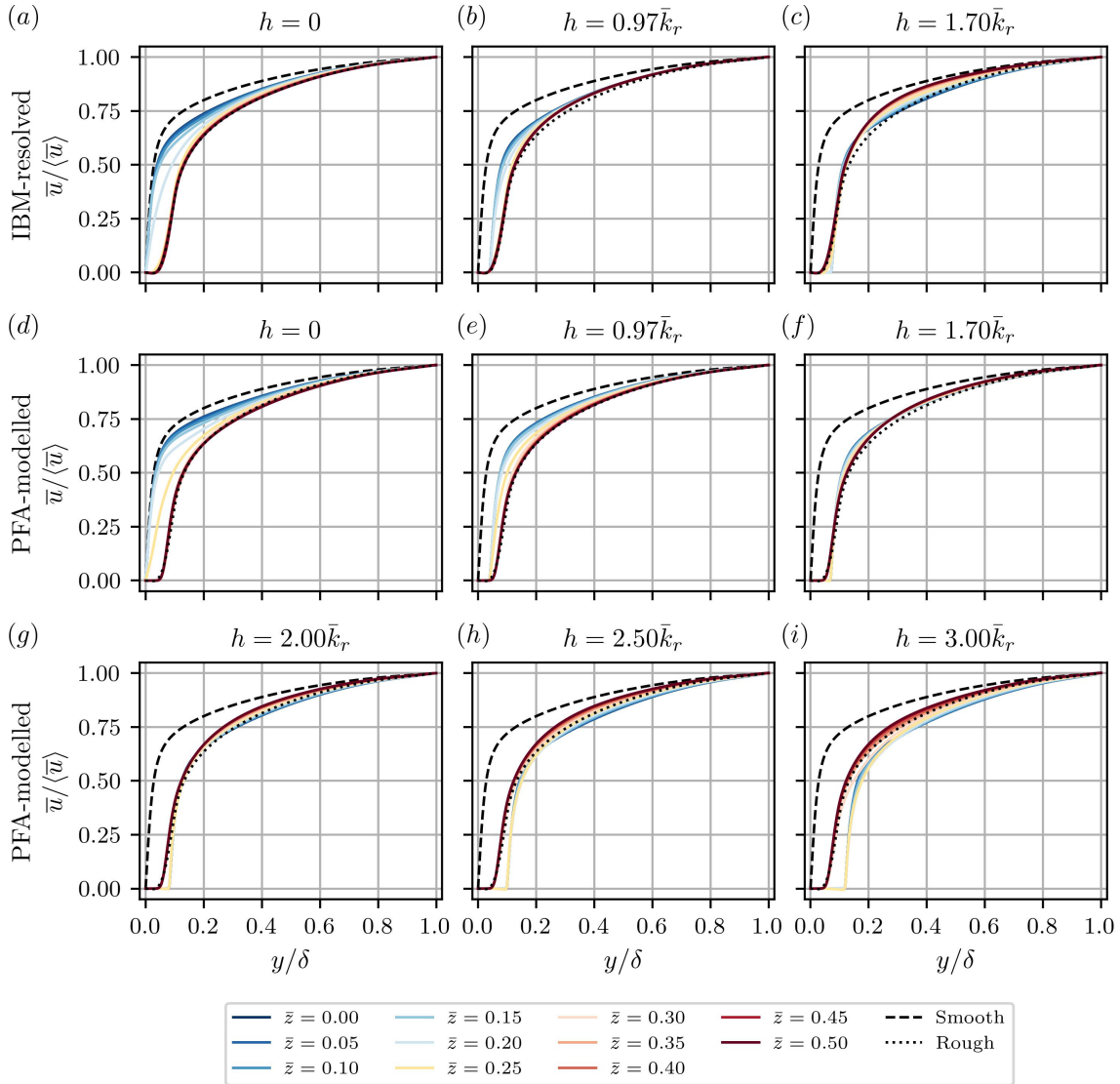


Figure 3.6: Mean streamwise velocity profiles at different spanwise locations $\bar{z} = z/\delta$. The dark blue line shows the centre of the smooth strip at $\bar{z} = 0.0$ and the dark red line the centre of the rough strip at $\bar{z} = 0.5$. The dashed and dotted black lines represent the streamwise mean velocity of the smooth and homogeneous rough case (IBM). Adopted from Schäfer et al. (2022b).

(i.e. a flow without secondary motions of Prandtl's second kind) above surfaces with varying friction drag. This spanwise inhomogeneity of \bar{u} is enhanced by the secondary motions typically found above ridge-type roughness, inducing a downwelling motion above the recessed area. This effect appears to be slightly stronger for the modelled roughness. Figure 3.6 (a, d) confirms that the increase of u_b^+ in case of PFA for $h = 0$ is related to the velocity difference at the transition between smooth- and rough-wall areas ($\bar{z} = 0.25$). (Schäfer et al. 2022b)

"In case of increased elevation of the smooth-wall area, the spanwise distribution of the streamwise velocity changes in the sense that high momentum pathways are located above the rough surface parts (red shaded colours). This can be observed in the case of $h = 1.70\bar{k}_r$ for the resolved roughness and for $h = 2.00 - [3.00] \bar{k}_r$ for the modelled roughness. This different behaviour is related to the reversed rotational direction of the secondary motions addressed in the following

section. It is interesting to note that the spanwise inhomogeneity is most pronounced in the outer flow region [for cases $h = 2.00-2.50\bar{k}_r$], while the classical ridge-type behaviour is dominated by large spanwise variations in the near-wall region [as seen for $h = 0$ and which starts to become again more dominant for case $h = 3.00$]."(Schäfer et al. 2022b)

3.2.2 Secondary motions

"Figure 3.7 shows the cross-sectional mean flow obtained for resolved and modelled inhomogeneous roughness. The secondary motion is extracted from a phase average (over $L/2$) of the mean flow field obtained through space averaging (along the streamwise direction) and temporal averaging. [...] The white lines with arrows in figure 3.7 represent the in-plane secondary motion, while the colour code corresponds to the streamwise mean velocity. Isolines of the streamwise mean velocity are plotted as grey lines to indicate the spanwise inhomogeneity of the mean flow."(Schäfer et al. 2022b)

First, the flow structures found for the IBM-resolved cases in figure 3.7 (*a-c*) are discussed before the comparison to the PFA model is made. "In all three [roughness-resolved] cases, pronounced secondary motion patterns can be observed. In the case of $h = 0$ (figure 3.7 (*a*)) the two main large-scale vortices originate from the edges of the rough ridge. Two additional counter-rotating small vortex pairs are located on the smooth wall and on top of the rough patch. The deformation of the streamwise velocity profile is shown with [gray] velocity isolines. It can be seen that a LMP is present over the rough surface part. This flow topology is similar to the secondary flows over ridge-type roughness (for example, Hwang and Lee (2018)). In contrast, the case with [$h = 1.70\bar{k}_r$] (figure 3.7 (*c*)) shows a downward bulging of the streamwise velocity field, and thus HMP over the rough surface part. In this case the secondary motion is given through a single counter-rotating vortex pair with an upward motion above the elevated smooth region. This flow topology resembles the secondary flow reported for strip-type roughness (for example, Willingham et al. (2014), Chung et al. (2018))."(Stroh et al. 2020b)

"The comparison of these two cases suggests that the alteration of the smooth-wall elevation is an additional parameter for the secondary motion formation, which might enable rearrangement of the secondary flow topology from the ridge-type regime (LMP over rough area) to the strip-type regime (HMP over rough area)."(Stroh et al. 2020b)

"The third case [$h = 0.97\bar{k}_r$] (figure 3.7 (*b*)) corresponds to an intermediate state between ridge- and strip-type roughness. In this flow a more complex secondary flow topology is present. The largest vortical structures do not cover the entire vertical domain. [...] The rotational direction of the vortex pair in the lower channel half corresponds to the one observed for [$h = 1.70\bar{k}_r$] and the small one located in the centre of the roughness for $h = 0$."(Stroh et al. 2020b)

The heterogeneous rough cases with modelled roughness in figure 3.7 (*d-l*) clearly show, "[...] that the PFA model is able to predict large-scale secondary motions. These are in very good agreement with the results for the resolved roughness in case of the protruding rough surface, $h = 0$ (see figure 3.7 (*a*), (*d*)), revealing an upward motion above the roughness strip that is strong enough

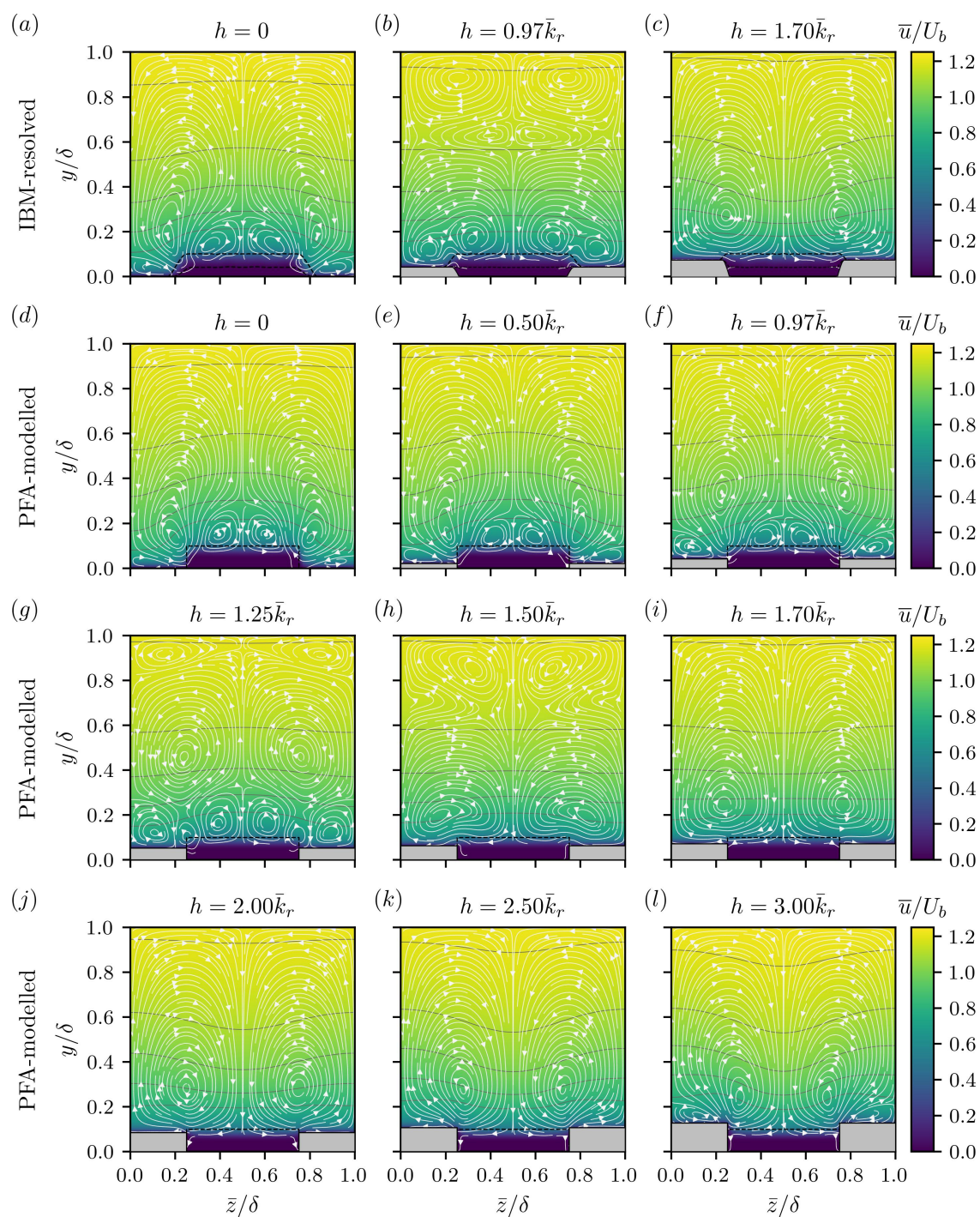


Figure 3.7: Contours of streamwise mean velocity and the induced secondary motion for resolved roughness cases (a) - (c) and modelled roughness cases (d) - (l). Adopted from Schäfer et al. (2022b).

to significantly deflect the isolines of streamwise mean velocity. In the near-wall region these deflections are slightly stronger for the modelled roughness. In the case of $h \approx \bar{k}_r$ (see figures 3.7 (b), (f)) the modelled roughness induces a secondary motion similar to the one at $h = 0$ along with the corresponding bulging of the streamwise flow while the resolved roughness does not reveal any bulging of the streamwise velocity isolines, indicating a weaker secondary motion. The PFA case thus behaves more like a ridge-type roughness. For the recessed roughness ($h = 1.70\bar{k}_r$ in

figures 3.7 (*c, i*) the secondary flow topology is similar between IBM and PFA in the sense that the upward motion is located above the smooth-wall strip for resolved and modelled roughness. However, the secondary motion induces a deflection of the streamwise mean flow in case of the resolved roughness (figure 3.7 (*c*)), especially at larger wall distance, while this cannot be observed for the modelled roughness (figure 3.7 (*i*)), indicating weaker secondary currents."(Schäfer et al. 2022b)

"The secondary flow topology in the case of recessed roughness, $h = 1.70\bar{k}_r$, encompasses only one large-scale vortex pair, while a more complex topology exists for smaller h . For $h = 0$, in addition to the dominating large-scale vortex pair that reflects in the mean flow bulging, two small vortex pairs can be observed for the resolved and the modelled roughness: one on top of the roughness strip and another one above the smooth-wall area. Both small vortex pairs have an opposite rotational direction compared with the dominating large-scale vortex pair such that a downward motion above the centre of the roughness and an upward motion above the centre of the smooth patch is found in the near-wall region."(Schäfer et al. 2022b)

"The additional PFA simulations with varying h reveal that this transition of the secondary flow topology can also be captured for the modelled roughness. In this case, a topology similar to (figure 3.7 (*b*)) is realised with an increased h of $h = 1.50\bar{k}_r$ (figure 3.7 (*h*)) which also does not induce any bulging of the streamwise mean flow isolines. The fact that the modelled case requires larger h values in order to match the secondary flow topology of the resolved roughness is also present for the more recessed roughness. The secondary flow and related isoline curvature generated for a resolved roughness with $h = 1.70\bar{k}_r$ (figure 3.7 (*c*)) is captured for a modelled roughness with $h = 2.00 - 2.50\bar{k}_r$ (figure 3.7 (*j, k*)) which is in agreement with the discussion in section 3.2.1."(Schäfer et al. 2022b)

For the largest case with $h = 3.00\bar{k}_r$ (figure 3.7 (*l*)) a small vortex pair emerges above the smooth-wall area. This indicates that h and the relative height difference is getting large enough such that for the secondary motion the ridge-type induced behaviour becomes more relevant. The increase in the strength of the secondary motion for larger h , as shown for the intensity of the secondary motion in figure 3.4 (*b*), is reflected by the stronger downward bulging of the isolines over the rough strip for $h = 3.00\bar{k}_r$, which is also more pronounced in the bulk region compared to cases with lower h .

"As a measure for the spatial extent and the strength of the secondary motion the spanwise-averaged wall-normal mean velocity magnitude $\langle \tilde{v}\tilde{v} \rangle$ is shown in figure 3.8. Since spanwise averages integrate a number of different features, especially in cases of complex flow topology, a colour map of the wall-normal spanwise distribution of \tilde{v} is provided in the Appendix in figure A.1."(Schäfer et al. 2022b)

"For the IBM case with protruding roughness ($h = 0$), $\langle \tilde{v}\tilde{v} \rangle$ spans a wide wall-normal range with a rather constant value with a local near-wall maximum around $y \approx k_{r,max}$. This can directly be related to the strong deflection at the smooth-rough interface. While small values for $\langle \tilde{v}\tilde{v} \rangle$ are found for $h \approx \bar{k}_r$, the recessed roughness case ($h = 1.70\bar{k}_r$) features a single strong peak around $y \approx 0.3\delta$. Interestingly, the streamwise mean velocity isolines at this wall-normal location exhibit

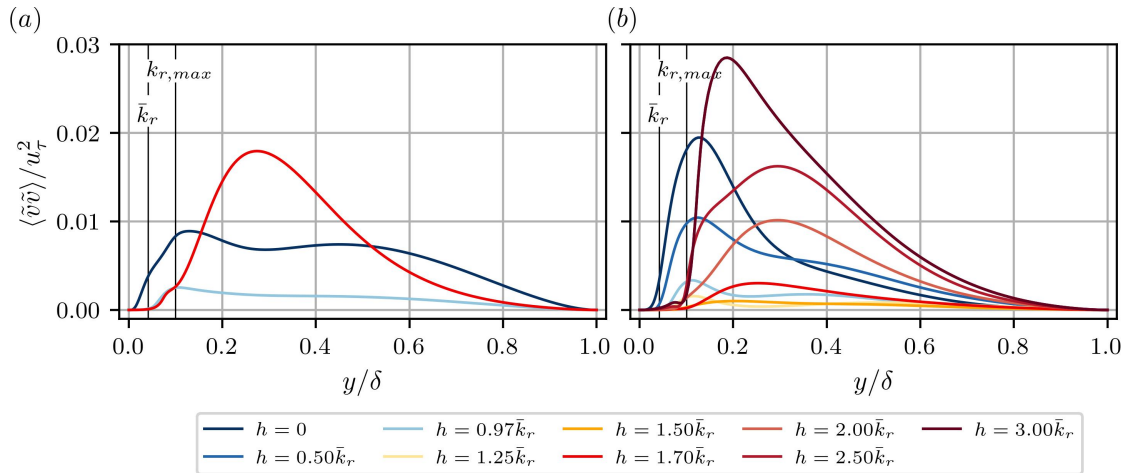


Figure 3.8: Spanwise averaged wall-normal dispersive stress profiles for IBM-resolved roughness cases in (a) and PFA-modelled roughness cases in (b). Adopted from Schäfer et al. (2022b).

a weak bulging only (see figure 3.7), indicating that the secondary motion acts to homogenize the spanwise distribution of streamwise mean velocity in this case. Comparing $\langle \tilde{v}\tilde{v} \rangle$ for the modelled roughness (figure 3.8 (b)) with the resolved one (figure 3.8 (a)) reveals a number of differences. For $h = 0$ the PFA model depicts a stronger peak around $y \approx k_{r,max}$ and lower values in the bulk of the flow. The stronger peak can be related to a stronger and more localised upward wall-normal velocity at the transition of the smooth to rough wall (see figure A.1), while for the IBM model these upward deflections are less intense in the transition region. In terms of $\langle \tilde{v}\tilde{v} \rangle$ the modelled roughness with $h = 0.50\bar{k}_r$ bears the largest resemblance to the resolved $h = 0$ case. For $h = 1.70\bar{k}_r$ the modelled roughness induces significantly lower values for $\langle \tilde{v}\tilde{v} \rangle$ as expected from the absence of isoline curvature in figure 3.7 (i). Actually, the wall nearest isoline in this figure shows a slight outward bulging above the roughness which a stronger secondary motion would annihilate and eventually reverse. For PFA this increase in secondary motion strength can be realised with an increase of h such that not only the secondary flow topology but also the corresponding intensity for $h = 1.70\bar{k}_r$ with IBM is reasonably well matched for $h = 2 - 2.5\bar{k}_r$ with PFA." (Schäfer et al. 2022b)

The strength of the secondary motion further increases for $h = 3\bar{k}_r$ and the peak value is now larger than for the protruding roughness case $h = 0$. An indication that the ridge-type behaviour becomes increasingly important for this case, is that the peak location now shifts closer to the wall than compared to the lower cases $h = 1.7-2.5\bar{k}_r$. However, this behaviour is likely to reverse at some point with increasing h since at the same time the wall-offset becomes also larger as h increases. This influence of the wall-offset can already be seen by the comparison with case $h = 0$, where the peak location is closer to the wall than for $h = 3\bar{k}_r$.

"Within the PFA modelled cases (figure 3.8 (b)) the sole influence of h on $\langle \tilde{v}\tilde{v} \rangle$ (employed here as a simple measure of the secondary flow strength) can nicely be analysed. On the one hand, protruding roughness induces very strong upward motions around $y \approx k_{r,max}$ which reduce in their intensity for a reduced protrusion of the roughness. On the other hand, recessed roughness also induces strong $\langle \tilde{v}\tilde{v} \rangle$; again with reduced intensity for decreased wall offsets. However, for recessed

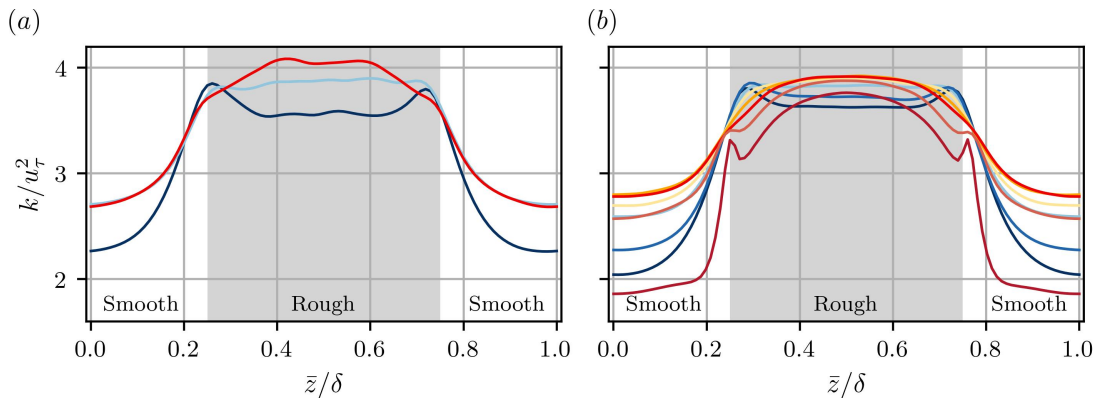


Figure 3.9: Spanwise variation of turbulent kinetic energy for resolved roughness cases in (a) and modelled roughness cases in (b) extracted at $y = 0.115\delta$. Line colours same as in figure 3.8. Adopted from Schäfer et al. (2022b).

roughness, the peak of $\langle \tilde{v}\tilde{v} \rangle$ is located at a larger wall-normal distance. This is in agreement with the observation made in respect to figure 3.6 (section 3.2.1), that spanwise inhomogeneity of the streamwise velocity profile is more pronounced in the outer flow region for recessed roughness and more pronounced in the near-wall region for protruding roughness. In the case of recessed roughness, the turbulence generated secondary motions homogenize the surface elevation induced inhomogeneities near the wall. Their influence on the streamwise mean flow is therefore more perceptible at larger wall distances up to which surface-induced inhomogeneities alone do not reach. In contrast, turbulence generated secondary motions over protruding roughness enhance surface-induced inhomogeneities of the flow field such that their combined influence is strongest near the wall."(Schäfer et al. 2022b)

"We note that the observed tendency of the decrease and increase of the wall-normal velocity magnitude with increasing h correlates well with the development of the skin friction coefficient of the PFA model (cf. table 3.1) and suggests that the appearance of strong secondary motions contributes to drag increase."(Schäfer et al. 2022b)

3.2.3 Turbulence flow properties

"The flow above rough walls is typically characterised by increased turbulent kinetic energy and shear stress. Foroughi et al. (2018) show that the PFA model captures these features relatively well for homogeneous rough surfaces. Figure 3.9 shows the spanwise variation of the turbulent kinetic energy $k = \frac{1}{2}(\overline{u''u''} + \overline{v''v''} + \overline{w''w''})$ slightly above the maximum roughness elevation at a wall-normal position of $y = 0.115\delta$ for the investigated inhomogeneous roughness cases [(case $h = 3\bar{k}_r$, not shown due to the larger wall-normal offset)]. The increased turbulent kinetic energy above the rough patches and also its spanwise distribution are well captured by the model. Comparing the magnitude of k between resolved and modelled roughness for the same smooth-wall elevation h indicates that the modelled roughness induces similar turbulent kinetic energy to the resolved one. Above the smooth-wall patches k is similar for resolved and modelled roughness in the case of $h = 0.97\bar{k}_r$ and $h = 1.70\bar{k}_r$, but differs for $h = 0$. The turbulent kinetic energy above the smooth area located in between resolved roughness elements is larger in this case. The

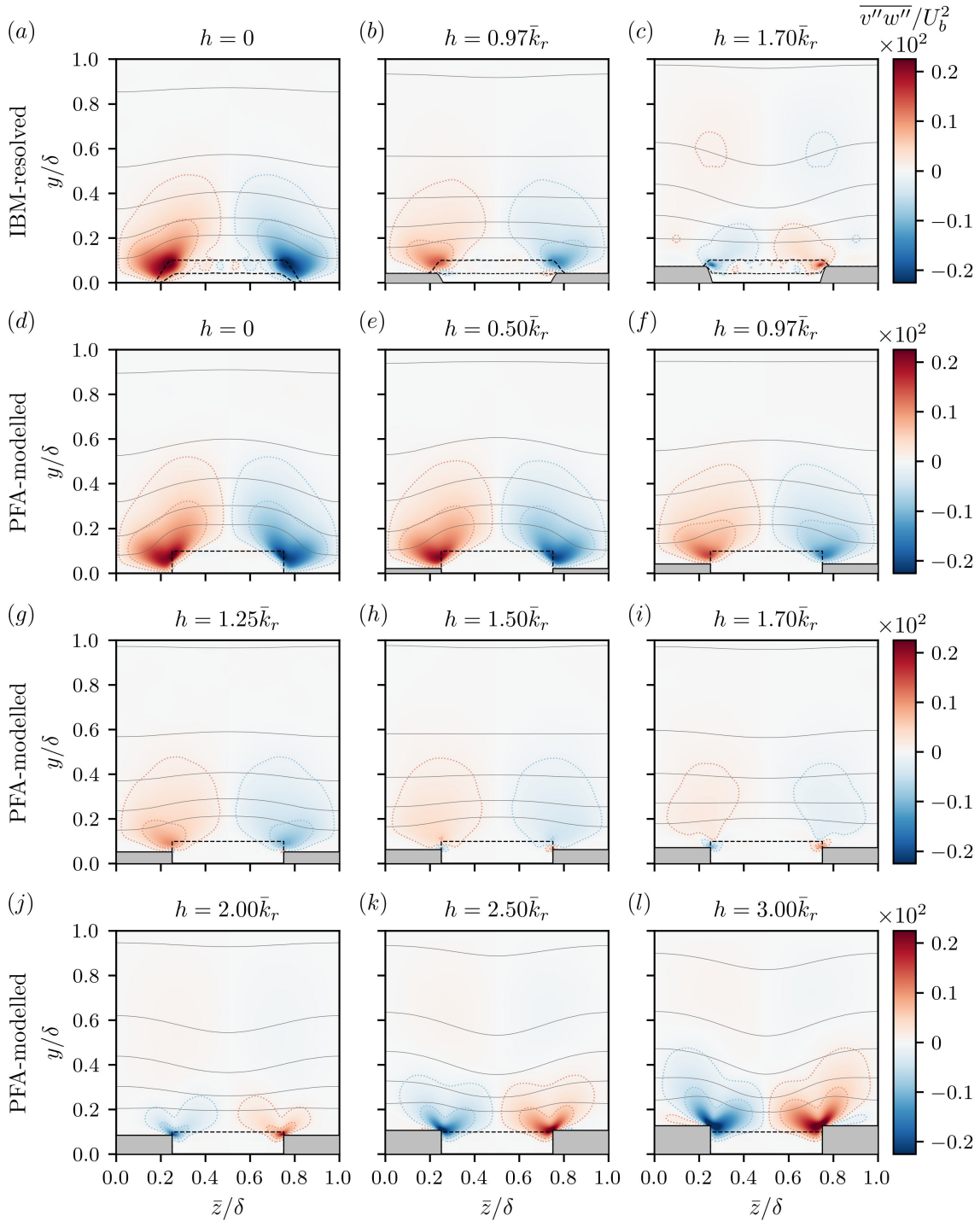


Figure 3.10: Contours of Reynolds shear stress component $\overline{v''w''}$ for resolved roughness cases (a) - (c) and modelled roughness cases with low resolution (d) - (l). The coloured dotted lines corresponds to $\overline{v''w''}/U_b^2$ values of $(\pm 0.0001, \pm 0.0005)$. Isolines of the streamwise mean velocity are shown in grey. Adopted from Schäfer et al. (2022b).

wall-normal location at which k is extracted corresponds to the one where $\langle \tilde{v}\tilde{v} \rangle$ is largest for the protruding roughness case and where a downwash is present above the smooth wall. The observed difference in k is thus probably related to the different strength of the secondary motion in these two cases." (Schäfer et al. 2022b)

"The local peaks of k at the edges of the protruding ($h = 0$) or partially protruding ($h = 0.5\bar{k}_r$) roughness are known for ridge-type roughness (Hwang and Lee (2018), Schäfer et al. (2019)) and can be related to the upwash that occurs on the corners, while the distribution of k above the recessed roughness is similar to the one above strip-type roughness (Anderson et al. 2015); i.e. with the largest values of k in the centre of the roughness strip. The PFA model captures these qualitative differences well. In particular it can be seen that the distribution of k resembles the one for strip-type roughness for $h = 1.25\bar{k}_r$ and $h = 1.50\bar{k}_r$. Starting from $h = 1.70\bar{k}_r$ local peaks of k at the transition between rough and smooth strips start to emerge again. These peaks are located further towards the smooth region than for smaller h , indicating that the elevated smooth surface starts to influence the turbulent flow in a ridge-type manner, despite the fact that k is generally larger above the rough-wall region at the considered wall-normal distance (see cross-sectional distribution of k shown in the Appendix in figure A.2)." (Schäfer et al. 2022b)

The spatial distribution of $\overline{v''w''}$ is shown in figure 3.10. Considering first the IBM-resolved roughness cases in (a-c) it can be observed that "the magnitude of $\overline{v''w''}$ is strongest for $h = 0$ and a switch of sign above the rough surface strip can be seen for $[h = 1.70\bar{k}_r]$. The distribution for $[h = 1.70\bar{k}_r]$ corresponds to the one found over strip-type roughness (Chung et al. 2018), while the distribution for $h = 0$ is in good agreement with the studies of ridge-type roughness (Hwang and Lee 2018, Vanderwel et al. 2019). The opposing signs of $\overline{v''w''}$ for $h = 0$ and $[h = 1.70\bar{k}_r]$ around the smooth-rough transition location can be directly related to the different deflection of spanwise velocity fluctuations. The sign of the generated correlation between v'' and w'' differs above the rough to smooth transition, depending on whether the roughness or the smooth part of the wall forms the protruding surface." (Stroh et al. 2020b)

"In the case of the recessed roughness ($[h = 1.70\bar{k}_r]$) the deflection on the protruding smooth surface part supports the $\overline{v''w''}$ distribution found on non-elevated surfaces with increased drag. In consequence, only one pair of secondary vortices is present, which coincides with the one found for strip-type roughness. For the protruding roughness ($h = 0$), on the other hand, the $\overline{v''w''}$ distribution opposes the one for strip-type roughness. In the present case, this influence of the local mean surface elevation dominates the secondary flow formation, and thus yields a different rotational direction than for $[h = 1.70\bar{k}_r]$. For the case with $[h = 0.97\bar{k}_r]$, where the melt-down height of the roughness is [roughly] the same as the smooth surface height, the $\overline{v''w''}$ distribution appears to be dominated by the protruding parts of the surface roughness for the present geometry. At the same time its influence on the secondary flow formation appears to be weak. [These results suggest] that the variation of rotational direction for different roughness heights is strongly related to the difference in the introduced wall-normal deflections of spanwise velocity fluctuations." (Stroh et al. 2020b)

Comparing the distributions of $\overline{v''w''}$ between the IBM-resolved and PFA-modelled cases shows that "the spatial extent of the $\overline{v''w''}$ contours for the protruding roughness cases in figure 3.10 (a) and (d) are similar; however, the modelled case (figure 3.10 (d)) exhibits a localised maximum region at the upper edge of the roughness region, while the region of large $\overline{v''w''}$ is more spread out for the resolved roughness (figure 3.10 (a)). This can directly be related to the highly localised transition from smooth to rough for the PFA model, which is obviously more gradual for the

resolved case if viewed from the streamwise-averaged perspective employed in the present plots. Along the same line the smaller penetration of the $\overline{v''w''}$ -contours into the modelled roughness region can also be explained with the spatial homogenization of the model in the rough surface region. The maximum intensity of $\overline{v''w''}$ is larger for figure 3.10 (a), indicating stronger deflection events at the transition from smooth to rough. This is likely to be caused by individual larger roughness elements which are not present in the roughness model."(Schäfer et al. 2022b)

"For the intermediate roughness case, $h \approx \bar{k}_r$, the $\overline{v''w''}$ contours resemble those of the protruding roughness ($h = 0$) but with slightly smaller wall-normal extent and lower magnitudes. In this scenario the resolved roughness case (figure 3.10 (b)) already comprises very small regions of oppositely signed $\overline{v''w''}$ at the smooth-wall edge inside the roughness region, indicating that deflections in the opposite direction are already present. This can only occur for flow located inside individual roughness valleys in which spanwise fluctuations towards the elevated smooth region are deflected upward. This effect is not present in the corresponding homogenized roughness model (figure 3.10 (f)). However, when h is elevated further for the modelled roughness the first indications of oppositely signed $\overline{v''w''}$ at the transition from a smooth to a rough surface occur for $h = 1.5\bar{k}_r$ (figure 3.10 (h)). This similarity in the qualitative distribution of $\overline{v''w''}$ between figures 3.10 (b) and (h) coincides with a similar secondary flow topology (see figure 3.7)."(Schäfer et al. 2022b)

"The fact that larger values of h are required for the modelled roughness in order to achieve a similar distribution of $\overline{v''w''}$ can also be seen for the recessed roughness. The resolved roughness $h = 1.70\bar{k}_r$ (figure 3.10 (c)) bears large similarities to the modelled roughness $h = 2.00\bar{k}_r$ (figure 3.10 (j)). Again, this case exhibits a highly similar secondary motion which also induces similar deflections to the streamwise mean velocity profile. In general, an increase in h induces a sign reversal of $\overline{v''w''}$, indicating that the smooth-wall area starts to act as the protruding surface part as already noted in respect to the spatial distribution of k . This is most pronounced for [$h = 3.00\bar{k}_r$] (figure 3.10 (k)). The sign reversal does not occur at identical h -values for resolved and modelled roughness but requires a larger smooth-wall elevation for the modelled roughness. This shift can be related to the homogenizing nature of the PFA model which does not capture the turbulence present in individual roughness valleys and its interaction with the elevated smooth wall. Overall, the present results confirm that $\overline{v''w''}$ has a strong impact on the formation of secondary flows and their respective strength."(Schäfer et al. 2022b)

"The limiting case of strip-type roughness, in which a smooth wall with different shear stress is considered, cannot be realised with the present scale separation where deflections at the roughness edges appear to be present in all cases. Considering the $\overline{v''w''}$ distribution, the case of $h = \bar{k}_r$ is still clearly dominated by the ridge-type behaviour of the rough surface part. For the PFA cases the minimum influence of $\overline{v''w''}$ appears to exist around $h = 1.5\bar{k}_r$ for the present roughness strips which is also the case with the lowest wall-normal mean velocities (cf. figure 3.8). Assuming $\overline{v''w''}$ to be an indicator for protrusion triggered secondary motion (Hwang and Lee 2018) suggests that $h \approx 1.5\bar{k}_r$ most closely generates a strip-type behaviour. For the present roughness configuration this case does not induce secondary motions that significantly alter the streamwise mean flow."(Schäfer et al. 2022b)

3.3 Discussion

3.3.1 Rotational direction of secondary motions

Ridge- and strip-type induced secondary motions show different rotational directions in the sense, that for ridge-type roughness the upwelling of the secondary motion is observed over the shear-inducing protruding ridge, while for strip-type roughness the upwelling occurs over the lower shear stress region. Which turbulent quantity is decisive for the different rotational direction between ridge- and strip-type induced secondary motion is not yet clearly determined.

For the present configuration "[...] the areas with high turbulent kinetic energy [...] are concentrated above the rough stripes for all investigated cases, [such that this quantity] cannot be directly related to the observed switch in rotational direction. The turbulence property that is found to be related to this switch is the $\overline{v''w''}$ Reynolds stress component. This quantity, which is related to the transport of turbulent kinetic energy (Hwang and Lee 2018) and whose spatial gradients occur in the mean momentum budget for \bar{v} and \bar{w} (Stroh et al. 2016), switches sign in agreement with the rotational direction of the secondary motion. This sign switch is related to the relative roughness height through the different deflections that spanwise velocity fluctuations experience for protruding or recessed roughness. For recessed roughness the generated $\overline{v''w''}$ -distribution is similar to the one for idealized strip-type roughness. Therefore, an elevated smooth surface part potentially enhances the strength of the secondary motion. For protruding roughness the deflections at the rough–smooth transition are such that a competing mechanism for the secondary flow formation is generated. With increasing roughness height this effect is increasingly dominant and can generate a switch of the large-scale rotational direction of the secondary motion. Thus the relative roughness height is identified as a key quantity for the rotational direction of secondary flow over spanwise heterogeneous roughness."(Stroh et al. 2020b)

"While the secondary flow generated above protruding rough strips ($h = 0$) resembles that of protruding smooth ridges with smooth valleys (Hwang and Lee 2018, Medjnoun et al. 2018, Stroh et al. 2020a) or ridges and valleys with identical roughness (Vanderwel and Ganapathisubramani 2015, Vanderwel et al. 2019), the present results indicate an interesting difference for a protruding smooth ridge with rough valleys [(up to $h = 2.5\bar{k}_r$)]. The latter encompasses one large-scale vortex pair only, while the other ridge-type cases typically contain three vortex pairs, as discussed in relation to figure 3.7 (a, d). This difference probably originates from the fact that the turbulent kinetic energy is consistently higher above the rough surface region than above the smooth one. In agreement with the suggestion of Hinze (1967, 1973), the secondary motion in the near-wall region is always directed from the region of high k towards the region of lower k (located above the smooth surface region). Deflections ($\overline{v''w''}$) on a protruding rough ridge counteract the secondary motion induced by the spanwise gradient of k , leading to the formation of multiple vortex pairs. However, the opposite occurs over surfaces with rough valleys. In this case deflections on the edges of the protruding smooth surface region enhance the secondary motion induced by the gradient of k such that the secondary motions do not indicate a difference between protruding ridge-type surface structures and non-protruding strip-type ones."(Schäfer et al. 2022b)

For the recessed roughness case $h = 3.00\bar{k}_r$ the protruding smooth-wall strip is sufficiently high, such that a small vortex pair can now emerge above the smooth-wall strip, which indicates that ridge-type behaviour becomes more dominant. This is accompanied by similar $\overline{v''w''}$ -distribution as the protruding roughness strip $h = 0$ and the distribution of turbulent kinetic energy in figure A.2 reveals the formation of stronger peaks at the edges of the protruding smooth strip. "It is likely that a further increase of h beyond the parameter space of the present study will [further] reduce the relevance of high k above the rough surface such that the peak of k in the near-wall region of the elevated smooth surface will eventually dominate along a wall-parallel line. In this case, a recovery of the classical ridge-type secondary flow topology is expected."(Schäfer et al. 2022b)

3.3.2 Modelling spanwise heterogeneous surfaces

"The PFA roughness model developed for the modelling of homogeneous rough surfaces (Busse and Sandham 2012, Forooghi et al. 2018) is used to predict the turbulent flow over spanwise heterogeneous roughness for different relative roughness elevations. [...] While the roughness model is applied in a clearly defined spanwise region of width W , the roughness-resolving IBM based DNS is not set up with a sharp cut at the edges of the rough region since this would have altered the roughness statistics of the rough strip. Instead, all roughness elements, whose centre position is located outside the rough region, are removed to create smooth strips. In consequence, foothills of roughness elements located close to the roughness edges can reach either onto the neighbouring smooth strips in the case of protruding rough strips or merge with the elevated neighbouring smooth strips in the case of recessed roughness. Therefore, the effective width of the rough strip is slightly larger for the protruding roughness ($h = 0$) and slightly smaller for the recessed roughness ($h = 1.70\bar{k}_r$). This difference directly reflects in the global flow properties in the sense that relatively larger drag is generated for resolved protruding roughness (due to effectively wider roughness strips) and relatively smaller drag is present for resolved recessed roughness (due to effectively narrower roughness strips)."(Schäfer et al. 2022b)

"The comparison of the global effective friction coefficient achieved with the resolved and modelled roughness approaches reflects the discussion above. Compared with the IBM based DNS, the PFA roughness model predicts a smaller friction coefficient for $h = 0$ and a larger one for $h = 1.70\bar{k}_r$ while good agreement is obtained for $h \approx \bar{k}_r$. In general, the relative drag increase of the heterogeneous roughness compared with the area-averaged mean value for smooth and rough contributions is well captured by the PFA model. Its simpler structure compared with IBM resolved roughness not only allows us to reduce the computational effort to the one of smooth-wall turbulent flow DNS but also to systematically investigate the effect of single parameters of heterogeneous rough surfaces, such as e.g. the relative roughness elevation in the present study, in a more straightforward manner."(Schäfer et al. 2022b)

"In this context, the present results show that the PFA roughness model is able to capture all salient features of heterogeneous rough surfaces. In particular, the PFA model captures the transition of secondary motion from ridge- to strip-type behaviour through variation of h and the related reversed rotational direction (Stroh et al. 2020b) which cannot be resolved with other numerical roughness

modelling approaches that rely on the prescription of an effective wall-shear stress (Anderson et al. 2015, Chung et al. 2018)."(Schäfer et al. 2022b)

"The relative drag increase of spanwise inhomogeneous surfaces in turbulent channel flows is to a first approximation qualitatively similar to the one obtained in corresponding laminar flow (Daschiel et al. 2012); i.e. relative drag increase is obtained for spanwise wavelengths of the order of the channel height (as in the present case) while relative drag decrease can be obtained with much larger wavelengths. The present PFA based results indicate the presence of a relatively constant drag coefficient in the range of $0.5\bar{k}_r < h < 1.5\bar{k}_r$ which coincides with weak secondary motions. An increasing strength of secondary motions induces an increase of the drag coefficient. In the case of protruding roughness ($h = 0$) this drag increase occurs because the secondary motion enhances the inhomogeneity of the streamwise velocity distribution. In case of recessed roughness, when the smooth-wall region starts to emerge as a protruding region, the secondary motion is such that it enhances low momentum pathways over the smooth regions and high momentum pathways in the rough regions. While this phenomenon occurs first in the bulk of the flow ($h = 1.70\bar{k}_r$) a further increase of h also induces clearly visible high momentum pathways in the near-wall region of the rough surface part ($h = 2.50\bar{k}_r$ and [$h = 3.00\bar{k}_r$]). Therefore, the relative influence of the rough region on the total drag is increased. Overall, the presence of secondary motions (which are triggered through protruding rough or smooth strips in the present study) generally leads to larger drag increase; however, the underlying physical mechanisms differ for protruding and recessed roughness strips."(Schäfer et al. 2022b)

"A direct comparison of the secondary flow topology between modelled and resolved roughness reveals that a shift towards larger values of h is required for the PFA model to reproduce the IBM results. This suggests that the PFA roughness model induces a larger wall offset when applied in heterogeneous instead of homogeneous rough-wall flow conditions. While the PFA forcing 3.3 is applied in streamwise and spanwise directions only, the local wall-normal mean velocity shown in figure A.1 shows that the PFA model nevertheless prevents the occurrence of downwash into the roughness region (negative values of \bar{v}) which is visible for the resolved roughness. The secondary motions present for heterogeneous roughness generally induce a net downward motion above the roughness centres which penetrates further into the resolved rough region. In consequence, the fluid in resolved roughness valleys can interact with neighbouring smooth regions. This is particularly important in the case of recessed roughness strips where wall-normal deflections of spanwise velocity fluctuations can occur at the edges of the protruding smooth-wall region. The reduced wall-normal penetration in case of the PFA model thus yields smaller values of $\overline{v''w''}$ which is known to be the primary driving force for the secondary motions above ridge-type roughness (Hwang and Lee 2018). The reduced secondary motion strength predicted with the PFA roughness model compared with IBM for $h = 1.70\bar{k}_r$ is thus caused by the reduced intensity of $\overline{v''w''}$. The comparison of the global drag for these two cases (see table 3.1) is governed by two factors: PFA induces lower drag due to weaker secondary motions, but higher drag due to the effectively narrower roughness strip width for IBM. The latter phenomenon dominates in the present set-up, which indicates a possible advantage of using a simplified roughness model instead of IBM if the sensitivity of global flow properties towards individual parameters is investigated. For such

investigations the PFA roughness model can be used without any particular fine tuning."(Schäfer et al. 2022b)

"We note that a pure strip-type behaviour can probably not be obtained with the scale separation (\bar{k}_r/δ) of the present DNS, since $\overline{v''w''}$ generated at any protruding surface part appears to have a strong influence on the secondary flow formation. However, the corresponding influence is weak for $h \approx 1.50\bar{k}_r$, indicating a small difference in the effective virtual wall location between smooth and rough surface parts for the present configuration. Since protruding smooth surface parts will enhance the ridge-type secondary flow, it is advisable to work with such a configuration if the effect of strip-type roughness is to be investigated numerically (with resolved roughness) or experimentally."(Schäfer et al. 2022b)

3.4 Summary

In this chapter DNS of turbulent open-channel flow over streamwise-aligned alternating smooth- and rough-wall strips are studied. The rough surfaces are modeled by two different numerical approaches. First, the individual roughness elements are fully resolved by an IBM, while in the second case the effects of the rough surface are numerically represented as a statistically homogeneous model by the PFA (Forooghi et al. 2018). "While the statistical properties of the roughness texture as well as the width and spacing of the rough areas are kept constant, the elevation of the smooth wall is systematically varied. This set-up allows identifying the relevance of protruding or recessed roughness for the secondary flow formation. In addition, it couples the effect of lateral drag variation and relative roughness elevation, whose effects on the secondary flow formation have been mostly studied separately in literature up to now (strip-type roughness versus ridge-type roughness)."(Stroh et al. 2020b)

The present results reveal that the rotational direction of the secondary motion depend on the relative mean height difference between the smooth- and rough-wall strips. For the case of protruding roughness the secondary motion induce an upward motion above the roughness strip, while for recessed roughness a downward motion is observed there. The flow topology and characteristics of the secondary motion for the protruding roughness resembles the behaviour of ridge-type induced secondary motions. The recessed roughness cases on the other hand show clear similarities to strip-type induced secondary motions, unless the relative height difference becomes sufficiently large. In the latter case the protruding smooth-wall edges introduce effects of ridge-type induced secondary motions such as the formation of tertiary vortices over the smooth-wall strip.

The relative drag increase over the heterogeneous rough surfaces correlates with the strength of the secondary motion. This in turn increases with larger relative height difference between smooth and rough strips, as can be seen for protruding roughness or protruding smooth-wall strips with recessed roughness. These two extreme cases also show typical ridge-type behaviour in the sense that they exhibit strongly pronounced wall-normal deflections of spanwise velocity $\overline{v''w''}$ with similar patterns at the protruding surfaces. This quantity and its distribution are also strongly linked to the reorientation of the secondary motion, since the switch of the rotational direction of

the secondary motions is accompanied by a change in the sign of $\overline{v''w''}$ at the smooth-to-rough strip transition.

The comparison between the roughness resolved and modelled cases shows "that the PFA roughness model is able to capture all salient features of heterogeneous rough surfaces. In particular, the PFA model captures the transition of secondary motion from ridge- to strip-type behaviour through variation of h and the related reversed rotational direction. [...] We conclude that the PFA roughness model constitutes an attractive alternative for roughness-resolving DNS when investigating not only the effect of homogeneously but also of heterogeneously rough surfaces in turbulent channel flows. The PFA roughness model allows one to systematically study the effect of individual roughness parameters which can often be strongly interlinked for the resolved case. We are of the opinion that such parameter studies do not necessarily require a fine tuning of the PFA model to a particular rough surface (which would require additional roughness-resolving DNS) but can be used in an *a priori* manner, at least for turbulent channel and equilibrium boundary layer flows. However, for significantly different flow conditions (especially including flow impingement on rough surfaces) the model should not be applied without further checks."(Schäfer et al. 2022b)

4 Interaction between secondary motions and turbulent large-scale structures

The objective of this chapter is to investigate the instantaneous characteristics of ridge-type induced secondary motions and their connection and distinction to turbulent large-scale structures occurring naturally in smooth-wall turbulent channel flows. The majority of studies to date have focused on the characteristics of time-averaged secondary motions, while only a few studies focused on the time-dependent characteristics of secondary motions, showing that these characteristics might be masked by the averaging procedure (Vanderwel et al. 2019, Zampiron et al. 2020, Wangsawijaya et al. 2020). Recent studies suggested that instantaneously secondary motions appear similar to large-scale motions (LSM/VLSM) as meandering low- and high-momentum streaks and in a mean sense as counter-rotating vortices. However, unlike turbulent large-scale structures, the secondary motions are spanwise locked at the ridges or at the transition of the wall heterogeneity for strip-type surfaces. Coexistence of secondary motions and VLSM was shown for strip-type surfaces (Wangsawijaya et al. 2020), however for streamwise-aligned ridges on hydraulically rough beds, the coexistence of secondary motions and VLSMs could not be found for small spanwise ridge spacings $S \leq 2\delta$ (Zampiron et al. 2020).

In this chapter the heterogeneous surface consists of streamwise-aligned Gaussian ridges. In particular, cases with larger S are investigated than in the previous experiments to study a possible interaction and coexistence between secondary motions and VLSM. This interaction is further examined by variation of the ridge height. Besides spectral analyses, the instantaneous characteristics of secondary motions and turbulent large-scale structures are further analysed by means of proper orthogonal decomposition. Furthermore, a passive scalar is considered in the simulations, which allows the investigation of the influence of the secondary motions on the heat transfer. Preliminary results of the data presented in this chapter were previously reported in (Schäfer et al. 2022).

4.1 Flow configuration

The present flow configuration is a turbulent open-channel flow with streamwise-aligned ridges and smooth-wall properties as depicted in figure 4.1. The continuity equation, Navier-Stokes equation and temperature equation are

$$\frac{\partial u_i}{\partial x_i} = 0, \quad \frac{\partial u_i}{\partial t} + \frac{\partial u_i u_j}{\partial x_j} = -\frac{1}{\rho_0} \frac{\partial p}{\partial x_i} + \nu \frac{\partial^2 u_i}{\partial x_j \partial x_j} + \Pi \delta_{i1} + F_{IBM,i}, \quad (4.1 \text{ a,b})$$

$$\frac{\partial T}{\partial t} + \frac{\partial T u_j}{\partial x_j} = \alpha \frac{\partial^2 T}{\partial x_j \partial x_j} + Q_s + Q_{IBM}, \quad (4.2)$$

which are numerically solved by the open-source code Xcompact3d, described in detail in section 2.4. The flow is driven by a constant pressure gradient Π and the volume force term $F_{IBM,i}$ and the heat source term Q_{IBM} are introduced to numerically represent the ridges in the open-channel flow. Periodic boundary conditions are applied in the horizontal directions, while at the wall no-slip boundary conditions and at the top of the domain symmetry boundary conditions ($v = 0, \partial u/\partial y|_{y=\delta} = \partial w/\partial y|_{y=\delta} = 0$) are imposed. For the temperature boundary conditions a constant bottom wall temperature T_b and a zero heat flux ($\partial T/\partial y|_{y=\delta} = 0$) at upper part of the domain are imposed. In order to prevent heating of the fluid by the selected boundary conditions, a volumetric cooling is introduced by the heat source term Q_s to maintain the volume-averaged fluid temperature at $0.5T_b$.

The considered flow is characterised by the friction Reynolds number Re_τ and Prandtl number Pr , which are set to $Re_\tau = 540$ and $Pr = 1$. The friction Reynolds number Re_τ is based on the effective half-channel height δ_{eff} , whose determination is defined in the following paragraph. A relative large domain size is used, $L_x, L_z = 36\delta, 12\delta$, to be able to capture the spatial characteristics of VLSMs. The spanwise ridge spacing S is systematically varied between $S/\delta = 0.5, 1, 2, 4, 12$, such that for the large S cases the interaction between secondary motions and VLSMs can be studied. All investigated cases are listed in table 4.1. The statistical convergence of the results is checked by the variation of the global properties and turbulent mean profiles of the flow for different time integration intervals. For dense ridge spacing cases $S \leq 2\delta$ time integration of at least $800t_b$ were collected, while for coarser ridge spacings at least $1400t_b$ were collected, in order to obtain converged results for streamwise and time-averaged quantities.

"The spanwise height distribution of the streamwise-aligned ridges follows a Gaussian distribution for each individual ridge, which is defined by

$$h_{Gauss}(z) = \sum_{i=1}^{n_g} h_g \exp(-(z - z_{c,i})^2/(2\sigma^2)), \quad (4.3)$$

where n_g is the total number of Gaussian ridges at one wall, h_g is the maximum height of a single Gaussian ridge, $z_{c,i}$ is the spanwise centre position of each individual ridge, given by $z_{c,i} = S(i + 0.5)$ with S as the spanwise spacing between two Gaussian ridges. The parameter σ represents the spanwise extent of an individual Gaussian ridge. In this study the parameters of

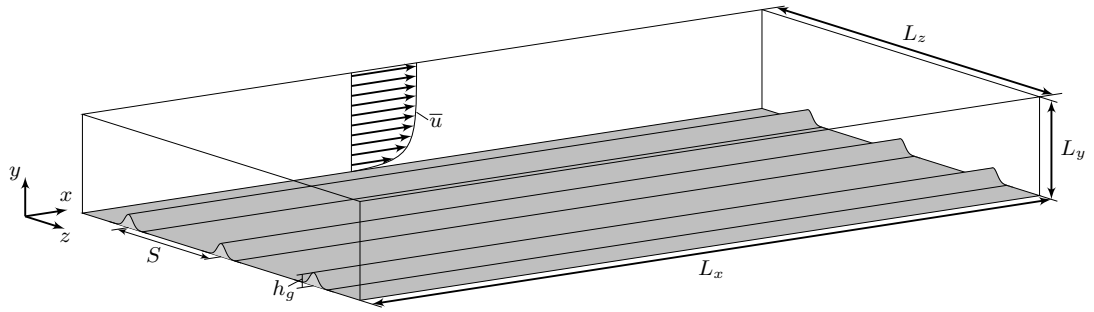


Figure 4.1: Sketch of the domain of the open-channel flow with streamwise-aligned Gaussian ridges at the wall.

the Gaussian ridges is set to $h_g = 0.1\delta$ and $\sigma = 0.05\delta$. The cross-sectional area occupied by a single ridge is given by $A_{Gauss} = \sqrt{2\pi} h_g \sigma$. Thus, the effective half-channel height is given by $\delta_{eff} = \delta - \delta_{melt}$ with the melt-down height $\delta_{melt} = n_g A_{Gauss} / L_z$. (Schäfer et al. 2022a) Due to the presence of the Gaussian ridges the wetted surface of the wall increases compared to the smooth-wall case. The wall length in the spanwise domain $-\delta/4 \leq z' \leq \delta/4$ with one Gaussian ridge centred at $z' = 0$ is given by

$$L_g = \int_{-\delta/4}^{\delta/4} \sqrt{1 + h_g^2 / \sigma^4 z^2 \exp(-z^2 / \sigma^2)} dz = 0.684\delta, \quad (4.4)$$

which is numerically integrated by the trapezoidal rule. The total wetted surface for different ridge spacings can thus be expressed by $L_s = L_z + n_g(L_g - 0.5\delta)$.

In this chapter the "spatial averages are based on intrinsic averaging. This procedure excludes the values at the grid points inside the immersed (solid) body, while the values on the surface are included in the integration. In consequence, the average is computed through normalisation with the fluid area only. This affects the evaluation of global quantities, e.g. the bulk velocity u_b , which are integrated in time and all three spatial directions and are defined for the present configuration as

$$\Phi = \frac{1}{2\delta_{eff} L_z} \int_0^{L_z} \int_{y_b(z)}^{\delta} \bar{\phi} dy dz, \quad (4.5)$$

where ϕ represents an arbitrary quantity and Φ is its volume- and time-average, while $y_b(z)$ [is] the wall-normal surface elevation at the bottom [...] wall." (Schäfer et al. 2022a)

4.2 Results

4.2.1 Mean flow properties

The results of the global flow properties are presented in table 4.1, where the different flow configurations are arranged with decreasing S and the smooth-wall case is indicated by $S = \infty$. The skin-friction coefficient $C_f = 2 u_\tau^2 / u_b^2$ characterises the drag of the flow, while the heat transfer is characterised by the Nusselt number defined as $Nu = \delta_{eff} q_w / (\alpha \Delta \langle \bar{T} \rangle)$. Both, u_τ and q_w are obtained by extrapolating the total shear stress and heat flux from the bulk region to the

$Re_{\tau,eff}$	S/δ	h_g/δ	δ_{eff}/δ	Re_b	C_f ($\cdot 10^{-3}$)	Nu	St ($\cdot 10^{-3}$)	K_c/u_τ^2 ($\cdot 10^{-2}$)	u_{sm}/u_b ($\cdot 10^{-2}$)
540	∞	-	1.0	9850.4	6.015	15.04	1.527	0.05	0.23
540	12	0.1	0.999	9777.8	6.100	15.12	1.546	0.52	1.32
540	4	0.1	0.997	9618.2	6.300	15.30	1.590	1.56	1.37
540	4	0.05	0.998	9775.4	6.101	15.11	1.546	0.51	0.73
540	4	0.025	0.999	9831.7	6.031	15.04	1.530	0.09	0.22
540	2	0.1	0.994	9410.0	6.596	15.56	1.654	2.71	1.32
540	1	0.1	0.987	9232.2	6.841	15.86	1.718	2.47	1.30
540	0.5	0.1	0.975	9097.5	7.051	16.20	1.781	1.56	1.04

Table 4.1: Global flow properties of DNS of smooth-wall case and streamwise-aligned Gaussian ridges with varying ridge spacing S and different ridge heights h_g .

wall-normal position $y_w = \delta - \delta_{eff}$, respectively (Chan-Braun et al. 2011). The introduction of the ridges increases the drag exerted on the flow compared to the smooth-wall conditions, which in case of a constant pressure gradient results in a reduction of u_b and Re_b , while C_f is increased. Similar, the ridges increase the heat transfer expressed in terms of the non-dimensionalized wall heat flux by Nu , which monotonically increases with smaller S . The relative increase of C_f and Nu for cases $S = 12\delta, 4\delta, 2\delta, \delta$ and 0.5δ with the smooth-wall case are 1.5%, 4.8%, 9.7%, 13.7%, 17.2% and 0.6%, 1.7%, 3.4%, 5.4%, 7.7%, respectively. In addition, the heat transfer of the flow is characterised by the Stanton number $St = Nu/(Re_b Pr)$, which accounts for the changes by the flow rate, which due to the reduction of Re_b with increasing S results in larger relative heat transfer increase, e.g. 16.6% for case $S = 0.5\delta$. The comparison with the relative increase of the wetted surface, which gives values of 1.5%, 4.6%, 9.2%, 18.4%, 36.8% for the considered ridge cases, shows a good agreement of the relative change between C_f and wetted surface, while for denser ridge spacings the relative increase of C_f is larger than the increase of wetted surface. The reduction of the ridge height for case $S = 4\delta$ shows a significant reduction of C_f and Nu of the cases $h_g = 0.05\delta$ and 0.25δ compared to case $h_g = 0.1\delta$ and for the smallest ridge height the values are almost identical to the smooth-wall case. A measure for the strength of the secondary motions is K_c , which is the volume average of the coherent turbulent kinetic energy $\tilde{k}_c = 0.5 \cdot (\tilde{v}\tilde{v} + \tilde{w}\tilde{w})$, which is shown in table 4.1. The maximum value of K_c occurs for $S = 2\delta$, followed by slightly smaller values for $S = \delta$. For comparison with the strength of secondary motions over alternating rough- and smooth-wall strips in chapter 3, the intensity u_{sm} is shown in addition in table 4.1, which is determined by equation 3.8. Note, that for the coarse ridge spacings $S > 2\delta$, only the spanwise region centred around the ridges with a spanwise window size of 2δ is considered for the determination of u_{sm} , since it will be shown later that the spanwise extent of mean secondary motions is in this order. Comparing the results with those obtained in chapter 3 it can be seen that the present ridge cases with $h_g = 0.1\delta$ induce stronger secondary motions than the largest relative height difference case $h = 3\bar{k}_r$ from chapter 3, while case $S = 0.5\delta$ has a comparable value.

Profiles of the mean streamwise velocity and mean temperature for the different spanwise ridge spacings S are shown in figure 4.2 in logarithmic scaling, where the mean temperature is scaled

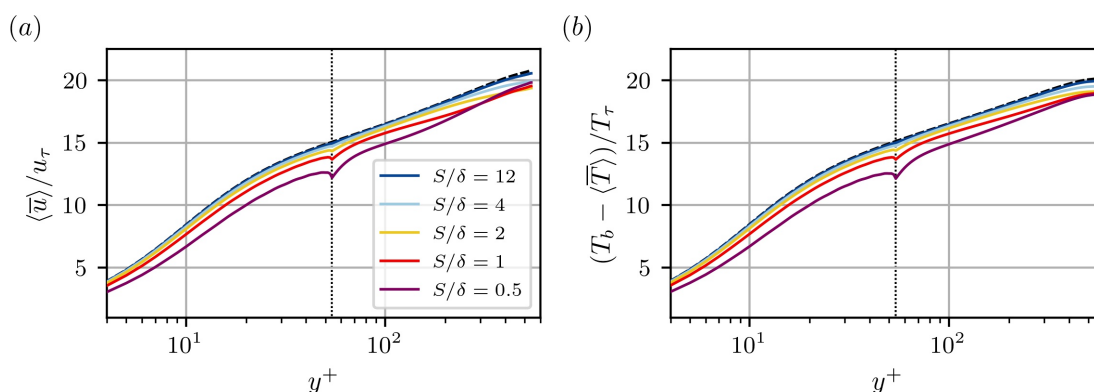


Figure 4.2: Mean streamwise velocity profile in (a) and mean temperature profile in (b) for varying ridge spacing S scaled in viscous units. Black dashed line indicates smooth-wall case and the ridge height $h_g = 0.1\delta$ is shown by the black dotted line.

by the the friction temperature $T_\tau = Q/\rho c_p u_\tau$. As can be seen, the reduction of S contributes to a successive reduction of the mean streamwise velocity and temperature, due to the additional drag introduced by the secondary motions. For small ridge spacings, the reduction of $\langle \bar{u} \rangle$ at the free surface is less pronounced compared to $S = 2\delta$, showing that the influence of the secondary motion becomes more limited to the near-wall region for these cases. For the mean temperature, this reversal cannot be observed, and the profiles at the free surface converge to similar values for smaller S , while near the wall, the temperature deficit increases with decreasing S .

The secondary motions introduce a spanwise heterogeneity of the mean flow field by large-scale counter-rotating vortices which is shown for different S in figure 4.3. The largest spatial extent of the secondary motions is found for $S \geq 2\delta$, which measures roughly 2δ in the spanwise direction, while for smaller S the spatial extent reduces and scales with S (Zampiron et al. 2020). Thus, for case $S = 2\delta$ the secondary motions fill the entire channel domain, which is also reflected by the observation of the strongest secondary motions in terms of K_c for this spacing (see table 5.1). The spatial reduction can be also observed for the centre position of the secondary motion cells, which is indicated by a blue cross for one secondary motion cell in figure 4.3. For $S = 4\delta$ an additional upward bulging of \bar{u} appears at the centre of the valleys with a smaller and weaker pair of counter-rotating vortices, which is referred to as tertiary flow (Vanderwel and Ganapathisubramani 2015). A similar observation was made by Zampiron et al. (2020) for their case with a single ridge in the centre of the channel, having a distance of 4δ to both sidewalls. In this case, the upward bulging in the valley is slightly asymmetric, since the sidewalls generate secondary motions with different strength and shape than the ridge-type induced secondary motions. For the larger ridge spacing case $S = 12\delta$ a slight upward bulging can still be observed in the vicinity of the ridge that occurs approximately 2δ to the side of the ridge. Thus, the upward bulging for $S = 4\delta$ in the valley can be understood as a superposition of the upward bulging of neighbouring ridges. The observed spatial heterogeneity of the mean streamwise velocity is also found for the mean temperature field, where large temperature values extending in the bulk region above the individual ridges (not shown here).

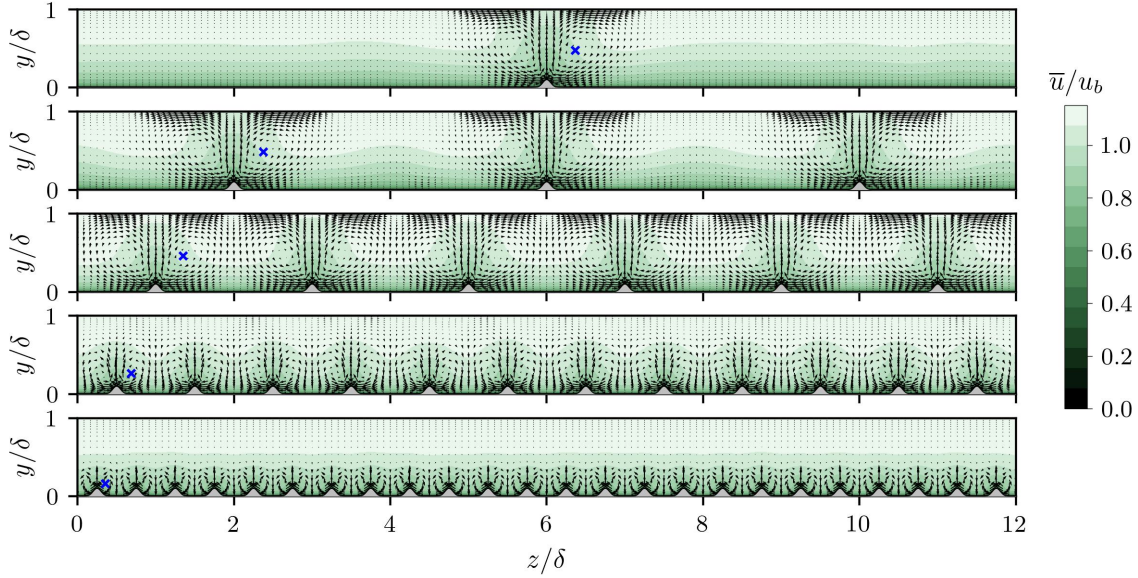


Figure 4.3: Mean streamwise velocity in cross-sectional plane for $Re_\tau = 540$ and varying ridge spacing S . The cross-sectional mean velocity components are illustrated by arrows and are scaled by u_b . Blue crosses indicate position of one secondary motion's cell-centre.

The trend of the wall-normal and spanwise position of the secondary motion's cell-centre, indicated by y_{sc} and z'_{sc} , with respect to S is shown in figure 4.4. The spanwise coordinate z' is obtained by applying phase-averaging such that it describes the spanwise distance to the centre position of the ridge ($z' = 0$). As shown by Zampiron et al. (2020) the wall-normal and spanwise position for small ridge spacings $S \leq 2\delta$ follows a linear trend with $y_{sc}/\delta = 0.0909 + 0.21S/\delta$ and $z'_{sc}/\delta \approx \pm 0.2S/\delta$ (here δ is obtained by averaging the mean channel heights for all flow cases). The present data also suggest a linear trend $y_{sc}/\delta = 0.0635 + 0.198S/\delta$ and $z'_{sc}/\delta = \pm 0.0208 \pm 0.166 S/\delta$ for $S \leq 2\delta$, displaying a smaller slope and offset for y_{sc} compared to Zampiron et al. (2020). The difference between the present relation and the one found in Zampiron et al. (2020) can be reduced if the wall-offset introduced by the micro-cylindrical roughness elements of the experiments, which reside in the valley, are taken into account. This results in a new relation of $y_{sc}/\delta = 0.0692 + 0.21S/\delta$ for the data of Zampiron et al. (2020), such that the difference to the present data is reduced below 10%. As can be seen in figure 4.4 the wall-normal and spanwise position of the secondary motion cell-centre saturate for large ridge spacings $S \geq 2\delta$, with values of $y_{sc} \approx 0.475$ and $z_{sc} \approx 0.36$. This illustrates that for sufficiently large ridge spacings the spatial extent of secondary motions is constrained by the channel height, while for denser ridge spacings $S \leq 2\delta$ the secondary motions does not experience this constraint. Consequently, the secondary motions does not grow beyond a spanwise extent of 2δ , which can be considered as the natural spanwise extent of secondary motions.

In figure 4.5 the spanwise distribution of the phase-averaged mean streamwise velocity is shown at the wall-normal location of the secondary motion cell centre $y = y_{sc}$ for the different S cases. The mean streamwise velocity is scaled with $\Delta U = \max[\bar{u}(z')] - \min[\bar{u}(z')]$, which is the difference between the maximum and minimum mean streamwise velocity \bar{u} . The minimum of streamwise velocity occurs above the ridge in the upward bulging of the secondary motion,

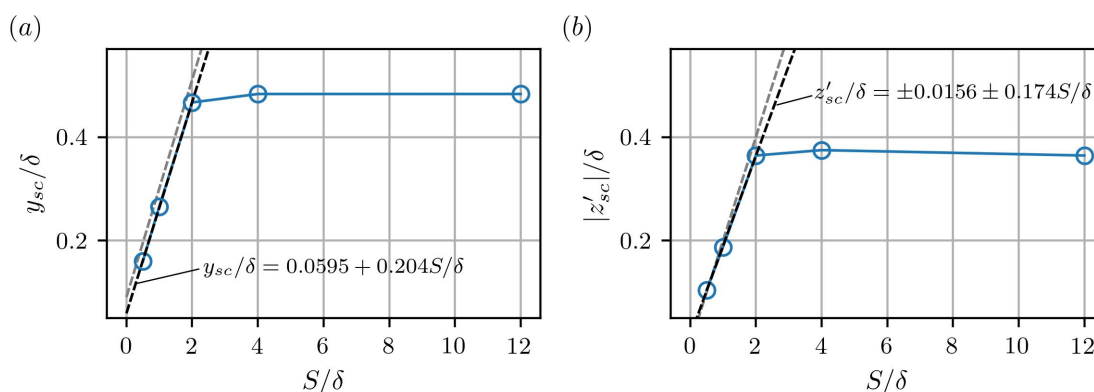


Figure 4.4: Wall-normal and spanwise cell-centre position of mean secondary motion for different ridge spacings S . Black dashed line indicates linear regression fit of present data and gray dashed line for the experimental data of Zampiron et al. (2020) for $S \leq 2\delta$.

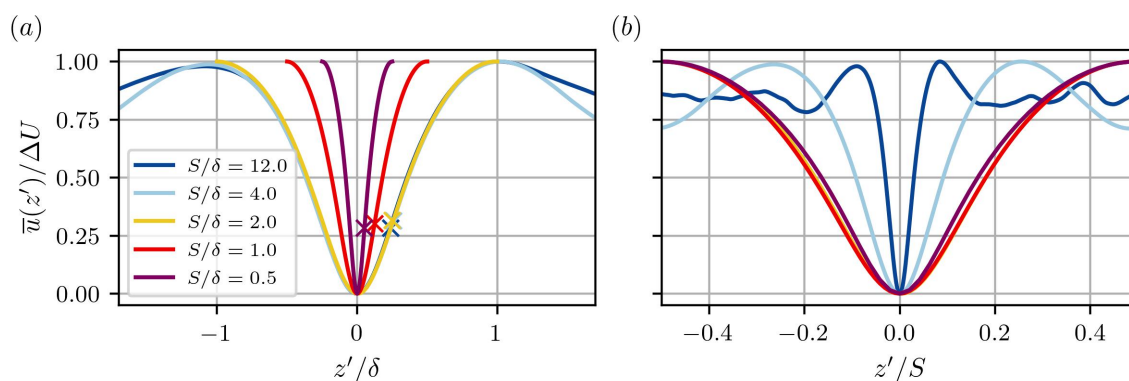


Figure 4.5: Phase-averaged spanwise distribution of mean streamwise velocity at $y = y_{sc}$. The spanwise coordinate z' is scaled with the half-channel height δ in (a) and with the ridge spacing S in (b). Crosses in (a) indicate spanwise position of the closest inflection point to the ridge.

while the maximum occurs in the downward region of the secondary motion (compare with figure 4.3). When the spanwise coordinate is scaled in outer units with δ the mean streamwise velocity profiles of the coarse ridge cases $S \geq 2\delta$ perfectly collapse. This self-similar distribution of the mean streamwise velocity in the ridge region supports the previous observations, that for large ridge spacing, the secondary motions has reached its natural size. Scaling the spanwise coordinate with S results in a self-similar distribution of the mean streamwise velocity profiles for $S \leq 2\delta$ as can be seen in figure 4.5 (b), reflecting the linear scaling of mean secondary motions with S (see figure 4.4). The second minimum of case $S = 4\delta$ and $S = 12\delta$ indicate the appearance of tertiary vortices adjacent to the ridges with the upward bulging of \bar{u} . Consequently, case $S = 2\delta$ marks the transition between the two different scaling regimes.

4.2.2 Instantaneous flow fields

The instantaneous streamwise velocity fluctuation u' at the horizontal midplane ($y = 0.5\delta$) is shown in figure 4.6, where instantaneous turbulent large-scale structures, such as low- and high-momentum regions (LMRs/HMRs), can be observed. As can be seen, the smooth-wall case $S = \infty$

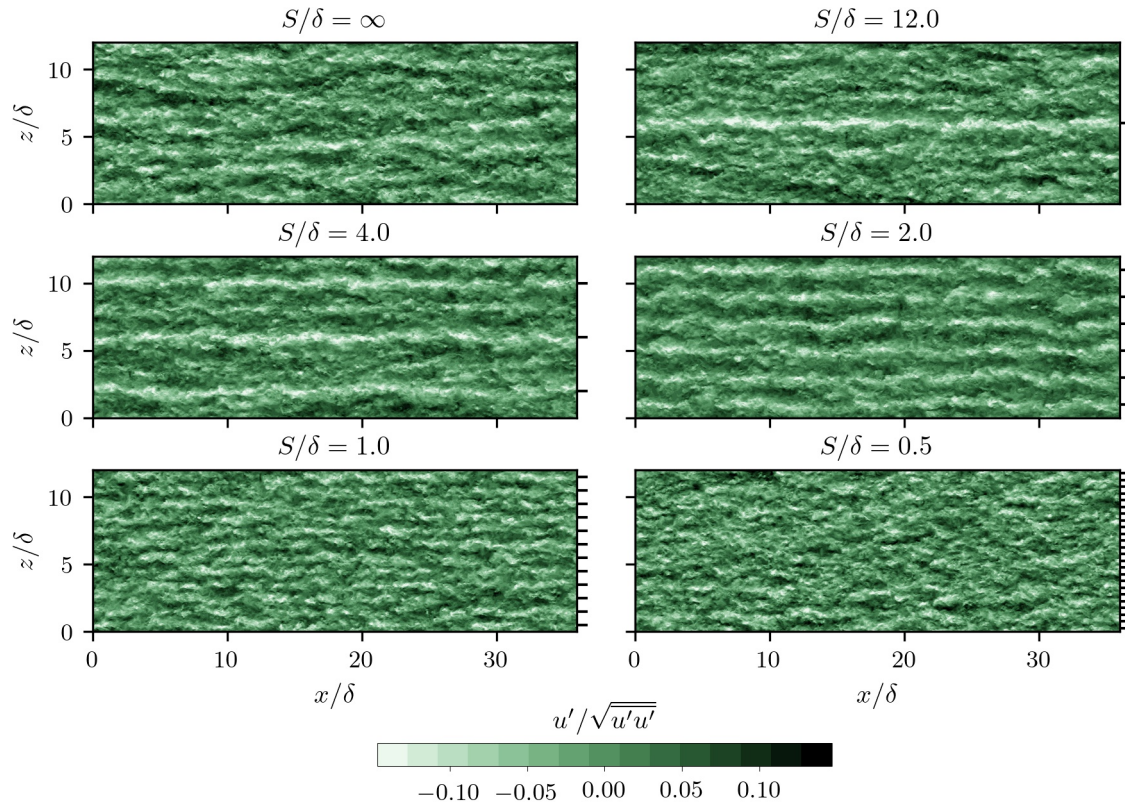


Figure 4.6: Instantaneous streamwise velocity fluctuations in horizontal plane at $y = 0.5\delta$ for different cases. The black horizontal lines at the outer right figure frame indicate the spanwise position of the ridges.

exhibits VLSMs with long meandering LMRs and HMRs. For example a high-momentum streak with a streamwise wavelength of $\lambda_x \approx 24$ is found at $z/\delta \approx 9$, while a long low-momentum streak appears at $z/\delta \approx 4$. For the ridge case $S = 12\delta$ a very pronounced LMR is located at the ridge position ($z/\delta = 6$), while in the centre of the valley region a long high-momentum streak similar to the smooth-wall case can be observed. Similar strong and long low-momentum streaks are found for the ridge cases $S = 4\delta$ and $S = 2\delta$ at each ridge position, which contribute to the upward bulging of the mean streamwise velocity above the ridges seen in figure 4.3. For $S = 4\delta$ a weaker but fixed long low-speed streak is found in the middle between adjacent ridges, which contributes to the upward bulging of \bar{u} in the centre of the valley as found in figure 4.3. For the two densest ridge spacings $S = \delta$ and $S = 0.5\delta$ the long streamwise coherence of the low-speed streaks found for the coarse ridge cases is broken. This suggests that the individual low-momentum streaks forming at each ridge can interact with their neighbouring streaks in such a way that the formation of long coherent low-momentum streaks is inhibited. While for $S = 4\delta$ VLSMs can still be seen in a weak form, no VLSMs are observed for the denser ridge spacings $S \leq 2\delta$. This is interesting to note, since for case $S = 0.5\delta$ the horizontal plane shown in figure 4.6 (f) is above the wall-normal location up to which the mean secondary motions extend (see figure 4.3), illustrating that secondary motions are able to prevent the formation of VLSMs for dense ridge spacings (Zampiron et al. 2020).

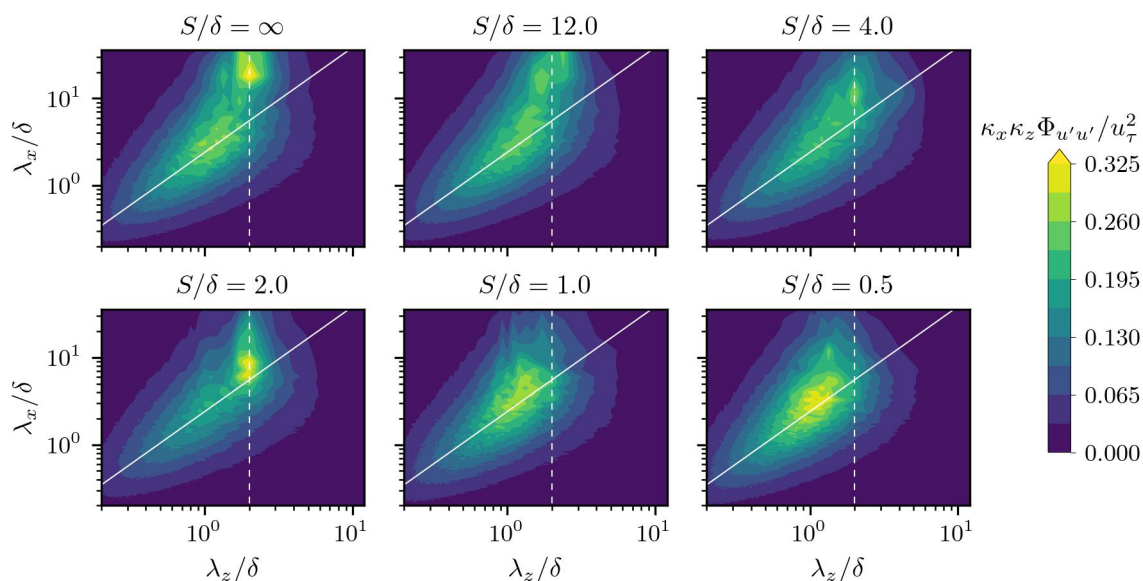


Figure 4.7: Contour lines of two-dimensional pre-multiplied streamwise energy spectra $\kappa_x \kappa_z \Phi_{u'u'}(\lambda_x, \lambda_z)$ at wall-normal height $y = 0.5\delta$ for smooth-wall case $S/\delta = \infty$ and different ridge spacings S . Dashed white line indicates $\lambda_z = 2\delta$, which is the spanwise wavelength at which VLSMs are fixed; solid white line illustrates that spanwise wavelength of turbulent structures increases linear with the streamwise wavelength (Cameron et al. 2017).

4.2.3 Spectral analysis

The large-scale low- and high-velocity streaks seen in the instantaneous velocity planes in figure 4.6 contain a large fraction of turbulent kinetic energy, which can be quantified by the two-dimensional power spectral density $\Phi_{u'u'}$ of the streamwise velocity, defined by

$$\langle \overline{u'u'} \rangle(y) = \int_0^\infty \int_0^\infty \Phi_{u'u'}(\kappa_x, y, \kappa_z) d\kappa_x d\kappa_z, \quad (4.6)$$

where $\kappa_x \equiv 2\pi/\lambda_x$ and $\kappa_z \equiv 2\pi/\lambda_z$ are the streamwise and spanwise wavenumber, while λ_x and λ_z are the streamwise and spanwise wavelength. Figure 4.7 presents the two-dimensional pre-multiplied streamwise energy spectra for the different S cases at the same wall-normal height $y = 0.5\delta$ as the instantaneous velocity fields shown in figure 4.6. The white inclined line illustrates that the streamwise length scale of turbulent structures scales with λ_z (Cameron et al. 2017), which holds approximately up to $\lambda_z = 2$ (white dashed line), where structures of significantly larger λ_x start to emerge.

The smooth-wall case displays a strong peak in the spectra at large wavelengths ($18 \leq \lambda_x/\delta \leq 36$, $1.71 \leq \lambda_z/\delta \leq 2.4$) which corresponds to the presence of VLSMs and the second peak at $\lambda_x/\delta \approx 3$ is related to LSMs. This is consistent with previous experiments in rough-bed open-channel flows of Cameron et al. (2017) and Zampironi et al. (2020), where it was found that the spanwise wavelength of VLSMs is anchored near $\lambda_z \approx 2\delta$ with streamwise wavelengths in the range of $\lambda_x \approx 10\delta - 40\delta$. In case of wide ridge spacing $S = 12\delta$ the energy contribution of VLSMs at large λ_x is still apparent but reduced in strength compared to the smooth channel case. For $S = 4\delta$ the clear peak of VLSMs is no longer present, though high energy contributions up to

$\lambda_x \approx 18\delta$ at $\lambda_z = 2\delta$ can be observed with a energy peak around $\lambda_x \approx 9\delta - 12\delta$. This emergence of the energy peak at $\lambda_z = 2\delta$ is also found for $S = 2\delta$, which is stronger compared to case $S = 4\delta$ and its peak location is found at smaller λ_x in the range $\lambda_x \approx 5\delta - 10\delta$. The spanwise wavelength of this spectral feature coincides with the wavelength of the repetition of up- and downdrafts of secondary motions ($\approx 2\delta$) seen in the mean and instantaneous velocity fields in figure 4.3 and 4.6, and the location of its peak in terms of streamwise wavelength is located between the one of LSM and VLSM. Similar observations were made by Zampiron et al. (2020), who discovered a new spectral feature in one-dimensional streamwise energy spectra that also appears between the streamwise wavelength range of LSM and VLSM. This spectral feature was found at the transition between low- and high-momentum regions within the secondary motions, and Zampiron et al. (2020) named the associated mechanism to this spectral feature as "secondary current instability" (SCI), which will be further discussed at the end of this section. The densest ridge spacings $S \leq \delta$ also don't show an energy contribution of VLSM, whereas the energy is significantly increased in the range $\lambda_x = 2\delta - 7\delta$ and $\lambda_z = 0.7\delta - 2\delta$. The observation of Zampiron et al. (2020) that the formation of VLSMs is suppressed by ridge-induced secondary motion for small distances $S \leq 2\delta$, is supported by the present results and can be even extended to larger ridge spacings $S < 4\delta$, while for larger ridge spacings coexistence between secondary motions and VLSMs exists.

To illustrate at which spanwise locations VLSMs occur for wide ridge spacings the one-dimensional pre-multiplied streamwise energy spectra $\kappa_x \Phi_{u''u''}$ across the spanwise direction z at $y = 0.5\delta$ is shown in figure 4.8 (a). The one-dimensional power spectral density is defined by

$$\langle \overline{u''u''} \rangle(y, z) = \int_0^\infty \Phi_{u''u''}(\kappa_x, y, z) d\kappa_x. \quad (4.7)$$

For the smooth-wall case $S = \infty$ the energy contributions of the VLSM ($\lambda_x \geq 18\delta$) occur over the entire channel width. As can be seen individual peaks of VLSM are found, which are a result of the limited time integration of the simulation, such that individual VLSMs reside longer at certain spanwise locations and thereby contributing to these local peaks. For case $S = 12\delta$, a clear spanwise separation of the streamwise energy contribution can be seen for large λ_x , where the contribution of VLSM occurs only in the valley, while no contributions are found in the vicinity of the ridges. This illustrates that also for wide ridge spacings secondary motions suppresses the formation of the VLSMs in the vicinity of the ridges, such that they occur in areas that are not affected by the mean secondary motions. In the valleys of case $S = 4\delta$, contributions from VLSM can be observed, although they are much weaker than for the cases $S = \infty$ and $S = 12\delta$, which is the reason why they can hardly be seen in the two-dimensional spectrum in figure 4.7. No VLSMs occur for smaller ridge spacing $S \leq 2$, which is now illustrated by the lack of VLSMs in the valleys of ridges. The presence of instantaneous structures of secondary motions can be seen by increased values of $\Phi_{u''u''}$ at the ridge position in the range of $\lambda_x \approx 2\delta - 12\delta$, which are in addition demarcated by areas of low values on both sides of the ridges. This concise pattern in the streamwise energy spectra of secondary motion at each ridge is similar for $S \geq 2\delta$, which is a further indicator of the self-similarity of secondary motions for coarse ridge spacings. As the ridge spacing decreases $S \leq \delta$, this pattern diminishes and is further weakened, reflecting the mutual influence of neighbouring ridges on the formation of instantaneous secondary motions.

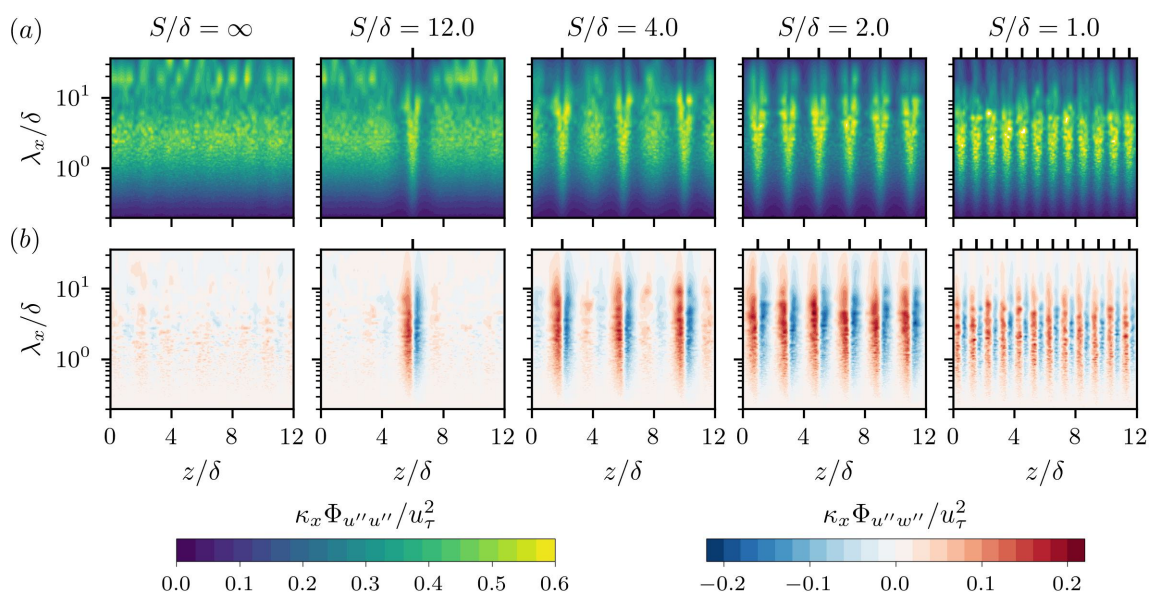


Figure 4.8: Pre-multiplied spectra $\kappa_x \Phi_{u''u''}(\lambda_x, z)$ (a) and co-spectra $\kappa_x \Phi_{u''w''}(\lambda_x, z)$ (b) for different S and $y = 0.5\delta$. The black vertical lines at the outer top figure frame indicate the spanwise position of the ridges.

The spectral feature associated with secondary motions (SCI) is also observed in the one-dimensional pre-multiplied co-spectra $\kappa_x \Phi_{u''w''}$ in the vicinity of the ridges (Zampiron et al. 2020), which is shown in figure 4.8 (b) for the present cases. The secondary motion induce a spatial heterogeneity of the mean velocity near the ridges, such that turbulent spanwise fluctuations w'' in this region lead to a non-vanishing contribution of the covariance $\overline{u''w''}$. The different signs of the co-spectra $\Phi_{u''w''}$ on each side of the ridges in figure 4.8 (b) can be explained by the spanwise profiles of \bar{u} in figure 4.5, such that positive w'' lead to positive u'' on the left side of the ridge and, conversely, to negative u'' on the right side. In the case of the smooth channel, these contributions do not occur as the turbulent structures can travel over the entire width of the channel and thus these contributions vanish for long time integration. As can be seen in figure 4.8 (b) for $S \geq 2\delta$, the contributions of the co-spectra $\Phi_{u''w''}$ occur in a similar range of λ_x as the enhanced values of $\Phi_{u''u''}$ of the secondary motions in figure 4.8 (a), with strong contribution at $\lambda_x \approx 2\delta - 10\delta$. While for the densest ridge spacing cases $S = \delta$ and $S = 0.5\delta$ (not shown here) the intensity of $\Phi_{u''w''}$ decreases and the peak values shift to smaller λ_x , examinations of $\Phi_{u''w''}$ in horizontal planes closer to the wall ($y = 0.15\delta/0.25\delta$) show that the co-spectrum $\Phi_{u''w''}$ becomes more similar to those of the coarse ridge spacings and likewise high contributions at the ridges are observable up to $\lambda_x \approx 12\delta$.

A linear relationship between the characteristic wavelength of the SCI and the vorticity thickness was found by Zampiron et al. (2020), which suggests that the meandering of the instantaneous secondary motions is caused by instabilities resulting from inflection points in the spanwise profile of mean streamwise velocity. This characteristic wavelength $\lambda_{x,SCI}$ is determined by Zampiron et al. (2020) based on the maximum value of the phase-averaged one-dimensional pre-multiplied spectra $\kappa_x F_{u''u''}$ at $y = y_{sc}$ and $z' = \pm 0.2S$. Since it has been shown for the present cases that for large S the spectral properties of the secondary motions no longer grow into the spanwise direction and are self-similar, $\lambda_{x,SCI}$ is determined for the present cases at the spanwise position of

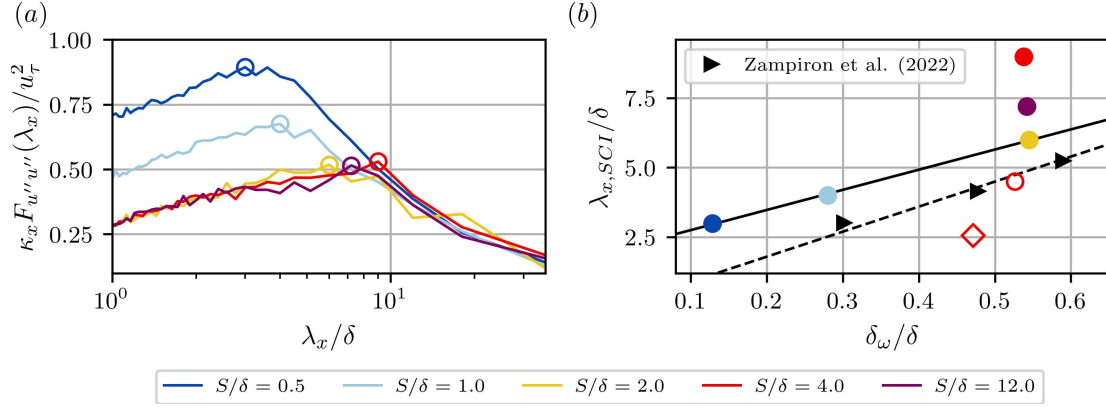


Figure 4.9: Phase-averaged one-dimensional pre-multiplied spectra of streamwise variance at $y = y_{sc}$ and $z = z_{sc}$ for different S in (a). The position of $\lambda_{x,SCI}$ at the maximum value of $\kappa_x F_{u''u''}$ is indicated by open circles. In (b) streamwise wavelength of secondary current instability $\lambda_{x,SCI}$ over vorticity thickness δ_ω for different ridge spacings S . Black triangles indicate ridge cases $1 \leq S/\delta \leq 2$ of Zampiron et al. (2020) and black dashed line represents the fitted relation $\lambda_{x,SCI}/\delta \approx 9.0\delta_\omega/\delta$ for these cases. Black solid line represents linear fitted relation $\lambda_{x,SCI}/\delta \approx 7.24\delta_\omega/\delta + 2.03$ based on cases $S \leq 2\delta$. In (b) the cases $h_g = 0.05\delta$ and $h_g = 0.025\delta$ for $S = 4\delta$ are indicated by a red open circle and square, respectively.

the secondary motion cell's centre $z = z_{sc}$. The corresponding pre-multiplied streamwise energy spectra at $y = y_{sc}$ and $z = z_{sc}$ is shown in figure 4.9 (a) for the different ridge cases and the maximum values are indicated by open circles. As can be seen, $\lambda_{x,SCI}$ increases monotonically with S for $S \leq 2\delta$, and the largest ridge spacings $S \geq 2\delta$ remain in a similar range of $\lambda_{x,SCI} \approx 6\delta - 9\delta$. Note that the exact determination of the maxima is limited due to the coarse discrete resolution of the spectrum in this range of wavelengths (resolution of discrete wavelengths is $\lambda_x = L_x/n$, with $n = 1, \dots, N_x/2$) such that the maxima for the cases $S \geq 2\delta$ occur at adjacent discrete locations ($\lambda_x = 6.0, 7.2, 9.0$).

The vorticity thickness δ_ω , which is a characteristic length scale describing the width of mixing layers (Raupach et al. 1996), is defined as $\delta_\omega = \Delta U / \max|\partial\bar{u}/\partial z'|_{y=y_{sc}}$ which is the ratio of the maximum velocity difference ΔU of the spanwise velocity profile $\bar{u}(y = y_{sc}, z')$ and the maximum spanwise velocity gradient (Zampiron et al. 2020). The relationship between $\lambda_{x,SCI}$ and δ_ω for the present cases is shown in figure 4.9 as well as for the cases of Zampiron et al. (2020) ($\delta \geq S \geq 2\delta$) which are used to obtain the linear relationship $\lambda_{x,SCI} \approx 9.0\delta_\omega$ (dashed black line). Smaller ridge spacing cases were neglected for the fit by Zampiron et al. (2020) due to complications in the determination of $\lambda_{x,SCI}$ caused by overlapping of spectral properties of LSMs. Using the cases $S \leq 2\delta$, a linear fit of $\lambda_{x,SCI}/\delta \approx 7.24\delta_\omega/\delta + 2.03$ is obtained for the present configurations. Despite the differences in Reynolds number, ridge geometry and wall properties of the valleys of the open-channel flow between experiments and current simulations, as well as in the approach to determine $\lambda_{x,SCI}$ (Taylor's frozen hypothesis for experiments), the current results confirm the tendency of a linear trend between $\lambda_{x,SCI}$ and δ_ω . This linear relation suggests that the analogy between turbulent mixing layer and canopy flows from Raupach et al. (1996) might be applied to the formation of instantaneous secondary motions as well. This implies that the streamwise meandering of instantaneous secondary motions is the result of a Kelvin-Helmholtz wave in the horizontal plane, with positive and negative fluctuations in wall-normal vorticity ω_y'' having a streamwise wavelength of $\lambda_{x,SCI}$ (Finnigan et al. 2009).

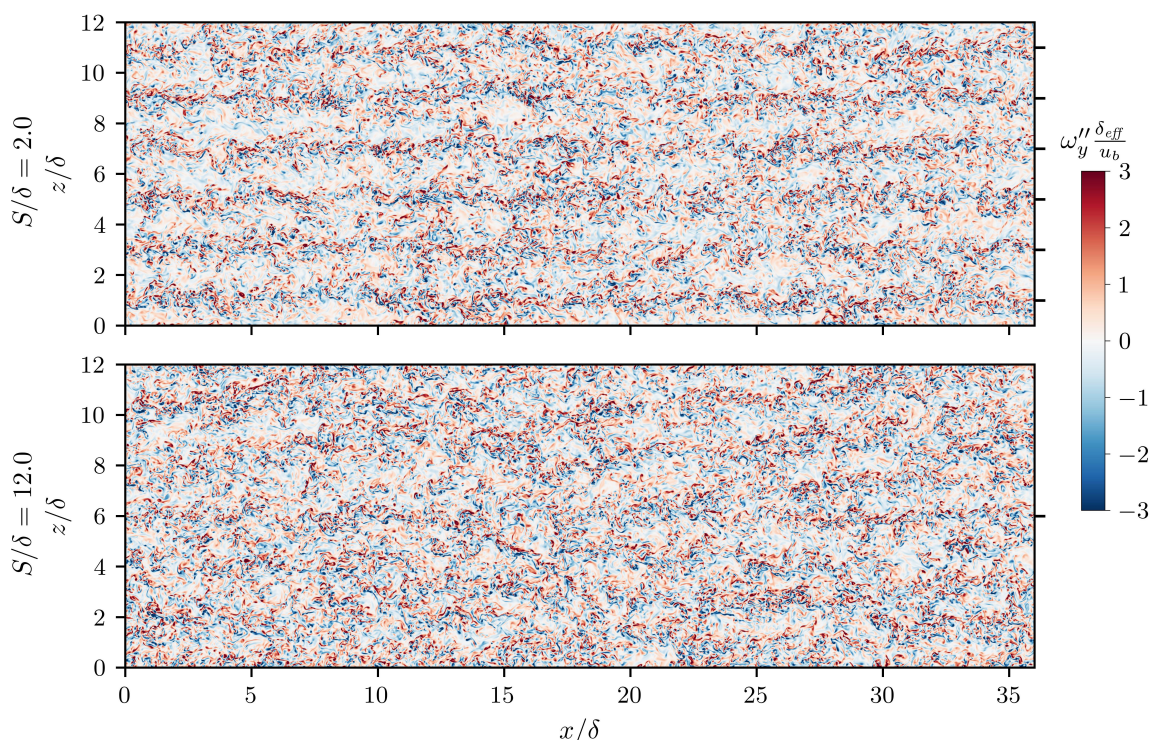


Figure 4.10: Instantaneous random fluctuations of wall-normal vorticity ω''_y in horizontal plane at $y = 0.5\delta$ for case $S = 2\delta$ and $S = 12\delta$. The black horizontal lines at the outer right figure frame indicate the spanwise position of the ridges.

As a first indication for this relation, figure 4.10 presents the random fluctuations of wall-normal vorticity ω''_y exemplary for case $S = 2\delta$ and $S = 12\delta$ in the horizontal midplane $y = 0.5\delta$. It can be seen for $S = 2\delta$ that there are increased fluctuations of ω''_y in the low-momentum regions over all ridges, which extend over the entire channel length and exhibiting streamwise waviness of $\mathcal{O}(5\delta)$. Thereby, clockwise and counter-clockwise rotating vortices (red and blue contours) appear jointly at the upper and lower regions of the LMRs, which is consistent with the view of a Kelvin Helmholtz instability described before. For $S = 12\delta$, similar fluctuations of ω''_y can be found at the ridge location (e.g. $x \approx 17\delta - 36\delta$). In addition, the fluctuations occurring in the smooth-wall valley region have similar intensities as those at the ridges with comparable long streamwise coherence, but in contrast they are not spanwise fixed and can extend laterally along the spanwise direction. This illustrates the similarity of turbulent instantaneous structures that occur over the smooth-wall region and the those associated with instantaneous secondary motions at the ridges.

4.2.4 Ridge height influence on secondary motions

In the previous section it was shown that VLSMs are suppressed by the presence of ridge-induced secondary motions. In this section, the effect of the ridge height h_g on the suppression or weakening of VLSMs is investigated. For this purpose, the ridge case $S = 4\delta$ is used, for which it was shown that VLSMs are strongly weakened and only small energy contributions are found in the valleys as shown in figure 4.8 (a). The ridge height is reduced from $h_g = 0.1\delta$ to $h_g = 0.05\delta$ and

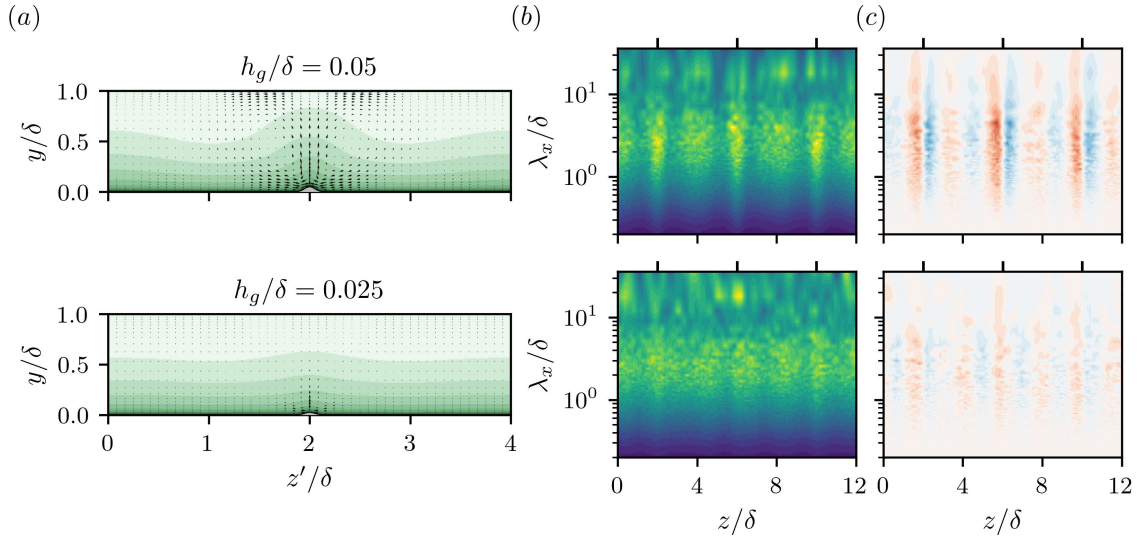


Figure 4.11: Influence of the ridge height on mean streamwise velocity \bar{u} in (a), pre-multiplied spectra $\kappa_x F_{u''u''}(\lambda_x, z)$ in (b) and co-spectra $\kappa_x F_{u''w''}(\lambda_x, z)$ in (c). The spectra are shown at the wall-normal location $y = 0.5\delta$. Top row presents $h_g = 0.05\delta$ and bottom row $h_g = 0.025\delta$. The colour ranges of the spectra are the same as used in figure 4.3 and 4.8.

$h_g = 0.025\delta$. The reduction of the ridge height leads to a weakening of the mean secondary motion, which is characterised by a weaker upward bulging of \bar{u} above the ridges, which can be seen in figure 4.11 (a). The centre position of the mean secondary motions reduce to $(y_{sc}, |z_{sc}|) = (0.44\delta, 0.35\delta)$ and $(0.38\delta, 0.30\delta)$ for $h_g = 0.05\delta$ and 0.025δ , respectively. The strength of the secondary motion decreases in terms of K_c by 70.5% for $h_g = 0.05\delta$ and 93.5% for $h_g = 0.025\delta$ compared to $h_g = 0.1\delta$ (see table 4.1). The effect of the ridge height on the instantaneous secondary motions is shown for the one-dimensional pre-multiplied streamwise energy spectra $\kappa_x F_{u''u''}$ in figure 4.11 (b). As can be seen, more energy contributions of VLSMs are present in the valleys than observed for case $h_g = 0.1\delta$ (shown in figure 4.8 (a)). For $h_g = 0.05\delta$ energized wavelengths $\lambda_x \approx 2\delta - 5\delta$ at the ridges are still observable as well as the separation regions with reduced energy contributions to the sides of the ridges in $\kappa_x F_{u''u''}$, which is no longer clearly visible for $h_g = 0.025\delta$. For the latter case VLSMs are able to form above the ridges, as seen for example at $z = 6\delta$ in figure 4.11 (b), suggesting that small ridges don't represent a spatial barrier to the lateral movement of VLSMs anymore, as expected for smooth-wall conditions. Another indicator of the weakening of instantaneous secondary motions can be seen in the co-spectrum $\kappa_x F_{u''w''}$ figure 4.11 (c), where the energy contributions of $\overline{u''w''}$ on both sides of the ridges decrease continuously with decreasing h_g . While the upward bulging of the mean streamwise velocity is significantly less pronounced for smaller ridge heights, the vorticity thickness reduces slightly from 0.54 ($h_g = 0.1\delta$) to 0.53 ($h_g = 0.05\delta$) and 0.47 ($h_g = 0.025\delta$), as can be also seen in figure 4.9 (b). The characteristic wavelength of the instantaneous secondary motion $\lambda_{x,SCI}$ however reduces with decreasing h_g to $\lambda_{x,SCI} = 4.5\delta$ for $h_g = 0.05\delta$ and $\lambda_{x,SCI} = 2.57\delta$ for $h_g = 0.025\delta$. This illustrates that $\lambda_{x,SCI}$ correlates with the strength of the mean secondary motions and for small ridge heights (e.g. $h_g = 0.025\delta$) approaches the streamwise wavelength of LSMs of smooth-wall conditions ($\lambda_x \approx 2 - 3\delta$).

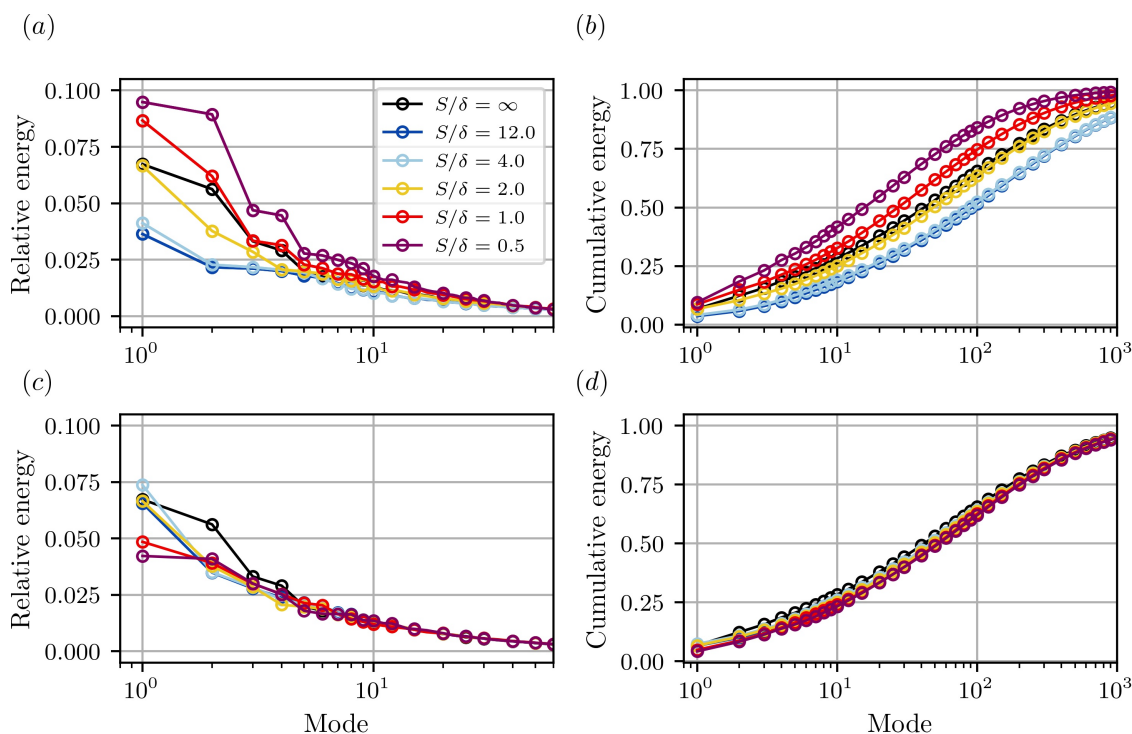


Figure 4.12: Relative energy contribution of POD modes in (a, c) and cumulative energy contribution in (b, d). Spanwise window size to compute POD modes corresponds to S , except for case $S = 12$ with $L_{z,win} = 4\delta$ and smooth-wall case $S = \infty$ with $L_{z,win} = 2\delta$. In (c, d) the spanwise window size is $L_{z,win} = 2\delta$ for all S cases

4.2.5 Proper orthogonal decomposition

The characteristics of instantaneous secondary motions is further investigated by applying the proper orthogonal decomposition to extract energetically dominant flow structures. The spatial modes are computed by means of the snapshot POD, which is described in section 2.5. The instantaneous snapshots for the computation of the POD modes are collected at nine cross-sectional planes which are spaced 4δ apart in the streamwise direction. The cross-sectional planes are further divided into non-overlapping windows of width $L_{z,win}$ and in case of ridges, the windows are centred at ridge positions. A total of at least 22000 snapshots were used for all cases, and the time interval between each time step is $\Delta t \approx 0.92t_b$, except for case $S = 12\delta$, where a smaller time step $\Delta t \approx 0.35t_b$ was used due to the smaller number of ridge windows. The convergence of the POD results for case $S = 12\delta$ is examined by using only half and one third of the total number of snapshots, which yields a change of less than 1% for the eigenvalues of the most energetic POD modes.

The relative and cumulative energy contributions of the k th POD mode for the different S cases is shown in figure 4.12. For the computation of the POD modes in figure 4.12 (a, b) a spanwise window size of $L_{z,win} = S$ is applied, which has been used in previous studies (Vanderwel et al. 2019, Zampiron et al. 2020). For the coarsest ridge spacing case $S = 12\delta$ the window size is limited to $L_{z,win} = 4\delta$, in order to neglect energetic structures present in the smooth-wall valley region. Since the spanwise width of VLSM is anchored around 2δ the window size for the smooth-wall

case is $L_{z,win} = 2\delta$ (Cameron et al. 2017). The results shown in 4.12 (a) are similar to the one obtained by Zampiron et al. (2020), where the relative energy contribution of the lowest POD modes increases with decreasing S , which was assumed to be an effect of the different window sizes (Zampiron et al. 2020). As the cumulative energy contributions in figure 4.12 (b) show, this leads to the energy being distributed among more POD modes for larger S . The number of modes to represent 50% of the energy agrees very well with those of Zampiron et al. (2020), for example 15 and 48 modes are needed for cases $S = 0.5\delta$ and $S = 2\delta$, while 15 and 50 modes are required for cases $S = 0.39\delta$ and $S = 1.97\delta$ of Zampiron et al. (2020). The two largest ridge spacings $S = 4\delta$ and $S = 12\delta$ require a similar number of modes, namely 87 and 91, but it should be noted that this is an effect of the same window size being used. Figure 4.12 (c, d) present the relative and cumulative energy for the different S cases with the same window size $L_{z,win} = 2\delta$ used for the POD computation. The choice of $L_{z,win} = 2\delta$ is discussed in more detail in the following text. As can be seen the relative and cumulative energy distribution equalize among the different S cases, and for the reconstruction of 50% of the energy, between 46 and 53 modes are now required.

The spatial pattern of the first six POD modes with $L_{z,win} = S$ are shown in figure 4.13. This number of spatial POD modes is commonly used in previous studies since these modes are associated with large-scale δ -scale motion of the instantaneous secondary motions (Vanderwel et al. 2019, Zampiron et al. 2020). As can be seen, the first POD modes form large-scale vortices for all S cases, and as observed in previous studies, the size of the spatial pattern decreases with the POD mode number (here for $S \leq 2\delta$). Comparison of the modes with Zampiron et al. (2020) for $S \leq 2\delta$ and Vanderwel et al. (2019) for $S = \delta$ shows very good agreement with the present corresponding S cases. The first two POD modes, as seen for $S \leq 2\delta$, form the dominant energetic modes (see figure 4.12 (a)) and are characterised by large-scale motion filling the entire channel height. This pair of modes was also identified as a distinctive dynamical behaviour associated with lateral shifts of the instantaneous secondary motions (Vanderwel et al. 2019). The first mode represents the sideways-leaning of the instantaneous secondary motion, while the second mode (e.g. $S \leq 2\delta$) indicates whether low- or high-momentum streaks are located above the ridge. For case $S = 4\delta$ the first mode possesses a similar energetic pattern as seen for $S \leq 2\delta$, which has a maximum spanwise extent of approximately 2δ (also seen for case $S = 12\delta$, not shown here). The second mode of the cases $S \leq 2\delta$ with counter-rotating vortices can be found for $S = 4\delta$ in an attenuated form in mode 6. The modes between the first and the sixth of $S = 4\delta$ represent turbulent large-scale structures that appear in the valley region and are not related to instantaneous secondary motions at the ridges.

As seen in the previous section, the first two characteristic POD modes of instantaneous secondary motions are constrained in the spanwise direction for small ridge spacings ($S \leq \delta$), while their maximum spanwise extent is approximately 2δ for $S \geq 2\delta$. Therefore, a window width of $L_{z,win} = 2\delta$ is used in the following part for the computation of the POD modes. The corresponding POD modes are shown in figure 4.14 and it can be seen that for the first two modes the shape and spatial extent are similar among all S cases. Only for $S = 0.5\delta$ the first two modes are reversed compared to the other S cases, due to similar relative energy contributions as seen in figure 4.12 (c). For small ridge spacings $S \leq \delta$, the mutual influence neighbouring ridges can be seen by changes

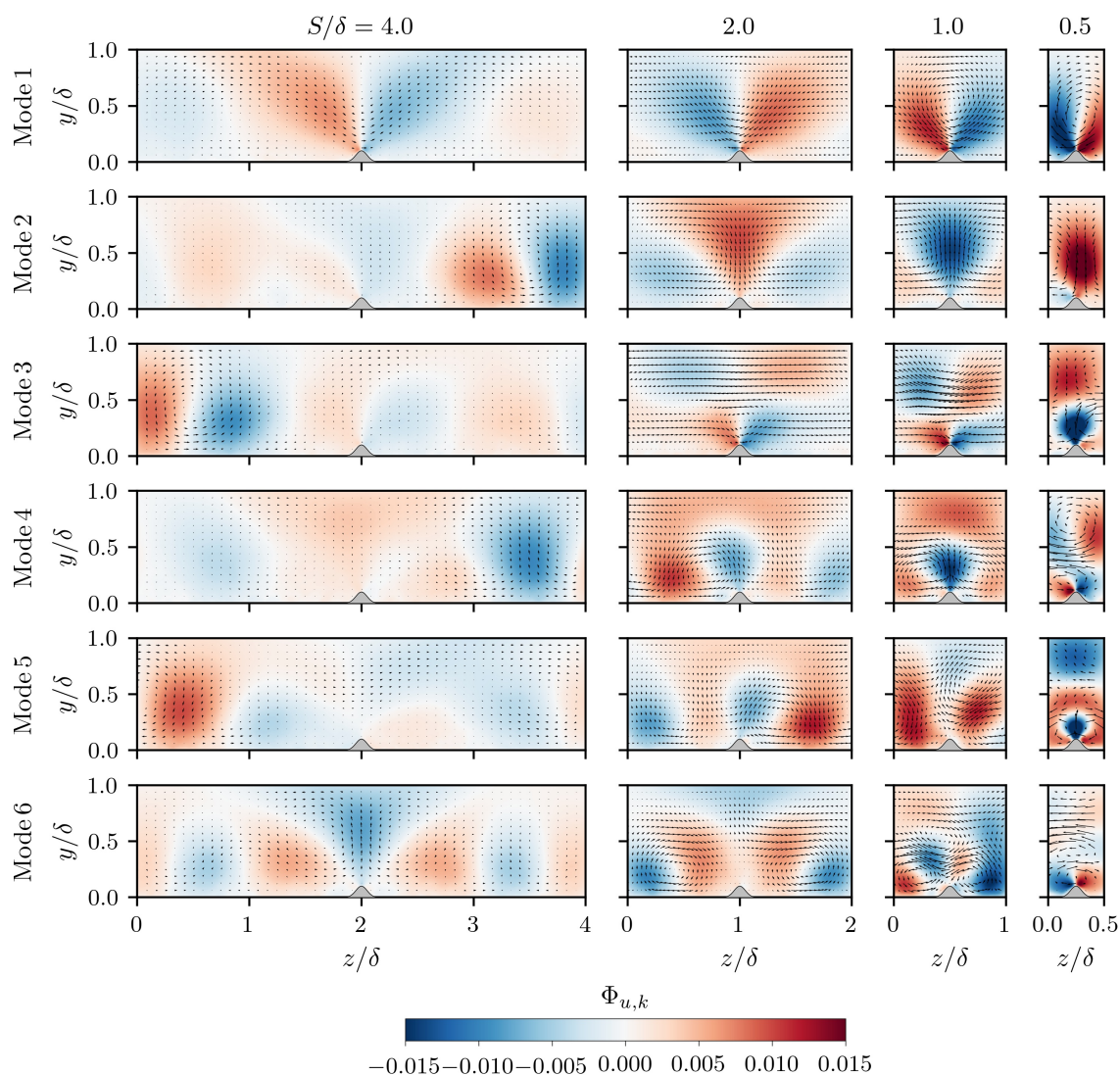


Figure 4.13: First six POD spatial modes of streamwise component $\Phi_{u,k}$ ($k = 1, \dots, 6$) for different ridge spacings S . The arrows represent the wall-normal $\Phi_{v,k}$ and spanwise component $\Phi_{w,k}$ of the k th POD mode. The spanwise window size used for the POD is $L_{z,win} = S$.

in the shape and distribution of the first two modes. As a consequence the central vortex of the first POD mode loses its spanwise spread in the upper half of the channel, while the second POD mode no longer depicts a clear funnel-like opening towards the bulk region. The instantaneous structures at the neighbouring ridges for $S \leq \delta$ appear for lower mode numbers, where spatial structures with similar dimensions to those seen for the first two modes appear at the neighboring ridges. The results illustrate that the dominant structures of the instantaneous secondary motions have similar spatial dimensions and shapes and are independent of the ridge spacing S . This could not be observed for small ridge spacings in the previous studies due to the a priori specification of the POD window size of $L_{z,win} = S$.

The influence of the ridge height for case $S = 4\delta$ on the first four POD modes is shown in figure 4.15, as well as the POD modes obtained for the smooth-wall case $S = \infty$. The first two POD modes of case $h_g = 0.05\delta$ are similar to the one obtained for $h_g = 0.1\delta$ in 4.14, while

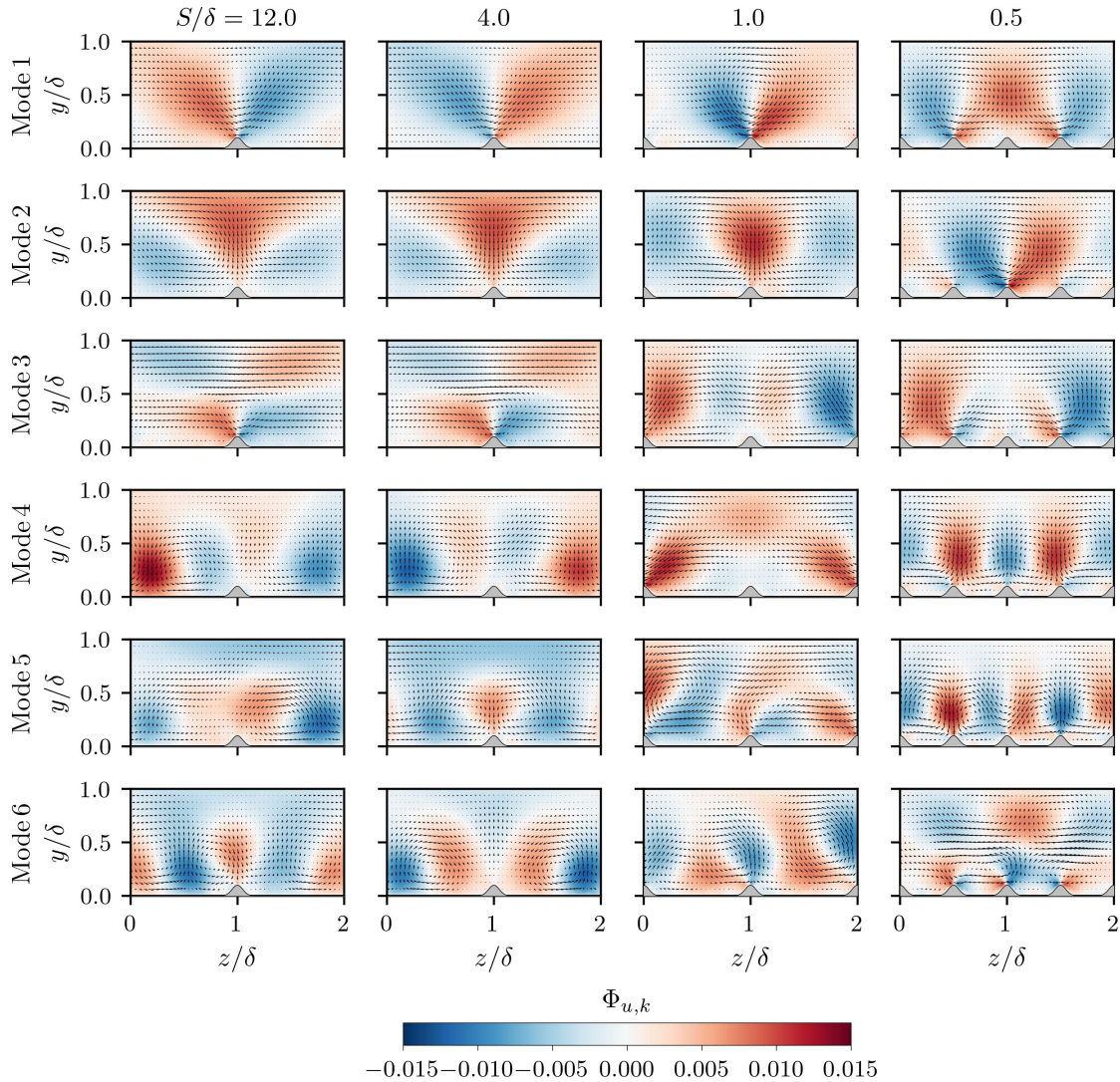


Figure 4.14: Spatial POD modes for different ridge spacings S ($k = 1, \dots, 6$). The colour contour represents the streamwise component and the arrows the cross-sectional components of the POD modes. The same spanwise window size $L_{z,win} = 2\delta$ is used for all cases.

for $h_g = 0.025\delta$ the first POD mode does not depict anymore the large-scale vortex centred at the ridge. For the latter case the first two modes represent large-scale counter-rotating vortices and their upward motion is centred slightly to the sides of the ridge. The first two modes of the smooth-wall case $S = \infty$ exhibit a pair of large-scale counter-rotating vortices with wavelength 2δ , which are shifted with respect to each other by a quarter wavelength in the spanwise direction. These modes show similarities to the POD mode with counter-rotating vortices found for ridge cases, as for example for the second mode of cases $S \geq \delta$. Comparing the modes of $h_g = 0.025\delta$ with the ones of the smooth-wall case show a very close resemblance, however the first two modes for $h_g = 0.025\delta$ are centred at the ridge with a slight shift to the sides. This indicates that the ridges are less able to lock intense structures at the ridge position when h_g decreases, such that the energetic structures will approach a similar behaviour to those found for smooth-wall conditions.

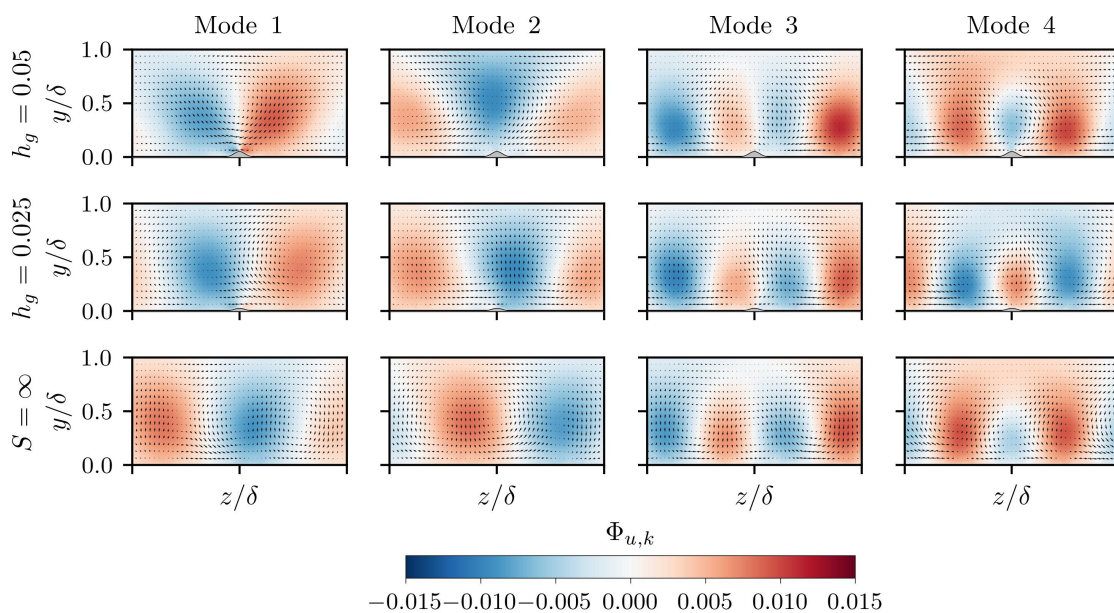


Figure 4.15: Influence of ridge height on POD modes for case $S = 4\delta$ in the first two rows and the smooth-wall case is shown in the bottom row. The colour contour represents the streamwise component and the arrows the cross-sectional components of the POD modes. A window size $L_{z,win} = 2\delta$ is used for all cases.

In the following, the time coefficients of the first two POD modes are considered in more detail, since they represent the instantaneous large-scale structures of secondary motions. The time variation of these two time coefficients is shown for example for case $S = 4\delta$ in figure 4.16 for a small time section of the entire time series. Both time coefficients are normalised by the corresponding root-mean-square value $a_{i,rms}$, which is equivalent to the standard deviation, since the time coefficients have zero mean. As can be seen, the time coefficients fluctuate around the mean and stay most of the time in a range within $\pm a_{i,rms}$ (marked by black dashed lines), while extreme values occur occasionally. These extreme events however contribute particularly strongly to the turbulent kinetic energy, since by definition (see equation 2.56) the time coefficients enters k by a_i^2 .

The coloured vertical lines in the upper part of figure 4.16 illustrate times at which both time coefficients fulfill different conditions. Extreme positive or negative values of the first time coefficient $a_1(t)$ indicate strong lateral movement to the right and left of the instantaneous secondary motion, while positive and negative values of the second time coefficient $a_2(t)$ indicate whether the symmetric counter-rotating vortices move down- or upward above the central ridge (compare figure 4.14). Thus, the dark blue colour illustrates strong leftwards directed motion above the central ridge, while the opposite is indicated by the red colour. For the light blue and orange colours, an additional stronger upward motion occurs over the central ridge compared to dark blue and red events. The yellow colour represents events with strong upward motion above the central ridge, while no strong lateral motions to the right or left are present. As can be seen by the colour sequence in figure 4.16, these events mostly occur isolated, while there are few sequences where these events follow each other (for example $t/t_b \approx 12$ from orange to red). This illustrates that the

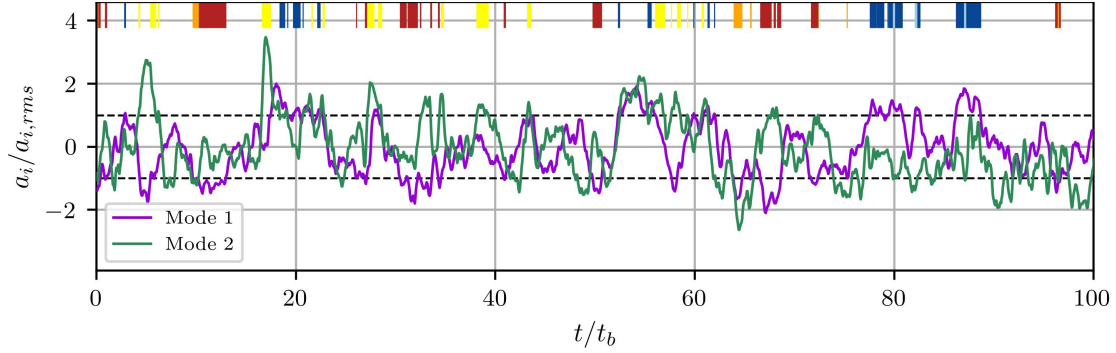


Figure 4.16: First two POD time coefficients of case $S = 4\delta$ normalised by the root mean square value of the respective time coefficient. For clarity the time coefficients are shown for a smaller subset of the complete time series. Dashed black lines indicate values of $a_i = \pm 1$. coloured vertical line in top panel indicate different conditions of POD time coefficients: dark blue $a_1/a_{1,rms} \geq 1$ and $-1 < a_2/a_{2,rms} < 1$; light blue $a_1/a_{1,rms} \geq 1$ and $a_2/a_{2,rms} \leq -1$; yellow $-1 < a_1/a_{1,rms} < 1$ and $a_2/a_{2,rms} \leq -1$; orange $a_1/a_{1,rms} \leq -1$ and $a_2/a_{2,rms} \leq -1$; red $a_1/a_{1,rms} \leq -1$ and $-1 < a_2/a_{2,rms} < 1$.

left- or right-leaning behaviour of the instantaneous secondary motion do not alternate in time, but rather suggest intermittent events.

These conditions of the first two time coefficients are used in the following to compute conditional averages of the instantaneous snapshots to extract time-dependent behaviour of the secondary motions (Bai et al. 2021). The conditional averages of the mean velocity field in the cross-sectional plane based on different pairs of conditions are shown in figure 4.17 for the smooth-wall case and different ridge cases $S \leq 2\delta$. Conditional averages based on the value of one of the two time coefficients are shown in (a-d), while the one based on the values of both time coefficients are depicted in (e-i). For a better comparison of the POD modes between the different ridge cases, the order of the first two POD modes of case $S = 0.5\delta$ is reversed for the following analyses. The results for case $S = 4\delta$ and $S = 12\delta$ are very similar to case $S = 2\delta$, such they are not presented here. The conditional-averaged velocity fields in (a) and (b) show events, when the first time coefficient has large negative or positive values, respectively, which for the ridge cases corresponds to the sideways-leaning behaviour of the instantaneous secondary motions. For the extreme conditions $a_2/a_{2,rms} \geq 1$ in (c) and $a_2/a_{2,rms} \leq -1$ in (d), the secondary motion is either strongly restricted in their spatial extent ($S = 2\delta$) or clearly enhanced compared to the mean secondary motion (compare figure 4.3). Interestingly, for narrow ridge spacings $S \leq \delta$, the opposite behaviour occurs simultaneously at the neighboring ridges than found at the central ridge, such that for the neighbouring ridges an upward bulging occurs in (c) and a downward bulging in (d). For the smooth-wall case the conditional averages reveal similar counter-rotating vortices for all conditions and their up- and downward motion appears at different spanwise locations, since they are not spanwise locked by the presence of ridges. The conditional averages in (a-d) account for 16.1%-18.2%, 14.3%-17.2% and 14.8%-18.7% of the total number of snapshots among the different ridge spacings S .

Examining the conditional averages based on both time coefficients draws a more differentiated picture of the instantaneous structures, which is shown in figure 4.17 (e - i). In (e), first the case can be seen when both time coefficients fall within the standard deviation $1 > a_1/a_{1,rms} > -1$

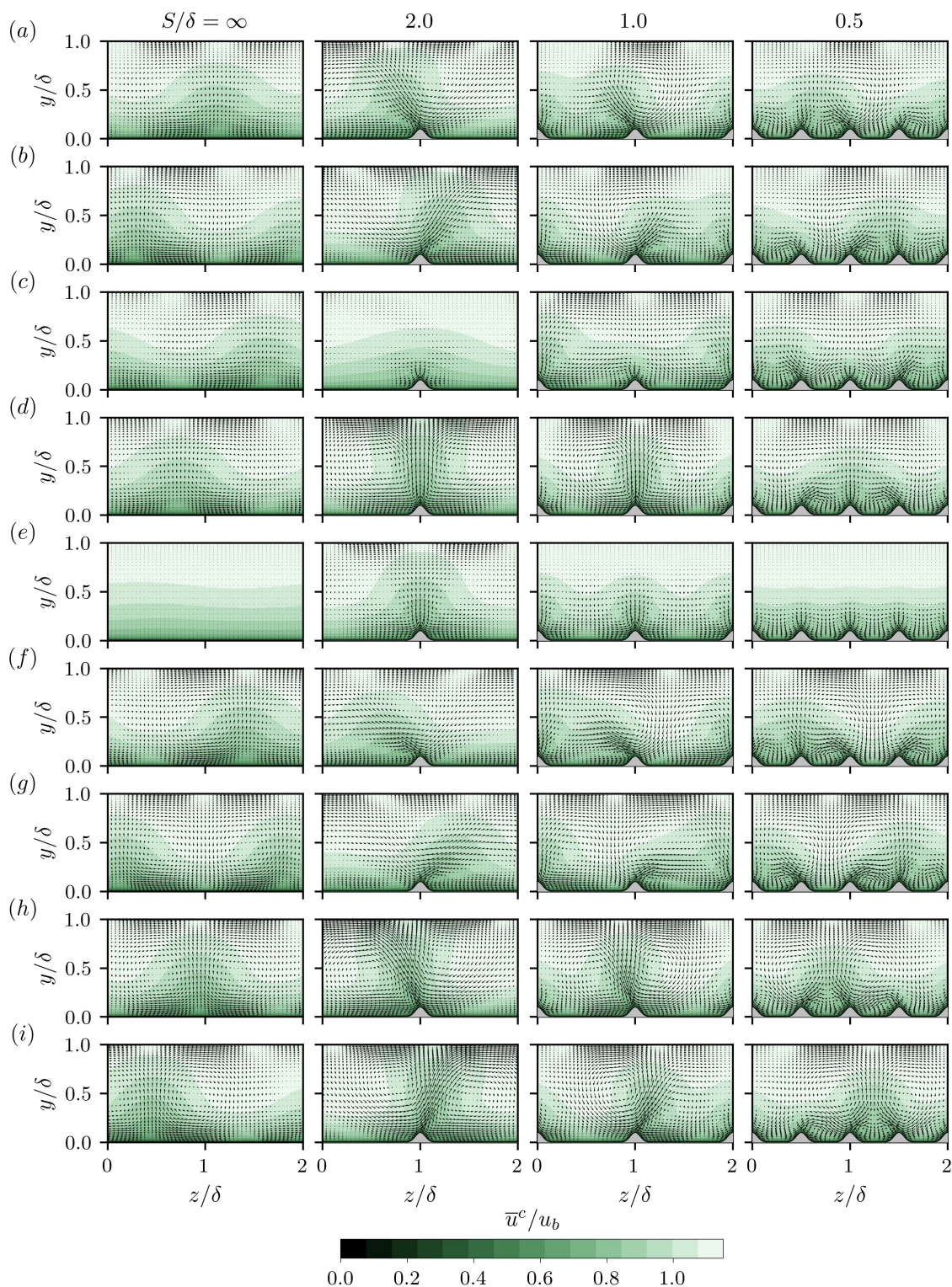


Figure 4.17: Conditional-averaged velocities arranged by the first two POD time coefficients for smooth-wall case and ridge cases $S \leq 2\delta$. Contours represent conditional-averaged mean streamwise velocity \bar{u}^c and arrows cross-sectional velocity components \bar{v}^c and \bar{w}^c . Conditions based on value of single time coefficients: $a_1/a_{1,rms} \geq 1$ in (a), $a_1/a_{1,rms} \leq -1$ in (b), $a_2/a_{2,rms} \geq 1$ in (c), $a_2/a_{2,rms} \leq -1$ in (d), and conditions based on values of two time coefficients: $1 > a_1/a_{1,rms} > -1$ and $1 > a_2/a_{2,rms} > -1$ in (e), $a_1/a_{1,rms} \geq 1$ and $a_2/a_{2,rms} \geq 1$ in (f), $a_1/a_{1,rms} \leq -1$ and $a_2/a_{2,rms} \geq 1$ in (g), $a_1/a_{1,rms} \geq 1$ and $a_2/a_{2,rms} \leq -1$ in (h), $a_1/a_{1,rms} \leq -1$ and $a_2/a_{2,rms} \leq -1$ in (i).

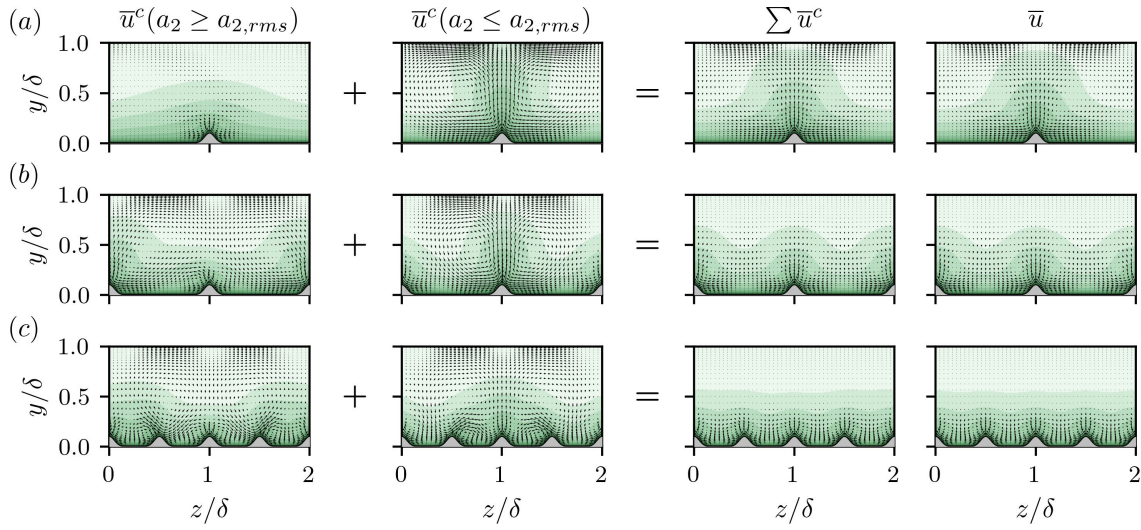


Figure 4.18: Comparison of sum of conditional averaged mean streamwise velocities \bar{u}^c and mean streamwise velocity \bar{u} of case $S = 2\delta$ in (a), case $S = \delta$ in (b) and case $S = 0.5\delta$ in (c). First two column represent conditional averages from 4.17 (c, d), and their sum is shown in the third column. The used colour bar is the same as in figure 4.17.

and $1 > a_2/a_{2,rms} > -1$ (43.0% - 45.3% of the snapshots), and the resulting conditional averages are almost identical to the mean secondary motions for all ridge cases, while for $S = \infty$ a spanwise homogeneous velocity field similar to the mean is found. This illustrates that the instantaneous events of the positive and negative time coefficients compensate for each other. The sideward leaning of the instantaneous secondary motions from the conditional average in (a) and (b) can be further distinguished by considering the condition of the second time coefficient, e.g. in (f) and (g). These cases represent occasions when the second mode takes strongly positive values ($a_2/a_{2,rms} \geq 1$), meaning that a downward motion occurs above the central ridge. As a result, the leaning of the instantaneous secondary motion is more pronounced to the sides, and more high momentum flow from the bulk can impinge on the central ridge. For dense ridge spacings $S \leq \delta$, the upward bulging of the sideward-leaning secondary motion combines with the upward bulging at the adjacent ridge, resulting in a stronger upward bulging at the corresponding side. The cases where in addition to the sideward-leaning behaviour of the instantaneous secondary motion (in (a) and (b)), a strong upward bulging now also occurs above the central ridge ($a_2/a_{2,rms} \leq -1$) are shown in figure 4.17 (h) and (i). Compared to the conditional averages in (a) and (b), stronger secondary motions are now observed whose leaning is less pronounced. For the densest ridge spacing $S = 0.5\delta$, it can be seen that the upward bulging is concentrated between the central and adjacent ridge, and the adjacent ridge contributes to the upward bulging in a similar manner as the central ridge. For the smooth-wall case the conditions in (f - i) depict similar counter-rotating vortices as in (a - d), however at spanwise locations in between the latter ones. This demonstrates that instantaneous large-scale structures over smooth walls can appear at any spanwise location of the channel.

The conditional averages in figure 4.17 show for dense ridge spacings $S \leq \delta$, that instantaneously large-scale secondary motions can form, which fill the entire channel height and extend over neighbouring ridges, which is not expected by considering the mean secondary motions. This

means that for these cases the instantaneous extent of the secondary motions is masked by the averaging procedure, which is further illustrated in figure 4.18. For the ridge cases $S \leq 2\delta$ the conditional averages with $a_2/a_{2,rms} \geq 1$ and $a_2/a_{2,rms} \leq -1$ are shown in the first two columns (compare figure 4.17 (c) and (d)), and the result of averaging both conditional averages is shown in the third column. The aforementioned mechanism of the averaging can be nicely observed and for dense ridge spacings $S \leq \delta$ the strong upward bulging of secondary motion over the central ridge (column 2) superimpose with downward motion of the strong secondary motion at the neighbouring ridges (column 1) resulting on average in smaller and spatially confined secondary motions.

4.3 Discussion and summary

This chapter investigates the interaction between secondary motions and turbulent large-scale structures and their similarities in turbulent open-channel flow with streamwise-aligned Gaussian ridges.

Recent experiments of secondary motions over strip-type surfaces have shown the coexistence between secondary motions and turbulent large-scale structures (LSM/VLSM) (Wangsawijaya et al. 2020), while coexistence between secondary motions and VLSMs was not found for ridge-type surface (Zampiron et al. 2020). The investigation in the present chapter confirms this observation that ridge-type induced secondary motions suppress the formation of VLSMs for ridge spacings of $S \leq 2\delta$ and ridge heights $h_g = 0.1\delta$. In addition, the present results show that for larger ridge spacings, coexistence between secondary motions and VLSMs begins at $S \approx 4\delta$. The large ridge spacing cases illustrate that the spanwise extent of the mean secondary motions is fixed around 2δ , such that VLSMs can form in the smooth-wall valley region between the ridges. However, for $S = 4\delta$ the VLSMs occurring in the valley are weakened compared to the VLSMs observed in smooth channel flows, indicating that the secondary motions at the ridges are still able to affect the valley region. This influence of the secondary motions is further illustrated by the formation of tertiary vortices in the middle of the valley, though these cause a much weaker upward bulging of \bar{u} than the one observed at the ridges by the secondary motion. For larger ridge spacings $S = 12\delta$, the width of the valleys is sufficiently large, such that areas exist that are not influenced by the mean secondary motion, where eventually VLSMs can form with similar strength and characteristics as those occurring in smooth channel flows.

The suppression of the VLSMs by the secondary motions is attributed to the strong spatial heterogeneity of the mean velocity field at the ridges (Zampiron et al. 2020). By reducing the ridge height h_g the strength of secondary motions and the induced flow heterogeneity can be reduced, and these effects on the interaction between secondary motions and turbulent large-scale structures are considered in the present configuration for case $S = 4\delta$. While for $h_g = 0.1\delta$ the VLSMs in the valleys are weaker compared to the ones observed for smooth walls, the reduction of h_g shows that VLSMs first increase in strength for $h_g = 0.05\delta$ ($h_g^+ = 27$) and eventually for $h_g = 0.025\delta$ ($h_g^+ = 13.5$) are able to appear in the entire channel width. In the latter case the ridge height is sufficiently small and the VLSMs are strong enough such that the ridges do not represent a

spatial barrier for the lateral movement of the VLSMs anymore. The comparison with the intensity of secondary motions over alternating smooth- and rough-wall strips from chapter 3, shows that case $h_g = 0.025\delta$ induces secondary motions with similar strength as the pure strip-type surface cases $h = 1.5\bar{k}_r - 1.70\bar{k}_r$. Consequently, the different observations of the coexistence of secondary motions and VLSMs over strip- and ridge-type surfaces are a consequence of the different strength of the respective secondary motions.

Regarding the question of the formation mechanism of secondary motions it is still not clear whether there is a single mechanism that describes the formation of both strip- and ridge-type induced secondary motions, or whether two different mechanisms exist. Based on the results of instantaneous secondary motions over strip-type surfaces, Wangsawijaya et al. speculated that secondary motions might be natural VLSMs that are spanwise phase-locked at the roughness transition. However, this explanation seems not suitable for ridge-type surfaces due to the suppression of VLSMs by secondary motions. On the other hand, Zampiron et al. (2020) suggested that the meandering of instantaneous secondary motions might be related to an instability caused by inflection points in the spanwise profile of mean streamwise velocity. This hypothesis was supported by the finding of a linear relationship between the characteristic streamwise wavelength of the instantaneous secondary motions $\lambda_{x,SCI}$ and the vorticity thickness δ_ω . The trend of a linear relationship is also found for the present cases, but the slope differs from the one found in the experiments of Zampiron et al. (2020), which is attributed to differences in surface conditions and Reynolds number between the experiments and the present simulations, as well as different approaches to determine the velocity spectra. While the characteristic streamwise wavelength of secondary motions $\lambda_{x,SCI}$ lies for ridge heights of $h_g = 0.1\delta$ between those of LSMs and VLSMs, reducing h_g leads to smaller values of $\lambda_{x,SCI}$ approaching the typical streamwise wavelength of LSM ($\lambda_x \approx 2\delta - 3\delta$). This behaviour shows some interesting similarities to a recently proposed model describing the formation mechanism of LSMs in turbulent channel flows (de Giovanetti et al. 2017). In this model, an artificial body forcing is used to create a streamwise uniform low-momentum streak in the outer region, with similarities to VLSMs, and for sufficient forcing this streak undergoes an instability forming streamwise vortical flow structures with similar properties as naturally occurring LSMs. For moderate forcings the LSMs in the model exhibit streamwise wavelengths of $1-2\delta$, while stronger body forces can lead to larger $\lambda_x \approx 10\delta$, which is in a similar range as the $\lambda_{x,SCI}$ of the secondary motions found for different ridge heights h_g in the present study. Thus, an increase of the body forcing in the model might correspond to the effects of increasing the ridge height. In this sense, the instantaneous secondary motions arise similar to the LSM in the model, by an streak-vortex instability of the streamwise coherent low-momentum streaks over the ridges. Interestingly, it has recently been observed that LSMs in open-channel flows are responsible for the formation of sediment ridges (Scherer et al. 2022). These sediment ridges in turn induce for time averages of $\mathcal{O}(10)$ time bulk units secondary motions, which are considered as statistical footprints of the spanwise organised LSMs. Further investigations for alternating smooth- and rough-wall strips with variations in relative height differences, similar to the cases in chapter 3, could clarify if the streak-vortex instability mechanism might be also applicable for the formation of strip-type induced secondary motions.

The instantaneous characteristics of secondary motions are further examined by means of proper orthogonal decomposition. First, it is shown that the dominant POD modes which are associated with instantaneous structures of secondary motions are strongly affected by the choice of spanwise POD window size. In previous studies a POD window size of S was used (Vanderwel et al. 2019, Zampiron et al. 2020), and the present results demonstrate that this choice constrains the spatial extent of dominant structures associated with secondary motions for small ridge spacings ($S < 2\delta$). For all S cases the dominant POD modes are large-scale structures with spanwise extents of roughly 2δ and the shape and structure of these modes are similar among the different ridge spacing cases. Unlike the mean secondary motions for small ridge spacing suggests, the instantaneous secondary motions for these cases can extend over adjacent ridges. The smooth-wall case depicts counter-rotating vortices as dominant POD modes, which have close resemblance to the second POD mode found at the ridges for the different S cases. Since for the latter cases VLSM are absent at the ridges, and LSM are characterised by strong cross-sectional coherent motion, this further illustrates the similarities between instantaneous secondary motions and naturally occurring LSMs. Conditional averages, based on the first two POD time coefficients, reveal stronger secondary motions than observed in the complete time mean. Furthermore, the conditional averages depict a lateral sideways-leaning behaviour of instantaneous secondary motions, which has been also observed for secondary motions appearing over converging-diverging riblets (Kevin et al. 2017) and strip-type induced secondary motions (Wangsawijaya et al. 2020). For dense ridge spacings $S \leq \delta$, large-scale counter-rotating vortices are also detected in the conditional mean, such that the upward motion forms at one ridge, while suppressing the upward motion at the neighbouring ridges and vice versa, depending on the time instances. Consequently the superposition of these events by the averaging procedure results in a masking of the instantaneous behaviour of secondary motions, and thus the mean secondary motions appear smaller and scale with S for ($S \leq \delta$).

5 The effects of heterogeneous surfaces on mixed convection

In the previous chapter it was shown that heterogeneous surfaces, in form of streamwise-aligned ridges, increase the momentum and heat transfer of turbulent forced convection flows. The objective of this chapter is to investigate how these effects of heterogeneous surfaces translate to turbulent channel flows under mixed convection conditions. These flows are known to generate different large-scale flow structures as outlined in section 2.3.3, depending on the relative importance between buoyancy and shear effects. How heterogeneous surfaces influence these flow structures, and how the transitions between the different flow regimes are affected, i.e. from forced convection structure to streamwise rolls and from these to convective cells, are not yet sufficiently investigated. Similar to the previous chapter, streamwise-aligned ridges are chosen to represent heterogeneous surfaces, such that secondary motions are present under forced convection conditions. By systematically varying the strength of buoyancy, their effect on the formation of secondary motion is investigated in more detail. In addition, the possibility of an interaction between secondary motions with streamwise rolls occurring under mixed convection conditions, can be thus examined. The effect of increased momentum and heat transfer by the heterogeneous surface on mixed convection is controlled by systematically varying the spanwise ridge spacing.

This chapter is based on the publication *The effect of spanwise heterogeneous surfaces on mixed convection in turbulent channels* (Schäfer et al. 2022a). Compared to the publication, some symbols of physical quantities have been adapted to be consistent with the notation introduced in this thesis. Additional discussions regarding the dynamics of streamwise rolls for different heterogeneous surface conditions, which go beyond the results presented in the publication, are complemented in section 5.2.5.

5.1 Flow configuration

The present flow configuration is a turbulent channel flow with streamwise-aligned Gaussian ridges sketched in figure 5.1. The governing equations are solved by the simulation code Xcompact3d,

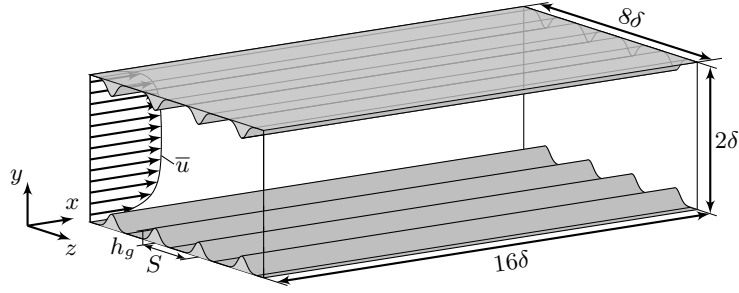


Figure 5.1: Sketch of the numerical channel domain with streamwise-aligned Gaussian ridges at the walls. Adopted from Schäfer et al. (2022a)

as presented in section 2.4. The continuity equation, Navier-Stokes equation under Boussinesq approximation, and temperature equation are

$$\frac{\partial u_i}{\partial x_i} = 0, \quad (5.1)$$

$$\frac{\partial u_i}{\partial t} + \frac{\partial u_i u_j}{\partial x_j} = -\frac{1}{\rho_0} \frac{\partial p}{\partial x_i} + \nu \frac{\partial^2 u_i}{\partial x_j \partial x_j} + \beta g T \delta_{i2} + \Pi \delta_{i1} + F_{IBM,i}, \quad (5.2)$$

$$\frac{\partial T}{\partial t} + \frac{\partial T u_j}{\partial x_j} = \alpha \frac{\partial^2 T}{\partial x_j \partial x_j} + Q_{IBM}, \quad (5.3)$$

where the forcing term Π maintains a constant volume flow rate. The Gaussian ridges are represented in the momentum and temperature equation by the volume forcing term $F_{IBM,i}$ and temperature source term Q_{IBM} , respectively. Periodic boundary conditions are applied in the horizontal directions and Dirichlet boundary conditions are applied in the wall-normal direction to impose zero velocities and constant temperatures throughout the structured walls. "The simulations were performed on a domain size $L_x \times L_y \times L_z = 16\delta \times 2\delta \times 8\delta$, which is in agreement with Pirozzoli et al. (2017), who reported for this domain size insensitivity of the mean velocity and temperature profiles.[...] The existing code was extended for the simulation of buoyancy effects and the code was validated with the data base for mixed convection and Rayleigh-Bénard flows of Pirozzoli et al. (2017) as documented in Appendix A.2."(Schäfer et al. 2022a) Spatial averages in this chapter are based on intrinsic averaging, and the definitions are outlined in section 4.1, which also apply for the present configuration.

"The considered flow is characterised by three non-dimensional numbers, namely the Prandtl number Pr , which is the ratio of momentum and thermal diffusivity, the bulk Reynolds number Re_b , describing the ratio of inertial and viscous effects, and the Rayleigh number Ra , characterising the ratio of buoyant and viscous effects, and their definitions are given by

$$Pr = \frac{\nu}{\alpha}, \quad Re_b = \frac{u_b \delta_{eff}}{\nu}, \quad Ra = \frac{(2 \delta_{eff})^3 \beta g \Delta T}{\alpha \nu}. \quad (5.4 \text{ a,b,c})$$

The bulk velocity is defined as $u_b = 1/(2\delta_{eff} L_z) \int_0^{L_z} \int_{y_b(z)}^{y_t(z)} \bar{u} dy dz$. Here, ΔT is the imposed and constant temperature difference between the bottom and top wall surfaces $\Delta T = T_b - T_t$. The

Prandtl number is set to $Pr = 1$ for all considered cases. Following the work by Pirozzoli et al. (2017), the bulk Richardson number is defined as

$$Ri_b = \frac{2\delta_{eff} \beta g \Delta T}{u_b^2} = \frac{Ra}{4Re_b^2 Pr}, \quad (5.5)$$

to characterise the relative importance of buoyancy and inertial effects. Please note that positive values of Ri_b indicate convectively unstable conditions, while in atmospheric flows positive values commonly indicate convectively stable conditions (Wyngaard 2010). Another quantity widely used in the ABL community to categorise the flow is the ratio of the boundary layer depth z_i and the Obukhov length L , which is known as the stability parameter $-z_i/L$ (Wyngaard 2010). For the present channel flow configuration with ridges, this translates into the ratio of δ_{eff} and L , with $L = -u_\tau^3/(\kappa q_w \beta g)$, where κ is the von Kármán constant with $\kappa = 0.4$ (Wyngaard 2010), while u_τ and Q are the friction velocity and the vertical heat flux, respectively (both defined in the next paragraph). (Schäfer et al. 2022a)

"The drag exerted on the flow is quantified by the skin friction coefficient C_f and friction Reynolds number Re_τ , which are defined as $C_f = 2u_\tau^2/u_b^2$ and $Re_\tau = u_\tau \delta_{eff}/\nu$. [...] The wall-shear stress is determined by extrapolating the total shear stress from the bulk region ($0.5 \leq y/\delta \leq 1.5$) to the virtual wall location $y_0 = \delta - \delta_{eff}$ (Chan-Braun et al. 2011). The heat transfer of the flow is characterised by the Nusselt number $Nu = 2\delta_{eff} q_w/(\alpha \Delta T)$, [where q_w equals the constant total heat flux q of the system which is] determined by evaluating the time and horizontally averaged temperature transport equation at the half-channel height $q = \langle v'T' \rangle|_\delta - \alpha \partial \langle \bar{T} \rangle / \partial y|_\delta$ (Stroh et al. 2020a). (Schäfer et al. 2022a)

"The turbulence level is quantified in this study by the Reynolds number $Re_k = \sqrt{K} \delta_{eff}/\nu$, where K corresponds to the time- and volume-averaged turbulent kinetic energy. This quantity is computed by applying the averaging procedure given in equation 4.5 [to] $k = 0.5 \cdot \overline{u_i' u_i'}$. A characteristic velocity scale for natural convection is the free-fall velocity $v_f = (2\delta_{eff} \beta g \Delta T)^{1/2}$ and together with the effective channel height the free fall time t_f can be defined $t_f = 2\delta_{eff}/v_f = (2\delta_{eff}/(\beta g \Delta T))^{1/2}$. The time scale characterising the forced convection processes is the bulk time unit $t_b = \delta_{eff}/u_b$. From the given definitions, the ratio of t_b and t_f results in the following relationship $t_b/t_f = \sqrt{Ri_b}/2$. (Schäfer et al. 2022a)

5.1.1 Cases

"The transition between forced convection structures and streamwise rolls as well as the transition between streamwise rolls and convective cells in mixed convection flows is controlled by the mean shear and buoyancy forcing, which are determined by the imposition of the Reynolds Re_b and Rayleigh number Ra . There are several possibilities which may be used to vary these two dimensionless numbers to achieve the same Richardson number Ri_b , as depicted by the black solid and dashed lines in figure 5.2 (a). The simplest approach is to fix one of the dimensionless numbers, while varying the other one and vice versa. In the study of Pirozzoli et al. (2017), a smooth-wall channel flow is explored for a large parameter space of Re_b and Ra , covering all flow

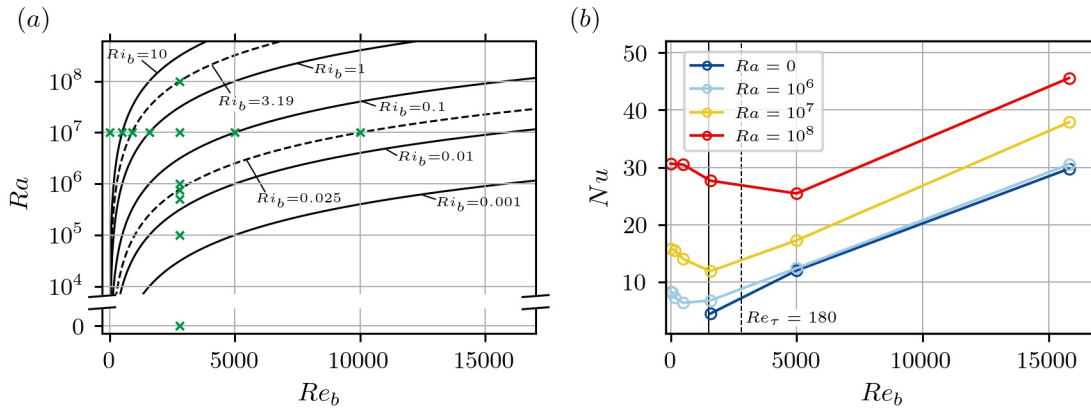


Figure 5.2: Parameter space of Rayleigh Ra and bulk Reynolds number Re_b in (a). The green marks in (a) indicate the flow parameters of the present simulations and solid and dashed black lines represent isolines with constant Ri_b . The dashed lines highlight Ri_b values, for which Re -effects are investigated. The Nusselt number Nu over bulk Reynolds number Re_b of the turbulent mixed convection channel flow from Pirozzoli et al. (2017) for various Rayleigh numbers is shown in (b). The vertical solid black line separates the transitional and turbulent range for pure forced convection flows. Adopted from Schäfer et al. (2022a)

regimes, which is shown in terms of the resulting Nu in figure 5.2 (b). For fixed Ra , the initial reduction of Nu with increasing Re_b is associated with the emergence of streamwise rolls, which reduce the effective heat exchange of the convective plumes from the natural convection case. For larger values of Re_b the flow transitions to the forced convection regime where Nu increases with increasing Re_b ."(Schäfer et al. 2022a)

"In the current study the spanwise spacing of the Gaussian ridges S is varied in the range of $S/\delta = 0.5, 1, 2, 4, \infty$, where $S = \infty$ corresponds to the smooth-wall case. This translates into an effective half-channel height of $\delta_{eff}/\delta = 0.975, 0.987, 0.994, 0.997$ for the four ridge cases, respectively. Furthermore, the bulk Richardson number Ri_b is varied in such a way as to cover the different flow regimes of mixed convection and their transition ranges. The variation of Ri_b is achieved by two parameter sweeps, one at constant $Ra = 10^7$ and varying Re_b and the other sweep for changing Ra at constant $Re_b = 2800$. These two parameter sweeps for the simulations of the present study are represented in figure 5.2 (a) with green crosses, which results in a total number of 65 direct numerical simulations. These two parameter sweeps intersect in the vicinity of the minimum of Nu for $Ra = 10^7$ shown in figure 5.2 (b), which allows us to study the parameter sensitivity of the transition processes from two sides. The two black dashed lines in figure 5.2 (a) indicate isolines of constant Ri_b at which the two transition ranges of mixed convection occur. As will be shown later, the lower isoline $Ri_b = 0.025$ lies within the transition range of forced convection structures to streamwise rolls, while the upper isoline $Ri_b = 3.19$ is in the transition range between streamwise rolls to convective cells. For the present simulations two parameter points with similar Ri_b exist within the two transition ranges, allowing us to study the effect of Re on the flow organisation."(Schäfer et al. 2022a)

"From forced convection flows it is known that the strongest secondary motion occurs for $S/\delta \approx \mathcal{O}(1)$ with a spanwise extent of $\approx \delta$ (Vanderwel et al. 2019). Since secondary motions of Prandtl's second kind occur only in turbulent flows, the parameter sweep with fixed $Re_b = 2800$ will

accommodate these secondary motions for all Ra , which will allow us to study the effect of buoyancy on the secondary motions as well. In the case of the Ra -sweep, this will partly be the case. The spanwise extent of the convection cells and streamwise rolls found in Pirozzoli et al. (2017) are roughly 4δ , such that the chosen values of S cover the width of the different aforementioned flow structures."(Schäfer et al. 2022a)

"The grid resolutions for the simulations are chosen according to those used by Pirozzoli et al. (2017) for a second-order finite difference code. The grid requirements for mixed convection simulations in conjunction with Gaussian ridges represented by an IBM were investigated in a resolution study presented in Appendix A.3. It is found that the present grid resolution for smooth-wall mixed convection cases at $Ra = 10^7$ is sufficient for the representation of streamwise Gaussian ridges and a further increase of the resolution results in no significant differences of the mean quantities and profiles. Only for lower Ra does the spanwise grid resolution need to be slightly increased to achieve grid-independent statistical results for the streamwise-aligned ridge cases. The statistical time integration is carried out over at least $1500 t_b$ for cases $Ri_b \leq 0.32$, except for the high Re_b cases with $Ri_b = 0.025$ with time integration of at least $300 t_b$. For cases with $Ri_b \geq 1.0$ the time integration comprises at least $400 t_f$, while the high Ra cases with $Ri_b = 3.2$ and $Ra = 10^8$ were averaged over at least $120 t_f$."(Schäfer et al. 2022a)

5.2 Results

5.2.1 Global flow properties

"The results of the global flow properties for the different simulations are presented in table 5.1, where the configurations are arranged according to the parameter triad $(Ra, Re_b, S/\delta)$. The smooth-wall configurations are indicated by $S = \infty$ and the configurations with streamwise-aligned ridges are listed with decreasing S . Since the forced and mixed convection cases are run at constant flow rate (CFR), the presence of the Gaussian ridges will increase the drag, which translates into an increase of C_f and Re_τ compared to the respective case with smooth-wall conditions. As can be seen for all considered cases, the steady decrease of S leads to a monotonic increase of C_f and Re_τ compared to the smooth-wall case. For forced convection the increase of C_f is up to 26%, while the largest increase is found for $Ri_b = 10$ with 45%. Due to the changing friction drag, the ridge height in wall units h_g^+ changes for all cases as well, and ranges between $7 \leq h_g^+ \leq 60$ for the current configurations. In case of pure forced convection, turbulent secondary motions induced by streamwise-aligned ridges are known to increase the global friction as well as the heat transfer of the flow compared to smooth-wall conditions (Stroh et al. 2020a). This behaviour is also observed for the present forced convection case with streamwise-aligned Gaussian ridges, where for the densest ridge spacing $S = 0.5\delta$ the heat transfer increases 16% compared to the smooth-wall case. In a similar range with 17% is the increase for the natural convection case, and the largest increase is found for $Ri_b = 3.2$ with 32%."(Schäfer et al. 2022a)

Ra	Re _b	Ri _b	S/δ	N _x × N _y × N _z	Re _τ	Re _k	C _f (·10 ⁻³)	Nu	-δ _{eff} /L
0	2800	0	∞	512 × 193 × 384	178.5	228.1	8.1	7.4	-
0	2800	0	4	512 × 193 × 384	180.0	236.9	8.3	7.5	-
0	2800	0	2	512 × 193 × 384	181.7	244.1	8.5	7.7	-
0	2800	0	1	512 × 193 × 384	184.2	250.8	8.8	8.0	-
0	2800	0	0.5	512 × 193 × 384	196.3	258.5	10.2	8.6	-
10 ⁵	2800	0.003	∞	512 × 193 × 256	179.3	229.1	8.2	7.5	0.003
10 ⁵	2800	0.003	4	512 × 193 × 384	180.4	238.3	8.3	7.7	0.003
10 ⁵	2800	0.003	2	512 × 193 × 384	182.0	244.7	8.5	7.8	0.003
10 ⁵	2800	0.003	1	512 × 193 × 384	184.7	251.2	8.9	8.1	0.003
10 ⁵	2800	0.003	0.5	512 × 193 × 384	196.7	259.1	10.2	8.6	0.003
5.0 · 10 ⁵	2800	0.016	∞	512 × 193 × 256	180.5	234.3	8.3	8.1	0.017
5.0 · 10 ⁵	2800	0.016	4	512 × 193 × 384	181.8	240.9	8.5	8.1	0.017
5.0 · 10 ⁵	2800	0.016	2	512 × 193 × 384	183.2	247.3	8.6	8.2	0.017
5.0 · 10 ⁵	2800	0.016	1	512 × 193 × 384	186.1	253.0	9.0	8.4	0.016
5.0 · 10 ⁵	2800	0.016	0.5	512 × 193 × 384	198.1	261.1	10.4	9.0	0.014
7.5 · 10 ⁵	2800	0.024	∞	512 × 193 × 256	180.4	249.1	8.3	9.4	0.030
7.5 · 10 ⁵	2800	0.024	4	512 × 193 × 384	181.8	249.5	8.5	9.2	0.029
7.5 · 10 ⁵	2800	0.024	2	512 × 193 × 384	183.6	252.2	8.7	9.1	0.028
7.5 · 10 ⁵	2800	0.024	1	512 × 193 × 384	187.0	254.1	9.1	8.6	0.025
7.5 · 10 ⁵	2800	0.024	0.5	512 × 193 × 384	199.4	262.7	10.5	9.2	0.022
10 ⁶	2800	0.032	∞	512 × 193 × 256	178.9	257.1	8.2	9.7	0.042
10 ⁶	2800	0.032	4	512 × 193 × 384	180.9	256.7	8.4	9.7	0.041
10 ⁶	2800	0.032	2	512 × 193 × 384	183.2	261.1	8.6	9.8	0.040
10 ⁶	2800	0.032	1	512 × 193 × 384	186.8	261.4	9.1	9.6	0.037
10 ⁶	2800	0.032	0.5	512 × 193 × 384	198.9	266.2	10.5	10.0	0.032
10 ⁷	0	∞	∞	1024 × 257 × 512	-	237.2	-	15.7	∞
10 ⁷	0	∞	4	1024 × 257 × 512	-	236.9	-	16.0	∞
10 ⁷	0	∞	2	1024 × 257 × 512	-	236.7	-	16.3	∞
10 ⁷	0	∞	1	1024 × 257 × 512	-	238.9	-	16.9	∞
10 ⁷	0	∞	0.5	1024 × 257 × 512	-	245.7	-	18.4	∞
10 ⁷	500	10.0	∞	1024 × 257 × 512	71.0	250.0	40.3	13.9	9.743
10 ⁷	500	10.0	4	1024 × 257 × 512	72.1	243.7	41.8	14.2	9.461
10 ⁷	500	10.0	2	1024 × 257 × 512	73.2	239.9	43.2	14.4	9.213
10 ⁷	500	10.0	1	1024 × 257 × 512	77.5	226.9	48.8	15.1	8.122
10 ⁷	500	10.0	0.5	1024 × 257 × 512	83.9	235.7	58.4	17.2	7.275
10 ⁷	885	3.19	∞	1024 × 257 × 512	97.7	263.4	24.4	12.6	3.373
10 ⁷	885	3.19	4	1024 × 257 × 512	99.3	262.5	25.2	12.9	3.300
10 ⁷	885	3.19	2	1024 × 257 × 512	101.0	252.5	26.2	13.1	3.174
10 ⁷	885	3.19	1	1024 × 257 × 512	105.5	240.0	28.9	13.6	2.903
10 ⁷	885	3.19	0	1024 × 257 × 512	111.7	236.1	33.0	15.2	2.729
10 ⁷	1581	1.0	∞	1024 × 257 × 512	134.2	304.1	14.4	11.9	1.231
10 ⁷	1581	1.0	8	1024 × 257 × 512	135.2	300.6	14.7	12.0	1.210
10 ⁷	1581	1.0	4	1024 × 257 × 512	136.7	300.2	15.0	12.1	1.184
10 ⁷	1581	1.0	2	1024 × 257 × 512	138.9	285.6	15.6	12.2	1.140
10 ⁷	1581	1.0	1	1024 × 257 × 512	143.1	278.5	16.7	12.6	1.072
10 ⁷	1581	1.0	0.5	1024 × 257 × 512	152.5	275.2	19.3	13.9	0.979

Ra	Re_b	Ri_b	S/δ	$N_x \times N_y \times N_z$	Re_τ	Re_k	$C_f(\cdot 10^{-3})$	Nu	$-\delta_{eff}/L$
10^7	2800	0.32	∞	$1024 \times 257 \times 512$	190.4	353.2	9.3	12.3	0.446
10^7	2800	0.32	4	$1024 \times 257 \times 512$	193.9	350.6	9.6	12.7	0.434
10^7	2800	0.32	2	$1024 \times 257 \times 512$	198.1	352.8	10.1	13.1	0.422
10^7	2800	0.32	1	$1024 \times 257 \times 512$	204.9	348.8	10.9	13.8	0.401
10^7	2800	0.32	0.5	$1024 \times 257 \times 512$	216.2	349.8	12.4	15.1	0.373
10^7	5000	0.1	∞	$1024 \times 257 \times 512$	304.5	499.1	7.4	17.1	0.152
10^7	5000	0.1	4	$1024 \times 257 \times 512$	306.4	497.0	7.5	17.3	0.150
10^7	5000	0.1	2	$1024 \times 257 \times 512$	311.4	501.7	7.8	17.7	0.146
10^7	5000	0.1	1	$1024 \times 257 \times 512$	316.9	499.9	8.2	18.2	0.143
10^7	5000	0.1	1	$1024 \times 257 \times 512$	328.9	504.0	8.9	19.3	0.135
10^7	10000	0.025	∞	$1536 \times 513 \times 1024$	552.2	847.6	6.1	28.4	0.042
10^7	10000	0.025	4	$1536 \times 513 \times 1024$	555.0	822.7	6.2	28.1	0.041
10^7	10000	0.025	2	$1536 \times 513 \times 1024$	558.3	841.3	6.3	28.4	0.041
10^7	10000	0.025	1	$1536 \times 513 \times 1024$	570.5	825.5	6.6	28.1	0.038
10^7	10000	0.025	0.5	$1536 \times 513 \times 1024$	585.2	831.9	7.0	27.1	0.034
10^8	2800	3.19	∞	$2048 \times 513 \times 1024$	246.1	749.3	15.5	25.6	4.297
10^8	2800	3.19	4	$2048 \times 513 \times 1024$	249.5	791.9	15.9	26.9	4.327
10^8	2800	3.19	2	$2048 \times 513 \times 1024$	259.3	718.1	17.3	27.6	3.964
10^8	2800	3.19	1	$2048 \times 513 \times 1024$	269.3	695.1	18.7	29.4	3.761
10^8	2800	3.19	0.5	$2048 \times 513 \times 1024$	295.1	710.6	22.8	33.7	3.277

Table 5.1: List of simulation configurations with flow parameters and resulting global flow properties. Adopted from Schäfer et al. (2022a)

"While the skin friction drag increases with decreasing S and increasing wetted surface area, this behaviour is not found for the heat transfer for all present cases. This is illustrated for the two parameter sweeps at constant $Re_b = 2800$ in figure 5.3 (a) and at constant $Ra = 10^7$ in figure 5.3 (b). The forced convection case $Ra = 0$ and weak convective case $Ra = 10^5$ in figure 5.3 (a) show the successive increase of Nu with decreasing ridge spacing S . An increase of Ra or Ri_b introduces an additional buoyant contribution to the vertical mixing, resulting in larger heat transfer and for large Rayleigh numbers ($Ra > 10^6$), which represent configurations where buoyancy is comparable to shear or even stronger, the monotonic increase of Nu with decreasing S is also found. However, for the particular cases $Ra = 7.5 \cdot 10^5$ ($Ri_b = 0.024$) and $Ra = 10^6$ ($Ri_b = 0.032$) heat transfer does not monotonically increase with decreasing S , which is visible in the inset of figure 5.3 (a)." (Schäfer et al. 2022a)

"In figure 5.3 (b) the natural convection case is given by $Re_b = 0$ and the influence of buoyancy is successively reduced by increasing Re_b . The minimum found for Nu is associated with the break-up of the thermal plumes of the Rayleigh-Bénard case, when shear is added, and has been reported for unstable thermal stratification in Poiseuille and Couette flows (Scagliarini et al. 2014, Blass et al. 2020). The non-monotonic behaviour of Nu with decreasing S seen in figure 5.3 (a) also occurs for the largest $Re_b = 10000$ case ($Ri_b = 0.025$), which is in a similar bulk Richardson number range as the former cases. Thus, all cases which depict a non-monotonic behaviour of Nu with respect to S fall within a range of bulk Richardson values $Ri_b = 0.016 - 0.032$, where shear

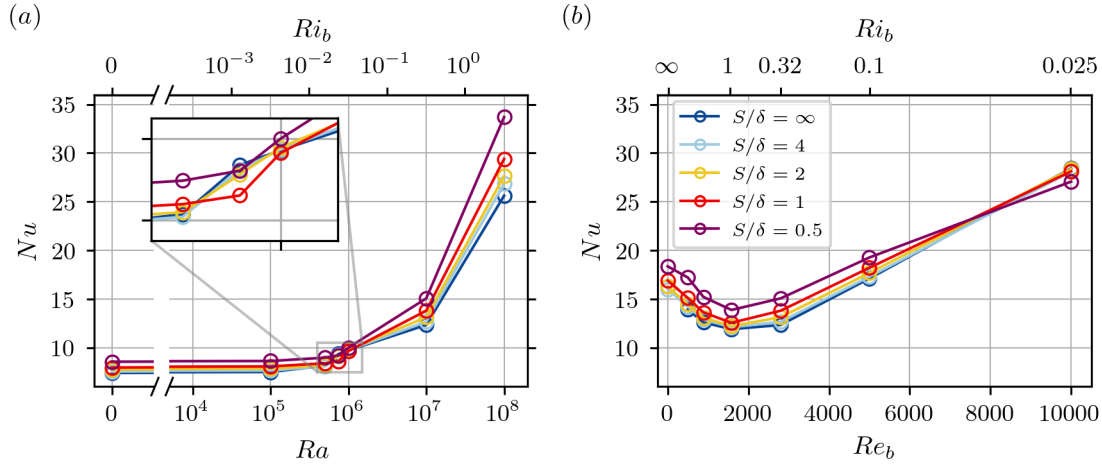


Figure 5.3: Nusselt number Nu as a function of Rayleigh number Ra in (a) and bulk Reynolds number Re_b in (b) for different ridge spacings S . In (a) the bulk Reynolds number $Re_b = 2800$ and in (b) the Rayleigh number $Ra = 10^7$ is kept constant. Adopted from Schäfer et al. (2022a)

effects are strong and buoyancy effects are weak. It will be shown that this range of Richardson numbers marks the transition from forced convection structures to streamwise rolls and the ridge spacing S affects and alters this transition."(Schäfer et al. 2022a)

"In case of mixed convection, turbulence is driven by two generation mechanisms, the production by shear and by buoyancy, and the exact turbulence level cannot be inferred a priori by Ra and Re_b . The same holds for the bulk Richardson number Ri_b . To rule out effects caused by the different turbulence levels or Reynolds number effects, which will be discussed in section 5.2.6 we separate those cases with significantly higher turbulence levels from the cases with comparable values. For the subsequent discussion and sections only cases which fall in a range of Reynolds number values $Re_k = 200 - 355$ are considered. This selection includes only those cases of the two parameter sweeps for which $Ra \leq 10^7$ and $Re_b \leq 2800$. Instead of using the pairs of Ra and Re_b , the bulk Richardson number Ri_b is used in the following to characterise the relative importance of buoyancy and shear effects. In analogy to $Ri_b = Ra/(4Re_b^2Pr)$, Nu is replaced by the Stanton number $St = Nu/(Re_bPr)$. The corresponding results are presented in figure 5.4 (a) and reveal an increase of St with Ri_b ."(Schäfer et al. 2022a)

"The relative increase between heat and momentum transfer is characterised by the ratio St/C_f which is shown in figure 5.4 (b). For each S it can be seen that larger values of Ri_b induce larger St/C_f values. This implies that buoyancy effects lead to a larger increase of heat transfer than of momentum transfer. In addition, a consistent influence of the ridges can be observed in this representation. A decrease of S results in less St/C_f for all Ri_b . This is also reflected in the stability parameter $-\delta_{eff}/L$ in table 5.1, which is another quantity to compare the relative heat and momentum transfer. The most distinct property of figure 5.4 (b) is the strong increase of St/C_f in the range $Ri_b = 0.016 - 0.032$. This increase is delayed to larger Ri_b with decreasing S and can be linked to a reorganisation of the turbulent flow structures as discussed in the following section."(Schäfer et al. 2022a)

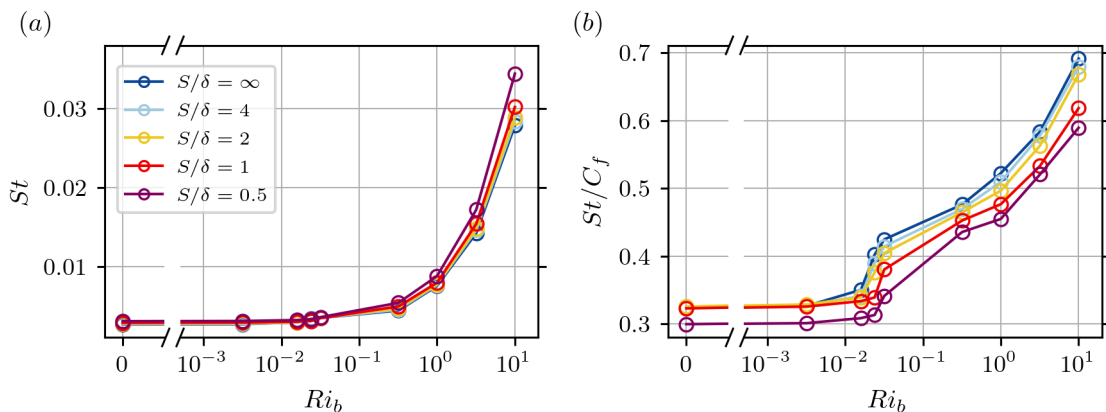


Figure 5.4: Stanton number St in (a) and ratio of St to C_f in (b) as a function of bulk Richardson number Ri_b for different ridge spacings S . The selected cases have values of the Reynolds number Re_k in a similar range. Adopted from Schäfer et al. (2022a)

5.2.2 Instantaneous flow fields

"The different flow organisation of mixed convection flows observed over smooth-wall conditions can be visualised by instantaneous velocity or temperature fluctuations in horizontal planes (Salesky et al. 2017). The influence of heterogeneous surfaces on this flow organisation is shown for various pairs of Ri_b and S for the instantaneous temperature fluctuations in wall-parallel planes located at the half-channel height ($y = \delta$) in figure 5.5 and slightly above the top of the ridges ($y = 0.15\delta$) in figure 5.6. Please note that the discussion for the near-wall region refers to the bottom wall, unless stated otherwise. Both horizontal planes display the same instantaneous realisation of the flow field and comprise cases that fall in a similar range of turbulent Reynolds number Re_k . The Ri_b increases from top to bottom, starting with the forced convection case $Ri_b = 0$ ($Re_b = 2800$, $Ra = 0$) at the top and the natural convection case $Ri_b = \infty$ ($Re_b = 0$, $Ra = 10^7$) at the bottom panel. The ridge spacing S/δ decreases from left to right, with the smooth-wall case at the outer left panel side."(Schäfer et al. 2022a)

"Considering the smooth-wall cases $S = \infty$ first, the flow topology of the forced convection case has a spotty organisation which is also the case for the mild convective case $Ri_b = 0.003$ ($Re_b = 2800$, $Ra = 10^5$) in figure 5.5. The transition to streamwise rolls takes place for slightly larger buoyant forcing at case $Ri_b = 0.016$ ($Re_b = 2800$, $Ra = 5 \cdot 10^5$), but the rolls still display some patchiness. This transition also results in a change of the near-wall structures as can be seen in figure 5.6, where strong elongated temperature fluctuations preferentially locate in regions of the streamwise roll updrafts, while less pronounced in the downdraft region. These elongated temperature fluctuations coincide with the near-wall low-speed streaks (not shown here), since for neutral and moderately convective cases the temperature behaves like a passive scalar with strong correlation with the streamwise velocity (Khanna and Brasseur 1998). The formation mechanism of streamwise rolls is strongly linked to localised buoyancy forces, which concentrate in low-speed streaks and thereby create linear updrafts (Khanna and Brasseur 1998). Multiple updrafts can merge to a strong buoyancy-enhanced streak, forming the updraft region of the streamwise roll in figure 5.5. This updraft is reaching the opposing wall and reduces or destroys the coherence of the

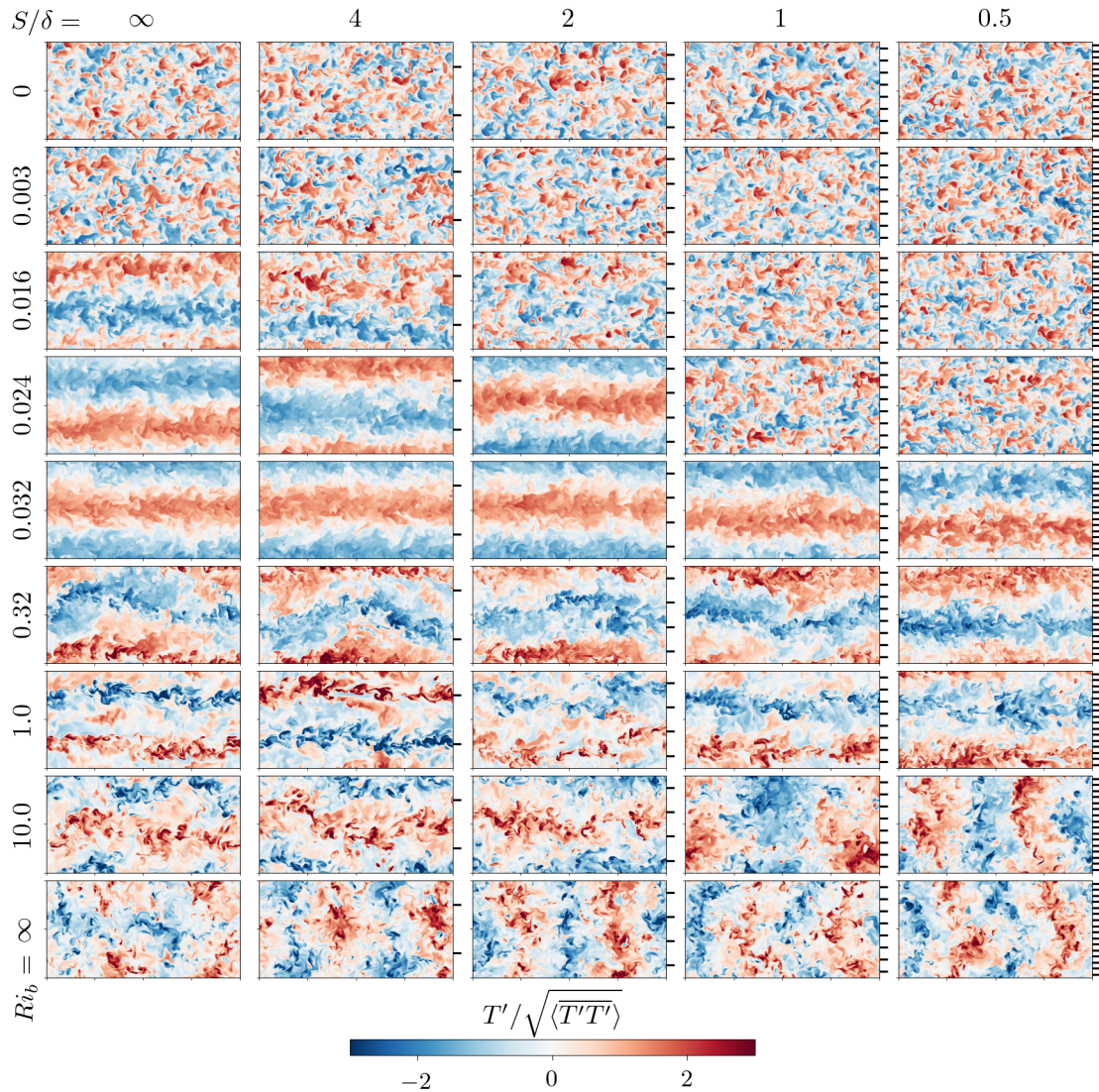


Figure 5.5: Instantaneous temperature fluctuation fields at the half-channel height position $y = \delta$ for varying Richardson number Ri_b and different spanwise spacing S of the Gaussian ridges. The spanwise position of the ridges is indicated by the black lines on the right outer frame of the figures. The horizontal sections show the full simulation domain of size $16\delta \times 8\delta$. Adopted from Schäfer et al. (2022a)

low-speed streaks there. At the same time, between these impingement region of the updrafts at the opposite wall, buoyancy-enhanced low-speed streaks can form, which in turn generate a strong localised downdraft and in combination with the updrafts result in a large-scale streamwise roll motion in the cross-section."(Schäfer et al. 2022a)

"In contrast to case $Ri_b = 0.016$, the streamwise roll of case $Ri_b = 0.024$ in figure 5.5 is more articulated in its structure, which is associated with a sudden increase of St/C_f in figure 5.4 (b). The streamwise rolls persist up to $Ri_b = 1$ in figure 5.5 with a spanwise wavelength of approximately 8δ , such that the chosen domain size is able to accommodate a single pair of counter-rotating rolls as reported by Pirozzoli et al. (2017). For the cases $Ri_b = 0.32$ and $Ri_b = 10$ in figure 5.5 the rolls show a strong waviness of the thermal up- and downdrafts, which is also seen

in the near-wall region where the updraft region encompasses spanwise inclined near-wall streaks in figure 5.6. When buoyancy forces become more important, the streamwise roll is more disrupted and reduce its streamwise coherence, since thermal plumes become dynamically more important (see case $Ri_b = 10$ in figure 5.5) (Salesky et al. 2017). The increased influence of buoyancy also modifies the near-wall structures, where cell-like structures appear in the updraft region, which still depict some streamwise coherence, as seen in figure 5.6. For the Rayleigh-Bénard case $Ri_b = \infty$ ($Re_b = 0$, $Ra = 10^7$) in figure 5.5, the streamwise roll is not present any more and the flow organises in convective cells. These structures have a preferential roll orientation in the x - and z -direction, also seen in the near-wall region in figure 5.6, which is due to the rectangular domain size (Pirozzoli et al. 2017)."(Schäfer et al. 2022a)

"The introduction of the ridges displays no significant differences of the flow structures in the channel centre for the forced convection case $Ri_b = 0$ and weak buoyancy case $Ri_b = 0.003$ compared to the smooth-wall case. However, the elongated high temperature fluctuations in the near-wall region are more coherent in the streamwise direction in case of ridge spacings $S = \delta, 2\delta, 4\delta$, for which they preferentially occur at the spanwise ridge position. For mild buoyancy effects, these elongated temperature regions collapse with low-speed streaks (not shown here), forming low-momentum pathways directly above the ridges. As such the preferential position of the low-speed streaks coincides with the mean upward motion of the secondary motions, which will be shown in section 5.2.3. For the densest ridge spacing $S = 0.5\delta$ these elongated structures still occur at the ridges, however they appear less coherent in the streamwise direction."(Schäfer et al. 2022a)

"Significant effects of the ridges can be seen for the transition between forced convection structures and streamwise rolls in figure 5.5 for cases $Ri_b = 0.016 - 0.032$. As shown before, the transition towards streamwise rolls for smooth-wall conditions takes place at $Ri_b = 0.016$ and this transition can be also observed for the coarsest ridge spacing $S = 4\delta$, which however is more interrupted by individual turbulent spots than the smooth-wall case. This is also reflected in a change of the near-wall structures, where for case $S = 4\delta$ the elongated high temperature fluctuations still favour the updraft region, but in contrast to the smooth-wall case, also occur inside the downdraft region at the ridge position (figure 5.6). For denser ridge spacing $S < 4\delta$ the preferred concentration of low-speed streaks is not observed anymore. Therefore the streamwise roll is not visible in the channel core and the flow structures resemble those seen for the forced convection and weak buoyancy cases $Ri_b = 0.003$. For slightly larger bulk Richardson number $Ri_b = 0.024$ the streamwise roll is now clearly visible for the two coarsest ridge spacings $S = 4\delta$ and $S = 2\delta$ in figure 5.5, and strong enough to reorganise the near-wall structures seen in figure 5.6, while for the denser ridge spacings the streamwise roll is not present. Eventually, the streamwise roll is observed for all ridge spacings S at $Ri_b = 0.032$, while for the denser ridge spacings still some spot-like structures overlap with the rolls. Considering figure 5.4 (b) the delayed transition between forced convection structures and streamwise rolls with decreasing S can be related to the increased drag introduced by the ridges. Denser ridge spacings introduce more drag and shear in the near-wall region, and in consequence larger buoyancy forces are required to form the streamwise rolls which in turn induce an increase in heat transfer."(Schäfer et al. 2022a)

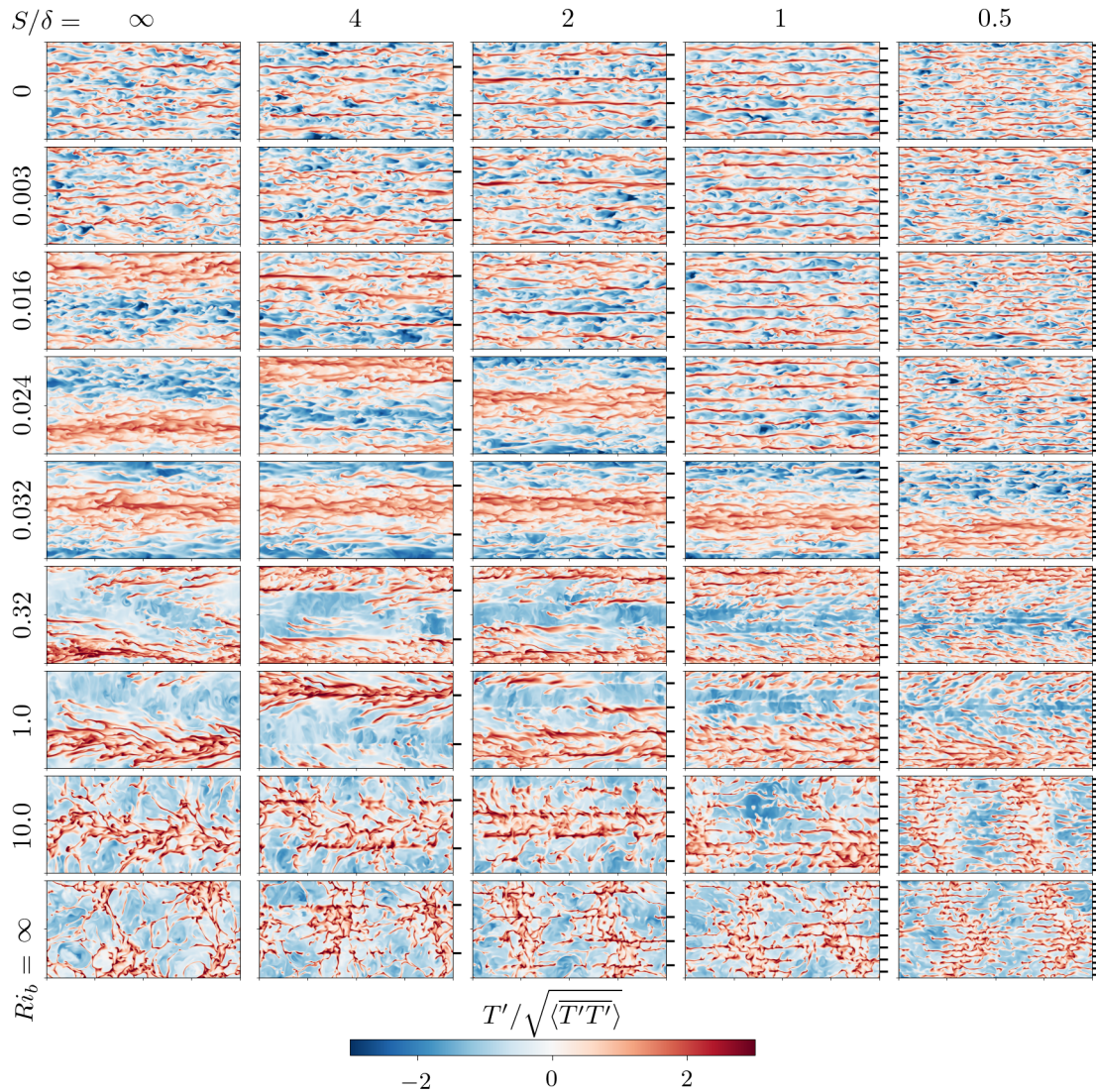


Figure 5.6: Instantaneous temperature fluctuation fields at $y = 0.15\delta$ for varying Richardson number Ri_b and different spanwise spacing S of the Gaussian ridges. Adopted from Schäfer et al. (2022a)

"The streamwise roll, present for the intermediate Richardson number $Ri_b = 0.32$ and $Ri_b = 1.0$ cases (figure 4.6), displays no significant influence of the ridges. This is likewise the case for the near-wall region in figure 5.6, where it can be seen that the formation of high temperature fluctuations occur inside the updraft region of the roll."(Schäfer et al. 2022a)

"At higher convective conditions for $Ri_b = 10.0$ the streamwise roll is present for the smooth-wall case and the two coarsest ridge spacing $S = 2\delta, 4\delta$, while it completely disappears for denser ridge spacings $S \leq \delta$. For $S = \delta$ the streamwise roll is replaced by convection cells, resembling the one found for the Rayleigh-Bénard case with a spacing of $S = 4\delta$. For the densest ridge spacing $S = 0.5\delta$ rolls with a preferential orientation in the spanwise direction occur, which has similarities to the densest ridge spacing $S = 0.5\delta$ of the Rayleigh-Bénard case. This transition from roll to cell structures is also reflected in a transition of the nearwall structures in figure 5.6. The roll-to-cell transition is also observed for the lower bulk Richardson case $Ri_b = 3.2$ (higher Re_k) for the same

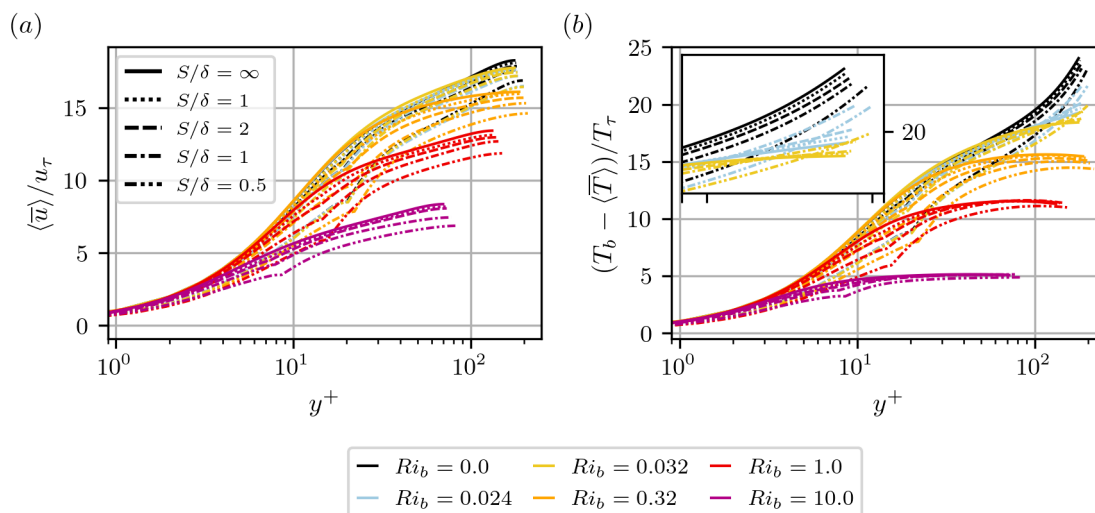


Figure 5.7: Effect of Richardson number Ri_b and S on wall-normal profiles of streamwise mean velocity and mean temperature for different ridge spacings S scaled in wall units. Adopted from Schäfer et al. (2022a)

ridge spacings S (not shown). This result is remarkable, since the transition between roll to cell structures over homogeneous wall conditions in atmospheric boundary layer is expected to begin at larger values of the stability parameter $-z_i/L \approx 26$ (Salesky et al. 2017), while the stability parameter for the cases $Ri_b = 3.2$ and $Ri_b = 10.0$ are ranging between $-\delta_{eff}/L = 3.4 - 9.7$. This illustrates that streamwise-aligned ridges reduce significantly the range of Ri_b or $-\delta_{eff}/L$ in which streamwise rolls appear. This suggest, that heterogeneous rough surfaces can trigger the roll-to-cell transition at smaller buoyancy forces."(Schäfer et al. 2022a)

"As can be seen for the Rayleigh-Bénard case $Ri_b = \infty$ in figure 5.5 decreasing the ridge spacings S results in an increasingly preferential orientation of the convective cell towards the spanwise direction z . The rolls with orientation in the x -direction experience increasing lateral drag as S decreases, and for $S \leq 2\delta$ these rolls can eventually no longer emerge and only rolls in the z -direction whose circulation is along the ridge direction occur. This observation will be discussed further in section 5.2.4. The increase of Nu for smaller S is also reflected by intensified thermal up- and downdrafts in the channel centre plane. We note that additional simulations for $S = \infty$ and $S = 0.5\delta$ in a wider domain ($L_x = L_z = 16\delta$) do not indicate a domain size dependence of the obtained results."(Schäfer et al. 2022a)

5.2.3 Mean flow properties

"The effect of ridge spacing S and the relative strength of shear and buoyancy effects on the time and horizontally averaged mean streamwise velocity and temperature profiles are shown in figure 5.7. The mean temperature is represented as the difference from the bottom wall temperature T_b and scaled by the friction temperature $T_\tau = Q/\rho c_p u_\tau$. Starting from forced convection, the trend of the mean profiles to become flatter with increasing Ri_b is consistent with the results of Pirozzoli et al. (2017). The logarithmic region of $\langle \bar{u} \rangle$ found for weak convective condition starts to deviate at $Ri_b = 0.032$. The reduction of the spanwise ridge spacing S leads to a decrease of the mean

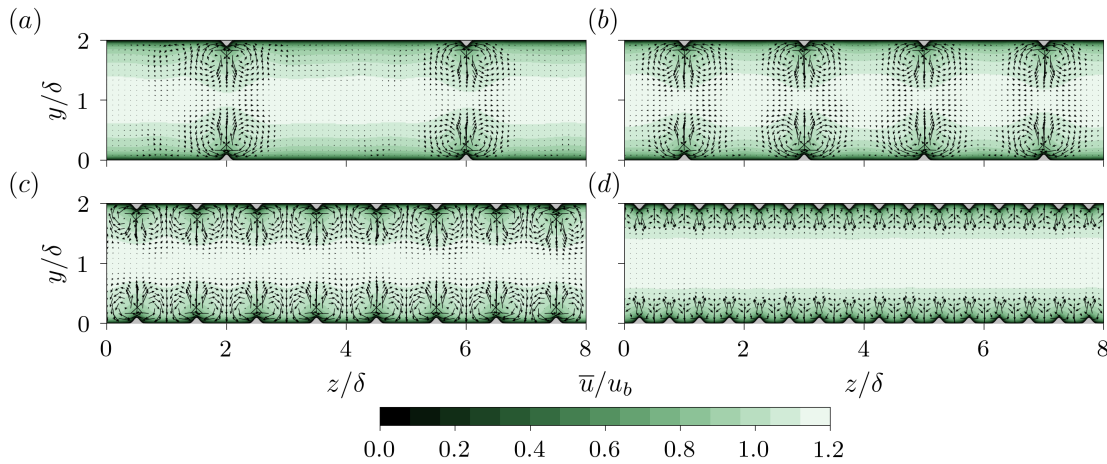


Figure 5.8: Effect of spanwise spacing on mean streamwise velocity for forced convection case $Ri_b = 0$ ($Re_b = 2800$, $Ra = 0$). The spanwise spacing of the Gaussian ridges ranges from $S = 4\delta$ (a), $S = 2\delta$ (b), $S = \delta$ (c) and $S = 0.5\delta$ (d). Arrows indicate cross-sectional velocity components and are scaled by bulk velocity. Adopted from Schäfer et al. (2022a)

streamwise velocity and temperature profile, which is in agreement with increased surface drag (see table 5.1 and figure 5.4 (b)). However, temperature profiles within the transition range from forced convection structures to streamwise rolls show deviations from this behaviour close to the channel core, which is highlighted by the inset of figure 5.7 (b). In this, it can be seen for $Ri_b = 0.024$ and $Ri_b = 0.032$ that the temperature takes larger values with decreasing S in the channel centre and at the same time the slope of the temperature increases. This indicates that the thermal mixing of the flow is increasingly weakened by the ridges. The transition from streamwise rolls to spot-like structures for case $Ri_b = 0.024$ can be also inferred from the similar slope of $S = \delta$ and $S = 0.5\delta$ to the one of the forced convection cases. Interestingly, for case $Ri_b = 0.032$, where all S feature streamwise rolls, the slope of the temperature profile for $S = 0.5\delta$ also resembles the one of the forced convection cases, which indicates that the transition point is already close. As can be seen, the influence and effects of the ridge spacing S is of the same order as a change of the bulk Richardson number Ri_b ." (Schäfer et al. 2022a)

"The occurrence of secondary motions over streamwise-aligned ridges in forced convection flows is observed in time- and streamwise-averaged velocity fields in the channel cross-section, which is shown for case $Ri_b = 0$ in figure 5.8. The relative strength of the coherent motion among the different ridge spacings can be directly compared, due to the same scaling of the cross-sectional velocity components in bulk units. The smooth channel flow exhibits no coherent motion in the cross-section (not shown here), while for streamwise-aligned ridges the secondary motions appear in the mean flow field as counter-rotating vortices at each ridge in figure 5.8. These vortices introduce an upward motion above each ridge and a downward motion is located to the side of each ridge. As can be seen the secondary motion induces a bulging of the mean streamwise velocity above the ridge, transporting low momentum into the bulk region, and for large spacings $S = 4\delta$ and $S = 2\delta$ reaching almost the half-channel height. The spacing between the ridges of case $S = 4\delta$ in figure 5.8 (a) is large enough, so that a homogeneous region unaffected by the secondary motion can form between the ridges. Decreasing the spanwise spacing S , the secondary motions

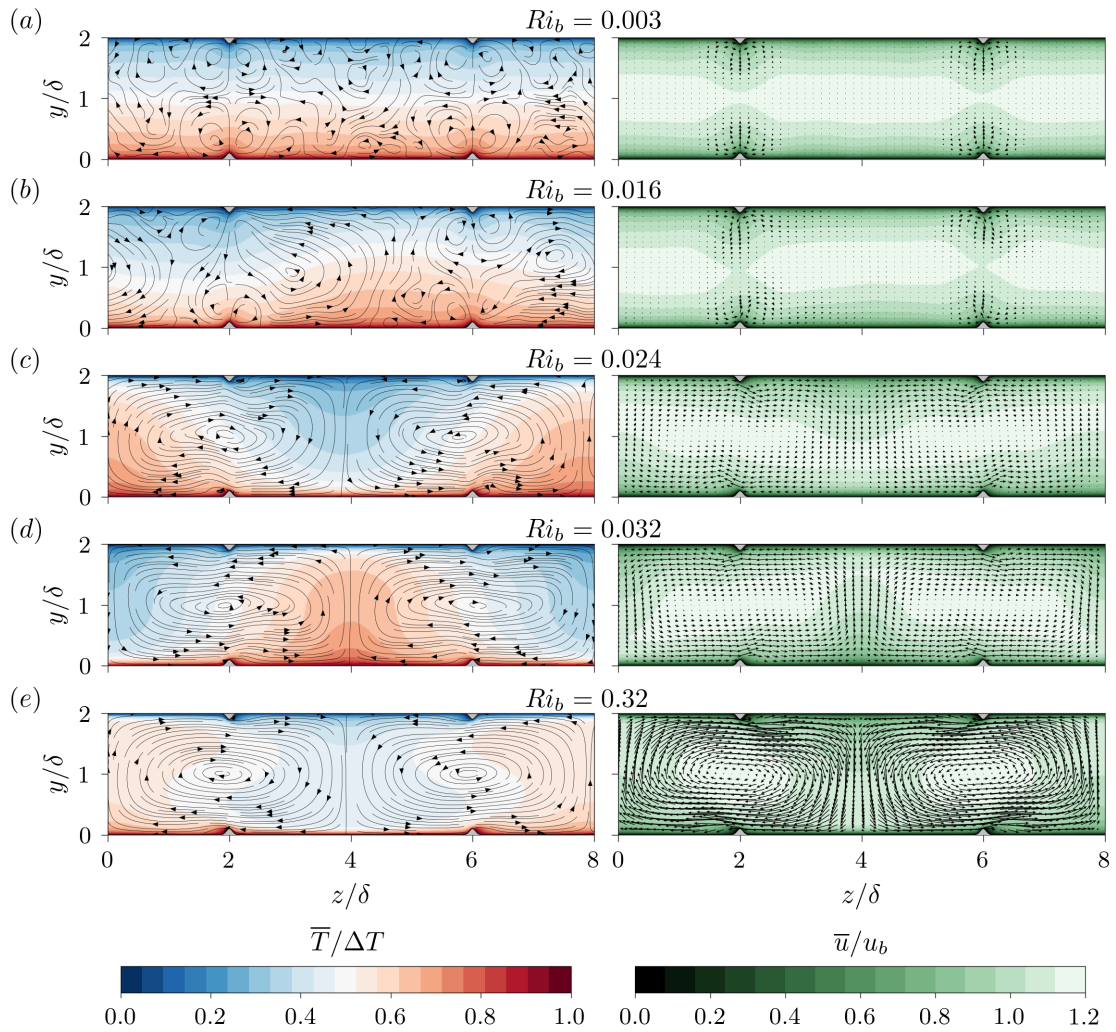


Figure 5.9: Effect of buoyancy on streamwise mean velocity and temperature for constant $Re_b = 2800$ and $S = 4\delta$ for different Richardson numbers. Arrows indicate cross-sectional velocity components and are scaled by bulk velocity. Adopted from Schäfer et al. (2022a)

fill almost the entire channel domain for case $S = 2\delta$ (figure 5.8 (b)) and case $S = \delta$ (figure 5.8 (c)). However, for case $S = \delta$ the wall-normal extent of the secondary motions is slightly reduced compare to case $S = 2\delta$, which indicates that the secondary motions of adjacent ridges affect each other at a spacing of $S = \delta$. Further decrease of the ridge spacing to $S = 0.5\delta$ (figure 5.8 (d)) shows a significant reduction of the spatial extent of the secondary motion in the wall-normal direction."(Schäfer et al. 2022a)

"The investigation of the horizontal fields of the instantaneous temperature have shown that the transition of the flow topology for smooth-wall conditions is affected by the introduction of the streamwise-aligned ridges. This reorganisation is also reflected in the mean streamwise velocity and temperature field in the cross-section, which is shown in figure 5.9 for the transition from forced convection structures to streamwise rolls at a ridge spacing of $S = 4\delta$. The strength of the cross-sectional velocity components are represented by the arrows in the mean streamwise velocity field, while their flow topology is visualised by streamlines in the mean temperature field. The

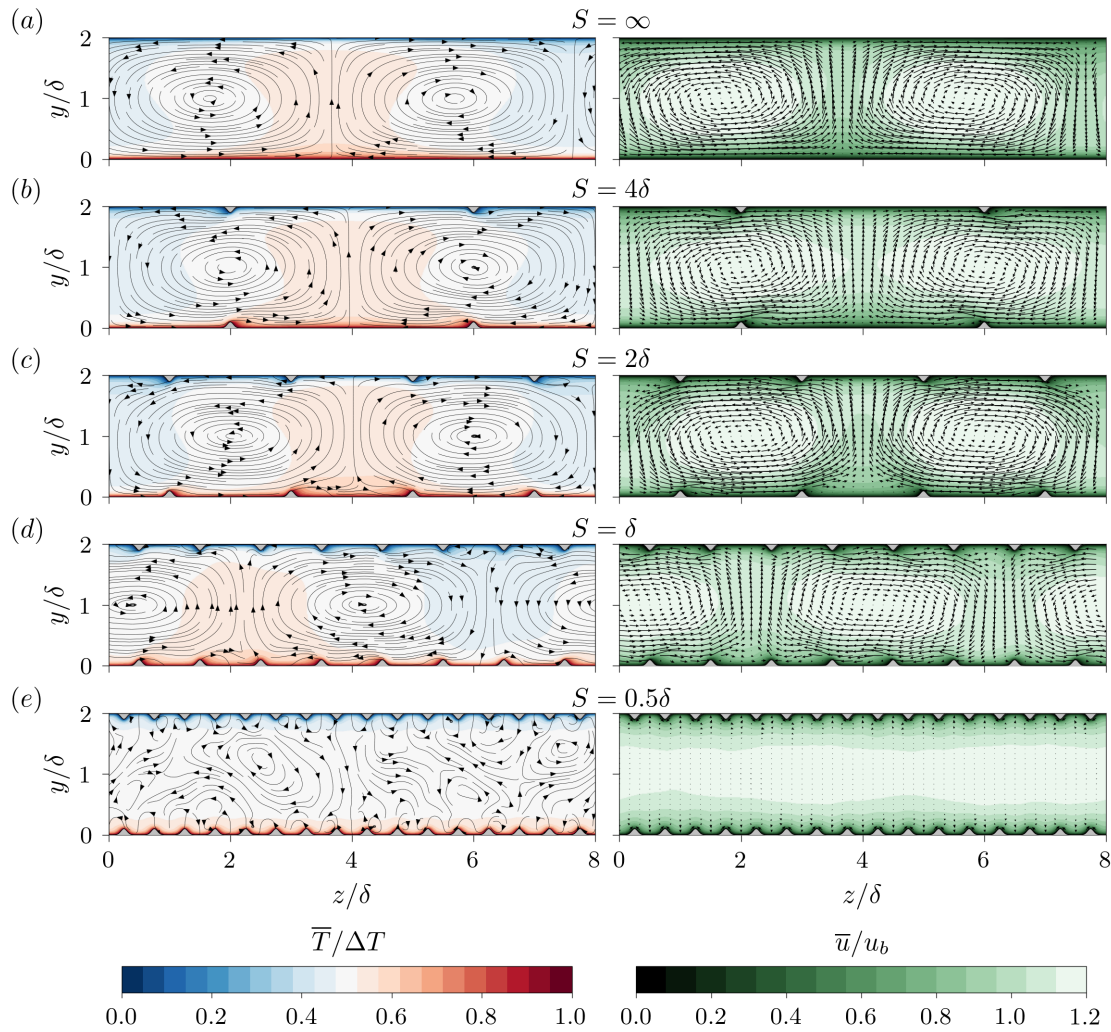


Figure 5.10: Effect of ridge spacing S on streamwise mean velocity and temperature for constant $Ri_b = 10$. Adopted from Schäfer et al. (2022a)

weak buoyancy case $Ri_b = 0.003$ is shown in figure 5.9 (a) and similar as the forced convection case in figure 5.8 secondary motions are present in the mean velocity field which also leads to a bulging of the mean temperature at the ridges."(Schäfer et al. 2022a)

"The transition towards streamwise rolls has been seen to occur for smooth-wall conditions at $Ri_b = 0.016$, while for $S = 4\delta$ a slight tendency towards rolls was present. Figure 5.9 (b) shows that secondary motions can still occur at the ridges, though two diminished roll structures emerge that extend to the opposite wall. This in turn replaces the local bulging of the mean temperature at the ridge by a significant wider bulging of the mean temperature. As Ri_b increases to $Ri_b = 0.024$ the secondary motions are replaced by streamwise roll. The upward and downward motion of the convective rolls is located in the valley between two Gaussian ridges and each roll has a spanwise extent of four half-channel heights. As can be seen in the streamwise mean velocity field, the rolls induce stronger cross-sectional velocity in the entire channel, which introduces a recirculation zone at the leeward side of the Gaussian ridges. The cross-sectional velocities of the streamwise roll

further intensify as Ri_b increases, as can be seen for case $Ri_b = 0.32$ in figure 5.9 (e)."(Schäfer et al. 2022a)

"Figure 5.10 shows the effect of S on the mean temperature and mean streamwise velocity for case $Ri_b = 10$, which features the transition between streamwise rolls and convective cells. The bulging of \bar{T} and \bar{u} due to the streamwise roll is found for smooth-wall conditions and $S \geq \delta$, while this is not found for the densest ridge spacing $S = 0.5\delta$. For the latter case this reflects the transition from streamwise rolls to convective cells with preferential orientation in z -direction found in the instantaneous temperature fields in figure 5.5 and 5.6, which results in the disappearance of the cross-sectional motion in figure 5.10 (e). The up- and downdrafts of the streamwise rolls for $S = 4\delta$ and $S = 2\delta$ are located in the valleys between adjacent ridges. For the former case the lateral movement of the roll encounters the ridge in the middle between up- and downdrafts, where large spanwise velocities of the roll occur. The ridges close to the up- and downdrafts for case $S = 2\delta$ support the wall-normal motion of the roll by the upward deflection at the ridges, which results in stronger bulging of \bar{u} at the up- and downdraft region compared to $S = 4\delta$. As can be seen for case of $S = \delta$ in figure 5.10 (d) the strength of the cross-sectional motion is reduced compared to the coarser S cases, since the roll experience more lateral drag by crossing the ridges due to decreasing S ."(Schäfer et al. 2022a)

5.2.4 Turbulent properties

"The mean velocity and temperature fields presented in the previous section have shown that secondary motions and streamwise rolls manifest as large-scale coherent motion in the cross-sectional plane. The energetics of these structures is further analysed by applying the decomposition procedures of equations 2.38 and 4.5 to the turbulent kinetic energy $k = 0.5 \cdot \overline{u'_i u'_i}$. This separates the turbulent kinetic energy k into its coherent contribution \tilde{k} and random contribution k'' given by $k = \tilde{k} + k''$. In order to extract the influence of the cross-sectional motion, the coherent turbulent kinetic energy \tilde{k} is decomposed into its cross-sectional $\tilde{k}_c = 0.5 \cdot (\tilde{v}\tilde{v} + \tilde{w}\tilde{w})$ and streamwise part $\tilde{k}_s = 0.5 \cdot \tilde{u}\tilde{u}$. Since the global mean velocity components $\langle \tilde{v} \rangle$ and $\langle \tilde{w} \rangle$ are zero, the coherent components \tilde{v} and \tilde{w} represent the mean velocity motion in the cross-sectional plane (seen for instance in figure 5.9). The coherence of the large-scale motion is quantified by K_c , which is the volume average of the coherent turbulent kinetic energy of the cross-sectional components \tilde{k}_c [...]. While K_c is a good measure of coherence for the majority of cases considered here, it will be shown later that there are two cases for which K_c is not a useful measure. The first case applies when the coherent motion involves strong temporal dynamics leading to a reduction of the coherent velocities \tilde{v} and \tilde{w} by long time averages. The second case concerns any coherent motion in the x - y plane, so that this coherence is masked in the random velocity variance contribution."(Schäfer et al. 2022a)

"The influence of the transition between forced convection structures and streamwise rolls on K_c is illustrated in figure 5.11 (a). As can be seen the forced convection case $Ri_b = 0$ and weakly convective case $Ri_b = 0.003$ for smooth-wall conditions display no coherent energy in the cross-sectional components due to the missing presence of coherent motion. However, the

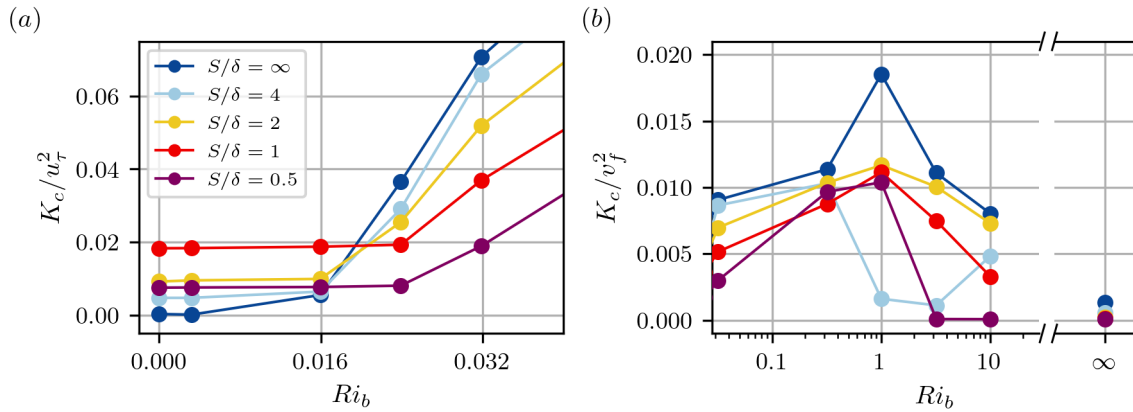


Figure 5.11: Volume-averaged coherent turbulent kinetic energy of the cross-sectional components for low Ri_b cases scaled in wall-units in (a) and for large Ri_b cases scaled in free-fall units in (b). Adopted from Schäfer et al. (2022a)

introduction of the Gaussian ridges and the appearance of secondary motions results in a coherent kinetic energy contribution K_c with the highest value for a ridge spacing of $S = \delta$, consistent with recent studies (Medjnoun et al. 2020, Wangsawijaya et al. 2020). At $Ri_b = 0.016$ the streamwise rolls emerge for the smooth-wall case, which is reflected by an increase of K_c . This increase induced by the streamwise rolls is eventually also present for ridge spacings $S = 4\delta$ and $S = 2\delta$ for case $Ri_b = 0.024$. As shown in the previous sections, the two densest ridge spacing cases display secondary motions at higher Ri_b , which leads to an unchanged and constant value of K_c up to $Ri_b = 0.024$ for $S = \delta$ and $S = 0.5\delta$. This behaviour is consistent with the observation of the delayed increase in Nu with increasing Ra for these two cases in figure 5.3 (a), illustrating the importance of the flow structures on the scaling of global quantities. Due to the presence of streamwise rolls for all cases at $Ri_b = 0.032$, K_c also increases for all S , whose values almost double compared to $Ri_b = 0.024$."(Schäfer et al. 2022a)

"The change of coherence due to the transition between streamwise rolls and convective cells with increasing Ri_b is shown in figure 5.11 (b). For this range of values Ri_b , K_c is scaled in free-fall units, which ease the comparison with the natural convection case $Ri_b = \infty$. For the smooth-wall condition the coherence increases up to $Ri_b = 1$ and subsequently decreases to the natural convection case. This maximum of K_c occurs for a value of $-\delta_{eff}/L = 1.23$, which is consistent with recent findings in ABL, for which the maximum coherence of streamwise rolls are found at $-z_i/L = 1.08$ (Jayaraman and Brasseur 2021). For the rough-wall cases the coherence decreases monotonically with decreasing S only for $Ri_b = 0.032$ and $Ri_b = \infty$, while this behaviour is not found for values in between. Comparing to the smooth-wall cases the introduction of coarsely spaced ridges $S = 4\delta$ yield a large drop of K_c for $Ri_b = 1$ and $Ri_b = 3.2$. The reason for this reduction is the aforementioned temporal variability of the streamwise rolls, which causes the up- and downdrafts to slowly move in the spanwise direction over a long period of time instead of being fixed, thereby reducing averaged values of \tilde{v} and \tilde{w} and thus K_c . This will be discussed in more detail in the following section 5.2.5."(Schäfer et al. 2022a)

"For $Ri_b = 10$ the value of K_c for $S = 4\delta$ is below $S = 2\delta$, indicating that the coherence of the streamwise roll is more affected by the coarser ridge spacing. In this case the reduction of K_c is not related to time variability of the streamwise rolls, but to the relative position of the ridges to the up- and downdrafts. As can be seen in figure 5.10 the up- and downdrafts for $Ri_b = 10$ occur between the ridges, which for $S = 4\delta$ results in the roll encountering a ridge in the middle of its lateral motion, which causes stronger lateral drag and thereby weaken the roll motion. For $S = 2\delta$, the ridges do not interfere the roll motion at their strongest lateral velocity. Instead, the adjacent ridges at the up- and downdrafts support the upward motion of the roll by its wall-normal deflection at the ridges. Even though denser ridge spacings contribute to more drag, the support of the deflections compensate a part of the losses in K_c for $S = 2\delta$, while this does not occur for $S = 4\delta$."(Schäfer et al. 2022a)

"For $Ri_b = 3.2$ and $Ri_b = 10$ the value of K_c vanishes for the densest ridge spacing $S = 0.5\delta$, which reflects that streamwise rolls are not present for these cases as can be seen in the instantaneous temperature fields in figure 5.5. Also for the natural convection case the value of K_c approaches zero for $S \leq 2\delta$, even though the instantaneous temperature fields in figure 5.5 suggest an increase of the coherence in the x -direction due to rolls aligned in the z -direction. This reflects the property of K_c that only coherent motion in the z -direction can be detected, while any coherence in the x -direction is masked. Consequently, for the current ridge cases, a reduction of S leads to a weakening of the coherence in z -direction, which is equivalent to a weakening of rolls with orientation in x -direction. Note, that for a further reduction of S down to the limit of $S \rightarrow 0$ the surface will approach a smooth wall again with a reduced cross-sectional area. Since Re_b and Ra are kept constant while varying S we expect the flow for $S \rightarrow 0$ to be similar to the present smooth-wall case $S = \infty$."(Schäfer et al. 2022a)

"The strength of the different large-scale coherent motion is associated with different wallnormal regions, where coherence is dominant. This is shown for the transition between the forced convection structures and streamwise rolls for the horizontally averaged velocity stresses and temperature variance in figure 5.12 for three different Ri_b cases. The dashed line represents the Reynolds stresses (e.g. $\langle \overline{u'u'} \rangle$), while the solid line indicates the coherent stress (e.g. $\langle \tilde{u}\tilde{u} \rangle$). The difference of both contributions results in the random stress, e.g. $\langle \overline{u''u''} \rangle = \langle \overline{u'u'} \rangle - \langle \tilde{u}\tilde{u} \rangle$. For the forced convection case $Ri_b = 0$ and rough-wall condition the coherent streamwise stress $\langle \tilde{u}\tilde{u} \rangle$ is concentrated close to the wall, with increasing peak values with decreasing S down to $S = \delta$. The densest ridge spacing $S = 0.5\delta$ has a similar peak value as $S = \delta$, however extending less into the bulk region, consistent with the reduced spatial extent of the mean secondary motions for this ridge spacing seen in figure 5.8. This is also reflected by the wall-normal location of the peak values of $\langle \tilde{v}\tilde{v} \rangle$ and $\langle \tilde{w}\tilde{w} \rangle$, which is located closer to the wall for $S = 0.5\delta$. The coherent temperature variance displays a similar trend as $\langle \tilde{u}\tilde{u} \rangle$ with respect to S , since temperature is a passive scalar for this case resulting in a strong correlation between the streamwise velocity and temperature."(Schäfer et al. 2022a)

"As discussed before, streamwise rolls are present for case $Ri_b = 0.024$ and $S = \infty, 4\delta, 2\delta$, which can be seen most clearly by increased values of $\langle \tilde{T}\tilde{T} \rangle$ and $\langle \overline{T'T'} \rangle$ within the entire bulk region in figure 5.12 (k). For these cases the coherent temperature variance $\langle \tilde{T}\tilde{T} \rangle$ contributes for

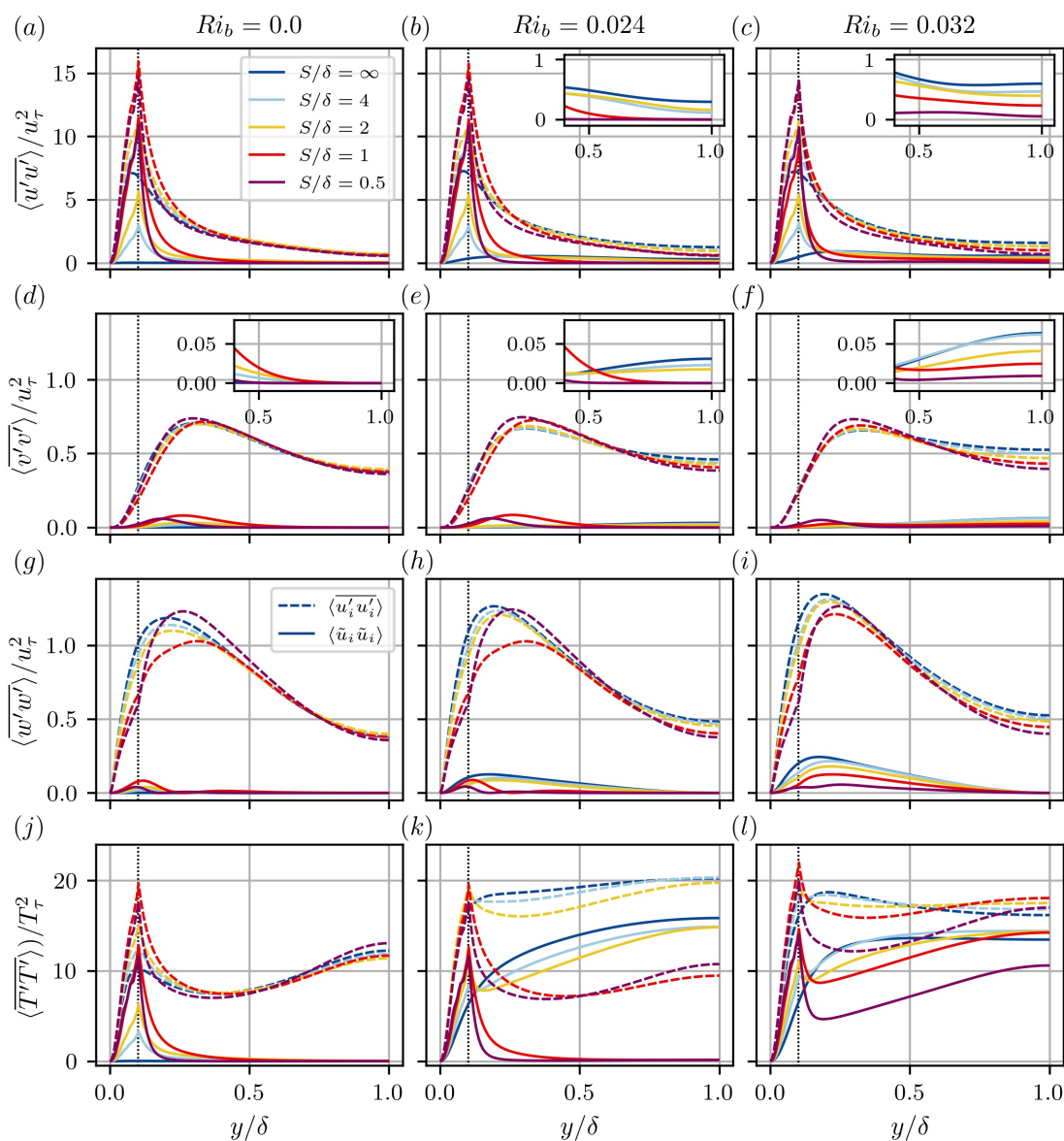


Figure 5.12: Velocity and temperature variances scaled in inner units for low bulk Richardson number Ri_b cases at transition from forced convection structures to streamwise rolls. Black vertical dotted line indicates the height of the Gaussian ridges. Adopted from Schäfer et al. (2022a)

a large fraction of the temperature variance $\langle T'T' \rangle$, which reflects the strong bulging of the mean temperature seen in figure 5.9 (c). The induced coherence by streamwise rolls is also seen in the coherent velocity stresses but less pronounced. Among them this is most noticeable for the spanwise coherent velocity stress $\langle \tilde{w}\tilde{w} \rangle$ in figure 5.12 (h), where stronger spanwise coherent stresses are observed with respect to the forced convection cases (figure 5.12 (g)). A slight increase of $\langle \tilde{u}\tilde{u} \rangle$ and $\langle \tilde{v}\tilde{v} \rangle$ can be also found for these cases in the bulk region, which is illustrated by the figure insets in figure 5.12 (b) and (e). Although the coherent velocity stresses of the streamwise rolls are for this case rather weak, this motion is sufficient to cause a strong imprint in the coherent temperature variance. For the two densest ridge spacings $S = \delta$ and $S = 0.5\delta$ where secondary motions occur, the velocity stresses and temperature variances remain similar to the forced convection cases at

$Ri_b = 0$. This further supports the fact that the increased drag and vertical mixing due to the ridges for these two cases is strong enough to inhibit the formation of streamwise rolls."(Schäfer et al. 2022a)

"For case $Ri_b = 0.032$, when all ridge configurations exhibit streamwise rolls, the two densest ridge spacings S now also show a significant increase in the coherent temperature variance $\langle \tilde{T}\tilde{T} \rangle$, although their values are lower than for the streamwise roll cases of $Ri_b = 0.024$. Likewise, the increase of coherent velocity stresses, which initiated at $Ri_b = 0.024$, continues, which is clearly seen by $\langle \tilde{w}\tilde{w} \rangle$ in figure 5.12 (i). As can be seen the successive reduction of the ridge spacing S results in a decrease of the coherent velocity stresses, indicating that the streamwise rolls are damped by the presence of the ridges. For $S = 0.5\delta$ only a mild increase of $\langle \tilde{u}\tilde{u} \rangle$ and $\langle \tilde{v}\tilde{v} \rangle$ is found in the bulk region (figure 5.12 (c, f)), and the near-wall peak of $\langle \tilde{v}\tilde{v} \rangle$, introduced by the secondary motions, is still visible. The persistence of stronger wall-normal coherent motions near the wall for $S = 0.5\delta$, similar to the forced convection cases, is consistent with the streamwise rolls to appear more spot-like as seen in figure 5.5."(Schäfer et al. 2022a)

"Figure 5.13 shows the velocity stresses and temperature variance for the transition from streamwise rolls to natural convection. For case $Ri_b = 1$ the streamwise roll displays the strongest coherent cross-sectional motion, which is illustrated by larger values of $\langle \tilde{w}\tilde{w} \rangle$ compared to the $\langle \tilde{u}\tilde{u} \rangle$. At the same time the wall-normal Reynolds stresses have comparable magnitude to the streamwise Reynolds stress in the channel centre region. The decrease of coherent velocity stresses with decreasing S is found for the three densest ridge spacings, while case $S = 4\delta$ display significantly lower values due to the time variability of the streamwise rolls. At the same time, the coherent temperature variance in the bulk region increases with decreasing S (inset figure 5.13 (j)) and $\langle \overline{T'T'} \rangle$ exhibits larger values in the near-wall region compared to the smooth-wall case."(Schäfer et al. 2022a)

"As discussed in relation to figure 5.14 the coherence of streamwise rolls is reduced when increasing Ri_b beyond values of $Ri_b \approx 1$, which is reflected by a reduction of the coherent velocity stresses for $Ri_b = 10$. For $Ri_b = 10$ and dense ridge spacings $S = \delta$ and $S = 0.5\delta$ the instantaneous temperature fields in figure 5.5 have shown a transition from the streamwise rolls to convection cells, which is reflected here by significant lower coherent stresses $\langle \tilde{v}\tilde{v} \rangle$ and $\langle \tilde{w}\tilde{w} \rangle$ compared to the smooth-wall case. The increased peak value of $\langle \overline{T'T'} \rangle$ with decreasing S indicates that ridges are more efficient in mixing temperature close to the wall. For the densest ridge spacing $S = 0.5\delta$ the convection cells are oriented along the spanwise direction, which is in agreement with the observation of zero coherent spanwise stresses $\langle \tilde{w}\tilde{w} \rangle$ in figure 5.13 (h)."(Schäfer et al. 2022a)

"The observation that the coherence of convective cells oriented along the x -direction is significantly reduced for $S \leq 2\delta$ is also reflected by the coherent velocity stresses and coherent temperature variance. The coherent contribution of $\langle \tilde{w}\tilde{w} \rangle$ for $S = 4\delta$ is significantly reduced compared to smooth-wall conditions, as can be seen in figure 5.13 (i). The only increase of coherence can be found for $\langle \tilde{T}\tilde{T} \rangle$ in the near-wall region with decreasing S in figure 5.13 (l), while it vanishes in the bulk region for dense spacings. The preferred orientation of the convective cells in the spanwise direction, as seen in figure 5.5, needs to result in larger streamwise motion, which is reflected

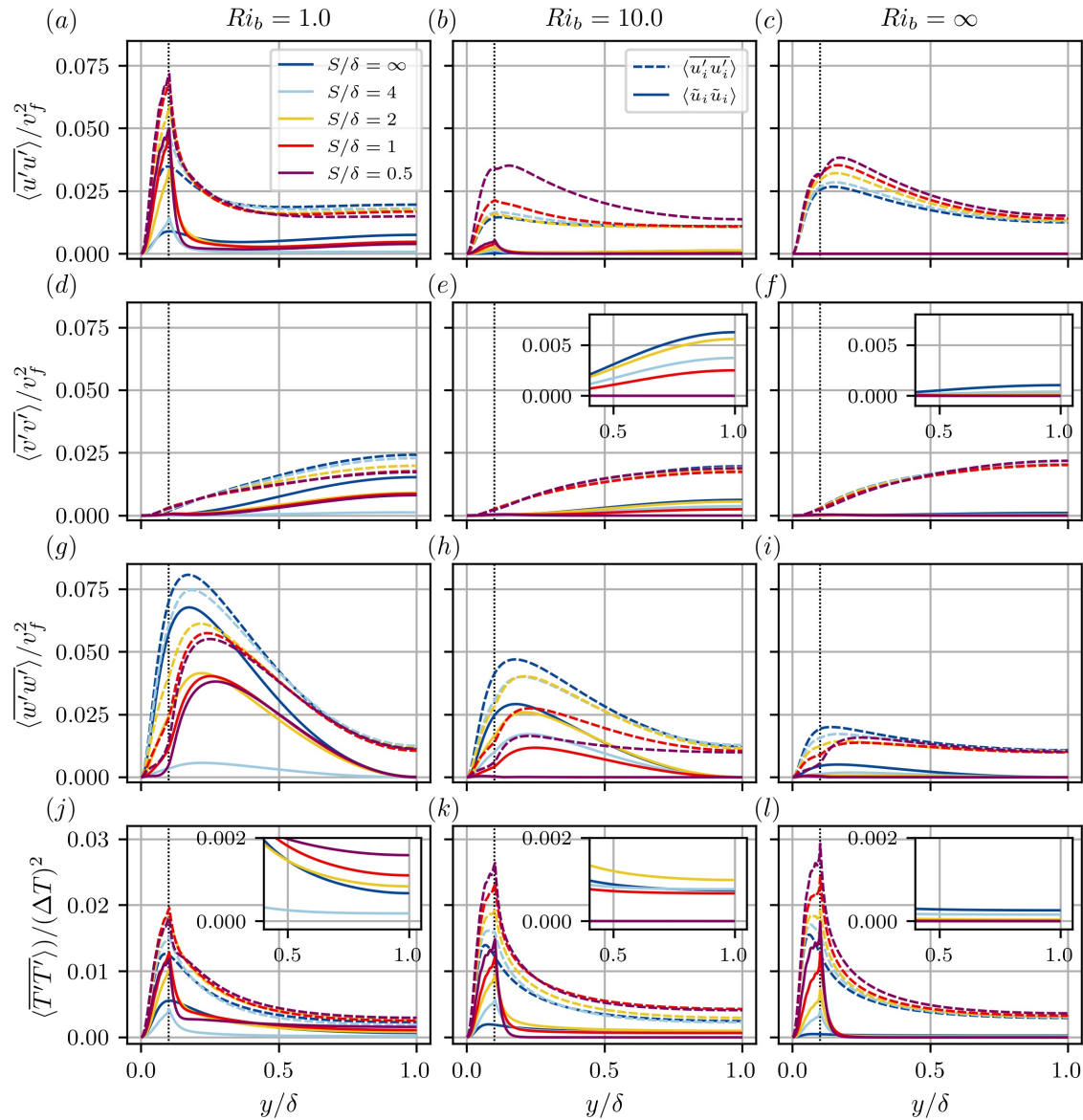


Figure 5.13: Velocity and temperature variances scaled in free fall units for high bulk Richardson number Ri_b cases at transition from streamwise rolls to natural convection. Adopted from Schäfer et al. (2022a)

in the steady increase of $\langle \overline{u'u'} \rangle$ with S (figure 5.13 (c)). This is also accompanied by a steady increase of $\langle \overline{T'T'} \rangle$ with decreasing S , which suggest that the aligned ridges induce stronger thermal plumes. Note, that in a square domain with smooth-wall condition the streamwise and spanwise stresses have the same distribution due to the directional invariance of the cells (Pandey et al. 2018). However, the smooth-wall case already displays slightly larger values for $\langle \overline{u'u'} \rangle$ than $\langle \overline{w'w'} \rangle$ and this indicates that the convection cell are slightly more oriented in the spanwise direction before introducing the aligned ridges." (Schäfer et al. 2022a)

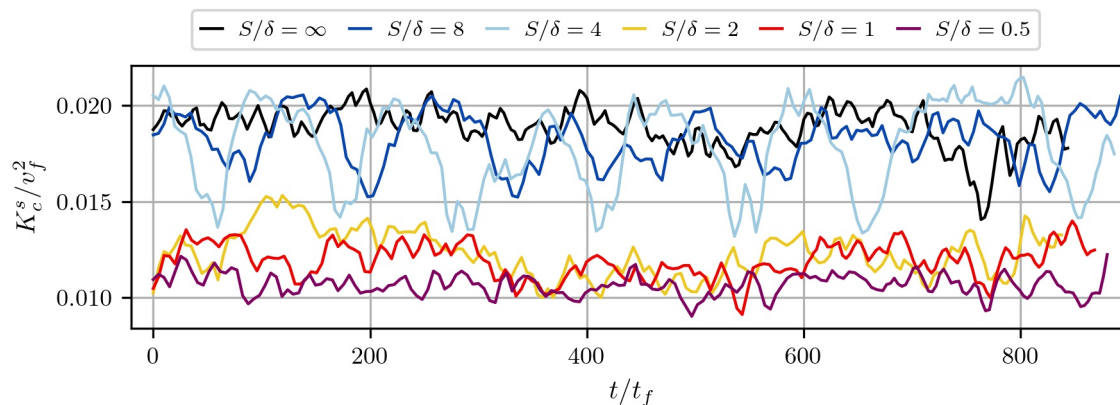


Figure 5.14: Short-time-averaged coherent kinetic energy K_c^s of case $Ri_b = 1$ and different ridge spacings over time. The values of K_c^s are averaged for time intervals $\Delta t_s \approx 3.4t_f$. Adopted from Schäfer et al. (2022a)

5.2.5 Dynamics of streamwise rolls

"In the previous section it was found that the coherence of the streamwise rolls for coarse ridge spacings $S = 4\delta$ drops significantly for case $Ri_b = 1$ and $Ri_b = 3.2$ compared with the denser values of S , indicating weaker cross-sectional motion of the roll. However, the instantaneous temperature visualisations in figures 5.5 and 5.6 for this specific case do not indicate weaker streamwise rolls, suggesting that a time-varying behaviour of the streamwise rolls might be present. For this purpose, the volume-averaged coherent turbulent kinetic energy of the cross-sectional components K_c , which is based on the average of the entire time series, is now averaged for shorter time windows. The short-time-averaged coherent turbulent kinetic energy K_c^s (superscript s indicates the short-time average) is computed over a time range of $\Delta t_s \approx 3.4t_f$. Note that the value of the short-time average is the shortest available data for the present simulations. The time evolution of K_c^s for consecutive short-time intervals is shown for case $Ri_b = 1$ in figure 5.14. As can be seen, all cases feature a relatively slow dynamics and for $S = \infty$ and $S \leq 2\delta$ the time variations vary mildly around their full time-averaged values K_c in figure 5.11 (b). For $S = 4\delta$ the time variation is more pronounced and the dynamics shows a clearly visible periodic reduction of K_c^s with a period of $\mathcal{O}(t) \approx 100t_f$, which corresponds to $\mathcal{O}(t) \approx 200t_b$. For this analysis an additional simulation with $S = 8\delta$ is performed and it shows similar time variation compared with $S = 4\delta$, however, with smaller amplitude. This observed dynamics is significantly slower than observations in ABL where the dynamics of the flow reaches a statistically quasi-steady state in roughly $6t_f$ (Moeng and Sullivan 1994). The time mean value of K_c^s is significantly larger than the value K_c , which suggests that the streamwise rolls of $S = 4\delta$ and $S = 8\delta$ feature some time variability, which is masked by considering quantities based on the average of the entire time series. This time-varying behaviour is also found for $Ri_b = 3.2$ and $S = 4\delta$, which also displayed a significant reduction of K_c in figure 5.11." (Schäfer et al. 2022a)

"The variability of the streamwise rolls is illustrated by the time evolution of the short-time- and streamwise-averaged temperature \bar{T}^s at the wall-normal channel centre $y = \delta$ along the spanwise direction z in figure 5.15. The spanwise position of the thermal up- and downdrafts of the streamwise roll is represented by the higher and lower temperature values, respectively. While the

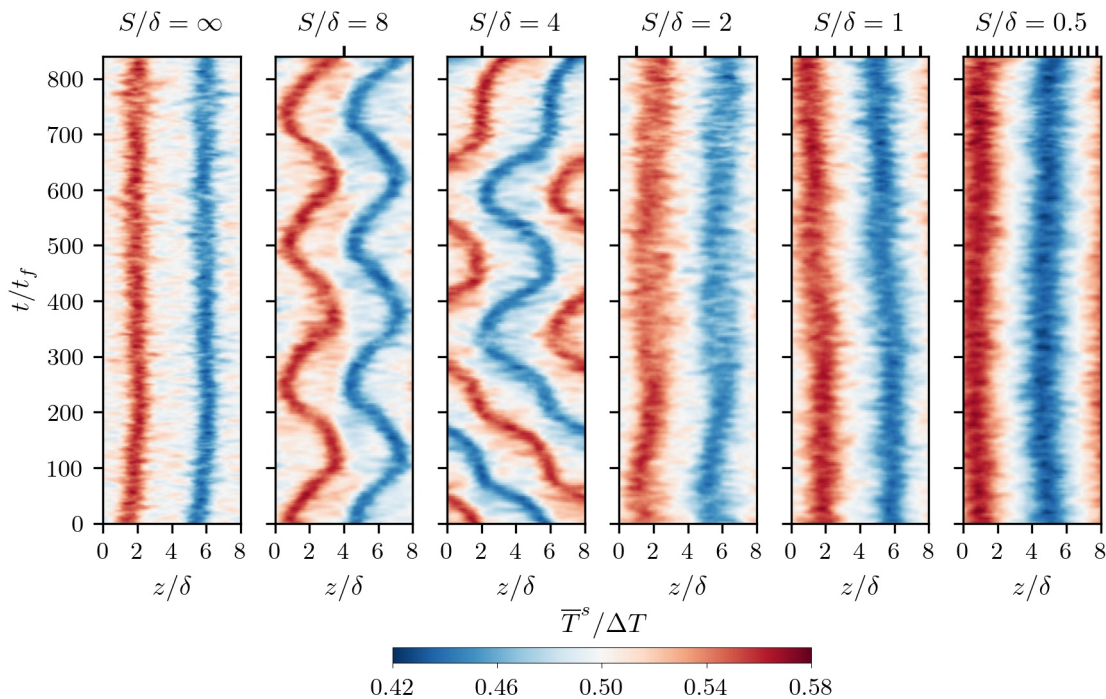


Figure 5.15: Streamwise and short-time-averaged temperature \bar{T}^s over time and spanwise position at the wall-normal channel centre location $y = \delta$ for cases $Ri_b = 1$. The spanwise position of the ridges is indicated by the black lines at the top figure frame. Adopted from Schäfer et al. (2022a)

spanwise location of the up- and downdrafts remain at the same position for $S = \infty$ and $S \leq 2\delta$, the spanwise location of the up- and downdrafts of case $S = 4\delta$ and $S = 8\delta$ is strongly varying in time. The up- and downdrafts for these two cases exhibit strong lateral movement. While this movement is almost periodic for $S = 8\delta$ and remains between the ridges, the up- and downdrafts of $S = 4\delta$ are able to cross the ridges at some time instances, e.g. $t/t_f \approx 100$, while they are not able to cross them at other time instances, e.g. $t/t_f \approx 350$. The large values of K_c^s of $S = 4\delta$ and $S = 8\delta$ in figure 5.14 correspond to occasions when the up- and downdrafts are located close to or directly at the ridges, e.g. $t = 700 - 800t_f$, while small values of K_c^s correspond to locations of the up- and downdrafts in between the ridges. This increase of K_c^s can be interpreted by the formation mechanism of streamwise rolls proposed by Khanna and Brasseur (1998), which relates them to the organisation of localised buoyancy forces within near-wall streaks. When the up- and downdrafts are located at ridges, the ridges support the formation of strong localised buoyancy forces, leading to strong local up- and downdrafts. Due to the symmetric arrangement of the ridges at both walls, the up- and downdrafts impinge at another ridge on the opposite wall, which is supposed to counteract the impinging roll by the formation of localised buoyancy forces with opposing direction. Thus, for $S = 4\delta$ the ridges support the formation of strong up- and downdrafts, however, they cannot remain at the spanwise location due to the counteraction of the opposing ridge, leading to the lateral evasion. For case $S = 8\delta$ this enhancement at the ridges occurs only for the up- or the downdraft and not simultaneously as for $S = 4\delta$, which might be an explanation for the observation that up- and downdrafts are not able to cross the ridges."(Schäfer et al. 2022a)

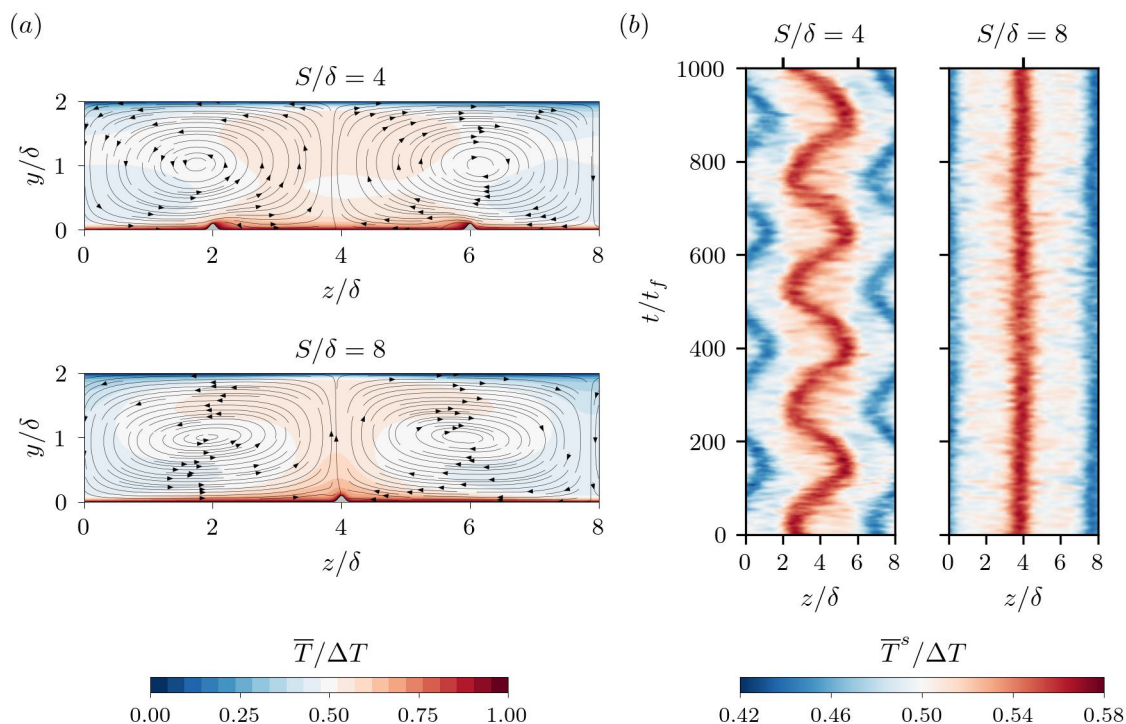


Figure 5.16: Mean temperature in cross-section in (a) and short-time-averaged temperature \bar{T}^s over time and spanwise position at $y = \delta$ in (b) for cases $Ri_b = 1$ and ridge spacing $S = 4\delta$ and $S = 8\delta$ with ridges only placed at the bottom wall of the channel.

"For case $S = 2\delta$ a short time interval $t \approx 120t_f$ with large values of K_c^s is present, which corresponds to a time interval in which the up- and downdrafts are located above ridges. However, most of the time the up- and downdrafts remain in between adjacent ridges, as has been shown in figure 5.10, and only a slight meandering within this range is observed. The examination of time series of cases $Ri_b = 0.32$ and $Ri_b = 10$ does not reveal this strong lateral movement of the up- and downdraft locations, while for $Ri_b = 3.2$ and $S = 4\delta$ a similar lateral movement is found. The results suggest that the dynamics of the streamwise rolls is very sensitive to ridge spacings of the order of the spanwise rolls' width, as seen for $S = 4\delta$ and $S = 8\delta$. For denser ridge spacings $S \leq 2\delta$ several adjacent ridges contribute by localised buoyancy forces to the formation of the up- and downdrafts which might be strong enough to inhibit disturbances by the opposing ridges and thereby prevent lateral movement of the streamwise rolls."(Schäfer et al. 2022a)

The hypothesis that the opposing ridges causing the instability and lateral movement of the streamwise rolls is further examined by considering cases with only ridges located at the bottom wall for $Ri_b = 1$ and ridge spacings $S = 4\delta$ and $S = 8\delta$. The mean temperature in the cross-section of the channel is shown for both cases in figure 5.16 (a), where it is already evident that the mean up- and downdrafts of the streamwise rolls are stronger for $S = 8\delta$ than compared to $S = 4\delta$, which is also seen in terms of K_c/v_f^2 amounting 0.0087 for $S = 4\delta$ and 0.0193 for $S = 8\delta$. While the updraft is located at the single bottom ridge for $S = 8\delta$, the up- and downdrafts occur for $S = 4\delta$ between the two bottom ridges. Inspection of the short-time- and streamwise-averaged temperature \bar{T}^s at $y = \delta$ in figure 5.16 (b) reveals that the streamwise rolls for $S = 4\delta$ laterally meander and the up-

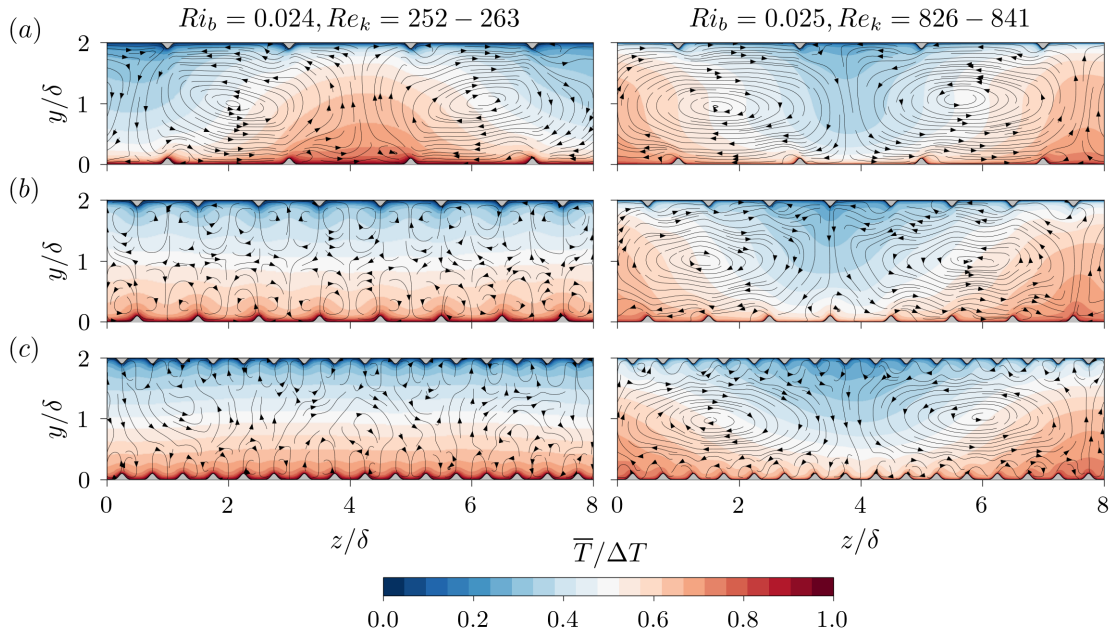


Figure 5.17: Effect of turbulent Reynolds number Re_k and spanwise ridge spacing S on mean temperature for case $Ri_b = 0.024$, $Re_k = 252-263$ ($Ra = 7.5 \cdot 10^5$, $Re_b = 2800$) on the left side and case $Ri_b = 0.025$, $Re_k = 826-841$ ($Ra = 10^7$, $Re_b = 10000$) on the right side. The spanwise spacing of the Gaussian ridges ranges from $S = 2\delta$ (a), $S = \delta$ (b) and $S = 0.5\delta$ (c). Adopted from Schäfer et al. (2022a)

and downdrafts remain between the two bottom ridges, similar to case $S = 8\delta$ with ridges on both walls in figure 5.15. This behaviour is in contrast to case $S = 4\delta$ with ridges on both walls (see figure 5.15), where the rolls are also able to laterally cross the ridges at some time instances. These observations suggest that the upper ridges are critical for this crossing and it is likely that a coupled behaviour between the up- and downdrafts of the rolls favors this crossing. As can be seen for $S = 8\delta$ with only bottom ridges (figure 5.16 (b)) the up- and downdrafts now remain fixed in span, which is in contrast to case $S = 8\delta$ with ridges on both walls. The direct comparison between these cases confirms that the counteraction of the opposing ridges are causing the lateral movement of the streamwise rolls. The fixation of the rolls for case $S = 8\delta$ results in slightly stronger values of K_c than compared to the smooth-wall case (see figure 5.11). Another way to fix the rolls with ridges on both walls might be a staggered arrangement with $S = 8\delta$, such that the ridges across the walls are staggered by half a wavelength of the streamwise rolls and thus both up- and downdrafts are supported and locked by ridges. A similar behaviour has been shown for secondary motions where "the comparison of a symmetric and staggered arrangement of streamwise-aligned ridges in forced convection flows (Stroh et al. 2020a) has shown that a staggered arrangement promotes the coherence of the large-scale secondary motion." (Schäfer et al. 2022a)

5.2.6 Reynolds and domain size effects

"In the previous section the flow organisation of mixed convection flows was considered in terms of varying bulk Richardson number Ri_b and ridge spacing S , while the Reynolds number Re_k was approximately constant. The effect of Re_k on the transition between forced convection structures

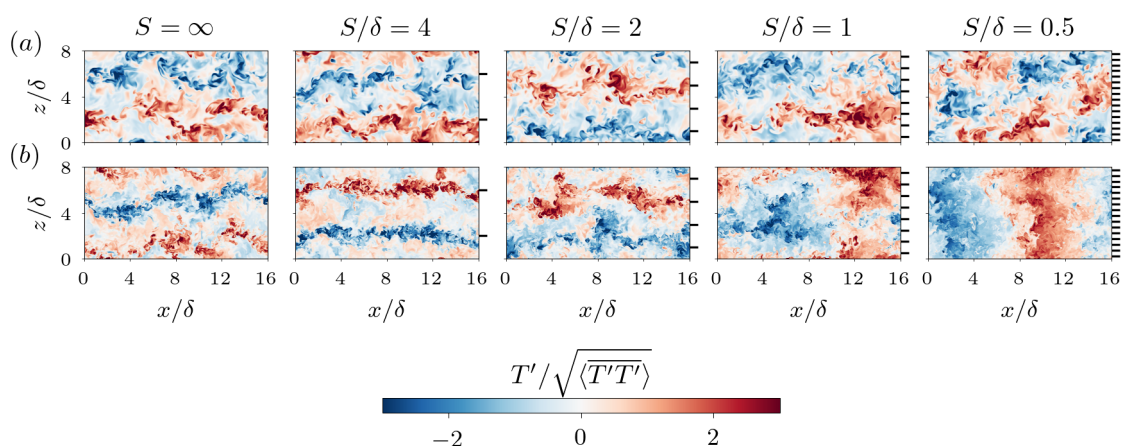


Figure 5.18: Instantaneous temperature fluctuation fields at the half-channel height position $y = \delta$ for cases $Ri_b = 3.2$ with $Re_k = 236-263$ ($Ra = 10^7$, $Re_b = 885$) in (a) and $Re_k = 695-792$ ($Ra = 10^8$, $Re_b = 2800$) in (b) for different spanwise ridge spacing S . Adopted from Schäfer et al. (2022a)

and streamwise rolls is shown in figure 5.17, which presents the cross-sectional mean temperature and flow topology for case $Ri_b = 0.024$ with values of $Re_k = 252-263$ and case $Ri_b = 0.025$ with threefold larger values of $Re_k = 826-841$. As can be seen figure 5.17 (a) both cases feature a streamwise roll down to a ridge spacing of $S = 2\delta$ (not shown for $S = \infty$ and $S = 4\delta$). The comparison of the temperature fields between the low and high Re_k cases depicts that the thermal boundary layer is reduced for higher Re_k due to the more efficient mixing of the flow in the near-wall region. As shown in the previous sections, the streamwise rolls are replaced by secondary motions for the lower Re_k cases with $Ri_b = 0.024$ and $S \leq \delta$, while for the larger Re_k cases the streamwise roll remains for these ridge spacings. However, the streamwise roll appears more distorted and affected by the ridges, as can be seen for $S = \delta$ and $S = 0.5\delta$. In addition, secondary motion in the form of one pair of counter-rotating vortices emerges at one ridge at the bottom wall lying in the downdraft region of the roll. This illustrates that the ridges on the opposing wall of the up- and downdraft regions are able to form coherent structures that counteract the large-scale roll formation. For the densest ridge spacing $S = 0.5\delta$ in figure 5.17 (c) the streamwise roll for the large Re_k case is now confined to a smaller wall-normal region in the bulk flow. This is associated with the recirculation zones at the leeward side of the ridges, which are connected between the up- and downdraft regions, thereby forming a roughness sublayer which inhibits the attachment of the lateral movement of the streamwise roll at the wall. These results suggest that the transition range between forced convection structures and streamwise rolls with heterogeneous rough surfaces is not solely determined by the pair of Ri_b and S , but also by the value of the Reynolds number Re_k . Due to the increased turbulent mixing for larger values of Re_k the streamwise rolls can counteract the additional shear by the ridges, such that the transition between forced convection structures and streamwise rolls is shifted towards smaller values of Ri_b ."(Schäfer et al. 2022a)

"The influence of Re_k on the roll-to-cell transition is illustrated for two cases with $Ri_b = 3.2$ and different Re_k by the temperature fluctuation in the horizontal mid-plane in figure 5.18. As can be seen, both cases exhibit streamwise rolls for smooth-wall conditions and $S \geq 2\delta$, while differences in the flow structures start to appear at $S = \delta$. At this ridge spacing the lower Re_k case still shows

streamwise rolls (figure 5.18 (a)), while for the larger Re_k case the streamwise rolls are disturbed by strong thermal plumes spanning almost the entire spanwise domain. For the lower Re_k case with $S = 0.5\delta$ no coherent streamwise rolls can be observed and, similar to $S = \delta$, for the larger Re_k case thermal plumes emerge, which indicates the beginning of the transition to convective cells. This shows that increasing Re_k has a comparable effect on the flow organisation to the reduction of the ridge spacing S . While smaller values of S increase the friction of the flow and weaken the lateral motion of the streamwise rolls, the higher Re_k increases the thermal mixing near the wall, and both effects promote the formation of thermal plumes. The loss of coherence of the streamwise rolls for case $S = 0.5\delta$ in figure 5.18 (a) is also supported by a vanishing value of K_c in figure 5.11 (b). Also the inspection of the time series of K_c^s reveals only a very weak contribution, which is an order magnitude lower than for case $S = \delta$. The observation that only convective cells with preferential orientation in the z -direction occur for the natural convection cases $S \leq 2\delta$ and for $Ri_b = 10$ with $S = 0.5\delta$ is also seen for the large Re_k case with $S = 0.5\delta$. The influence of Re_k on the transition between streamwise rolls and convective cells is such that higher values of Re_k initiate this transition to convective cells at smaller Ri_b , thus reducing the range of streamwise rolls."(Schäfer et al. 2022a)

5.3 Discussion and summary

In this chapter, turbulent channel flows under mixed convection conditions and heterogeneous surface properties are investigated using simulation results of DNS.

The investigation shows that "heterogeneous surfaces in form of streamwise-aligned Gaussian ridges have a significant influence on the flow organisation of mixed convection flows. The appearance of streamwise rolls is considerably reduced for dense ridge spacings S , which is related to the increased drag introduced by the ridges. Therefore, the formation of the rolls requires larger buoyancy forces, such that the transition from forced convection structures to streamwise rolls is delayed by the ridges towards higher Ri_b values than expected for smooth-wall conditions. Specifically, this transition occurs for the smooth channel at $Ri_b = 0.016$, while for large ridge spacings of $S \geq 2\delta$ this transition occurs first at $Ri_b = 0.024$ and for denser ridge spacings $S \leq \delta$ at $Ri_b = 0.032$."(Schäfer et al. 2022a)

"The strongest influence of the heterogeneous surface on the flow organisation occurs between the roll-to-cell transition range, where a change of the surface properties has a comparable effect to a change of Ri_b for homogeneous wall conditions. This behaviour is observed by the inspection of the instantaneous and mean cross-sectional velocity and temperature fields. In the range of $Ri_b = 3.2 \sim 10$, where streamwise rolls are present for smooth-wall conditions, dense ridge spacings already trigger the transition from roll to cell structures. This is surprising, since this range of bulk Richardson number, which corresponds to a range of stability parameter $-\delta_{eff}/L = 3.4 \sim 9.7$, is below the range where commonly cell structures are observed in the ABL (Salesky et al. 2017). The results show that the increased lateral drag introduced by the densely spaced ridges diminishes the coherence of the streamwise rolls, and eventually leads to the transition to convective

cells at smaller Ri_b . In addition to the earlier roll-to-cell transition the ridges also affect the orientation of the convection cells for denser ridge spacings. While the convective cells have no preferential orientation for the smooth-wall natural convection case, they increasingly prefer to orient perpendicular to the ridges with decreasing S . This is also explained by the additional drag, which is experienced by ridge-aligned convective cells, such that the lateral near-wall motion of these cells is increasingly disturbed for smaller S . This will eventually lead to their breakdown and the flow prefers to stream only along the ridges, resulting in the occurrence of spanwise coherent convective cells."(Schäfer et al. 2022a)

"For the moderate values of Reynolds numbers that can be afforded for the present simulations, we find that an increase in Re favours the transition from forced convection structures to streamwise rolls at smaller Ri_b , which is associated with the increased thermal vertical mixing at larger Re . At the roll-to-cell transition range, an increase of Re promotes the transition towards convective cells, such that convective cells appear for larger S if Re is increased."(Schäfer et al. 2022a)

"One particular observation is that the dynamics of streamwise rolls is very sensitive to ridge spacings of the order of the rolls' width, which is found for $Ri_b = 1$ and $Ri_b = 3.2$. For the specific ridge spacing $S = 4\delta$ the up- and downdraft regions move over the entire channel slowly in time, with time periods of approximately 100 free-fall time units or 200 time bulk units, which is in contrast to denser ridge spacings and smooth-wall conditions, where the spanwise location of the rolls is fixed. Due to this variation of streamwise rolls in the former case, some statistical features of the rolls are masked by long time integration. This is seen for example for the strength of the roll's coherence, which almost vanishes for long time intervals. Inspection of consecutive short-time averages reveals that the strength of the roll's coherence depends on the spanwise location of the up- and downdraft regions. The coherence is reduced if the up- and downdraft regions occur in the valley of adjacent ridges, and is increased if they occur in the vicinity of the ridges. In the former case the rolls experience stronger lateral drag due to their horizontal movement above the ridges, while in the latter case the ridges support the formation of localised buoyancy forces at the ridges, which in turn strengthens the up- and downdraft regions. Although the ridges reinforce the rolls, they do not reside there permanently."(Schäfer et al. 2022a)

This lateral movement of the rolls is attributed to the mutual influence of opposing ridges on the up- and downdraft due to the symmetric ridge arrangement. In this case, when up- and downdrafts form over ridges, they impinge on a ridge on the opposing wall, which causes local buoyancy forces acting in the opposite direction of the up- and downdrafts. By removing the ridges on the upper wall, the hypothesis of this mutual influence of the ridges is demonstrated, such that for ridge distances $S = 8\delta$ corresponding to the roll's wavelength, the updrafts are fixed at the ridge on the bottom wall. "While the formation mechanism of streamwise rolls is still not clear and under debate (Etling and Brown 1993, Salesky et al. 2017), the present observations indicate that the formation and the dynamics of streamwise rolls are very sensitive to heterogeneous surfaces."(Schäfer et al. 2022a)

6 Conclusion and Outlook

This thesis shows that heterogeneous surfaces strongly influence the formation of turbulent large-scale structures and how their characteristics depend on surface properties and buoyancy effects. In particular, spanwise heterogeneous surfaces are considered, where the surface heterogeneity occurs perpendicular to the main flow direction. These surfaces are known to form turbulent secondary motions appearing as large-scale counter-rotating vortices in the mean velocity field. The thesis demonstrates that the strength of secondary motions is strongly related to relative height differences that occur in the spanwise heterogeneous surfaces. Besides, the relation of secondary motions to other turbulent large-scale structures, which also occur over smooth surfaces, are investigated and how their instantaneous characteristics are affected by variations in the surface properties. Finally, the effect of spanwise heterogeneous surfaces on the formation of buoyancy-induced large-scale structures is explored, demonstrating that their occurrence is significantly reduced by the presence of heterogeneous surfaces. As a main means of investigation, direct numerical simulations (DNS) has been chosen. While the observations of each investigation are summarized at the end of the respective chapter, this conclusion reflects on selected findings and their relation with regard to the objectives of the thesis.

Previous studies have concentrated mainly on the characterisation and formation of secondary motions over pure ridge- or strip-type surfaces, while combined effects of lateral drag variations and relative wall height differences have not been systematically studied. These combined effects are investigated in chapter 3, where spanwise alternating rough- and smooth-wall strips with different relative height differences are studied in turbulent open-channel flow. It is shown that the parametric forcing approach (PFA) can reproduce all characteristic flow features of spanwise heterogeneous rough surface, such that surface parameter studies can be performed with less numerical effort compared to roughness-resolved simulations with an immersed boundary method (IBM). The results reveal that the rotational direction of the secondary motion depends on whether the roughness strip is protruding or recessed. In the former case, the secondary motions resemble the one found over ridge-type surfaces, while in the latter case it resembles the one over strip-type roughness. When the smooth-wall strip is elevated significantly above the recessed roughness (relative height difference of $\Delta h^+ \approx 40$), ridge-type behaviour becomes more pronounced, which is evident by the formation of tertiary vortices above the smooth-wall strips. The strength of the secondary motion is observed to increase steadily with increasing relative height difference independent of whether the roughness strip is recessed or protruding. A similar relation is found for ridge-type induced secondary motions in chapter 4 where the strength reduces with decreasing ridge height. The switch of rotational direction from protruding to recessed roughness strips cannot be explained by the formation mechanism considering the imbalance between production

and dissipation of turbulent kinetic energy, which was suggested for strip-type induced secondary motions (Hinze 1967, 1973, Anderson et al. 2015). However, it is found that this switch is related to the wall-normal deflections of spanwise velocity at the smooth-to-rough transition which change direction when the relative height differences between smooth and rough strip reverse. These deflections have been previously found to play an important role for the formation of ridge-type induced secondary motions, where they significantly contribute to the transport of turbulent kinetic energy (Hwang and Lee 2018). Overall, these observations illustrate that the formation of secondary motion strongly depends on the relative height differences and the associated velocity deflections.

Similarities are found between the instantaneous structures associated with secondary motions over strip-type surfaces and turbulent large-scale structures (LSM/VLSM) (Wangsawijaya et al. 2020, Wangsawijaya and Hutchins 2022). These results suggest that both might share a similar formation mechanism and that secondary motions are spanwise locked turbulent large-scale structures. On the other hand, it was found that ridge-type induced secondary motion suppress the formation of VLSM (Zampiron et al. 2020). The investigation in chapter 4 further examines the relation between secondary motion and turbulent large-scale motions in an open-channel flow with streamwise-aligned ridges. The results support the recent findings that VLSM are suppressed by secondary motions for dense ridge spacings $S \leq 2\delta$. In addition, it is shown that coexistence between secondary motion and VLSM is possible for larger spacings $S \geq 4\delta$, such that VLSM form in the valleys between the ridges, which are unaffected by secondary motions. The suppression of the VLSM is related to the strength of secondary motions, and by reducing the ridge height, being accompanied by a weakening of the spatial flow heterogeneity, VLSM can eventually reappear at the ridge locations. Thus, the coexistence of VLSM and secondary motions over strip-type surfaces can be explained by the observation that secondary motions over pure strip-type surfaces are weaker in intensity than those occurring over surfaces with larger relative height differences, as shown in chapter 3. The streamwise wavelength associated with instantaneous secondary motions also depends on the strength of mean secondary motion. This indicates similarities to the streak-vortex instability model proposed for the formation of LSM (de Giovanetti et al. 2017), where the streamwise wavelength of LSM depends on the strength of the amplified low-speed large-scale streak. Further evidence for the similarity between secondary motions and LSM comes from the observation that instantaneously large-scale counter-rotating vortices are found at the ridges for small ridge spacings ($S \leq \delta$), even though the mean secondary motion is much smaller in its spatial extent and scales with S . This instantaneous behaviour is obscured by the averaging procedure since the instantaneous secondary motions occur at adjacent ridges at different time instances such that the superposition of these events by the averaging procedure masks the large-scale motion in the mean. Interesting to note is, that LSMs have been recently observed to form streamwise-aligned sediment ridges in open-channel flows, which in turn induce mean secondary motions for time intervals of $\mathcal{O}(10)$ bulk time units (Scherer et al. 2022). Overall, the results shown in this investigation illustrate that the similarities between turbulent large-scale motion and secondary motion are also observable for ridge-type surfaces, suggesting a similar formation mechanism of secondary motions regardless of the surface type.

The effects of spanwise heterogeneous surfaces on convective large-scale structures, which are driven by the combined effects of shear and buoyancy, are examined in a turbulent channel flow with streamwise-aligned ridges in chapter 5. It is observed that secondary motions, which are studied in the previous chapters under pure forced convection condition, are already suppressed by the presence of mild buoyancy effects. They are replaced by large-scale streamwise rolls, which occur under mixed convection conditions where the flow is driven by the combined effects of buoyancy and shear. At the same time, the effect of increasing drag due to denser ridge spacings delays the transition from secondary motions towards streamwise rolls, such that larger buoyancy effects are required for the roll's formation. The influence of heterogeneous surfaces on the flow organisation of mixed convection is particularly pronounced at the transition from rolls to convective cells, where due to increased drag the transition to cells already occurs for lower Ri_b (at $Ri_b \approx 3.1$ for $S = 4\delta$, instead of $Ri_b > 10$ for smooth-wall conditions). As a consequence, the range of Ri_b under which streamwise rolls can occur is significantly reduced compared to smooth-wall conditions. Besides, it is found that ridges induce a slow dynamic of streamwise rolls for $Ri_b \approx 1-3.1$ when the spanwise ridge spacing is of the order of the roll's width, such that the up- and downdrafts of the rolls meander across the entire channel width. This behaviour is a consequence of the symmetrical arrangement of the ridges on the upper and lower walls, which hinders the formation of the roll's up- and downdrafts at the ridges due to the flow interaction with opposing ridges. This relation is further illustrated by removing the ridges at the upper wall, such that the lateral movement of the rolls can be locked and the formation of their updrafts are fixed at ridges on the bottom wall. This effect could also be of relevance for the example of the sand dunes in the atmospheric boundary layer in chapter 1, suggesting that streamwise rolls are preferentially located at already existing longitudinal sand dunes. Altogether, the study presented here illustrates that spanwise heterogeneous surfaces have a strong influence on the formation and dynamics of streamwise rolls and compared to smooth-wall conditions severely alter the flow organisation of mixed convection flows.

Overall, this thesis has investigated new facets of the effects of spanwise heterogeneous surfaces on the exchange processes of turbulent flows and their interaction with turbulent large-scale structures. However, due to the variety of different surface properties and arrangement as well as various flow conditions, a number of effects remain unexplored and should be addressed in future investigations. For instance, the influence of secondary flow on heat transfer is still not systematically examined. As shown in this thesis, the secondary motions over ridge-type surfaces increase the heat transfer compared to smooth-wall conditions, but investigations for strip-type surfaces are missing so far. Especially the reorientation of the secondary motions observed over protruding and recessed roughness strips observed in chapter 3, represents an interesting scenario to study the effects of lateral variations in drag and wall height differences on the heat transfer of secondary motions. This could be of relevance for technical applications, where local enhancement or decrease of the heat transfer is desired and can be imposed by heterogeneous surfaces. For this purpose, the PFA used to model the effects of heterogeneous rough surfaces in chapter 3 is a promising approach which could be extended for heat transfer problems, such that parameter studies of surface properties can be performed with less numerical effort.

While the influence of the surface parameters on the mean characteristics of secondary motions are well studied, the knowledge about the dynamics and instantaneous structures of secondary motion are not complete. The similarities between instantaneous secondary motions and turbulent large-scale structures found over strip-type surfaces are also observed for ridge-type surfaces in this thesis. However, an investigation bridging these observations over strip- and ridge-type surfaces is pending. This could clarify if the similarities between secondary motions and LSMs are independent of the heterogeneous surface type, and thereby resolving the question if secondary motions over strip- and ridge-type surfaces share the same formation mechanism. For this purpose, the investigation of chapter 4 with large open-channel flow domains could be extended by introducing the alternating rough- and smooth-wall strips from chapter 3, such that the strip- and ridge-type behaviour can be controlled by the lateral variation of the relative wall height differences.

Regarding the strong influence of spanwise heterogeneous surfaces on the flow organisation in mixed convection flows, future investigations should examine to what degree this is related to the drag increase by the ridges and to what extent to the spatial orientation of the heterogeneous surfaces. One way to elucidate this is to study the flow organisation of mixed convection flows over homogeneous rough surfaces, where the rolls do not experience different drag due to directional dependence of the surface structure. Furthermore, it remains to be clarified how these observations can be transferred to other flow configurations, such as for example atmospheric boundary layer flows, where in addition the changing orientation of the wind direction to the heterogeneous surface plays an important role. In conclusion, the results of this work and future studies based on them, will contribute to a better understanding of turbulent flow phenomena over heterogeneous surfaces that are, i.a., necessary to improve current weather and climate models and their predictions.

Bibliography

- R. J. Adrian, C. D. Meinhart, and C. D. Tomkins. Vortex organization in the outer region of the turbulent boundary layer. *J. Fluid Mech.*, 422:1–54, 2000. doi: 10.1017/S0022112000001580.
- W. Anderson, J. M. Barros, K. T. Christensen, and A. Awasthi. Numerical and experimental study of mechanisms responsible for turbulent secondary flows in boundary layer flows over spanwise heterogeneous roughness. *J. Fluid Mech.*, 768:316–347, 2015. doi: 10.1017/jfm.2015.91.
- H. Bai, J. Gong, and Z. Lu. Energetic structures in the turbulent boundary layer over a spanwise-heterogeneous converging/diverging riblets wall. *Phys. Fluids*, 33(7):075113, 2021. doi: 10.1063/5.0055767.
- J. M. Barros and K. T. Christensen. Observations of turbulent secondary flows in a rough-wall boundary layer. *J. Fluid Mech.*, 748:R1, 2014. doi: 10.1017/jfm.2014.218.
- P. Bartholomew, G. Deskos, R. A. S. Frantz, F. N. Schuch, E. Lamballais, and S. Laizet. Xcompact3D: An open-source framework for solving turbulence problems on a Cartesian mesh. *SoftwareX*, 12:100550, July 2020. doi: 10.1016/j.softx.2020.100550.
- A. Blass, X. Zhu, R. Verzicco, D. Lohse, and R. J. A. M. Stevens. Flow organization and heat transfer in turbulent wall sheared thermal convection. *J. Fluid Mech.*, 897, 2020. doi: 10.1017/jfm.2020.378.
- E. Bou-Zeid, W. Anderson, G. G. Katul, and L. Mahrt. The Persistent Challenge of Surface Heterogeneity in Boundary-Layer Meteorology: A Review. *Boundary-Layer Meteorol.*, 177(2): 227–245, 2020. doi: 10.1007/s10546-020-00551-8.
- P. Bradshaw. Turbulent secondary flows. *Annu. Rev. Fluid Mech.*, 19(1):53–74, 1987. doi: 10.1146/annurev.fl.19.010187.000413.
- A. Busse and N. D. Sandham. Parametric forcing approach to rough-wall turbulent channel flow. *J. Fluid Mech.*, 712:169–202, 2012. doi: 10.1017/jfm.2012.408.
- S. M. Cameron, V. I. Nikora, and M. T. Stewart. Very-large-scale motions in rough-bed open-channel flow. *J. Fluid Mech.*, 814:416–429, 2017. doi: 10.1017/jfm.2017.24.
- C. Chan-Braun, M. García-Villalba, and M. Uhlmann. Force and torque acting on particles in a transitionally rough open-channel flow. *J. Fluid Mech.*, 684:441–474, 2011. doi: 10.1017/jfm.2011.311.

- M. Chevalier, P. Schlatter, A. Lundbladh, and D. S. Henningson. Simson – A pseudo-spectral solver for incompressible boundary layer flows. Technical Report TRITA-MEK 2007-07, KTH Stockholm, Stockholm, Sweden, 2007.
- D. Chung, J. P. Monty, and N. Hutchins. Similarity and structure of wall turbulence with lateral wall shear stress variations. *J. Fluid Mech.*, 847:591–613, 2018. doi: 10.1017/jfm.2018.336.
- D. Chung, N. Hutchins, M. P. Schultz, and K. A. Flack. Predicting the Drag of Rough Surfaces. *Annu. Rev. Fluid Mech.*, 53(1):439–471, 2021. doi: 10.1146/annurev-fluid-062520-115127.
- M. Colombini. Turbulence-driven secondary flows and formation of sand ridges. *J. Fluid Mech.*, 254:701–719, Sept. 1993. doi: 10.1017/S0022112093002319.
- M. Colombini and G. Parker. Longitudinal streaks. *J. Fluid Mech.*, 304:161–183, 1995. doi: 10.1017/S0022112095004381.
- G. Daschiel, T. Baier, J. Saal, and B. Frohnapfel. On the flow resistance of wide surface structures. *PAMM*, 12(1):569–570, 2012. doi: 10.1002/pamm.201210273.
- M. de Giovanetti, H. J. Sung, and Y. Hwang. Streak instability in turbulent channel flow: the seeding mechanism of large-scale motions. *J. Fluid Mech.*, 832:483–513, 2017. doi: 10.1017/jfm.2017.697.
- J. W. Deardorff. Numerical Investigation of Neutral and Unstable Planetary Boundary Layers. 1972. doi: 10.1175/1520-0469(1972)029<0091:NIONAU>2.0.CO;2.
- D. Etling and R. A. Brown. Roll vortices in the planetary boundary layer: A review. *Boundary-Layer Meteorol.*, 65(3):215–248, 1993. doi: 10.1007/BF00705527.
- J. J. Finnigan, R. H. Shaw, and E. G. Patton. Turbulence structure above a vegetation canopy. *J. Fluid Mech.*, 637:387–424, 2009. doi: 10.1017/S0022112009990589.
- P. Forooghi, B. Frohnapfel, F. Magagnato, and A. Busse. A modified parametric forcing approach for modelling of roughness. *Int. J. Heat Fluid Flow*, 71:200–209, 2018. doi: 10.1016/j.ijheatfluidflow.2018.03.019.
- B. Ganapathisubramani, E. K. Longmire, and I. Marusic. Characteristics of vortex packets in turbulent boundary layers. *J. Fluid Mech.*, 478:35–46, 2003. doi: 10.1017/S0022112002003270.
- R. Gautier, S. Laizet, and E. Lamballais. A DNS study of jet control with microjets using an immersed boundary method. *Intl J. Comput. Fluid Dyn.*, 28(6-10):393–410, July 2014. doi: 10.1080/10618562.2014.950046.
- D. Goldstein, R. Handler, and L. Sirovich. Modeling a no-slip flow boundary with an external force field. *J. Comput. Phys.*, 105(2):354–366, 1993. doi: 10.1006/jcph.1993.1081.
- D. B. Goldstein and T.-C. Tuan. Secondary flow induced by riblets. *J. Fluid Mech.*, 363:115–151, 1998. doi: 10.1017/S0022112098008921.

- S. R. Hanna. The Formation of Longitudinal Sand Dunes by Large Helical Eddies in the Atmosphere. *Journal of Applied Meteorology and Climatology*, 8(6):874–883, 1969. doi: 10.1175/1520-0450(1969)008<0874:TFOLSD>2.0.CO;2.
- J. O. Hinze. Secondary Currents in Wall Turbulence. *Phys. Fluids*, 10(9):S122, 1967. doi: 10.1063/1.1762429.
- J. O. Hinze. Experimental investigation on secondary currents in the turbulent flow through a straight conduit. *Appl. Sci. Res.*, 28(1):453–465, 1973. doi: 10.1007/BF00413083.
- P. Holmes, J. L. Lumley, G. Berkooz, and C. W. Rowley. *Turbulence, Coherent Structures, Dynamical Systems and Symmetry*. Cambridge University Press, 2012. doi: 10.1017/CBO9780511919701.
- N. Hutchins and I. Marusic. Evidence of very long meandering features in the logarithmic region of turbulent boundary layers. *J. Fluid Mech.*, 579:1–28, 2007. doi: 10.1017/S0022112006003946.
- H. G. Hwang and J. H. Lee. Secondary flows in turbulent boundary layers over longitudinal surface roughness. *Phys. Rev. Fluids*, 3(1), 2018. doi: 10.1103/PhysRevFluids.3.014608.
- Y. Hwang. Statistical structure of self-sustaining attached eddies in turbulent channel flow. *J. Fluid Mech.*, 767:254–289, 2015. doi: 10.1017/jfm.2015.24.
- B. Jayaraman and J. G. Brasseur. Transition in atmospheric boundary layer turbulence structure from neutral to convective, and large-scale rolls. *J. Fluid Mech.*, 913, 2021. doi: 10.1017/jfm.2021.3.
- K. Kevin, J. P. Monty, H. L. Bai, G. Pathikonda, B. Nugroho, J. M. Barros, K. T. Christensen, and N. Hutchins. Cross-stream stereoscopic particle image velocimetry of a modified turbulent boundary layer over directional surface pattern. *J. Fluid Mech.*, 813:412–435, 2017. doi: 10.1017/jfm.2016.879.
- K. Kevin, J. Monty, and N. Hutchins. Turbulent structures in a statistically three-dimensional boundary layer. *J. Fluid Mech.*, 859:543–565, 2019. doi: 10.1017/jfm.2018.814.
- S. Khanna and J. G. Brasseur. Three-Dimensional Buoyancy- and Shear-Induced Local Structure of the Atmospheric Boundary Layer. *J. Atmos. Sci.*, 55(5):710–743, 1998. doi: 10.1175/1520-0469(1998)055<0710:TDBASI>2.0.CO;2.
- J. Kim, P. Moin, and R. Moser. Turbulence statistics in fully developed channel flow at low Reynolds number. *J. Fluid Mech.*, 177:133–166, 1987. doi: 10.1017/S0022112087000892.
- K. C. Kim and R. J. Adrian. Very large-scale motion in the outer layer. *Phys. Fluids*, 11(2): 417–422, 1999. doi: 10.1063/1.869889.
- S. J. Kline, W. C. Reynolds, F. A. Schraub, and P. W. Runstadler. The structure of turbulent boundary layers. *J. Fluid Mech.*, 30(4):741–773, 1967. doi: 10.1017/S0022112067001740.
- P. K. Kundu, I. M. Cohen, and D. R. Dowling, editors. *Fluid Mechanics*. Academic Press, Boston, 2016. doi: 10.1016/B978-0-12-405935-1.01001-7.

- S. Laizet and E. Lamballais. High-order compact schemes for incompressible flows: A simple and efficient method with quasi-spectral accuracy. *J. Comput. Phys.*, 228(16):5989–6015, 2009. doi: 10.1016/j.jcp.2009.05.010.
- E. Lamballais, V. Fortuné, and S. Laizet. Straightforward high-order numerical dissipation via the viscous term for direct and large eddy simulation. *J. Comput. Phys.*, 230(9):3270–3275, 2011. doi: 10.1016/j.jcp.2011.01.040.
- S. K. Lele. Compact finite difference schemes with spectral-like resolution. *J. Comput. Phys.*, 103(1):16–42, 1992. doi: 10.1016/0021-9991(92)90324-R.
- M. A. LeMone. The Structure and Dynamics of Horizontal Roll Vortices in the Planetary Boundary Layer. *J. Atmos. Sci.*, 30(6):1077–1091, 1973. doi: 10.1175/1520-0469(1973)030<1077:TSADOH>2.0.CO;2.
- J. Lumley. The structure of inhomogeneous turbulent flows. *Atmospheric Turbulence and Radio Wave Propagation*, pages 166–178, 1967. Publisher: Nauka.
- L. Mahrt. Stratified Atmospheric Boundary Layers. *Boundary-Layer Meteorol.*, 90(3):375–396, 1999. doi: 10.1023/A:1001765727956.
- T. Medjnoun, C. Vanderwel, and B. Ganapathisubramani. Characteristics of turbulent boundary layers over smooth surfaces with spanwise heterogeneities. *J. Fluid Mech.*, 838:516–543, 2018. doi: 10.1017/jfm.2017.849.
- T. Medjnoun, C. Vanderwel, and B. Ganapathisubramani. Effects of heterogeneous surface geometry on secondary flows in turbulent boundary layers. *J. Fluid Mech.*, 886, 2020. doi: 10.1017/jfm.2019.1014.
- R. Mittal and G. Iaccarino. Immersed Boundary Methods | Annual Review of Fluid Mechanics. *Annu. Rev. Fluid Mech.*, 37(1):239–261, 2005. doi: 10.1146/annurev.fluid.37.061903.175743.
- C. Moeng and P. P. Sullivan. A Comparison of Shear- and Buoyancy-Driven Planetary Boundary Layer Flows. *J. Atmos. Sci.*, 51(7):999–1022, 1994. doi: 10.1175/1520-0469(1994)051<0999:ACOSAB>2.0.CO;2.
- A. S. Monin and A. M. Obukhov. Basic laws of turbulent mixing in the surface layer of the atmosphere. *Contrib. Geophys. Inst. Acad. Sci. USSR*, 151(163):e187, 1954.
- J. P. Monty, N. Hutchins, H. C. H. Ng, I. Marusic, and M. S. Chong. A comparison of turbulent pipe, channel and boundary layer flows. *J. Fluid Mech.*, 632:431–442, 2009. doi: 10.1017/S0022112009007423. doi: 10.1017/S0022112009007423.
- NASA Earth Observatory. Cloud Streets Near Antarctica, September 12, 2018. Aqua - MODIS. url: <https://earthobservatory.nasa.gov/images/92768/cloud-streets-near-antarctica>.
- NASA Earth Observatory. Namib Sand Sea, January 20, 2020. SeaHawk - HawkEye. url: <https://earthobservatory.nasa.gov/images/149130/namib-sand-sea>.

- J. Nikuradse. *Untersuchung über die Geschwindigkeitsverteilung in turbulenten Strömungen*. VDI-Verlag, 1926.
- A. M. Obukhov. Turbulence in an atmosphere with inhomogeneous temperature. *Tr. Inst. Teor. Geofiz. Akad. Nauk SSSR*, 1:95–115, 1946.
- A. Pandey, J. D. Scheel, and J. Schumacher. Turbulent superstructures in Rayleigh-Bénard convection. *Nat. Commun.*, 9(1):2118, 2018. doi: 10.1038/s41467-018-04478-0.
- S. Pirozzoli, M. Bernardini, R. Verzicco, and P. Orlandi. Mixed convection in turbulent channels with unstable stratification. *J. Fluid Mech.*, 821:482–516, 2017. doi: 10.1017/jfm.2017.216.
- S. B. Pope. *Turbulent Flows*. Cambridge University Press, 2000. doi: 10.1017/CBO9780511840531.
- L. Prandtl. Über die ausgebildete Turbulenz. *Verhandlungen des II. Internationalen Kongresses für Technische Mechanik*, 1926.
- M. R. Raupach and R. H. Shaw. Averaging procedures for flow within vegetation canopies. *Boundary-Layer Meteorol.*, 22(1):79–90, 1982. doi: 10.1007/BF00128057.
- M. R. Raupach, J. J. Finnigan, and Y. Brunei. Coherent eddies and turbulence in vegetation canopies: The mixing-layer analogy. *Boundary-Layer Meteorol.*, 78(3):351–382, 1996. doi: 10.1007/BF00120941.
- S. T. Salesky, M. Chamecki, and E. Bou-Zeid. On the Nature of the Transition Between Roll and Cellular Organization in the Convective Boundary Layer. *Boundary-Layer Meteorol.*, 163(1): 41–68, 2017. doi: 10.1007/s10546-016-0220-3.
- A. Scagliarini, Á. Gylfason, and F. Toschi. Heat-flux scaling in turbulent Rayleigh-Bénard convection with an imposed longitudinal wind. *Phys. Rev. E*, 89(4):043012, 2014. doi: 10.1103/PhysRevE.89.043012.
- M. Scherer, M. Uhlmann, A. G. Kidanemariam, and M. Kraymer. On the role of turbulent large-scale streaks in generating sediment ridges. *J. Fluid Mech.*, 930:A11, 2022. doi: 10.1017/jfm.2021.891.
- Y. Shao. *Physics and modelling of wind erosion*. Number 37 in Atmospheric and oceanographic sciences library. Springer, 2008. doi: 10.1007/978-1-4020-8895-7.
- L. Sirovich. Turbulence and the Dynamics of Coherent Structures Part I: Coherent Structures. *Quarterly of Applied Mathematics*, 45(3):561–571, 1987.
- A. Stroh, Y. Hasegawa, J. Kriegseis, and B. Frohnäpfel. Secondary vortices over surfaces with spanwise varying drag. *J. Turbul.*, 17(12):1142–1158, 2016. doi: 10.1080/14685248.2016.1235277.
- K. Taira, S. L. Brunton, S. T. M. Dawson, C. W. Rowley, T. Colonius, B. J. McKeon, O. T. Schmidt, S. Gordeyev, V. Theofilis, and L. S. Ukeiley. Modal Analysis of Fluid Flows: An Overview. *AIAA Journal*, 55(12):4013–4041, Dec. 2017. doi: 10.2514/1.J056060.

- M. E. Taslim, T. Li, and D. M. Kercher. Darryl E. Metzger Memorial Session Paper: Experimental Heat Transfer and Friction in Channels Roughened With Angled, V-Shaped, and Discrete Ribs on Two Opposite Walls. *Journal of Turbomachinery*, 118(1):20–28, 1996. doi: 10.1115/1.2836602.
- D. J. Tritton. *Physical Fluid Dynamics*. Springer Netherlands, Dordrecht, 1977. doi: 10.1007/978-94-009-9992-3.
- S. Türk, G. Daschiel, A. Stroh, Y. Hasegawa, and B. Frohnapfel. Turbulent flow over superhydrophobic surfaces with streamwise grooves. *J. Fluid Mech.*, 747:186–217, 2014. doi: 10.1017/jfm.2014.137. doi: 10.1017/jfm.2014.137.
- C. Vanderwel and B. Ganapathisubramani. Effects of spanwise spacing on large-scale secondary flows in rough-wall turbulent boundary layers. *J. Fluid Mech.*, 774:1–12, 2015. doi: 10.1017/jfm.2015.292.
- C. Vanderwel, A. Stroh, J. Kriegseis, B. Frohnapfel, and B. Ganapathisubramani. The instantaneous structure of secondary flows in turbulent boundary layers. *J. Fluid Mech.*, 862:845–870, 2019. doi: 10.1017/jfm.2018.955.
- Z.-Q. Wang and N.-S. Cheng. Time-mean structure of secondary flows in open channel with longitudinal bedforms. *Adv. Water Resour.*, 29(11):1634–1649, 2006. doi: 10.1016/j.advwatres.2005.12.002.
- D. D. Wangsawijaya and N. Hutchins. Investigation of unsteady secondary flows and large-scale turbulence in heterogeneous turbulent boundary layers. *J. Fluid Mech.*, 934, 2022. doi: 10.1017/jfm.2021.1152.
- D. D. Wangsawijaya, R. Baidya, D. Chung, I. Marusic, and N. Hutchins. The effect of spanwise wavelength of surface heterogeneity on turbulent secondary flows. *J. Fluid Mech.*, 894, 2020. doi: 10.1017/jfm.2020.262.
- D. Willingham, W. Anderson, K. T. Christensen, and J. M. Barros. Turbulent boundary layer flow over transverse aerodynamic roughness transitions: Induced mixing and flow characterization. *Phys. Fluids*, 26(2):025111, 2014. doi: 10.1063/1.4864105.
- J. C. Wyngaard. *Turbulence in the Atmosphere*. 2010. doi: 10.1017/CBO9780511840524.
- J. Yang and W. Anderson. Numerical Study of Turbulent Channel Flow over Surfaces with Variable Spanwise Heterogeneities: Topographically-driven Secondary Flows Affect Outer-layer Similarity of Turbulent Length Scales. *Flow Turbul. Combust.*, 100(1):1–17, 2017. doi: 10.1007/s10494-017-9839-5.
- A. Zampiron, S. Cameron, and V. Nikora. Secondary currents and very-large-scale motions in open-channel flow over streamwise ridges. *J. Fluid Mech.*, 887:A17, 2020. doi: 10.1017/jfm.2020.8.

List of Figures

1.1	Longitudinal sand dunes in Namib Desert in (a) (taken and adopted from (NASA Earth Observatory 2020)) and cloud streets near Antarctica in (b) (taken and adopted from (NASA Earth Observatory 2018)). The black solid line in (a) indicates the alignment of one sand dune ridge with the main flow direction of the prevailing wind out of the south.	2
1.2	Simplified sketch of counter-rotating rolls aligned with longitudinal sand dunes as shown in figure 1.1 (a). The longitudinal sand dunes are located in the updraft region of the counter-rotating rolls. The rolls are aligned with the main flow direction, which is indicated by the mean velocity profile in the right part of the figure. Sketch was adapted and extended from Hanna (1969).	2
2.1	Illustration of the triple decomposition for the streamwise velocity u over a spanwise heterogeneous surface consisting of streamwise-aligned ridges. In the bottom panel the light blue lines represent isolines of constant \bar{u} and the green line indicates the wall-normal location at which the velocity profiles are shown in the upper panel. In the upper panel the instantaneous velocity u is represented by the green line, while the black line indicates the local mean \bar{u} and the dashed black line the global mean $\langle \bar{u} \rangle$	12
2.2	Schematic of secondary motions over spanwise heterogeneous surfaces of strip (a) and ridge-type (b). Ridge-type surfaces are characterised by spanwise differences in the wall elevation, while these are absent or negligible for strip-type surface and the heterogeneity consists of spanwise variations of wall-shear stress. The secondary motions are represented by large-scale counter-rotating vortices, where for strip-type surfaces the upward motion appears above the lower wall-shear stress strip and for ridge-type surfaces above the streamwise-aligned ridges. The light blue lines depict isolines of constant mean streamwise velocity and their up- and downward bulging is associated with low- and high-momentum pathways, respectively. 15	
2.3	Modified wavenumbers of first derivative in (a) and of second derivative in (b) for different differentiation schemes. The purple line in (b) represents a sixth-order compact finite difference scheme which is slightly over-dissipative compared to the exact differentiation scheme.	19
2.4	Illustration of polynomial reconstruction of the alternating direction immersed boundary method in Xcompact3d for a rectangular ridge in the y - z cross-section. The orange line in the bottom panel indicates the grid line along which the reconstruction in the z -direction is illustrated in the upper panel. The Lagrange polynomial is based on the red points in the fluid domain and the interface points, such that the interpolation of the velocity values inside the solid region results in the green points.	21

3.1	Schematic of the open channel domain with alternating rough- and smooth-wall strips at the bottom wall.	26
3.2	Variation of the smooth-wall elevation for fully-resolved roughness cases in (a, b, c) and modelled roughness cases (d, e, f) . Case (a) and (d) corresponds to protruding roughness, (b) and (e) to an intermediate roughness and (c) and (f) to a recessed roughness configuration.	26
3.3	The PFA model functions A and B over the wall-normal distance y normalised using the kinematic viscosity ν and the mean roughness height \bar{k}_r . Adopted from Schäfer et al. (2022b).	28
3.4	Influence of smooth-wall height h on skin friction coefficient C_f in (a) and intensity of secondary motions u_{sm} in (b) for the PFA modelled cases.	31
3.5	Comparison of the streamwise mean velocity profiles between IBM and PFA model cases for three smooth-wall elevations $h = 0$ (a) , $h = 0.97\bar{k}_r$ (b) and $h = 1.70\bar{k}_r$ (c) . In (a) the homogeneous rough PFA case is presented by the light blue line. Adopted from Schäfer et al. (2022b).	33
3.6	Mean streamwise velocity profiles at different spanwise locations $\bar{z} = z/\delta$. The dark blue line shows the centre of the smooth strip at $\bar{z} = 0.0$ and the dark red line the centre of the rough strip at $\bar{z} = 0.5$. The dashed and dotted black lines represent the streamwise mean velocity of the smooth and homogeneous rough case (IBM). Adopted from Schäfer et al. (2022b).	34
3.7	Contours of streamwise mean velocity and the induced secondary motion for resolved roughness cases $(a) - (c)$ and modelled roughness cases $(d) - (l)$. Adopted from Schäfer et al. (2022b).	36
3.8	Spanwise averaged wall-normal dispersive stress profiles for IBM-resolved roughness cases in (a) and PFA-modelled roughness cases in (b) . Adopted from Schäfer et al. (2022b).	38
3.9	Spanwise variation of turbulent kinetic energy for resolved roughness cases in (a) and modelled roughness cases in (b) extracted at $y = 0.115\delta$. Line colours same as in figure 3.8. Adopted from Schäfer et al. (2022b).	39
3.10	Contours of Reynolds shear stress component $\overline{v''w''}$ for resolved roughness cases $(a) - (c)$ and modelled roughness cases with low resolution $(d) - (l)$. The coloured dotted lines corresponds to $\overline{v''w''}/U_b^2$ values of $(\pm 0.0001, \pm 0.0005)$. Isolines of the streamwise mean velocity are shown in grey. Adopted from Schäfer et al. (2022b).	40
4.1	Sketch of the domain of the open-channel flow with streamwise-aligned Gaussian ridges at the wall.	51
4.2	Mean streamwise velocity profile in (a) and mean temperature profile in (b) for varying ridge spacing S scaled in viscous units. Black dashed line indicates smooth-wall case and the ridge height $h_g = 0.1\delta$ is shown by the black dotted line.	53
4.3	Mean streamwise velocity in cross-sectional plane for $Re_\tau = 540$ and varying ridge spacing S . The cross-sectional mean velocity components are illustrated by arrows and are scaled by u_b . Blue crosses indicate position of one secondary motion's cell-centre.	54

4.4	Wall-normal and spanwise cell-centre position of mean secondary motion for different ridge spacings S . Black dashed line indicates linear regression fit of present data and gray dashed line for the experimental data of Zampiron et al. (2020) for $S \leq 2\delta$	55
4.5	Phase-averaged spanwise distribution of mean streamwise velocity at $y = y_{sc}$. The spanwise coordinate z' is scaled with the half-channel height δ in (a) and with the ridge spacing S in (b). Crosses in (a) indicate spanwise position of the closest inflection point to the ridge.	55
4.6	Instantaneous streamwise velocity fluctuations in horizontal plane at $y = 0.5\delta$ for different cases. The black horizontal lines at the outer right figure frame indicate the spanwise position of the ridges.	56
4.7	Contour lines of two-dimensional pre-multiplied streamwise energy spectra $\kappa_x \kappa_z \Phi_{u'u'}(\lambda_x, \lambda_z)$ at wall-normal height $y = 0.5\delta$ for smooth-wall case $S/\delta = \infty$ and different ridge spacings S . Dashed white line indicates $\lambda_z = 2\delta$, which is the spanwise wavelength at which VLSMs are fixed; solid white line illustrates that spanwise wavelength of turbulent structures increases linear with the streamwise wavelength (Cameron et al. 2017).	57
4.8	Pre-multiplied spectra $\kappa_x \Phi_{u''u''}(\lambda_x, z)$ (a) and co-spectra $\kappa_x \Phi_{u''w''}(\lambda_x, z)$ (b) for different S and $y = 0.5\delta$. The black vertical lines at the outer top figure frame indicate the spanwise position of the ridges.	59
4.9	Phase-averaged one-dimensional pre-multiplied spectra of streamwise variance at $y = y_{sc}$ and $z = z_{sc}$ for different S in (a). The position of $\lambda_{x,SCI}$ at the maximum value of $\kappa_x F_{u''u''}$ is indicated by open circles. In (b) streamwise wavelength of secondary current instability $\lambda_{x,SCI}$ over vorticity thickness δ_ω for different ridge spacings S . Black triangles indicate ridge cases $1 \leq S/\delta \leq 2$ of Zampiron et al. (2020) and black dashed line represents the fitted relation $\lambda_{x,SCI}/\delta \approx 9.0\delta_\omega/\delta$ for these cases. Black solid line represents linear fitted relation $\lambda_{x,SCI}/\delta \approx 7.24\delta_\omega/\delta + 2.03$ based on cases $S \leq 2\delta$. In (b) the cases $h_g = 0.05\delta$ and $h_g = 0.025\delta$ for $S = 4\delta$ are indicated by a red open circle and square, respectively.	60
4.10	Instantaneous random fluctuations of wall-normal vorticity ω_y'' in horizontal plane at $y = 0.5\delta$ for case $S = 2\delta$ and $S = 12\delta$. The black horizontal lines at the outer right figure frame indicate the spanwise position of the ridges.	61
4.11	Influence of the ridge height on mean streamwise velocity \bar{u} in (a), pre-multiplied spectra $\kappa_x F_{u''u''}(\lambda_x, z)$ in (b) and co-spectra $\kappa_x F_{u''w''}(\lambda_x, z)$ in (c). The spectra are shown at the wall-normal location $y = 0.5\delta$. Top row presents $h_g = 0.05\delta$ and bottom row $h_g = 0.025\delta$. The colour ranges of the spectra are the same as used in figure 4.3 and 4.8.	62
4.12	Relative energy contribution of POD modes in (a, c) and cumulative energy contribution in (b, d). Spanwise window size to compute POD modes corresponds to S , except for case $S = 12$ with $L_{z,win} = 4\delta$ and smooth-wall case $S = \infty$ with $L_{z,win} = 2\delta$. In (c, d) the spanwise window size is $L_{z,win} = 2\delta$ for all S cases	63

4.13	First six POD spatial modes of streamwise component $\Phi_{u,k}$ ($k = 1, \dots, 6$) for different ridge spacings S . The arrows represent the wall-normal $\Phi_{v,k}$ and spanwise component $\Phi_{w,k}$ of the k th POD mode. The spanwise window size used for the POD is $L_{z,win} = S$	65
4.14	Spatial POD modes for different ridge spacings S ($k = 1, \dots, 6$). The colour contour represents the streamwise component and the arrows the cross-sectional components of the POD modes. The same spanwise window size $L_{z,win} = 2\delta$ is used for all cases.	66
4.15	Influence of ridge height on POD modes for case $S = 4\delta$ in the first two rows and the smooth-wall case is shown in the bottom row. The colour contour represents the streamwise component and the arrows the cross-sectional components of the POD modes. A window size $L_{z,win} = 2\delta$ is used for all cases.	67
4.16	First two POD time coefficients of case $S = 4\delta$ normalised by the root mean square value of the respective time coefficient. For clarity the time coefficients are shown for a smaller subset of the complete time series. Dashed black lines indicate values of $a_i = \pm 1$. coloured vertical line in top panel indicate different conditions of POD time coefficients: dark blue $a_1/a_{1,rms} \geq 1$ and $-1 < a_2/a_{2,rms} < 1$; light blue $a_1/a_{1,rms} \geq 1$ and $a_2/a_{2,rms} \leq -1$; yellow $-1 < a_1/a_{1,rms} < 1$ and $a_2/a_{2,rms} \leq -1$; orange $a_1/a_{1,rms} \leq -1$ and $a_2/a_{2,rms} \leq -1$; red $a_1/a_{1,rms} \leq -1$ and $-1 < a_2/a_{2,rms} < 1$	68
4.17	Conditional-averaged velocities arranged by the first two POD time coefficients for smooth-wall case and ridge cases $S \leq 2\delta$. Contours represent conditional-averaged mean streamwise velocity \bar{u}^c and arrows cross-sectional velocity components \bar{v}^c and \bar{w}^c . Conditions based on value of single time coefficients: $a_1/a_{1,rms} \geq 1$ in (a), $a_1/a_{1,rms} \leq -1$ in (b), $a_2/a_{2,rms} \geq 1$ in (c), $a_2/a_{2,rms} \leq -1$ in (d), and conditions based on values of two time coefficients: $1 > a_1/a_{1,rms} > -1$ and $1 > a_2/a_{2,rms} > -1$ in (e), $a_1/a_{1,rms} \geq 1$ and $a_2/a_{2,rms} \geq 1$ in (f), $a_1/a_{1,rms} \leq -1$ and $a_2/a_{2,rms} \geq 1$ in (g), $a_1/a_{1,rms} \geq 1$ and $a_2/a_{2,rms} \leq -1$ in (h), $a_1/a_{1,rms} \leq -1$ and $a_2/a_{2,rms} \leq -1$ in (i).	69
4.18	Comparison of sum of conditional averaged mean streamwise velocities \bar{u}^c and mean streamwise velocity \bar{u} of case $S = 2\delta$ in (a), case $S = \delta$ in (b) and case $S = 0.5\delta$ in (c). First two column represent conditional averages from 4.17 (c, d), and their sum is shown in the third column. The used colour bar is the same as in figure 4.17.	70
5.1	Sketch of the numerical channel domain with streamwise-aligned Gaussian ridges at the walls. Adopted from Schäfer et al. (2022a)	76
5.2	Parameter space of Rayleigh Ra and bulk Reynolds number Re_b in (a). The green marks in (a) indicate the flow parameters of the present simulations and solid and dashed black lines represent isolevels with constant Ri_b . The dashed lines highlight Ri_b values, for which Re -effects are investigated. The Nusselt number Nu over bulk Reynolds number Re_b of the turbulent mixed convection channel flow from Pirozzoli et al. (2017) for various Rayleigh numbers is shown in (b). The vertical solid black line separates the transitional and turbulent range for pure forced convection flows. Adopted from Schäfer et al. (2022a)	78

5.3	Nusselt number Nu as a function of Rayleigh number Ra in (a) and bulk Reynolds number Re_b in (b) for different ridge spacings S . In (a) the bulk Reynolds number $Re_b = 2800$ and in (b) the Rayleigh number $Ra = 10^7$ is kept constant. Adopted from Schäfer et al. (2022a)	82
5.4	Stanton number St in (a) and ratio of St to C_f in (b) as a function of bulk Richardson number Ri_b for different ridge spacings S . The selected cases have values of the Reynolds number Re_k in a similar range. Adopted from Schäfer et al. (2022a)	83
5.5	Instantaneous temperature fluctuation fields at the half-channel height position $y = \delta$ for varying Richardson number Ri_b and different spanwise spacing S of the Gaussian ridges. The spanwise position of the ridges is indicated by the black lines on the right outer frame of the figures. The horizontal sections show the full simulation domain of size $16\delta \times 8\delta$. Adopted from Schäfer et al. (2022a)	84
5.6	Instantaneous temperature fluctuation fields at $y = 0.15\delta$ for varying Richardson number Ri_b and different spanwise spacing S of the Gaussian ridges. Adopted from Schäfer et al. (2022a)	86
5.7	Effect of Richardson number Ri_b and S on wall-normal profiles of streamwise mean velocity and mean temperature for different ridge spacings S scaled in wall units. Adopted from Schäfer et al. (2022a)	87
5.8	Effect of spanwise spacing on mean streamwise velocity for forced convection case $Ri_b = 0$ ($Re_b = 2800$, $Ra = 0$). The spanwise spacing of the Gaussian ridges ranges from $S = 4\delta$ (a), $S = 2\delta$ (b), $S = \delta$ (c) and $S = 0.5\delta$ (d). Arrows indicate cross-sectional velocity components and are scaled by bulk velocity. Adopted from Schäfer et al. (2022a)	88
5.9	Effect of buoyancy on streamwise mean velocity and temperature for constant $Re_b = 2800$ and $S = 4\delta$ for different Richardson numbers. Arrows indicate cross-sectional velocity components and are scaled by bulk velocity. Adopted from Schäfer et al. (2022a)	89
5.10	Effect of ridge spacing S on streamwise mean velocity and temperature for constant $Ri_b = 10$. Adopted from Schäfer et al. (2022a)	90
5.11	Volume-averaged coherent turbulent kinetic energy of the cross-sectional components for low Ri_b cases scaled in wall-units in (a) and for large Ri_b cases scaled in free-fall units in (b). Adopted from Schäfer et al. (2022a)	92
5.12	Velocity and temperature variances scaled in inner units for low bulk Richardson number Ri_b cases at transition from forced convection structures to streamwise rolls. Black vertical dotted line indicates the height of the Gaussian ridges. Adopted from Schäfer et al. (2022a)	94
5.13	Velocity and temperature variances scaled in free fall units for high bulk Richardson number Ri_b cases at transition from streamwise rolls to natural convection. Adopted from Schäfer et al. (2022a)	96
5.14	Short-time-averaged coherent kinetic energy K_c^s of case $Ri_b = 1$ and different ridge spacings over time. The values of K_c^s are averaged for time intervals $\Delta t_s \approx 3.4t_f$. Adopted from Schäfer et al. (2022a)	97

5.15	Streamwise and short-time-averaged temperature \overline{T}^s over time and spanwise position at the wall-normal channel centre location $y = \delta$ for cases $Ri_b = 1$. The spanwise position of the ridges is indicated by the black lines at the top figure frame. Adopted from Schäfer et al. (2022a)	98
5.16	Mean temperature in cross-section in (a) and short-time-averaged temperature \overline{T}^s over time and spanwise position at $y = \delta$ in (b) for cases $Ri_b = 1$ and ridge spacing $S = 4\delta$ and $S = 8\delta$ with ridges only placed at the bottom wall of the channel.	99
5.17	Effect of turbulent Reynolds number Re_k an spanwise ridge spacing S on mean temperature for case $Ri_b = 0.024$, $Re_k = 252-263$ ($Ra = 7.5 \cdot 10^5$, $Re_b = 2800$) on the left side and case $Ri_b = 0.025$, $Re_k = 826-841$ ($Ra = 10^7$, $Re_b = 10000$) on the right side. The spanwise spacing of the Gaussian ridges ranges from $S = 2\delta$ (a), $S = \delta$ (b) and $S = 0.5\delta$ (c). Adopted from Schäfer et al. (2022a)	100
5.18	Instantaneous temperature fluctuation fields at the half-channel height position $y = \delta$ for cases $Ri_b = 3.2$ with $Re_k = 236-263$ ($Ra = 10^7$, $Re_b = 885$) in (a) and $Re_k = 695-792$ ($Ra = 10^8$, $Re_b = 2800$) in (b) for different spanwise ridge spacing S . Adopted from Schäfer et al. (2022a)	101
A.1	Contours of local wall-normal mean velocity \tilde{v} for resolved roughness cases (a) - (c) and modelled roughness cases (d) - (l). Isolines of the streamwise mean velocity are shown in grey. Adopted from Schäfer et al. (2022b).	130
A.2	Contours of turbulent kinetic energy k for resolved roughness cases (a) - (c) and modelled roughness cases with low resolution (d) - (l). Isolines of the streamwise mean velocity are shown in grey. Adopted from Schäfer et al. (2022b).	131
A.3	Mean profiles for validation study for $Ra = 10^7$ and different bulk Reynolds numbers. The marks indicate the reference data of Pirozzoli et al. (2017), for clarity every fifth data point is shown. Adopted from Schäfer et al. (2022a).	133

List of Tables

3.1	Global flow properties from DNS of the homogeneous smooth- and rough-wall cases and the heterogeneous smooth-rough cases with varying smooth-wall distance h . Adopted from Schäfer et al. (2022b).	30
4.1	Global flow properties of DNS of smooth-wall case and streamwise-aligned Gaussian ridges with varying ridge spacing S and different ridge heights h_g	52
5.1	List of simulation configurations with flow parameters and resulting global flow properties. Adopted from Schäfer et al. (2022a)	81
A.1	Simulation parameters and global flow properties of validation study for Rayleigh-Bénard and Mixed Convection at $Ra = 10^6$ and $Ra = 10^7$. The skin friction coefficient and Nusselt number of Pirozzoli et al. (2017) are given by $C_{f,ref}$ and Nu_{ref} . Adopted from Schäfer et al. (2022a)	132
A.2	Grid refinement study for pure forced convection, mixed convection and pure Rayleigh-Bénard flow with Gaussian ridges at each side wall ($S/\delta = 1$). The domain size for the study is set to $L_x \times L_y \times L_z = 8\delta \times 2\delta \times 4\delta$. Adopted from Schäfer et al. (2022a).	135

Nomenclature

Abbreviations

Symbol	Description
CFR	Constant flow rate
CPG	Constant pressure gradient
DNS	Direct numerical simulation
HMP	High-momentum pathway
HMR	High-momentum region
IBM	Immersed boundary method
LMP	Low-momentum pathway
LMR	Low-momentum region
LSM	Large scale motion
PFA	Parametric forcing approach
POD	Proper orthogonal decomposition
SVD	Singular value decomposition
VLSM	Very-large-scale motion

Greek symbols and variables

Symbol	Description
α	Temperature diffusivity
α_1	Parameter of compact finite difference scheme for first derivative
α_2	Parameter of compact finite difference scheme for second derivative
β	Thermal expansion coefficient
δ	Half-channel height
δ_{eff}	Effective half-channel height
δ_{ij}	Kronecker delta
δ_ν	Viscous length scale
ε	Turbulent dissipation

ϵ	Porosity of rough surface
κ	Von Kármán constant
κ_x	Wavenumber in streamwise direction
κ_s	Scaled wavenumber
$\kappa_{s,c}$	Cutoff wavenumber
κ_s'	Modified wavenumber for first derivative
κ_s''	Modified wavenumber for second derivative
κ_T	Constant for temperature log-law relation
λ	Wavelength
λ_k	k -th eigenvalue of POD
ν	Kinematic viscosity
Φ_k	k -th spatial POD mode
μ	Dynamic viscosity
Π	Pressure gradient
ρ	Density
ρ_0	Reference density
σ	Parameter for spanwise extent of Gaussian ridges
Σ	Diagonal matrix with singular values of data matrix
τ	Total shear stress
τ_w	Wall-shear stress
τ_{ij}	Stress tensor
φ	Phase shift

Latin symbols and variables

Symbol	Description
a_1	Parameter of compact finite difference scheme for first derivative
a_2	Parameter of compact finite difference scheme for second derivative
a_k	k -th time coefficient of POD
A	PFA coefficient
A_w	Constant in velocity log-law
A_T	Constant in temperature log-law
A_{Gauss}	Cross-sectional area occupied by a single ridge
b_1	Parameter of compact finite difference scheme for first derivative
b_2	Parameter of compact finite difference scheme for second derivative

B	PFA coefficient
c_2	Parameter of compact finite difference scheme for second derivative
c_D	Effective drag coefficient for PFA model
C_f	Skin friction coefficient
\mathbf{C}	Correlation matrix
f	Frequency
$F_{IBM,i}$	Volume force term for immersed boundary method in i -direction
$F_{r,i}$	Forcing term of parametric forcing approach in i -direction
f_i	Volume body force term in i -direction
g	Gravitational acceleration
h	Smooth-wall strip height
h_g	Height of Gaussian ridge
i	Complex number
k	Turbulent kinetic energy
k_r	Roughness height
k_k	Empirical constant for PFA model
K_c	Volume-averaged coherent kinetic energy of cross-sectional velocity components
L	Obukhov length
L_s	Spanwise wavelength of one pair of alternating smooth- and rough-wall strips
L_x	Streamwise domain length
L_y	Wall-normal domain length
L_z	Spanwise domain length
n_g	Number Gaussian ridges
N_ϕ	Number of repeating phases for phase-averaging
N_x	Number grid points in streamwise direction
N_y	Number grid points in wall-normal direction
N_z	Number grid points in spanwise direction
Nu	Nusselt number
Pr	Prandtl number
q	Total heat flux
q_w	Wall heat flux
Q_s	Heat source term
Q_{IBM}	Heat source term for immersed boundary method

Ra	Rayleigh number
Re_b	Bulk Reynolds number
Re_τ	Friction Reynolds number
Ri_b	Bulk Richardson number
s	Total surface area of roughness
s_f	Total ‘windward-projected’ surface area of roughness
s_{ij}	Fluctuating rates of strain tensor
S	Spanwise spacing between streamwise-aligned ridges
St	Stanton number
t	Time
T	Temperature
T_0	Reference temperature
T_τ	Friction temperature
\mathcal{T}'	Turbulent transport of turbulent kinetic energy
u_i	Velocity component in i -direction
u_b	Bulk velocity
u_τ	Friction velocity
U	Data matrix for POD
ΔU	Spanwise difference between maximum and minimum streamwise velocity
W	Width of smooth-wall strip
W_ϕ	Spanwise width of phase window for phase-averaging
x	Streamwise coordinate
Δx	Distance between streamwise grid points
y	Wall-normal coordinate
z	Spanwise coordinate
z_i	Boundary layer depth

Mathematical operators

Symbol	Description
$\partial(\cdot)/\partial t$	Partial derivative in time
$\partial(\cdot)/\partial x_i$	Partial derivative in spatial i -direction
$D(\cdot)/Dt$	Material derivative
$\overline{(\cdot)}$	Time- and streamwise average

$\overline{(\cdot)}^s$	Short time average
$\langle(\cdot)\rangle$	Spanwise average

A Appendix

A.1 Additional cross-plane figures for ridge- and strip-type induced secondary motions

"As a supplementary illustration of the statements made in [chapter 3], the wall-normal spanwise distribution of the wall-normal velocity \tilde{v} and the turbulent kinetic energy k are shown for the resolved and modelled roughness cases in figures A.1 and A.2, respectively. The comparison of the wall-normal velocity distribution between the resolved and modelled roughness cases in figure A.1 demonstrates that the PFA model introduces a larger wall offset for the heterogeneous roughness to resemble the resolved roughness case for a given smooth-wall height h . Figure A.2 illustrates for ridge-type roughness that the turbulent kinetic energy distribution is characterised by local peaks at the transition between smooth and rough strips, while for strip-type roughness these are absent and an increased turbulent kinetic energy is found over the rough strip area. For the [higher] smooth-wall positions of the PFA model in figure A.2 [($k-l$)], two local peaks start to emerge at the transition region, indicating that the smooth wall is now starting to influence the turbulent flow in a ridge-type behaviour."(Schäfer et al. 2022b)

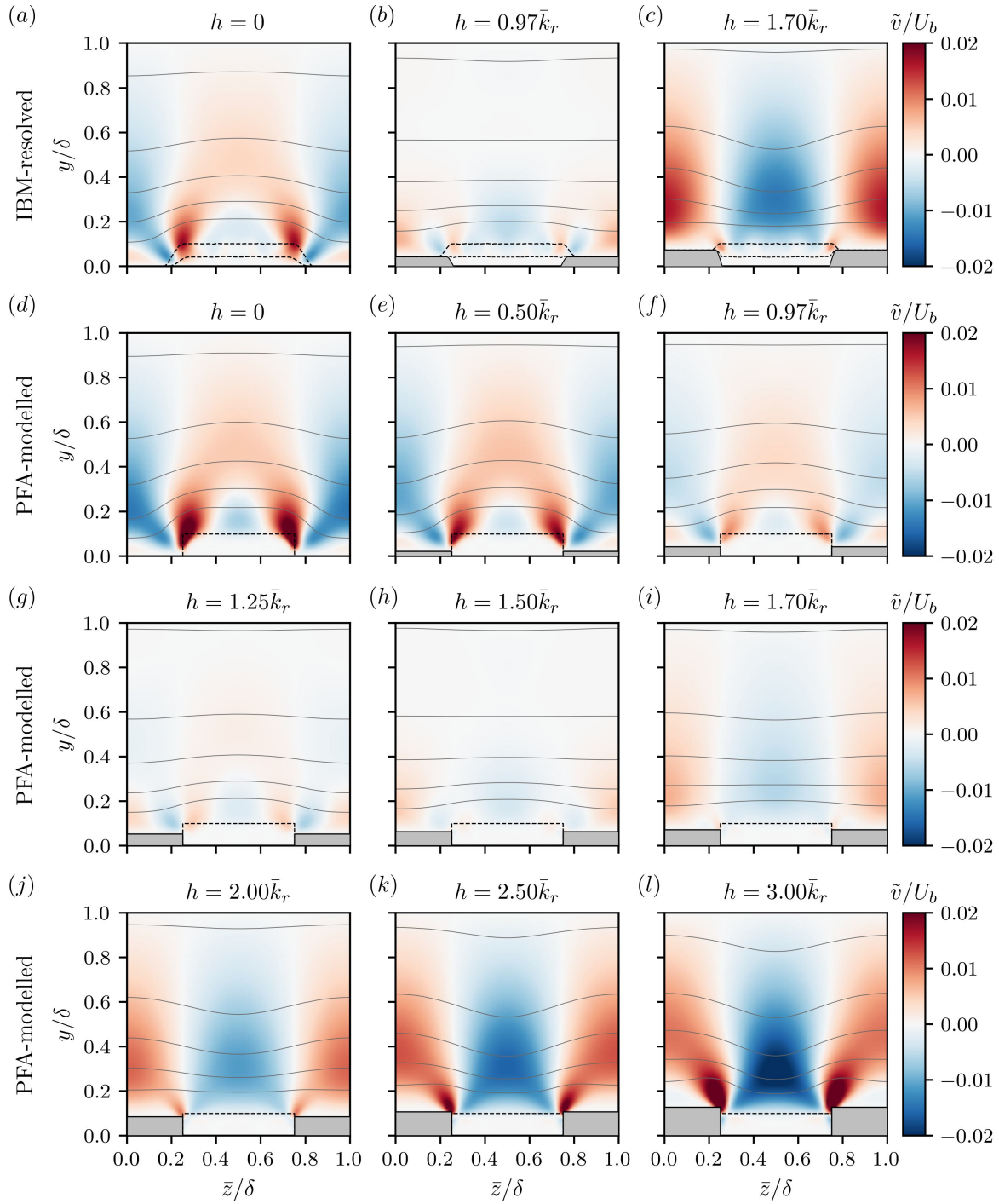


Figure A.1: Contours of local wall-normal mean velocity \tilde{v} for resolved roughness cases (a) - (c) and modelled roughness cases (d) - (l). Isolines of the streamwise mean velocity are shown in grey. Adopted from Schäfer et al. (2022b).

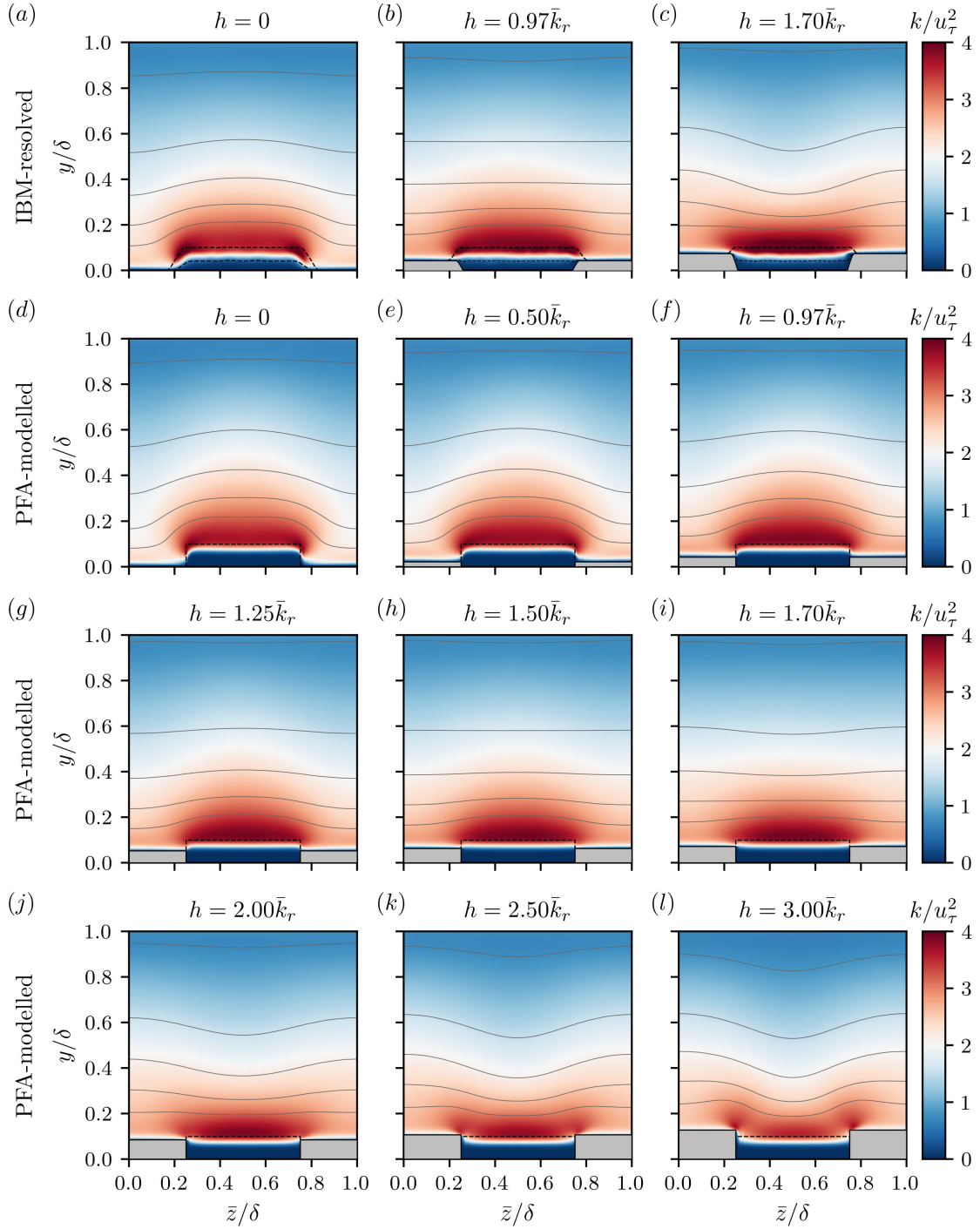


Figure A.2: Contours of turbulent kinetic energy k for resolved roughness cases (a) - (c) and modelled roughness cases with low resolution (d) - (l). Isolines of the streamwise mean velocity are shown in grey. Adopted from Schäfer et al. (2022b).

Ra	Re _b	Ri _b	S/δ	N _x × N _y × N _z	C _f	C _{f,ref}	ε _{C_f}	Nu	Nu _{ref}	ε _{Nu}
10 ⁶	0	∞	∞	512 × 193 × 256	-	-	-	8.257	8.288	0.38%
10 ⁶	158.1	10	∞	512 × 193 × 256	0.0719	0.0745	3.49%	7.284	7.318	0.46%
10 ⁶	500	1	∞	512 × 193 × 256	0.0267	0.0277	3.69%	6.312	6.356	0.70%
10 ⁶	1581	0.1	∞	512 × 193 × 256	0.0100	0.0102	1.79%	6.798	6.780	0.26%
10 ⁶	5000	0.01	∞	1024 × 257 × 512	0.00712	0.00715	0.39%	12.360	12.419	0.48%
10 ⁷	0	∞	∞	1024 × 257 × 512	-	-	-	15.687	15.799	0.71%
10 ⁷	500	10	∞	1024 × 257 × 512	0.0403	0.0403	0.06%	13.921	14.000	0.56%
10 ⁷	1581	1	∞	1024 × 257 × 512	0.0144	0.0146	1.28%	11.911	11.880	0.26%
10 ⁷	5000	0.1	∞	1024 × 257 × 512	0.00742	0.00754	1.63%	17.112	17.250	0.80%

Table A.1: Simulation parameters and global flow properties of validation study for Rayleigh-Bénard and Mixed Convection at $Ra = 10^6$ and $Ra = 10^7$. The skin friction coefficient and Nusselt number of Pirozzoli et al. (2017) are given by $C_{f,ref}$ and Nu_{ref} . Adopted from Schäfer et al. (2022a)

A.2 Validation of code implementation for mixed convection flows in Xcompact3d

"The implementation of the active scalar in Xcompact3d is validated against the Rayleigh-Bénard and mixed convection cases of Pirozzoli et al. (2017) at $Ra = 10^6$ and 10^7 . For a direct comparison the same grid resolution is used as in Pirozzoli et al. (2017), which is given in Table A.1. The mean difference in skin friction coefficient and Nusselt number with respect to the reference data is indicated by ε_{C_f} and ε_{Nu} . While for the skin friction coefficient the two low Reynolds number cases at $Re = 10^6$ show deviations up to 3.7%, this is reduced below 1.7% for the higher Rayleigh number cases. The Nusselt number is in very good agreement for both chosen Rayleigh numbers and stays below 0.8% for all simulation cases. The mean velocity and mean temperature profiles, as well as the variances $\overline{u'u'}$ - and $\overline{T'T'}$ -profiles, are shown in Figure A.3 and the comparison to the reference data shows very good agreement between the considered flow cases."(Schäfer et al. 2022a)

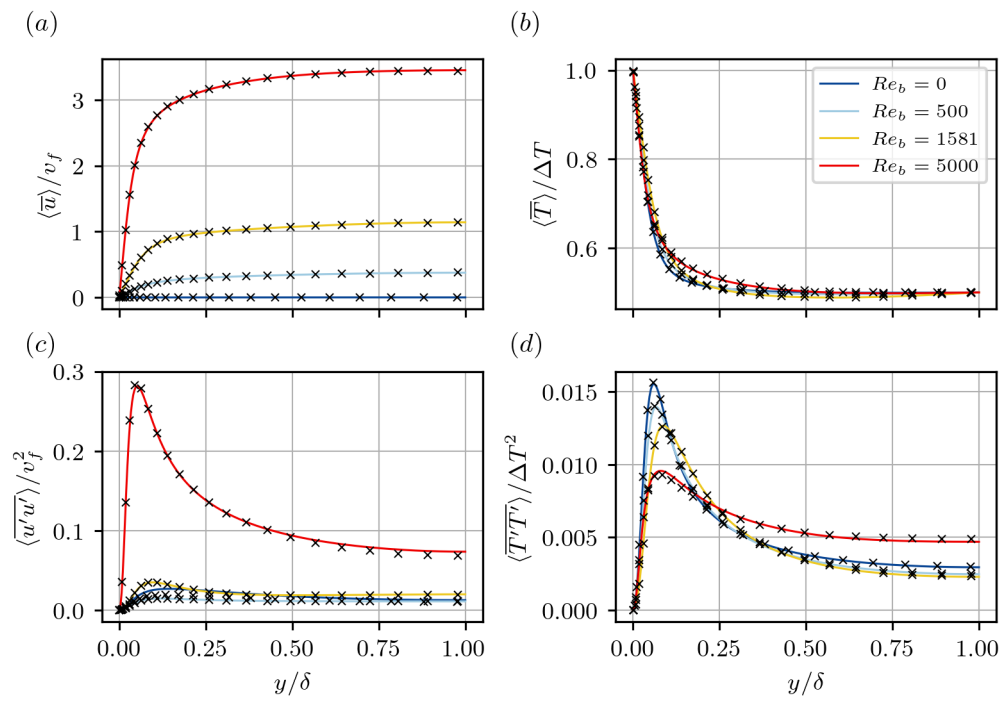


Figure A.3: Mean profiles for validation study for $Ra = 10^7$ and different bulk Reynolds numbers. The marks indicate the reference data of Pirozzoli et al. (2017), for clarity every fifth data point is shown. Adopted from Schäfer et al. (2022a).

A.3 Grid convergence study with Gaussian ridges for mixed convection flows

"The grid resolution requirements for the simulations with Gaussian ridges is studied for different flow configurations to show that the chosen grid resolution is sufficiently fine to capture the investigated flow physics. The grid refinement study is performed for three different flow configurations, namely pure forced convection, mixed convection and pure Rayleigh-Bénard flow. The domain size for this study was reduced to $L_x \times L_y \times L_z = 8\delta \times 2\delta \times 4\delta$ to keep the grid study computationally affordable. In all cases the spanwise spacing of the Gaussian ridges is $S/\delta = 1$, corresponding to four Gaussian ridges at each side wall. The different grid resolutions of the simulation cases and the resulting global flow properties are given in Table A.2."(Schäfer et al. 2022a)

"For the pure forced convection case the mean variation in skin friction coefficient and Nusselt number from the coarsest to the finest grid simulation is within a range of 0.5% and 0.7%, respectively. The grid refinement does not reveal any significant changes in the mean velocity, temperature and covariance profiles between all considered cases (not shown here). In order to satisfy the grid requirements proposed by Pirozzoli et al. (2017) for pure forced convection flows and being conservative with the spanwise grid resolution for the representation of the Gaussian ridges, the grid $N_x \times N_y \times N_z = 256 \times 193 \times 192$ is chosen to be appropriate. This results for the large domain simulation ($L_x \times L_y \times L_z = 16\delta \times 2\delta \times 8\delta$) in a grid of $N_x \times N_y \times N_z = 512 \times 193 \times 384$ for pure convection flows with Gaussian ridges."(Schäfer et al. 2022a)

"The grid refinement study for the mixed convection case is performed at $Ra = 10^7$, which requires a finer grid compared to the grid study of the pure forced convection case at $Re_b = 2800$ according to smooth-wall cases (see Table A.1). Furthermore, we increase the bulk Reynolds number to $Re_b = 5000$ in order to make this grid study more demanding in terms of the requirements of the shear induced turbulence. The mean difference of all cases in C_f and Nu with respect to the finest grid case, lies below 1.81% for the skin friction coefficient and 0.45% for Nusselt number. This demonstrates, that the grid resolution for the plane wall mixed convection cases is already sufficient for the additional numerical representation of Gaussian ridges by the immersed boundary method based on polynomial reconstruction. Similar results are obtained for the pure Rayleigh-Bénard case at $Ra = 10^7$, where the mean difference in Nu with respect to the finest grid case, is below 0.35% for all simulation cases. Consequently, for the investigation of mixed and natural convection at $Ra = 10^7$ a grid of $N_x \times N_y \times N_z = 1024 \times 257 \times 512$ for the large domain cases is chosen. For lower Ra cases, the chosen grid resolution of the pure forced convection study marks the lower bound to sufficiently represent the Gaussian ridges in these cases."(Schäfer et al. 2022a)

Ra	Re _b	Ri _b	S/δ	N _x × N _y × N _z	C _f (·10 ⁻³)	Nu	Δt _{tot} //t _b	Δt _{tot} //t _f
0	2800	0	1	256 × 193 × 128	8.834	7.991	4719	-
0	2800	0	1	192 × 193 × 192	8.766	7.957	4719	-
0	2800	0	1	256 × 193 × 192	8.781	7.958	4719	-
0	2800	0	1	256 × 193 × 256	8.822	7.997	5271	-
0	2800	0	1	256 × 257 × 192	8.823	8.014	4719	-
10 ⁷	5000	0.1	1	512 × 193 × 192	8.265	18.098	5423	864
10 ⁷	5000	0.1	1	512 × 193 × 256	8.201	18.170	4254	677
10 ⁷	5000	0.1	1	512 × 257 × 192	8.341	18.216	4301	684
10 ⁷	5000	0.1	1	512 × 257 × 256	8.194	18.081	4150	660
10 ⁷	5000	0.1	1	512 × 257 × 320	8.193	18.163	4123	657
10 ⁷	0	∞	1	512 × 193 × 192	0	16.974	-	1171
10 ⁷	0	∞	1	512 × 193 × 256	0	16.999	-	1026
10 ⁷	0	∞	1	512 × 257 × 192	0	16.921	-	1038
10 ⁷	0	∞	1	512 × 257 × 256	0	17.034	-	1135
10 ⁷	0	∞	1	512 × 257 × 320	0	16.981	-	1052

Table A.2: Grid refinement study for pure forced convection, mixed convection and pure Rayleigh-Bénard flow with Gaussian ridges at each side wall ($S/\delta = 1$). The domain size for the study is set to $L_x \times L_y \times L_z = 8\delta \times 2\delta \times 4\delta$. Adopted from Schäfer et al. (2022a).